Search for Supersymmetry with Hadronically and Leptonically Decaying Tau Leptons at the ATLAS Experiment

Dissertation
zur
Erlangung des Doktorgrades (Dr. rer. nat.)
der
Mathematisch-Naturwissenschaftlichen Fakultät
der
Rheinischen Friedrich-Wilhelms-Universität Bonn

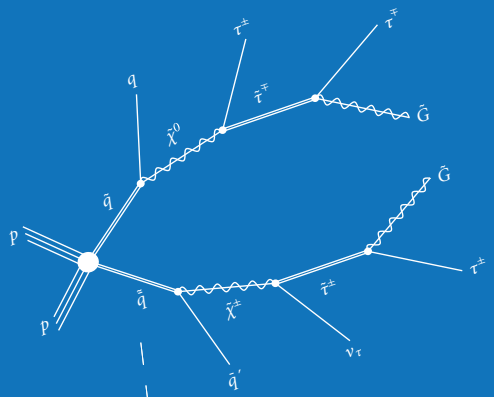

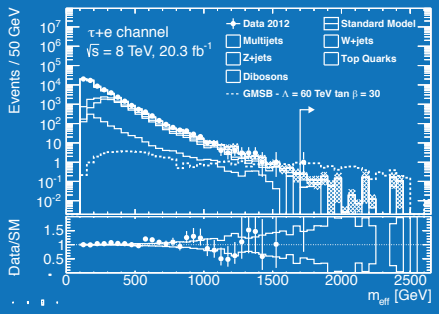

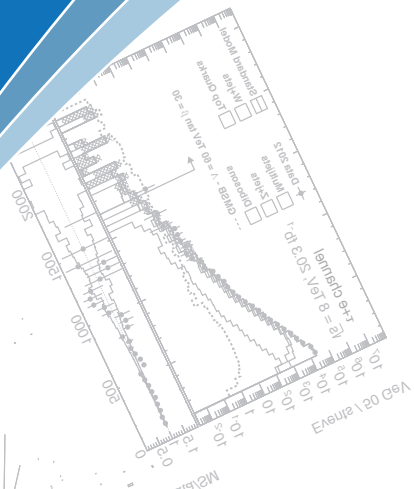

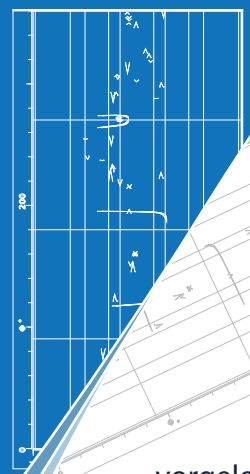

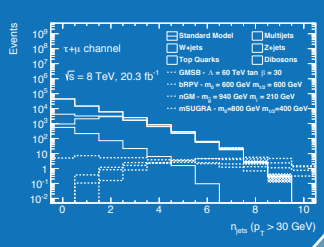

vorgelegt von
Martin Johannes Schultens
aus
Kirchen (Sieg)

Bonn 2016

Search for Supersymmetry with Hadronically and Leptonically Decaying Tau Leptons at the ATLAS Experiment

Dissertation
zur
Erlangung des Doktorgrades (Dr. rer. nat.)
der
Mathematisch-Naturwissenschaftlichen Fakultät
der
Rheinischen Friedrich-Wilhelms-Universität Bonn

vorgelegt von

Martin Johannes Schultens

aus
Kirchen (Sieg)

Bonn 2016

Dieser Forschungsbericht wurde als Dissertation von der Mathematisch-Naturwissenschaftlichen Fakultät der Universität Bonn angenommen und ist auf dem Hochschulschriftenserver der ULB Bonn `http://hss.ulb.uni-bonn.de/diss_online` elektronisch publiziert.

1. Gutachter:	Prof. Dr. Klaus Desch
2. Gutachter:	Prof. Dr. Jochen Dingfelder
Tag der Promotion:	29.11.2016
Erscheinungsjahr:	2017

To my parents.

Contents

CHAPTER 1

Introduction

"First, there's the room you can see through the glass – that's just the same as our drawing room, only the things go the other way. I can see all of it when I get upon a chair – all but the bit behind the fireplace. Oh! I do so wish I could see THAT bit!"

—Lewis Carroll, Through the Looking-Glass

Elementary Particle Physics

Since the beginning of the 20th century our understanding of nature has fundamentally changed. Physicists discovered a variety of subatomic particles and developed a theory to describe the elementary constituents of all matter as well as three out of the four fundamental forces that cause particles to interact. This theory is called the Standard Model of particle physics.

On a macroscopic level we only encounter two of the fundamental forces. While the effects of the gravitational force are obvious to everyone, some consequences of the electromagnetic interaction are more subtle but very important. Without it, no solid matter could form. All interactions between macroscopic objects that are not caused by gravity, are the result of the electromagnetic force. The other two forces can only be observed by performing dedicated experiments. The first one is the strong force which keeps protons and neutrons bound together in the atomic nucleus. Moreover, it also binds together the nucleons' basic constituents – the quarks. The second force is the weak force which is responsible e.g. for the beta decay.

The Standard Model describes all these forces but gravity. This fact alone can serve as motivation to find a more general theory. However, there are more reasons why physicists are not satisfied with our current understanding of nature. So far, the Standard Model proved itself to be a tremendously successful theory. It predicted particles like the Z and W bosons, the top quark and the Higgs boson – all these particles were eventually discovered in experiments. The Higgs boson was the last missing piece in the "Standard Model puzzle". But this theory has its limitations. For instance, it fails to explain the origin of dark matter. It also does not provide a solution to the hierarchy problem. A theory that describes physics beyond the Standard Model (BSM) and offers solutions to some of these issues is Supersymmetry (SUSY).

In an effort to find BSM physics a common approach is to investigate particles produced at particle colliders such as the Large Hadron Collider (LHC). Supersymmetric particles might emerge in these highly energetic collisions and can be studied by thorough analysis of the events that could contain their decay products. Due to their large mass, these new particles would appear with a high transverse momentum. Another characteristic feature of supersymmetric decay chains are particles that interact only weakly. They cannot be detected directly but lead to an imbalance in the momentum of all visible particles, called the missing transverse momentum $E_{\mathrm{T}}^{\mathrm{miss}}$. Aiming at event attributes like this enables physicists to select kinematic regions which are dominantly populated by supersymmetric processes. Any significant excess

in the event count over the expectation from the Standard Model can then be interpreted as evidence for new physics.

Supersymmetry offers a large variety of different models with a large parameter space. The choice of model affects the phenomenology of the theory and as a consequence supersymmetric decays could manifest themselves in very different ways. Because of this, there are many ongoing searches performed by different analysis groups at the ATLAS experiment. Each focuses on different final states and uses specialized selections which are tailored for specific SUSY models. Since the models that are considered for this thesis feature the appearance of multiple tau leptons, the tau lepton plays the key role for defining the signature. Furthermore, electrons and muons are considered in the selection as well as jets and missing transverse momentum.

About this Thesis

This thesis describes a search for supersymmetric particles produced in proton-proton collisions at the ATLAS experiment at the LHC. It is part of an ongoing combined analysis which incorporates different final states with tau leptons. Previous results were obtained from 2011 data at a center-of-mass energy of $\sqrt{s} = 7$ TeV [1]. The results that are presented in this thesis have been published in [2] and are based on 20 fb^{-1} of $\sqrt{s} = 8$ TeV data that were collected in 2012. The final states covered by this thesis include tau leptons and light leptons (an electron or a muon). Final states containing only tau leptons are covered by two other analysis channels. Those and previous analyses are described in other PhD theses [3–5].

This document is structured as follows. Chapter 2 provides a condensed description of the Standard Model and its limitations. As a possible solution to some of the remaining issues of the Standard Model, Supersymmetry is introduced. Four specific SUSY scenarios are investigated in this thesis. A discussion of their phenomenology motivates the considered signatures and therefore the event selection. At the end of the chapter a brief overview of the current status of Supersymmetry is presented.

Chapter 3 focuses on the experimental setup. After an introduction to the Large Hadron Collider, the ATLAS experiment and its various subdetectors are described in detail. This enables the reader to understand the identification and reconstruction of physics objects. The last section of this chapter deals with the simulation and data taking of physics events at ATLAS.

Chapter 4 starts with a motivation and description of the baseline selection of the analysis together with a refinement of the physics object selection criteria. Given this, the resulting Standard Model processes which lead to similar final states are studied. The correct description of Standard Model processes in simulated events is tested and possible deviations are corrected.

To obtain the best separation of signal and background an optimization of the event selection is performed, which is described at the beginning of chapter 5. The background and signal predictions in those optimized kinematic regions are then compared to observed data, taking into account uncertainties of statistical nature and uncertainties arising from limited detector precision or theoretical considerations. Based on the fact that no significant deviation from the Standard Model prediction is observed, the result is interpreted in terms of exclusion limits in the parameter spaces of the four investigated SUSY models.

In chapter 6 the possibility for improvement in the exclusion limit setting is explored. In the approach that is presented here the shapes of kinematic variables rather than the total event counts are exploited to calculate exclusion limits. The final chapter 7 presents a summary of the analysis and an outlook for future search efforts.

CHAPTER 2

Physics of the Standard Model and Beyond

The first chapter of this thesis is dedicated to the motivation behind supersymmetric extensions (SUSY) to the Standard Model of particle physics.

The first the sections (2.1–2.3) provide a brief overview of the Standard Model an its limitations. This is followed by a descriptions of the basic concepts of supersymmetry (2.4). After that, the phenomenological aspects of this theory are discussed to motivate the choice of final states used in the analysis (2.5). The last section of this chapter provides a general overview about the status of searches for supersymmetric particles at the Large Hadron Collider.

2.1 Particles and Their Interactions

In the search for a fundamental description of processes observed on a macroscopic scale, physicists of the 20th century discovered a set of basic building blocks of all matter. Up to today, these building blocks are considered to be *elementary particles*. Together with their interactions they are described by the *Standard Model* (SM) of particle physics [6–9] . An illustration of the Standard Model is displayed in figure 2.1. It will be briefly discussed on an empirical basis in this section.

There are two classes of elementary particles which are those with spin $\frac{1}{2}$, called fermions, and those with integer spin, called bosons. Fermions make up matter, while bosons describe the interactions between different particles. The matter particles can be further categorized into six flavors of quarks (in red in figure 2.1) and six types of leptons (blue), which both come in three generations. All observed ordinary macroscopic matter is made from first generation fermions. The second and third generation particles have the same properties as those from the first generation, but larger masses. Of particular interest for this thesis are the charged lepton from the third generation, the tau lepton, and its corresponding counterparts from the first and second generation – the electron and the muon. For each fermion an anti-particle with opposite electrical charge exists. In this thesis usually no distinction is made between particles and antiparticles. Statements about electrons, muons and tau leptons for example include their respective antiparticles as well. Finally, each quark comes in three *color charges* which are called red, green and blue. Anti-quarks respectively carry anti-color.

Three of the four fundamental forces are described by the Standard Model – the electromagnetic force, the weak force and the strong force. These fundamental interactions need mediators which are depicted in green in figure 2.1. The electromagnetic force carrier is the photon, while the strong force is mediated by the gluon and the weak force by the W and Z bosons. The mediators couple to different groups of particles and therefore not every particle can interact via every force. The gluon only couples to color-charged

particles and the photon only to electrically charged particles. The participation of the particles in the three interactions is indicated by the three layers of gray in figure 2.1.

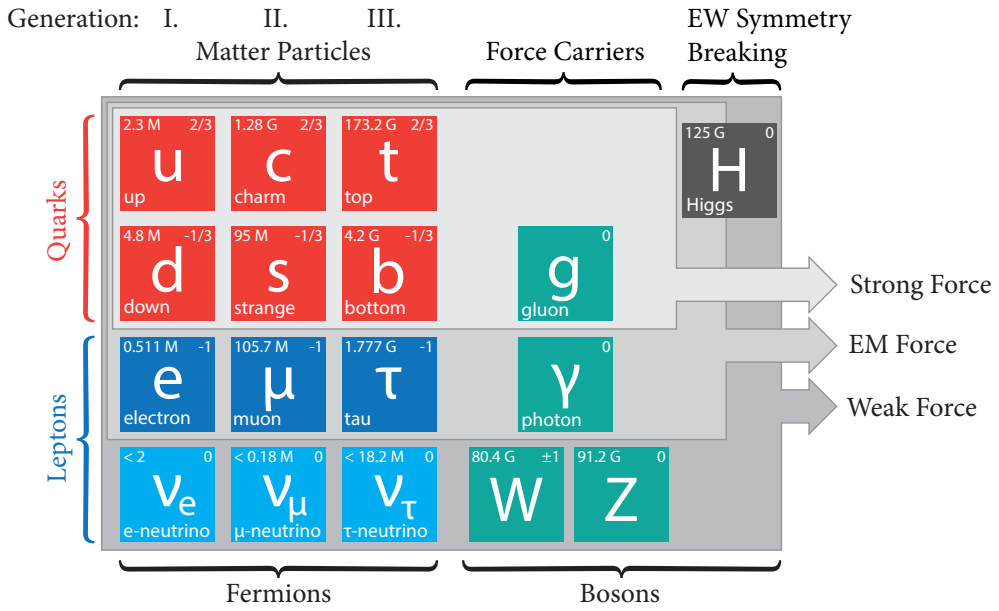

Figure 2.1: An illustration of the Standard Model of particle physics with three generations of quarks (red) and leptons (blue), the force carrying bosons (green) and the Higgs particle. The number in the upper left corner of each particle is the mass in eV as provided by [10]. The upper right corner shows the electrical charge.

2.2 Constructing the Standard Model Lagrangian

In this section the basic theoretical concepts of the Standard Model [6–9] are briefly discussed. More detailed descriptions of the formalism can be found e.g. in [11, 12].

The Standard Model is a quantum field theory which describes the motion of particles by the Euler-Lagrange equation

$$\frac{\partial}{\partial x_\mu}\left(\frac{\partial \mathcal{L}}{\partial(\partial\psi/\partial x_\mu)}\right) - \frac{\partial \mathcal{L}}{\partial \psi} = 0, \tag{2.1}$$

where ψ is the field in dependence of x_μ and $\mathcal{L}$ is the Lagrangian density.

The Standard Model formalism needs to describe all known particles together with their interactions, be invariant under Poincaré transformations and be renormalizable. Furthermore, it must be invariant under local gauge transformations obeying the symmetry given by the group $SU(3)_\mathrm{C} \times SU(2)_\mathrm{L} \times U(1)_\mathrm{Y}$. Here, $SU(3)_\mathrm{C}$ describes the strong interaction and $SU(2)_\mathrm{L} \times U(1)_\mathrm{Y}$ describes the unification of electromagnetic and weak interactions. The subscripts denote restrictions of the couplings to particles with color charge (C), hypercharge (Y) and left-handed fermions (L).

2.2.1 Quantum Electrodynamics

Quantum electrodynamics (QED) describes the interactions of relativistic particles due to the electromagnetic force. The underlying symmetry group is $U(1)$. The Lagrangian for QED must be invariant under

the local gauge transformation $\psi(x) \to e^{i\alpha(x)}\psi(x)$. The Lagrangian of the Dirac equation is

$$\mathcal{L} = i\overline{\psi}\gamma_\mu\partial^\mu - m\overline{\psi}\psi, \tag{2.2}$$

where $\partial^\mu \equiv \partial/\partial x_\mu$ and γ^μ are the Dirac matrices. To achieve local gauge invariance for 2.2, the derivative must be replaced by the covariant derivative

$$D_\mu \equiv \partial_\mu - ieA_\mu, \tag{2.3}$$

where the field A_μ transforms as

$$A_\mu \to A_\mu + \frac{1}{e}\partial_\mu\alpha(x). \tag{2.4}$$

The introduction of the new gauge field A_μ represents the photon and requires an additional term in the Lagrangian which corresponds to the kinetic energy. This term needs to be gauge invariant as well. With the field strength tensor

$$F_{\mu\nu} = \partial_\mu A_\nu - \partial_\nu A_\mu \tag{2.5}$$

we obtain the full Lagrangian for quantum electrodynamics

$$\mathcal{L}_{\text{QED}} = \overline{\psi}(i\gamma^\mu D_\mu - m)\psi - \frac{1}{4}F^{\mu\nu}F_{\mu\nu}. \tag{2.6}$$

2.2.2 Electroweak Unification

A unified description of the electromagnetic and the weak forces was proposed by Glashow, Salam and Weinberg [6–8] in the 1960s. Experimental evidence for this model was found at the Gargamelle experiment in 1973 with the observation of weak neutral currents between neutrinos and electrons [13]. The results could only be explained by a massive, neutral mediator of the observed interaction. This mediator had been predicted by the electroweak theory. The bosons of the weak theory, $W^\pm$ and Z^0, were eventually discovered at the UA1 and UA2 experiments within the predicted mass ranges in 1983 [14–17].

The weak interaction couples to left-handed particles and right-handed antiparticles. The electromagnetic interaction is independent of the chirality. Therefore, interactions in the electroweak theory arise from the $SU(2)_\text{L} \times U(1)_\text{Y}$ gauge symmetry, where the $SU(2)_\text{L}$ only affects the isospin of left-handed fermions and $U(1)_\text{Y}$ transformations conserves the hypercharge. For a lepton-neutrino pair the according Lagrangian is

$$\begin{aligned}\mathcal{L}_{\text{EW}} = {} & \overline{\chi}_\text{L}\gamma^\mu\left(i\partial_\mu - g\frac{1}{2}\vec{\tau}\cdot\vec{W}_\mu - g'\frac{Y}{2}B_\mu\right)\chi_\text{L} \\ & + \overline{e}_\text{R}\gamma^\mu\left(i\partial_\mu - g'\frac{Y}{2}B_\mu\right)e_\text{R} - \frac{1}{4}\vec{W}_{\mu\nu}\cdot\vec{W}^{\mu\nu} - \frac{1}{4}B_{\mu\nu}B^{\mu\nu},\end{aligned} \tag{2.7}$$

where $\chi_\text{L} = (\nu_\ell, \ell)_\text{L}$ is a left-handed fermion doublet, g, g' are the coupling constants and $\vec{\tau}$ are the Pauli spin matrices. The field strength tensors are given by

$$B^{\mu\nu} = \partial^\mu B^\nu - \partial^\nu B^\mu, \tag{2.8}$$

$$W_i^{\mu\nu} = \partial^\mu W_i^\nu - \partial^\nu W_i^\mu - g\varepsilon^{ijk}W_j^\mu W_k^\nu. \tag{2.9}$$

The charged bosons $W^{\pm}$ are described by the fields W^1_μ and W^2_μ by

$$W^{\pm}_\mu = \sqrt{\frac{1}{2}}\left(W^1_\mu \mp i W^2_\mu\right), \tag{2.10}$$

while the neutral fields W^3_μ and B_μ mix to generate the physical mass eigenstates

$$A_\mu = B_\mu \cos\theta_W + W^3_\mu \sin\theta_W \text{ and} \tag{2.11}$$

$$Z_\mu = -B_\mu \sin\theta_W + W^3_\mu \cos\theta_W, \tag{2.12}$$

where mixing is described by the *Weinberg* angle $\sin^2\theta_W \approx 0.231$ [10]. Here A_μ corresponds to the photon and Z_μ to the Z^0 boson.

2.2.3 Electroweak Symmetry Breaking

The symmetry of electroweak theory as described above leaves the gauge bosons and fermions massless. Adding mass terms to the Lagrangian however, would break the gauge invariance. In the Standard Model this issue is resolved by introducing the Higgs mechanism of electroweak symmetry breaking [18–20]. Four additional fields are introduced in a isospin doublet with hypercharge $Y = 1$:

$$\phi = \begin{pmatrix}\phi^+\\ \phi^0\end{pmatrix} = \frac{1}{\sqrt{2}}\begin{pmatrix}\phi_1 + i\phi_2\\ \phi_3 + i\phi_4\end{pmatrix}. \tag{2.13}$$

This doublet is incorporated into the Lagrangian as

$$\mathcal{L}_{\mathrm{H}} = \left|\left(i\partial_\mu - g\vec{\tau}\cdot\vec{W}_\mu - g'\frac{Y}{2}B_\mu\right)\phi\right|^2 - \underbrace{\left(\mu^2\phi^\dagger\phi + \lambda\left(\phi^\dagger\phi\right)^2\right)}_{V_{\mathrm{H}}}, \tag{2.14}$$

where the second term of the equation is the Higgs potential V_{H}. The parameter λ is the self-coupling and bounds the field from below. By choosing a negative mass parameter $\mu^2 < 0$ the resulting potential obtains its minimum at $\phi^\dagger\phi = -\frac{\mu^2}{2\lambda}$. The two imaginary components ϕ_2 and ϕ_4 and the real component ϕ_1 can be set to zero. With $v^2 \equiv \phi_3^2 = -\frac{\mu^2}{\lambda}$ this leaves:

$$\phi_0 = \begin{pmatrix}0\\ 1/\sqrt{2}v\end{pmatrix}. \tag{2.15}$$

Expanding the ground state by a real scalar field $h(x)$ as

$$\phi(x) = \frac{1}{\sqrt{2}}\begin{pmatrix}0\\ v + h(x)\end{pmatrix} \tag{2.16}$$

results in electroweak symmetry breaking. This leaves the photon massless, but generates masses for $W^{\pm}$ and Z^0. Furthermore, an additional scalar particle – the Higgs boson H – is created. The resulting masses of $W^{\pm}$, Z^0 and H are

$$m_W = \frac{1}{2}vg, \qquad m_Z = \frac{1}{2}v\sqrt{g^2 + g'^2} \qquad \text{and} \qquad m_H = \sqrt{2\lambda}\,v. \tag{2.17}$$

In 2.7 gauge invariance excludes fermionic mass terms. This can also be solved by the introduced Higgs doublet and the $SU(2)_{\mathrm{L}} \times U(1)_{\mathrm{Y}}$ invariant *Yukawa* Lagrangian which for electrons is

$$\mathcal{L} = -G_e \left(\overline{\nu}_e \overline{e}\right)_{\mathrm{L}} \begin{pmatrix} \phi^+ \\ \phi^0 \end{pmatrix} e_{\mathrm{R}} - G_e \overline{e}_{\mathrm{R}} \left(\phi^-, \overline{\phi}^0\right) \begin{pmatrix} \nu_e \\ e \end{pmatrix}_{\mathrm{L}}. \tag{2.18}$$

After using 2.16 for symmetry breaking and gauging away all fields but the neutral Higgs field as done before, $m_e = \frac{G_e v}{\sqrt{2}}$ can be identified as the mass parameter and the Lagrangian becomes

$$\mathcal{L} = -m_e \overline{e} e - \frac{m_e}{v} \overline{e} e h. \tag{2.19}$$

This can be performed similarly for the other leptons and for the quarks as well.

2.2.4 Quantum Chromodynamics

The LHC is a proton collider and therefore the interaction of proton constituents is an important part of the considered physics. The description of the strong force is formulated in *Quantum Chromodynamics* (QCD) [21]. Similarly to the construction of 2.6 the QCD Lagrangian is obtained by requiring local gauge invariance under transformation of a symmetry group which in this case is $SU(3)_{\mathrm{C}}$.

Eight gauge fields G^a_μ are introduced which correspond to eight different gluons. The field tensor is given by

$$G^a_\mu = \partial_\mu G^a_\nu - \partial_\nu G^a_\mu - g_S f_{abc} G^b_\mu G^c_\nu, \tag{2.20}$$

where f_{abc} are the structure constants of the $SU(3)_{\mathrm{C}}$ group and g_S is the coupling constant of the strong interaction.

With the $SU(3)_{\mathrm{C}}$ generators T_a that commute as $[T_a, T_b] = i f_{abc} T_c$, the Lagrangian is given by

$$\mathcal{L}_{\mathrm{QCD}} = \overline{q}(i\gamma^\mu \partial_\mu - m) - g_S(\overline{q}\gamma^\mu T_a q) G^a_\mu - \frac{1}{4} G^a_{\mu\nu} G^{\mu\nu}_a. \tag{2.21}$$

Since the mediating gluons also carry color charge, they couple to themselves where three and four gluon vertices are allowed.

QCD features two peculiarities which are a result of the running of the strong coupling constant. The first one is that even though gluons are massless particles, the reach of the strong force is limited due to *confinement* [22]. It excludes the existence of free colored particles. The self-coupling of gluons results in a force between separated quarks that increases with the distance between them. These quarks therefore hadronize either as a quark-antiquark pair (mesons) or to a bound state of three quarks (hadrons) to form a color-singlet. The second feature is *asymptotic freedom* [23, 24], which expresses the fact that the strong coupling constant decreases with higher energies. At short length scales therefore, quarks can be considered quasi-free.

Due to the fact that protons are not elementary particles the theoretical description of proton collisions at the LHC is rather complicated. Protons are made up from three valence quarks, gluons and sea-quarks which are virtual quark-antiquark pairs constantly created from the vacuum before disappearing again. A generic term for these proton constituents is *partons*. Each parton carries a fraction x_i of the total proton momentum. Therefore, in a proton proton collision two partons with unknown momentum interact with each other.

The cross-section of a process producing a particle X from a proton proton collision is described by parton distribution functions (PDF). The PDF $f_i(x, Q^2)$ gives the probability of finding a parton i with

momentum fraction x with a momentum transfer Q^2. The cross-section of the process $pp \to X$ is then given by

$$\sigma_{pp\to X} = \sum_{ij} \int dx_1 dx_2 f_i(x_1, Q^2) f_j(x_2, Q^2) \hat{\sigma}_{ij\to X}, \tag{2.22}$$

where $\hat{\sigma}$ is the partonic cross-section. The parton distribution functions have to be determined experimentally for different values of Q for various processes which are then extrapolated to obtain the description of the full kinematic range. They are provided for example by the MSTW [25] and CTEQ [26] groups.

2.3 Limitations of the Standard Model

The Standard Model provides a very successful description of particle physics over several orders of magnitude in energy. However, there are also some fundamental issues with this theory. In this section three of these issues are discussed: the hierarchy problem, dark matter and the unification of forces. These issues are the motivation for ongoing searches for physics beyond the Standard Model.

2.3.1 The Hierarchy Problem

The Higgs mass as given in 2.17 undergoes loop corrections from every particle that couples to the Higgs field. Figure 2.2 shows example contributions from a fermionic and a bosonic loop. With the Yukawa coupling $-\lambda_f H\bar{f}f$ for fermions the loop in figure 2.2a results in a correction [27]

$$\Delta m_H^2 = -\frac{|\lambda_f|^2}{8\pi^2}\Lambda_{\mathrm{UV}}^2 + \ldots, \tag{2.23}$$

where Λ_{UV} represents the ultraviolet cut-off scale energy above which the SM does not give a correct description anymore. In the absence of new physics a natural choice for this cut-off would be the *Planck* scale $M_{\mathrm{P}} \approx 2.43 \times 10^{18}$ GeV. It describes the energy where the gravitational force becomes so strong that it needs to be considered too. As a consequence however, the mass correction would be 30 orders of magnitude higher than the required value of m_H at the electroweak scale.

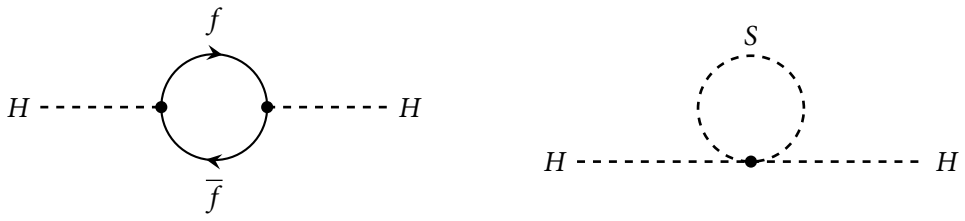

(a) Fermionic loop. (b) Bosonic loop.

Figure 2.2: Loop correction to the Higgs mass for scalar particles S (b) and fermions f (a).

To solve this problem within the SM formalism the parameter m_H^2 would have to be fine-tuned by introducing canceling terms in the Lagrangian. However, this fine-tuning would have to correct the mass over 17 orders of magnitude which does not satisfy the demand for an elegant theoretical model. This flaw in the Standard Model is also called the *hierarchy problem* [28–30].

A more natural way to obtain the needed cancellation of correction terms is the introduction of a new symmetry. Considering the bosonic loop in figure 2.2b yields another correction which is given by

$$\Delta m^2 = \frac{\lambda_S}{16\pi^2}\left[\Lambda_{\mathrm{UV}}^2 - 2m_S^2 \ln\left(\frac{\Lambda_{\mathrm{UV}}}{m_S}\right) + \dots\right]. \tag{2.24}$$

Comparing this correction to the fermionic one from 2.23, it is apparent that a symmetry between fermions and bosons would qualify to introduce such a cancellation due to the relative minus sign between the two different loop corrections [27].

2.3.2 Dark Matter

Astrophysical observations suggest the existence of a so far undiscovered type of matter which interacts gravitationally with visible matter, but is invisible for direct observation itself. Evidence can be found by studying the kinetic properties of galaxy clusters and the rotation curves of galaxies [31–33]. The measurements indicate that the total mass in these galaxies and clusters does not match the mass from visible stars and interstellar gas. The difference is widely considered to be due to unknown elementary particles that do not couple to the electromagnetic or the strong force, but only interact weakly and gravitationally.

Recent measurements by the Planck satellite [34] of temperature fluctuations in the cosmic microwave background indicate that the universe is made up from 69 % dark energy and 26 % dark matter. The baryonic matter contributes only 5 %.

2.3.3 Unification of the Forces

Motivated by the unified description of the electromagnetic and the weak interactions, theorists are searching for a theory that describes all forces of nature in a single model – a *Theory of Everything* (TOE). Another step towards a TOE would be the description of electromagnetic, weak and strong force in a so-called *Grand Unified Theory* (GUT).

Such a theory would embed the $SU(3)_{\mathrm{C}} \times SU(2)_{\mathrm{L}} \times U(1)_{\mathrm{Y}}$ Standard Model symmetry in a more generalized symmetry such as $SU(5)$. For this however, the gauge couplings of the three forces should unite to a single one at an energy scale of $\Lambda_{\mathrm{GUT}} \sim 10^{16}\,\mathrm{GeV}$. Although the couplings do in fact reach similar values they never converge completely in the Standard Model. The introduction of new particles could influence the running of the gauge couplings in such a way that it results in a unification of forces.

2.4 The Minimal Supersymmetric Extension of the Standard Model

Theorists have developed a variety of models of physics beyond the Standard Model which could solve some of the problems discussed in the previous section. One of the most promising among those theories is *supersymmetry* (SUSY) [27, 35–37]. This section provides a brief introduction to the fundamental concepts of supersymmetry. An in-depth overview of this theory is outside of the scope of this thesis and can be found in the cited literature.

2.4.1 Fundamentals of Supersymmetry

As discussed above, a symmetry between bosons and fermions would provide an elegant solution to the hierarchy problem. SUSY imposes such a symmetry by introducing a superpartner for each Standard Model particle. This supersymmetric partner shares the same quantum numbers apart from the spin,

particles		**bosons**	**fermions**	$SU(3)_C$	$SU(2)_L$	$U(1)_Y$
chiral supermultiplets		spin 0	spin ½			
squarks, quarks	Q	$(\tilde{u}_L, \tilde{d}_L)$	(u_L, d_L)	**3**	**2**	$1/3$
(three generations)	$\bar{u}$	$\tilde{\bar{u}}_L = \tilde{u}_R^\dagger$	$\bar{u}_L = (u_R)^c$	$\bar{\mathbf{3}}$	**1**	$-4/3$
	$\bar{d}$	$\tilde{\bar{d}}_L = \tilde{d}_R^\dagger$	$\bar{d}_L = (d_R)^c$	$\bar{\mathbf{3}}$	**1**	$2/3$
sleptons, leptons	L	$(\tilde{\nu}_L, \tilde{e}_L)$	(ν_L, e_L)	**1**	**2**	-1
(three generations)	$\bar{e}$	$\tilde{\bar{e}}_L = \tilde{e}_L^\dagger$	$\bar{e}_L = (e_R)^c$	**1**	**1**	2
higgs, higgsinos	H_u	(H_u^+, H_u^0)	$(\widetilde{H}_u^+, \widetilde{H}_u^0)$	**1**	**2**	1
	H_d	(H_d^0, H_d^-)	$(\widetilde{H}_d^0, \widetilde{H}_d^-)$	**1**	**2**	-1
gauge supermultiplets		spin 1	spin ½			
gluinos, gluons		g	$\tilde{g}$	**8**	**1**	0
winos, W bosons		$W^\pm, W^0$	$\widetilde{W}^\pm, \widetilde{W}^0$	**1**	**3**	0
bino, B boson		B	$\widetilde{B}$	**1**	**1**	0

Table 2.1: Chiral and gauge supermultiplets of the Minimal Supersymmetric Standard Model (adapted from [36]).

which differs by half a unit. That way, each SM fermion corresponds to a supersymmetric boson and each SM boson corresponds to a supersymmetric fermion.

The *Coleman-Mandula* theorem [38] states that the only possible symmetries of the S-matrix are the ones that are generated by the generators of the Poincaré group P_μ and $M_{\mu\nu}$ and additional internal symmetries [39]. However, this is only valid for bosonic generators. Haag, Łopuszański and Sohnius showed that spinor operators allow for a different set of symmetries [40]. Such a supersymmetric spinor operator $\mathcal{Q}$ transforms a fermionic state into a bosonic one and the other way around:

$$\mathcal{Q}|\text{fermion}\rangle = |\text{boson}\rangle, \qquad \mathcal{Q}|\text{boson}\rangle = |\text{fermion}\rangle. \tag{2.25}$$

The supersymmetric algebra in its simplest form satisfies a set of (anti)-commutator equations [36]

$$\{\mathcal{Q}_\alpha, \overline{\mathcal{Q}}_\beta\} = 2(\gamma^\mu)_{\alpha\beta} P_\mu, \tag{2.26}$$

$$\{\mathcal{Q}_\alpha, \mathcal{Q}_\beta\} = \{\overline{\mathcal{Q}}_\alpha, \overline{\mathcal{Q}}_\beta\} = 0, \tag{2.27}$$

$$[P^\mu, \mathcal{Q}_\alpha] = [P_\mu, \overline{\mathcal{Q}}_\alpha] = 0. \tag{2.28}$$

Fermionic and bosonic fields are placed in *supermultiplets*. The *minimal supersymmetric extension of the Standard Model* (MSSM) adds just one additional field for every known SM particle. Each supermultiplet contains both bosons and fermions as listed in table 2.1. The *chiral* or matter supermultiplet contains the SM fermions in form of two-component Weyl-Spinors together with an complex scalar field. The *gauge* supermultiplets contains spin-1 vector bosons and their superpartners, spin ½ chiral fermions.

Combinations of the operators $\mathcal{Q}$ and $\overline{\mathcal{Q}}$ transform one member of a supermultiplet into another one up to space-time translations and rotations. Due to the fact that these operators commute with the squared-mass operator $-P^2$ which itself commutes with space-time translations and rotations, fields in one supermultiplet should have the same eigenvalue of $-P^2$. The masses of particles from one supermultiplet should therefore be of equal mass. Furthermore, $\mathcal{Q}$ and $\overline{\mathcal{Q}}$ also commute with the gauge transformation generators. This means also charge, the weak isospin and color of the superpartners must be the same [27].

In common notation supersymmetric partners of SM particles are labelled with a tilde (~) above the normal symbol. The spin-0 partners of fermions are named by adding the character *s* in front of their normal names. The general names are therefore squarks and sleptons. As described in [27], the right- and left-handed parts of fermions can only behave differently under gauge transformations in the chiral supermultiplets. For that reason, the fermionic members of the chiral multiplet must be the Standard Model fermions. Due to the fact that the left-handed and right-handed parts of the charged fermions transform differently they also have to have their own scalar superpartner. These are indicated by the subscript R and L in table 2.1 which refers to the helicity of their SM partner particle. Since neutrinos are left-handed, there is only one superpartner for each flavor.

With spin 0 the Higgs scalar belongs to the chiral supermultiplet. However, the fermionic superpartner of the Higgs causes a gauge anomaly which does not cancel out. This is solved by introducing a second Higgs supermultiplet with opposite quantum numbers. Furthermore, a single Higgs doublet would not be able to give mass to both up- and down-type quarks. The two Higgs doublets are therefore $(H_{\mathrm{u}}^{+}, H_{\mathrm{u}}^{0})$ and $(H_{\mathrm{d}}^{0}, H_{\mathrm{d}}^{-})$ which couple to up-type (down-type) quarks, respectively [27].

The fermionic superpartners of SM bosons are generally referred to as *gauginos*. They are characterized by the suffix *ino* in their names. The superpartners of gluons are the *gluinos* ($\tilde{g}$), the ones of the $SU(2)_{\mathrm{L}}$ gauge bosons are *winos* $\widetilde{W}_i$ and the partner of the $U(1)$ gauge field is the *bino* ($\widetilde{B}$).

The $SU(3)_{\mathrm{C}} \times SU(2)_{\mathrm{L}} \times U(1)_{\mathrm{Y}}$ invariant *superpotential* of the MSSM is given by [36]

$$W = y_u^{ij} \bar{u}_i Q_j \cdot H_u - y_d^{ij} \bar{d}_i Q_j \cdot H_d - y_e^{ij} \bar{e}_i L_j \cdot H_d + \mu H_u \cdot H_d. \tag{2.29}$$

H_u, H_d, Q_j, L_j, $\bar{u}_i$, $\bar{d}_i$ and $\bar{e}_i$ are the chiral superfields which correspond to the chiral supermultiplets in table 2.1. The superpotential contains the Yukawa interactions of the fermions with the Higgs boson, given by the 3×3 matrices y_u^{ij}, y_d^{ij} and y_e^{ij}. The last term gives the mass terms for the Higgs boson.

2.4.2 Broken Supersymmetry

As discussed earlier, supersymmetric particles should have the exact same mass as their SM partners if SUSY was an exact symmetry. This obviously means that a light and charged particle like the scalar superpartner of the electron would have been already observed in many experiments. But since this is not the case, supersymmetry must be broken. For this, a mechanism is needed which causes the SUSY particles to have higher masses than their SM partners. The breaking should happen spontaneously which means the Lagrangian must be invariant unter supersymmetric transformations, while the vacuum state is not [27].

There is a variety of models with different possible mechanisms to extend the MSSM with this spontaneous symmetry breaking. The ones that are relevant for this thesis are discussed in sections 2.5.2 to 2.5.5. However, since the true origin of the breaking is not known, the MSSM includes it as explicit breaking terms in the Lagrangian. As described in [27], the cancellation of quadratic mass divergences in the hierarchy problem can be preserved by considering a *soft* symmetry breaking. This means the MSSM Lagrangian is of the form

$$\mathcal{L} = \mathcal{L}_{\mathrm{SUSY}} + \mathcal{L}_{\mathrm{soft}}, \tag{2.30}$$

where all gauge and Yukawa interactions are contained in $\mathcal{L}_{\mathrm{SUSY}}$ while $\mathcal{L}_{\mathrm{soft}}$ breaks supersymmetry but only contains mass terms and coupling parameters of positive mass. The Lagrangian including all soft

SUSY breaking terms is given by [36]

$$\mathcal{L}_{\text{soft}} = -\frac{1}{2}\left(M_3\tilde{g}^a\cdot\tilde{g}^a + M_2\widetilde{W}^a\cdot\widetilde{W}^a + M_1\widetilde{B}\cdot\widetilde{B} + \text{ h.c.}\right) \tag{2.31}$$

$$- m^2_{\widetilde{Q}ij}\widetilde{Q}^\dagger_i\cdot\widetilde{Q}_j - m^2_{\tilde{\bar{u}}ij}\tilde{\bar{u}}^\dagger_{Li}\tilde{\bar{u}}_{Lj} - m^2_{\tilde{\bar{d}}ij}\tilde{\bar{d}}^\dagger_{Li}\tilde{\bar{d}}_{Lj} \tag{2.32}$$

$$- m^2_{\widetilde{L}ij}\widetilde{L}^\dagger_i\cdot\widetilde{L}_j - m^2_{\tilde{\bar{e}}ij}\tilde{\bar{e}}^\dagger_{Li}\tilde{\bar{e}}_{Lj} \tag{2.33}$$

$$- m^2_{H_u}H^\dagger_u\cdot H_u - m^2_{H_d}H^\dagger_d\cdot H_d - (bH_u\cdot H_d + \text{ h.c.}) \tag{2.34}$$

$$- a^{ij}_u\tilde{\bar{u}}_{Li}\widetilde{Q}_j\cdot H_u + a^{ij}_d\tilde{\bar{d}}_{Li}\widetilde{Q}_j\cdot H_d + a^{ij}_e\tilde{\bar{e}}_{Li}\widetilde{L}_j\cdot H_d + \text{ h.c.} \tag{2.35}$$

In 2.31 M_3, M_2 and M_1 are the gaugino mass terms (gluino, wino and bino), where the index a runs from 1 to 8 in the gluino term and from 1 to 3 in the wino term. 2.32 contains the squark mass terms, 2.33 the slepton mass terms and 2.34 the higgs mass terms. Finally, 2.35 are the trilinear couplings. The indices i and j run from 1 to 3 in each case.

By this approach more than 100 additional free parameters are introduced to describe all the masses and couplings [41]. There are some constraints, like experimental results on CP and lepton flavor violating processes which would arise by some of these parameters [42]. But the resulting parameter space is still huge. Theoretical models that describe the origin of the symmetry breaking reduce the number of free parameters to a reasonable amount, enabling experimentalists to search for well-defined signatures as described in section 2.5.6.

2.4.3 *R*-Parity

The superpotential given in 2.29 describes the minimal supersymmetric extension of the Standard Model. However, there is a possibility to include additional gauge-invariant and renormalizable terms into the superpotential which are [36]

$$W_{\Delta L=1} = \lambda^{ijk}_e L_i\cdot L_j\bar{e}_k + \lambda^{ijk}_{\text{L}} L_i\cdot Q_j\bar{d}_k + \varepsilon^i_{\text{L}} L_i\cdot H_u \tag{2.36}$$

and

$$W_{\Delta B=1} = \lambda^{ijk}_B\bar{u}_i\bar{d}_j\bar{d}_k. \tag{2.37}$$

However, the terms in 2.36 violate lepton number conservation and those in 2.37 violate baryon number conservation since the superfields carry baryon number $B = 1/3$ for Q_i, $B = -1/3$ for $\bar{u}$, $\bar{d}$ and lepton number $L = 1$ for L_i, $L = -1$ for $\bar{e}$. Such processes are not observed in nature. The presence of the couplings λ_L and λ_B for example allows the decay of a proton into a positron and a neutral pion. This conflicts with the observed life-time of a proton of 2.1×10^{29} years [10].

In order to avoid this problem, the lepton and baryon number violating terms are ruled out by introducing a symmetry, namely the conservation of R parity [43], which is defined by

$$R \equiv (-1)^{3B+L+2S}. \tag{2.38}$$

Here, S is the spin of the particle. All SM particles have $R = +1$ while their supersymmetric partners carry $R = -1$. This forbids the mentioned couplings which would allow a proton to decay. It has also other crucial consequences which affect the phenomenology of the theory.

Since $R = -1$ holds for supersymmetric particles, they can only be produced in pairs from Standard Model particles. Furthermore, a sparticle cannot decay into SM particles only. At the end of each SUSY decay chain there must be therefore the *lightest supersymmetric particle* (LSP) which will be stable. The

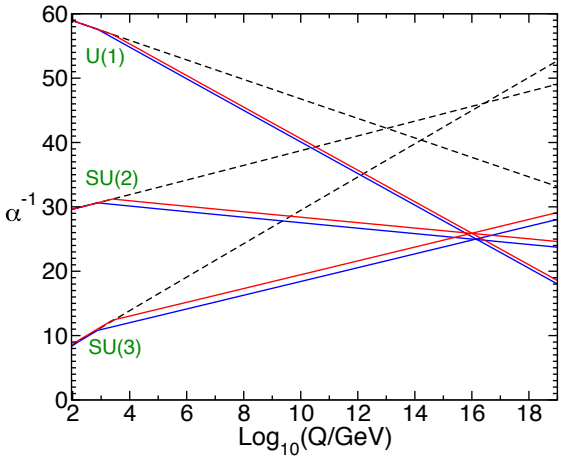

Figure 2.3: Running of the inverse gauge couplings $\alpha_a^{-1}(Q)$ in the Standard Model (dashed lines) and the MSSM (solid lines) [27].

LSP can only interact weakly with normal matter because it would have been already observed otherwise. Hence, the LSP is a good candidate for dark matter as described in section 2.3.2.

2.4.4 Gauge Couplings in the MSSM

In section 2.3.3 the possibility for a more general description of the Standard Model symmetries in form of a GUT model was mentioned. The required convergence of the three SM gauge couplings which is not featured within the Standard Model can be obtained due to the additional particle fields in the MSSM [44–47].

The couplings α_1, α_2 and α_3 are related to the gauge couplings g, g' and g_S by

$$\alpha_2 = \frac{g^2}{4\pi}, \qquad \alpha_3 = \frac{g_S^2}{4\pi} \qquad \text{and} \qquad \alpha_1 = \frac{5}{3}\frac{g'^2}{4\pi} \equiv \frac{g_1^2}{4\pi} \tag{2.39}$$

The dependence of the couplings on the momentum scale is then described by the one-loop order renormalization group equation (RGE) [27]

$$\frac{d}{dt}\left(\alpha_i^{-1}\right) = \frac{b_i}{2\pi}, \tag{2.40}$$

where $t = \ln(Q)$ and Q is the running energy scale. The coefficients b_i are determined by the gauge group:

$$(b_1, b_2, b_3) = \begin{cases} (41/10, -19/6, -7) & \text{SM} \\ (33/5, 1, -3) & \text{MSSM.} \end{cases} \tag{2.41}$$

Integrating gives a linear dependence of the inverse couplings α_i^{-1} on $\ln Q$:

$$\alpha_i^{-1}(Q) = \alpha_i^{-1}(Q_0) + \frac{b_i}{2\pi}\ln\left(\frac{Q}{Q_0}\right), \tag{2.42}$$

which is displayed in figure 2.3 for the Standard Model (dashed lines) and the MSSM (solid lines). The couplings become equal in the case of the MSSM at the scale

$$Q = m_U \approx 10^{16}\ \text{GeV}. \tag{2.43}$$

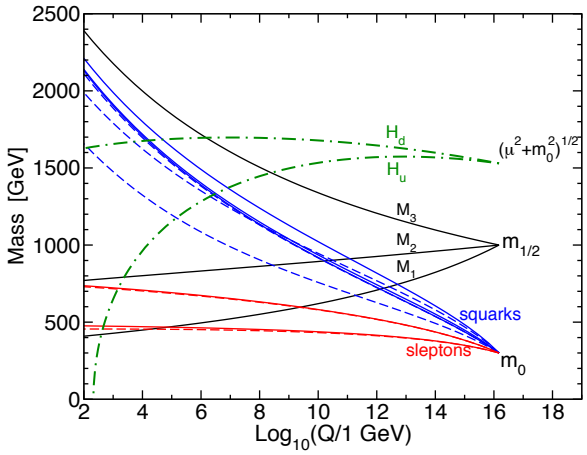

Figure 2.4: RG evolution of scalar and gaugino mass parameters in a mSugra model [27].

It can be assumed that the masses of SUSY fermions and bosons also unify at the GUT scale to mass values called $m_{1/2}$ and m_0:

$$M_3 = M_2 = M_1 = m_{1/2}, \tag{2.44}$$

$$\boldsymbol{m}^2_{\tilde{Q}} = \boldsymbol{m}^2_{\tilde{u}} = \boldsymbol{m}^2_{\tilde{d}} = \boldsymbol{m}^2_{\tilde{L}} = \boldsymbol{m}^2_{\tilde{e}} = m_0^2\mathbf{1}. \tag{2.45}$$

Here, $\mathbf{1}$ is the unit matrix in family space. Using the one-loop RGE for the gaugino mass parameters [36] and 2.40 one can show that the ratio M_a/g_a^2 is constant. Assuming the mass unification at the GUT scale, it follows that

$$\frac{M_1}{g_1^2} = \frac{M_2}{g_2^2} = \frac{M_3}{g_3^2} = \frac{m_{1/2}}{g_U^2} \tag{2.46}$$

is valid at any RG scale. Using 2.39, the Weinberg angle θ_W and the measured values for α_{EM} and α_{s} at the mass scale of the Z [10, 48], one can derive

$$M_1(m_Z) = \frac{\alpha_1(m_Z)}{\alpha_2(m_Z)} M_2(m_Z) = \frac{5}{3}\tan^2\theta_W(m_Z) M_2(m_Z) \approx 0.5 M_2(m_Z) \quad \text{and} \tag{2.47}$$

$$M_3(m_Z) = \frac{\alpha_3(m_Z)}{\alpha_2(m_Z)} M_2(m_Z) = \frac{\sin^2\theta_W(m_Z)}{\alpha_{\mathrm{EM}}(m_Z)} \alpha_{\mathrm{S}}(m_Z) M_2(m_Z) \approx 3.5 M_2(m_Z), \tag{2.48}$$

which results in the following relation between the three gaugino mass parameters

$$M_3(m_Z) : M_2(m_Z) : M_1(m_Z) \approx 7 : 2 : 1. \tag{2.49}$$

This implies that the gluino should be heavier than the particles from the electroweak sector. The dependence of the masses on the renormalization scale is displayed in figure 2.4 for the gaugino mass parameters as well as squarks, sleptons and the Higgs mass parameters in an example from a mSugra model.

2.4.5 Neutralinos and Charginos

In section 2.4.1 a set of four higgsinos and four electroweak gauginos was introduced. Electroweak symmetry breaking causes these fields to mix. The two neutral higgsinos $\widetilde{H}^0_{\mathrm{u}}$ and $\widetilde{H}^0_{\mathrm{d}}$ mix with the bino $\widetilde{B}$ and the neutral wino $\widetilde{W}^0$ to four neutral mass eigenstates which are called *neutralinos*. They are denoted

by $\tilde{\chi}_i^0 (i = 1, 2, 3, 4)$. The charged higgsinos $\widetilde{H}_\mathrm{u}^+$ and $\widetilde{H}_\mathrm{d}^-$ combine with the two charged winos $\widetilde{W}^+$ and $\widetilde{W}^-$ to two charged mass eigenstates called *charginos* which are denoted by $\tilde{\chi}_{1,2}^\pm$.

In gauge-eigenstate basis $\psi^0 = \left(\widetilde{B}, \widetilde{W}^0, \widetilde{H}_\mathrm{d}^0, \widetilde{H}_\mathrm{u}^0\right)$ the mass term of the Lagrangian which describes the neutralino fields is [27]

$$\mathcal{L}_{m_{\chi^0}} = -\frac{1}{2}(\psi^0)^T \boldsymbol{M}_{\tilde{\chi}^0} \psi^0 + \text{h.c.}, \tag{2.50}$$

where the mass matrix is given by

$$\boldsymbol{M}_{\tilde{\chi}^0} = \begin{pmatrix} M_1 & 0 & -c_\beta s_W m_Z & s_\beta s_W m_z \\ 0 & M_2 & c_\beta c_W m_Z & -s_\beta c_W m_z \\ -c_\beta s_W m_Z & c_\beta c_W m_z & 0 & -\mu \\ s_\beta s_W m_Z & -s_\beta c_W m_z & -\mu & 0 \end{pmatrix}, \tag{2.51}$$

with $c_\beta \equiv \cos\beta$, $s_\beta \equiv \sin\beta$, $c_W \equiv \cos\theta_W$, $s_W \equiv \sin\theta_W$. M_1 and M_2 are the gaugino mass parameters and $-\mu$ describe the supersymmetric higgsino mass terms. The mass eigenstates of the neutralinos are obtained by diagonalization. Given 2.47 is valid, the neutralino mixing would depend on only three parameters. The lightest neutralino $\tilde{\chi}_1^0$ is the LSP in many models and therefore a candidate for dark matter [49, 50]. For $m_Z \ll |\mu \pm M_1|, |\mu \pm M_2|$, the neutralino mass eigenstates become a bino-like $\tilde{\chi}_1^0$, a wino-like $\tilde{\chi}_2^0$ and higgsino-like $\tilde{\chi}_3^0$, $\tilde{\chi}_4^0$.

Equivalently, in the gauge-eigenstate basis $(\widetilde{W}^+, \widetilde{H}_\mathrm{u}^+, \widetilde{W}^-, \widetilde{H}_\mathrm{d}^-)$ the chargino mass part of the Lagrangian is given by [27]

$$\mathcal{L}_{m_{\chi^\pm}} = -\frac{1}{2}(\psi^\pm)^T \boldsymbol{M}_{\tilde{\chi}^\pm} \psi^\pm + \text{h.c.}, \tag{2.52}$$

where

$$\boldsymbol{M}_{\tilde{\chi}^\pm} = \begin{pmatrix} \boldsymbol{0} & \boldsymbol{X}^\mathbf{T} \\ \boldsymbol{X} & \boldsymbol{0} \end{pmatrix}, \quad \text{with} \quad \boldsymbol{X} = \begin{pmatrix} M_2 & \sqrt{2} s_\beta m_W \\ \sqrt{2} c_\beta m_W & \mu \end{pmatrix}. \tag{2.53}$$

From this the mass eigenstates can be calculated as shown in [36]. They are given by

$$\begin{pmatrix} |m_{\chi_1^\pm}|^2 \\ |m_{\chi_2^\pm}|^2 \end{pmatrix} = \frac{1}{2}\left(\left(M_2^2 + |\mu|^2 + 2m_W^2\right) \mp \sqrt{\left(M_2^2 + |\mu|^2 + 2m_W^2\right)^2 - 4|\mu M_2 - m_W^2 \sin 2\beta|^2}\right). \tag{2.54}$$

Similar to the neutralinos, for $m_Z \ll |\mu \pm M_1|, |\mu \pm M_2|$ the mass mixing results in a wino-like $\tilde{\chi}_1^\pm$ and a higgsino-like $\tilde{\chi}_2^\pm$.

2.4.6 Sfermion Mass Mixing

Mass mixing can in principle occur between any scalar particles that share the same electric charge, color charge and R-parity. Via the the SUSY breaking parameters in 2.33, 2.32 and 2.35 this mixing would be allowed across families. In this case, the masses are obtained by diagonalization of a 6×6 matrix for up-type quarks $(\tilde{u}_\mathrm{L})$, $(\tilde{c}_\mathrm{L})$, $(\tilde{t}_\mathrm{L})$, $(\tilde{u}_\mathrm{R})$, $(\tilde{c}_\mathrm{R})$, $(\tilde{t}_\mathrm{R})$, down-type quarks $(\tilde{d}_\mathrm{L})$, $(\tilde{s}_\mathrm{L})$, $(\tilde{b}_\mathrm{L})$, $(\tilde{d}_\mathrm{R})$, $(\tilde{s}_\mathrm{R})$, $(\tilde{b}_\mathrm{R})$ and charged sleptons $(\tilde{e}_\mathrm{L})$, $(\tilde{\mu}_\mathrm{L})$, $(\tilde{\tau}_\mathrm{L})$, $(\tilde{e}_\mathrm{R})$, $(\tilde{\mu}_\mathrm{R})$, $(\tilde{\tau}_\mathrm{R})$, and a 3×3 matrix for sneutrinos. However, most of these mixings must be very small due to experimental constraints on flavor changing processes. Because of the large Yukawa couplings and the very different masses of the third family compared to the first and second one, mixing is expected to be only significant in the pairs $(\tilde{t}_\mathrm{L}, \tilde{t}_\mathrm{R})$, $(\tilde{b}_\mathrm{L}, \tilde{b}_\mathrm{R})$, $(\tilde{\tau}_\mathrm{L}, \tilde{\tau}_\mathrm{R})$. The first and second family sfermions have negligible Yukawa couplings and appear in unmixed pairs. This prevents the otherwise large contributions to flavor-changing processes from virtual sparticles.

Considering the mixing that occurs for the third family the $(\text{mass})^2$ terms for $\tilde{t}$, $\tilde{b}$ and $\tilde{\tau}$ in the Lagrangian are written as [27]

$$-\left(\tilde{f}_{\mathrm{L}}^{\dagger}, \tilde{f}_{\mathrm{R}}^{\dagger}\right) \boldsymbol{M}_{\tilde{f}}^{2} \begin{pmatrix} \tilde{f}_{\mathrm{L}} \\ \tilde{f}_{\mathrm{R}} \end{pmatrix}, \tag{2.55}$$

where $\boldsymbol{M}_{\tilde{f}}^{2}$ for tau e.g. leptons is

$$\boldsymbol{M}_{\tilde{\tau}}^{2} = \begin{pmatrix} m_{\tilde{\nu}_{\tau L}, \tilde{\tau}_{\mathrm{L}}}^{2} + m_{\tau}^{2} + \Delta_{\tilde{e}_{\mathrm{L}}} & m_{\tau}(A_0 - \mu \tan\beta) \\ m_{\tau}(A_0 - \mu \tan\beta) & m_{\tilde{\tau}R}^{2} + m_{\tau}^{2} + \Delta_{\tilde{e}_{\mathrm{R}}}, \end{pmatrix} \tag{2.56}$$

with

$$\Delta_{\tilde{e}_{\mathrm{L}}} = \left(-\frac{1}{2} + \sin^2\theta_W\right) m_Z^2 \cos 2\beta \qquad \text{and} \qquad \Delta_{\tilde{e}_{\mathrm{R}}} = \frac{1}{3}\sin^2\theta_W m_Z^2 \cos 2\beta. \tag{2.57}$$

Diagonalizing the matrix $\boldsymbol{M}_{\tilde{\tau}}^{2}$ leads to two mass eigenstates $\tilde{\tau}_1$ and $\tilde{\tau}_2$. The value of $\tan\beta$ defines the magnitude of the mixing in the stau sector. If $\tan\beta$ is relatively small, mixing effects will not be very large, leaving the mass eigenstates relatively close to the gauge eigenstates. For larger values of $\tan\beta$ however the mixing becomes more significant. In this case the mass eigenstates can become much lighter than their counterparts from the other two families. This means the $\tilde{\tau}_1$ becomes the lightest slepton [36]. Assuming staus are the lightest sleptons has the consequence that they are frequently found in the decays of neutralinos and charginos. As a result tau-rich final states are expected in these scenarios, which are the focus of this thesis.

2.5 SUSY Phenomenology at the Large Hadron Collider

Where the previous sections laid the theoretical foundation to motivate searches for supersymmetric particles, this section focuses on their appearance in the experiment. The first part covers the production of sparticles from proton collisions. After that, the particular SUSY models that are relevant for this thesis are discussed. The decay chains of supersymmetric particles in these models define the signatures which motivate the event selection of the analysis described in chapter 5.

2.5.1 Production of Sparticles in Proton-Proton Collisions

Supersymmetric particles are potentially produced by the proton-proton collisions at the Large Hadron Collider. As it was discussed in section 2.4.3, the conservation of R-parity imposes the SUSY particles to be created in pairs. As a consequence, the s-channel contributions to the production processes must be mediated by Standard Model particles, while in the t- and u-channel the interaction takes place via a squark or a gluino. In the final state of all processes there must be an even number of supersymmetric particles.

Emerging from the interaction of two partons, gluon-gluon fusion and gluon-quark fusion producing squarks and gluinos are the dominating processes:

$$gg \to \tilde{g}\tilde{g}, \tilde{q}_i\tilde{q}_j^{*} \tag{2.58}$$

$$gq \to \tilde{g}\tilde{q}_i. \tag{2.59}$$

The contributing Feynman diagrams are displayed in figures 2.5h to 2.5q. However, also quark-antiquark

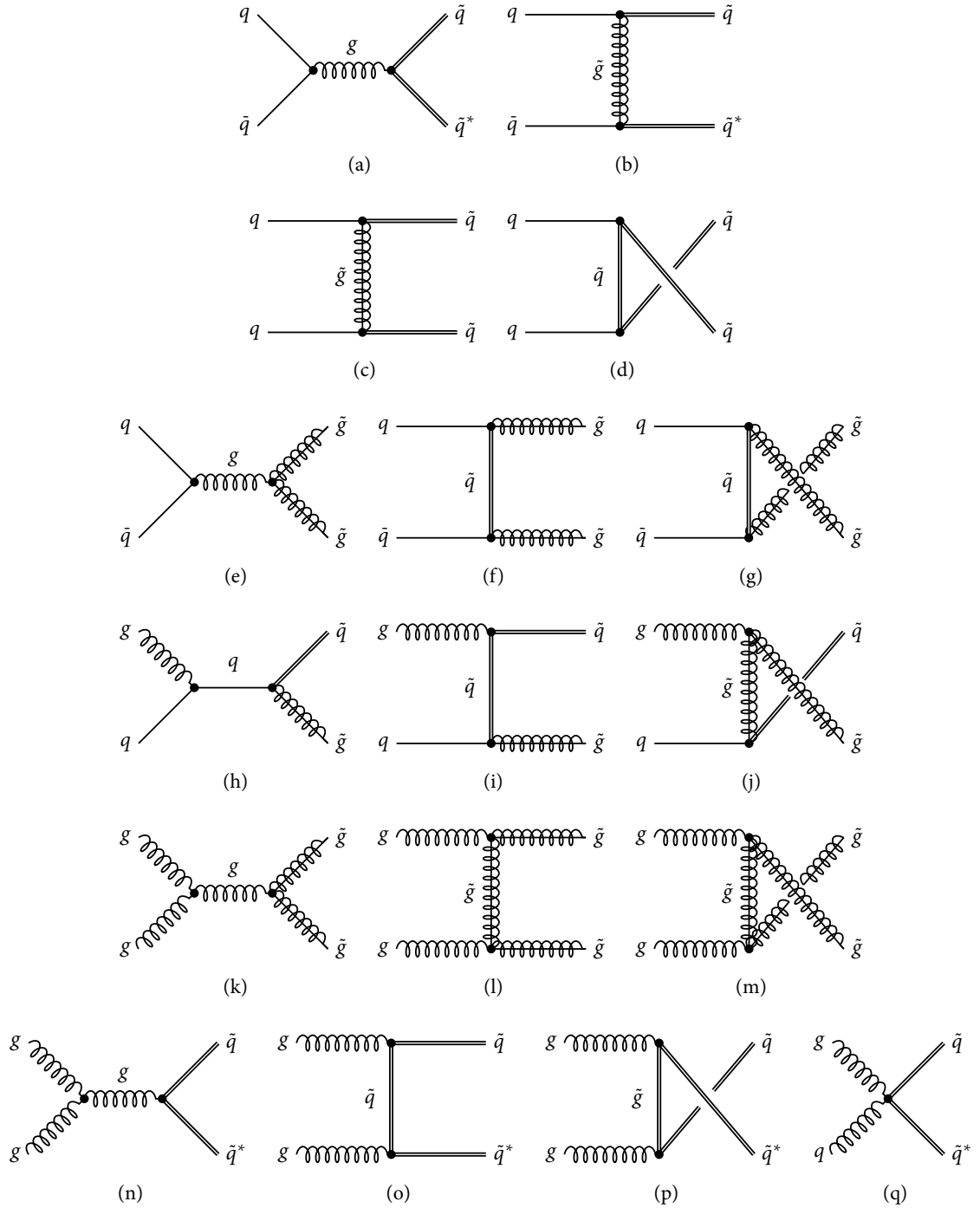

Figure 2.5: Feynman diagrams of gluino and squark production quark-antiquark annihilation, quark-quark, quark-gluon fusion and gluon-gluon fusion (adapted from [27]).

annihilation and quark-quark scattering are possible production modes:

$$q\bar{q} \to \tilde{g}\tilde{g}, \tilde{q}_i\tilde{q}_j^* \tag{2.60}$$

$$qq \to \tilde{g}\tilde{q}_i. \tag{2.61}$$

The according Feynman diagrams for the various processes are displayed in figures 2.5a to 2.5j. These types of processes are referred to as *strong production*. Another possibility for sparticle production are the electroweak processes resulting in the emergence of sleptons, charginos and neutralinos:

$$q\bar{q} \to \tilde{\chi}_i^+\tilde{\chi}_j^-, \tilde{\chi}_i^0\tilde{\chi}_j^0, \qquad u\bar{d} \to \tilde{\chi}_i^+\tilde{\chi}_j^0, \qquad d\bar{u} \to \tilde{\chi}_i^+\tilde{\chi}_j^0, \tag{2.62}$$

$$q\bar{q} \to \tilde{\ell}_i^+\tilde{\ell}_j^-, \tilde{\nu}_\ell\tilde{\nu}_\ell^+, \qquad u\bar{d} \to \tilde{\ell}_{\mathrm{L}}^+\tilde{\nu}_\ell, \qquad d\bar{u} \to \tilde{\ell}_{\mathrm{L}}^-\tilde{\nu}_\ell^*. \tag{2.63}$$

The according Feynman diagrams are depicted in figure 2.6. Via s-channel diagrams sleptons, charginos and neutralinos can be produced through one of the SM mediators of the electroweak force. In the t- and u-channel diagrams neutralinos and charginos are produced via squark exchange. These *electroweak production* processes are less relevant than those from strong production. They become important in SUSY scenarios where the masses of squarks and gluinos are too large to be produced at the given energy level.

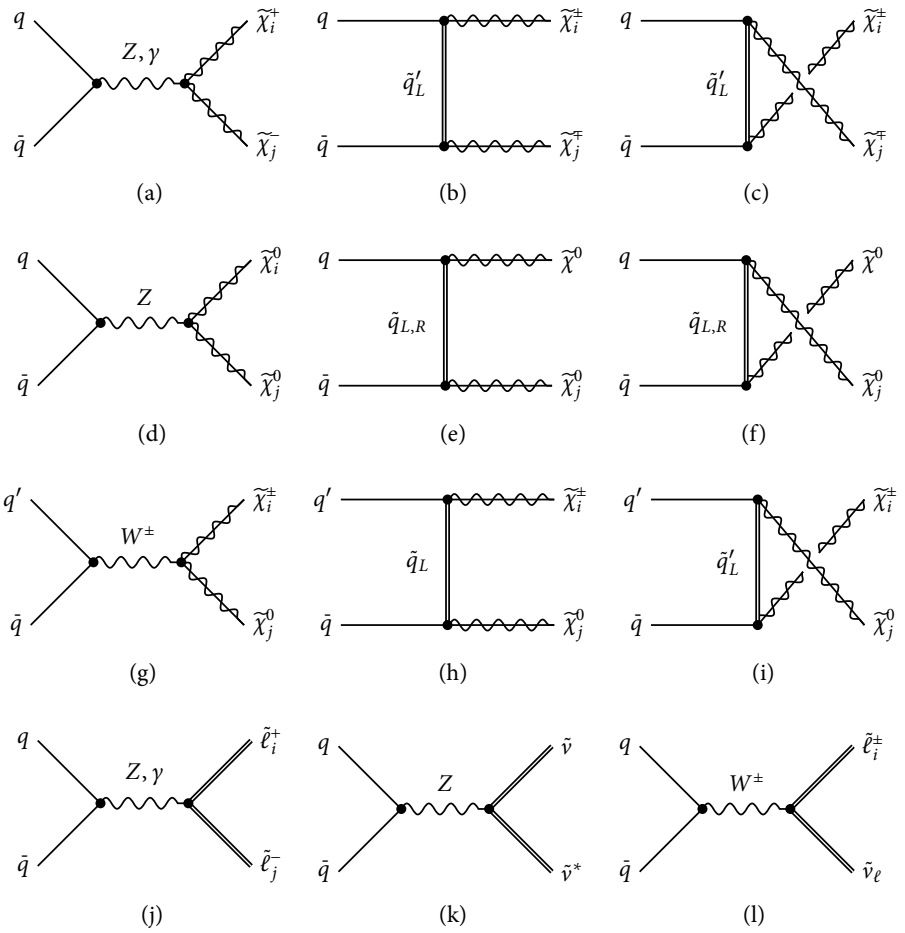

Figure 2.6: Feynman diagram for electroweak production of SUSY particles (adapted from [27]).

2.5.2 Gauge Mediated Supersymmetry Breaking

In section 2.4.2 it was mentioned that there is a variety of possible SUSY breaking mechanisms. One scenario is *Gauge Mediated Supersymmetry Breaking* (GMSB) [51–55]. As indicated by the name, here the gauge interactions are the reason for soft supersymmetry breaking. In this model so-called messenger fields are introduced. They are left-handed chiral supermultiplets $q, \bar{q}, \ell, \bar{\ell}$ that couple to the supersymmetry breaking which happens in a hidden regime. The content of these supermultiplets are messenger quarks $\psi_q, \psi_{\bar{q}}$, scalar quarks $q, \bar{q}$, messenger leptons $\psi_\ell, \psi_{\bar{\ell}}$ and scalar leptons $\ell, \bar{\ell}$. They couple to a gauge-singlet chiral supermultiplet S via a superpotential [27]

$$W_{\text{mess}} = y_2 S \ell \bar{\ell} + y_3 S q \bar{q}, \tag{2.64}$$

where the scalar component S and its auxiliary F-term have non-zero vacuum expectation values $\langle S \rangle$ and $\langle F_S \rangle$ which generates mass terms for fermions and scalars in the Lagrangian. The squared mass eigenvalues are

$$\ell, \bar{\ell}: \qquad m^2_{\text{fermions}} = |y_2 \langle S \rangle|^2, \qquad m^2_{\text{scalars}} = |y_2 \langle S \rangle|^2 \pm |y_2 \langle F_S \rangle|, \tag{2.65}$$

$$q\bar{q}: \qquad m^2_{\text{fermions}} = |y_3 \langle S \rangle|^2, \qquad m^2_{\text{scalars}} = |y_3 \langle S \rangle|^2 \pm |y_2 \langle F_S \rangle|. \tag{2.66}$$

The breaking of supersymmetry happens for $\langle F_S \rangle \neq 0$ and is communicated to the MSSM sparticles through loop diagrams. The Feynman diagram depicted in figure 2.7 shows the one-loop contributions from which the gauginos in the MSSM obtain their masses. The scalar particles obtain their masses from two-loop diagrams.

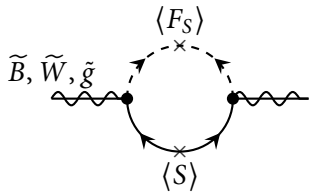

Figure 2.7: Feynman diagram depicting one-loop contributions to the MSSM gaugino masses in GMSB via virtual messenger particles.

The phenomenology of GMSB is determined by the end of the decay chain where the next-to-lightest supersymmetric particle (NLSP) decays into the LSP. In GMSB the LSP is the gravitino, which is the superpartner of the graviton[1].

There are six parameters that fully describe the GMSB model and further define the phenomenology. These parameters are listed below.

- $\langle S \rangle$: The mass scale of the messenger fields.
- Λ: The SUSY breaking scale, given by the ratio $\Lambda = \langle F_S \rangle / \langle S \rangle$.
- $\tan\beta$: The ratio of the vacuum expectation values of the two Higgs doublets.
- N_5: The number of messenger fields.

[1] The graviton is the mediator of the gravitational force. While this particle is not included in the SM, some supersymmetric models include gravity by imposing local supersymmetry (see section 7.5 in [27]).

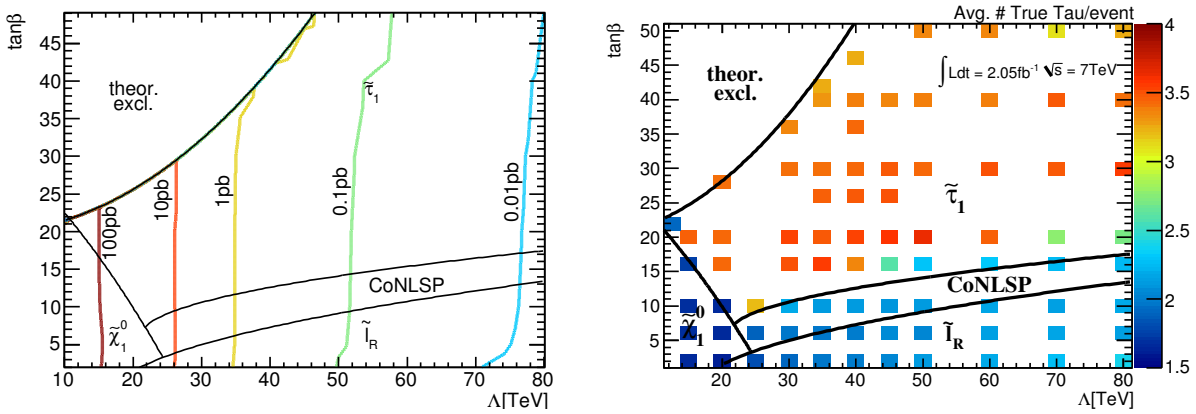

(a) NLO cross sections.

(b) Average Number of tau leptons.

Figure 2.8: Next-to-leading order cross-section 2.8a and average number of true tau leptons with $p_T > 20$ GeV for GMSB with the model parameter values used in this thesis [56].

- $C_{\widetilde{G}}$: The mass scale factor for the gravitino determines the life-time of the NLSP.
- $\mathrm{sgn}(\mu)$: The sign of the Higgs mass parameter.

The parameters Λ and N_5 determine the mass spectrum. Both the scalar and gaugino masses are proportional to Λ. Gaugino masses also scale proportional to N_5. The scalar masses however depend on $\sqrt{N_5}$. This means that for larger N_5 the gaugino masses become heavier than the sfermion masses. While the NLSP is the neutralino for $N_5 = 1$, it changes to the lightest sfermion (a slepton) for larger N_5. As discussed in section 2.4.6 the $\tilde{\tau}_1$ is the lightest slepton for high $\tan\beta$. In this case and with $N_5 = 3$ the end of the decay chain is characterized by

$$\tilde{\tau}_1 \to \tau \widetilde{G}, \tag{2.67}$$

where $\widetilde{G}$ denotes the gravitino.

Four of the mentioned six parameters are set to fixed values when considering this model for this thesis. The first one is $N_5 = 3$ to obtain a tau-rich model as described above. Furthermore, the parameter $\langle S \rangle$ is required to be sufficiently large to ensure that the mass scale of the hidden sector is out of the experimental reach. The mass scale factor of the gravitino $C_{\widetilde{G}}$ should not be too large because the NLSP otherwise becomes a long-lived particle. The last fixed parameter is $\mathrm{sgn}(\mu)$ which does not have a big impact on the appearance of supersymmetry at the considered energy scale.

This leaves two parameters free, which are Λ and $\tan\beta$. They are varied in the range of $\Lambda = 40 - 110$ TeV and $\tan\beta = 2 - 62$, while the other parameters are

$$N_5 = 3, \qquad \langle S \rangle = 250\,\mathrm{TeV}, \qquad C_{\widetilde{G}} = 1, \qquad \mathrm{sgn}(\mu) = +1. \tag{2.68}$$

Figure 2.8a shows the next-to-leading order production cross-section in dependence of Λ and $\tan\beta$. With increasing Λ the masses of the sparticles get larger which causes the cross-section to decrease. The average number of tau leptons in the final state for various points in the parameter space is shown in figure 2.8a. Figure 2.8b displays the average number of true tau leptons in the same parameter space where the dependence on $\tan\beta$ becomes clear.

2.5.3 Natural Gauge Mediation

The discovery of the Higgs boson with a mass of $m_{\mathrm{H}} = 125\,\mathrm{GeV}$ [57, 58] put some pressure on the GMSB model. The found mass value seems to be to high to be easily incorporated into this theory. Within the GMSB model the maximal mass of the lightest Higgs can only reach up to 121.5 GeV [59]. However, there are possibilities to explain a higher Higgs mass, for example by introducing additional vector-like matter supermultiplets as explained in [60]. But gauge mediated breaking mechanisms can also be modified in such a way that they are compatible with the observed Higgs mass. These scenarios are referred to as *natural gauge mediation* (nGM) [61].

In nGM the fine tuning of the Higgs sector is minimized while keeping the features of the gauge mediated supersymmetry breaking mechanisms. The masses of the involved particles are treated such that the Higgs mass can be fixed at 125 GeV. The gaugino, the stop and the Higgsino masses must be relatively light. The other particles do not have a big impact on the fine tuning in the Higgs sector and can remain decoupled. For the scenario that is investigated in this thesis the stau is required to be the NLSP. With the gravitino still being the LSP, the end of the decay chain is analogous to the one in GMSB as depicted in 2.67. Free parameters are $m_{\tilde{g}}$ and $m_{\tilde{\tau}}$, while

$$A_0 = 0, \qquad \mu = 400\,\mathrm{GeV}, \qquad m_0 = 2.5\,\mathrm{TeV} \qquad \text{and} \qquad M_1 = M_2 = 250\,\mathrm{TeV} \tag{2.69}$$

are fixed parameters. A more detailed description of this scenario can be found in [61].

2.5.4 Gravity Mediated Supersymmetry Breaking

The interaction between the hidden sector and the MSSM can also be communicated by the gravitational force. The according theory is referred to as *supergravity* [62–69]. One of the most commonly considered models which describes supersymmetry breaking is *minimal supergravity* (mSugra) [70–75].

This model is constrained by the unification of gaugino and scalar masses at the GUT scale as described earlier in section 2.4.4 and displayed in figure 2.4. Furthermore, all trilinear couplings are at the GUT scale equal to the parameter A_0. The model is then reduced to only five free parameters. For this analysis mSugra is considered in the parameter space of m_0 and $m_{1/2}$ while the fixed parameters are

$$\tan\beta = 30 \qquad A_0 = -2m_0 \qquad \text{and} \qquad \mathrm{sgn}(\mu) = +1. \tag{2.70}$$

One advantage over the previously described GMSB model is that mSugra allows for a light Higgs mass which is compatible with the discovery made at the LHC. The set of fixed parameters are chosen in such a way that they incorporate a Higgs mass of 125 GeV for a large part of the parameter space. For low m_0 and large $m_{1/2}$ the $\tilde{\tau}_1$ becomes the LSP as it is indicated by the black hatched area in figure 2.9. This possibility can be excluded however assuming that R-parity is conserved. Since the LSP is only allowed to interact weakly under this assumption, the $\tilde{\tau}_1$ is not a suitable candidate. The LSP in the considered parameter space of the mSugra scenario is the $\tilde{\chi}_1^0$. For some combinations of $m_{1/2}$ and m_0 the NLSP is again the stau which means the end of the decay chains predominantly becomes

$$\tilde{\tau}_1 \to \tau\tilde{\chi}_1^0. \tag{2.71}$$

Further constraints on the model come from measurements of the branching fractions of the rare $B_S \to \mu\mu$ decay [77] and the radiative decay $b \to s\gamma$ [78]. The first disfavors regions with small m_0 and

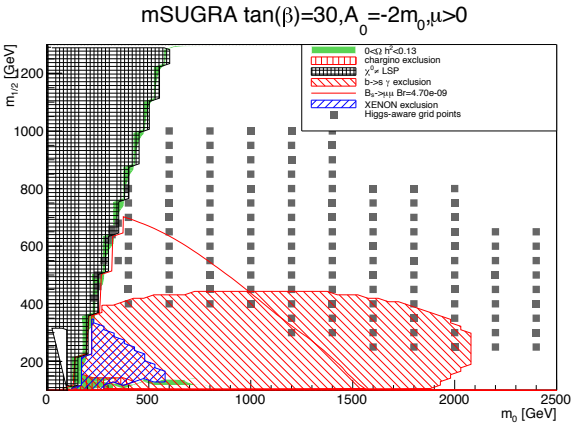

Figure 2.9: Experimental constraints on the mSugra in the parameter space of m_0 and $m_{1/2}$ (adapted from [76]).

small $m_{1/2}$, while the latter excludes a region in low $m_{1/2}$. In figure 2.9 these regions are indicated by a red line and a hatched red area respectively.

2.5.5 *R*-Parity Violating mSUGRA

In section 2.4.3 the conservation of R-parity was motivated. However, R-parity does not necessarily have to be an exact symmetry. It can be spontaneously broken at higher energy scales. A theory in which this is the case is *bilinear R-parity violation* (bRPV) [79–81]. Starting off with a mSugra model, the bilinear third term in 2.36 is included in the superpotential by itself to violate the lepton number while the baryon number is conserved:

$$W_{\text{bRPV}} = W_{\text{MSSM}} + \varepsilon_i L_i H_u. \tag{2.72}$$

The soft term breaking Lagrangian must then be extended by

$$\mathcal{L}_{\text{bRPV}} = \mathcal{L}_{\text{soft}} - B\varepsilon_i L_i H_u, \tag{2.73}$$

where B is the bilinear soft mass parameter. By introducing these additional terms, a mixing between neutralinos and neutrinos is generated. As a consequence, the neutrinos acquire mass. This fact can be used to constrain the new model parameters by existing mixing and mass measurements [80]. The other mSugra parameters remain the same and the model is investigated in the same parameter space of m_0 and $m_{1/2}$.

The most striking phenomenological consequence of R-parity violation is the fact that the LSP is no longer stable, but instead decays into Standard Model particles. There are several possible decay modes including direct decays into leptons and decays into leptons via intermediate state. This can be a gauge bosons or a scalar. With the neutralino being the LSP the interesting decay chains for this thesis are:

$$\tilde{\chi}_1^0 \to \nu\tau^+\tau^- \qquad \text{and} \qquad \tilde{\chi}_1^0 \to \nu\ell\tau. \tag{2.74}$$

With the rest of the mSugra decay chain remaining unchanged, there are many possibilities for final states including multiple tau and light leptons.

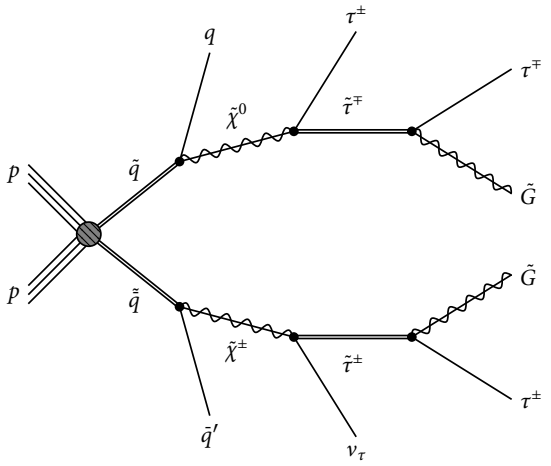

Figure 2.10: Feynman diagram showing an exemplary decay chain in the GMSB model.

2.5.6 SUSY Signatures

The occurrence of sparticles within the considered SUSY models results in unique signatures which can be searched for in the experiment.

Figure 2.10 depicts the Feynman diagram of a possible squark decay chain in the GMSB model which shall be considered as an example. The analysis described in this thesis aims mainly at strong production processes due to their dominance at the LHC. In the commonly assumed mass hierarchy gluinos are the heaviest sparticles, followed by squarks. The gluinos produced in proton-proton collisions can only decay into a squark and a quark. Squarks decay electroweak into a neutralino or chargino:

$$\tilde{g} \to \tilde{q}q, \qquad \tilde{q} \to \tilde{\chi}_i^0 q, \qquad \tilde{q} \to \tilde{\chi}_i^{\pm} q'. \tag{2.75}$$

In all cases the SM quarks result in high energetic particle jets (compare section 3.3.1). The subsequent decay chain depends on the mass hierarchy of gauginos and sleptons. As discussed in the previous section all considered models feature decay chains with tau leptons, which are the linchpin of the signature. Due to its decay, the tau lepton itself requires a thorough analysis of the final state. This is further described in sections 2.6 and 3.3.6.

At the end of the decay chain stands the LSP. In case of the R-parity conserving models this particle only interacts weakly and will not be detected. It therefore leaves an imbalance in the transverse momentum sum called the missing transverse momentum $E_{\mathrm{T}}^{\mathrm{miss}}$ (compare section 3.3.7). When R-parity is not conserved however, the LSP further decays, increasing the number of leptons. The neutrinos that are produced alongside this decay also result in increased $E_{\mathrm{T}}^{\mathrm{miss}}$.

To summarize, the signatures of sparticle decays in the considered model has three distinct features

- high energetic particle jets from squark and gluon decays
- large missing transverse momentum $E_{\mathrm{T}}^{\mathrm{miss}}$ from the LSP and/or neutrinos
- the occurrence of tau leptons.

Knowing this, one can adjust an event selection such that mostly final states from possible sparticle decays are extracted (compare section 5.1).

2.6 A Closer Look at Tau Leptons

As it was described in the last section, the tau lepton is of particular interest for this thesis. The decay properties of the tau make it unique with respect to identification and reconstruction. This section is therefore dedicated to deliver some insight into the physics of the tau decay.

With a mass of 1777 MeV the tau lepton is 170 times heavier than the muon and 3500 times heavier than the electron. While the electron is stable, muon and tau lepton decay via the weak interaction. Due to the very short mean life-time of the tau lepton of 2.9×10^{-13} s (at rest), a 20 GeV tau lepton travels just about 1 mm before it decays. The decay of a 25 GeV muon for comparison only happens after an average travel distance of 157 km. This means that the tau lepton does not even enter the volume of the tracking detectors but only its decay products are visible for reconstruction.

The tau lepton always decays into a tau (anti)neutrino and via an intermediate $W^{\pm}$ boson into two more fermions. These can be in the case of a leptonic decay (figure 2.11a) a muon or an electron together with the according lepton number conserving (anti)neutrino. The other basic decay mode of the W results in a quark antiquark pair (figure 2.11b). Due to the large mass of the tau lepton many combinations of mesons can appear in the hadronization process of these two quarks.

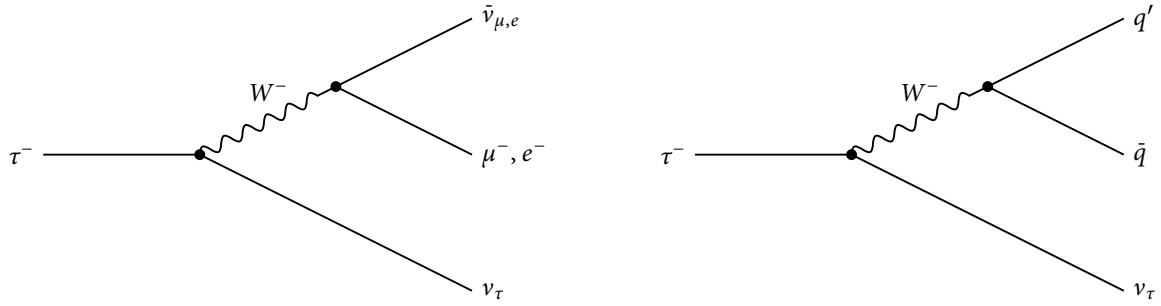

(a) Leptonic tau decay.

(b) Hadronic tau decay.

Figure 2.11: Feynman diagrams of a tau lepton decay

The shares of the main decay modes are displayed in the pie chart in figure 2.12a. The majority of 65 % leads to hadronic final states. The percentages of the various hadronic modes are given with respect to those 65 %. Most of the these decay modes include one or three charged pions which might be accompanied by neutral pions. However, also larger numbers of charged pions and decays including K mesons are possible.

The reconstruction of tau leptons can only rely on the decay products. At ATLAS the 35 % of leptonically decaying tau leptons can not be distinguished from prompt muons or electrons. In the analysis described in this thesis however, these tau leptons are considered by selecting final states which include light leptons alongside identifiable tau leptons[2]. In the hadronic mode the experimental challenge is to distinguish the resulting particle jets from those caused by quark and gluon jets (compare section 3.3.1).

The identification method relies on tau jet specific characteristics such as the number of charged particles or the spread of the object. As illustrated in figure 2.12b tau jets tend to be confined in a relatively narrow (signal) cone and must be well separated from quark/gluon jets which usually have a much wider spread. A detailed description of the tau identification methods at ATLAS follows in section 3.3.6.

[2] This happens under the assumption that in tau-rich final states of supersymmetric decays light leptons are likely to be the result of a leptonic tau decay.

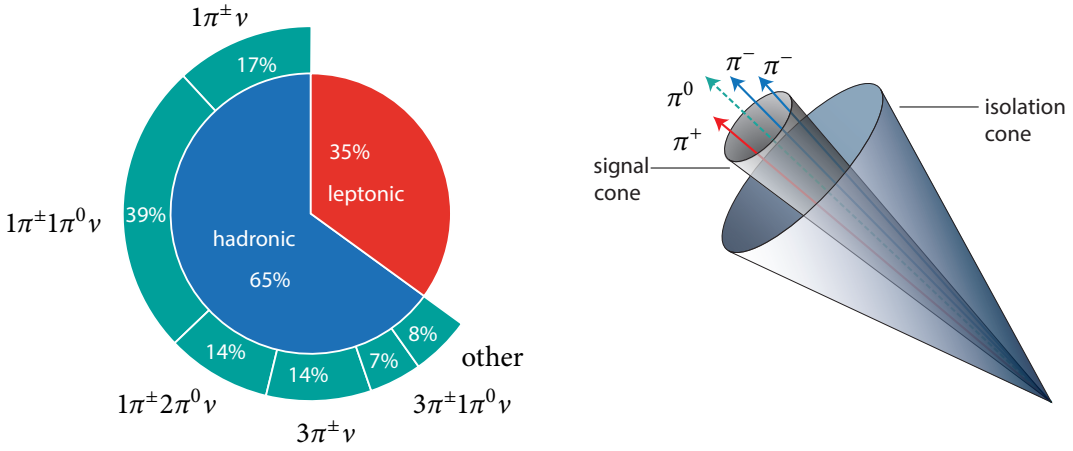

(a) Shares of hadronic and leptonic decay modes.

(b) Signal and isolation cone for tau reconstruction.

Figure 2.12: (a) shows a summary of the leptonic and most common hadronic τ decay modes with the respective branching fraction and the numbers of charged particles. The leptonic decay modes split almost evenly into muon and electron decays. All numbers are taken from [10]. (b) displays the signal cone for tau reconstruction which contains the observed decay products. They must be well separated from other objects by the isolation cone.

2.7 Supersymmetry at the LHC

Despite all efforts to find supersymmetric particles in the experiment, no significant signs for SUSY have been seen so far. In the 2012 $\sqrt{s}$ = 8 TeV LHC data some deviations from the Standard Model were observed. Noticeably excesses in data were seen in analyses which focused on supersymmetric particles in final states with two same-flavor leptons of opposite sign. The analyses targeted two SUSY models – one that includes the decay $Z \to \ell^+\ell^-$ and one with $\tilde{\chi}_2^0 \to \ell^+\ell^-\tilde{\chi}_1^0$. An excess with a significance of 3.0 σ was observed at the ATLAS experiment for $Z \to e^+e^-$ events [82]. In the search for an kinematic edge, indicating the second targeted decay chain, a local significance of 2.6 σ was observed at the CMS experiment [83]. Unfortunately, the recently published results for $\sqrt{s}$ = 13 TeV from the 2015 LHC run did not increase evidence for physics beyond the Standard Model. The ATLAS data still shows an excess in $Z \to \ell^+\ell^-$ events, but the significance has decreased to 2.2 σ. The new CMS data is consistent with the Standard Model expectation for both considered models [84]. There are more examples of promising hints that have disappeared with the accumulation of more data. At the time of writing this thesis all investigated kinematic regions in various analyses are in good agreement with the Standard Model expectation.

The non-observation of BSM physics has put supersymmetry under some pressure. The results are used to constrain the theory and exclude large parts of the parameter space of various models. The analysis that is described in this thesis are part of this process. Figure 2.13 shows a summary of various searches for supersymmetry. It lists limits on the masses of SUSY particles for all ongoing and published ATLAS analyses until March 2016, including the results presented in this thesis.

Constraints from other measurements and cosmological observations which were partly mentioned in section 2.5 can be used together with the direct searches to perform fits in a global parameter space. From these fits preferred parameter regions can be extracted. A model that incorporates many constraints from measured characteristics is the phenomenological MSSM (pMSSM) [85, 86].

The Higgs signal at 125 GeV, as observed at the LHC, can be interpreted in the pMSSM in various ways. As demonstrated in [87], the observed signal provide good fit results both in the case of a light $\mathcal{CP}$-even Higgs interpretation and in the case of a heavy $\mathcal{CP}$-even Higgs interpretation within the pMSSM. The fits

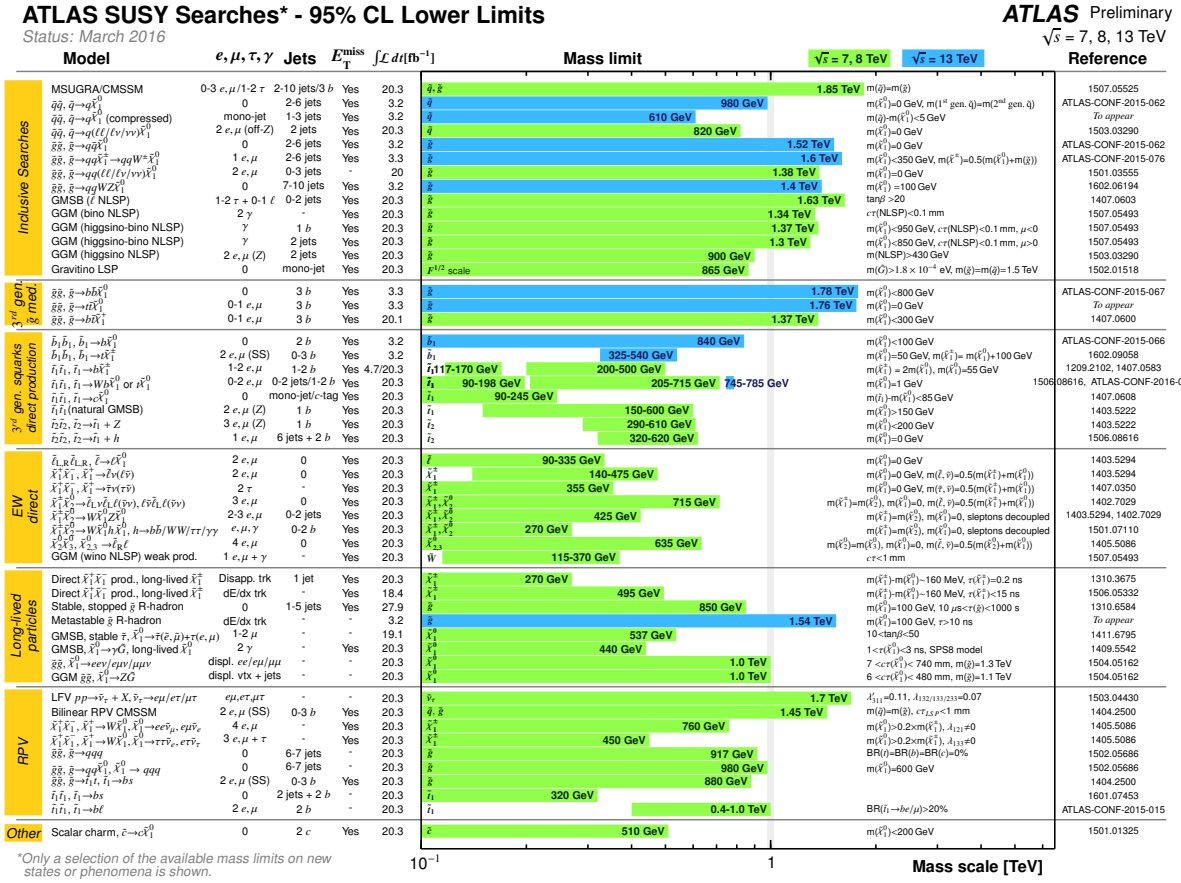

Figure 2.13: Summary of various SUSY analyses and their mass reach for exclusion [88].

in both cases provide results that are even slightly better than a SM-only interpretation. Improvements in the precision measurements of the Higgs boson properties at the LHC and searches for additional Higgs bosons will help to further constrain the parameter space.

CHAPTER 3

The ATLAS Experiment at the Large Hadron Collider

The ATLAS experiment is a joint effort of over 3000 scientists from 38 countries around the world. In this chapter the experimental setup of the detector at the Large Hadron Collider is described. A brief discussion of the LHC machine (3.1) is followed by a more detailed explanation of the various subdetectors of ATLAS (3.2). In the third part of the chapter (3.3) the physics objects used in this analysis are defined. The last part of this chapter (3.4) deals with simulating the experiment, software and the data samples used for analysis.

3.1 The Large Hadron Collider

Studying physics at the TeV energy scale requires the use of the world's largest particle accelerator – the Large Hadron Collider (LHC) [89–92]. Located at CERN, Geneva, near the Swiss-French border, the main part of the LHC is a proton-proton collider of 27 km circumference. With a center-of-mass energy $\sqrt{s}$ of up to 14 TeV, it holds the potential to reveal new physics. In its three-year run-time the LHC has been operated successfully with proton collisions at $\sqrt{s}$ = 7 TeV (2010–2011) and $\sqrt{s}$ = 8 TeV (2012). Collisions with lead nuclei are part of the physics program as well. Since these data are not relevant to the content of this thesis, they shall not be further discussed.

Figure 3.1 shows a schematic view of the complete LHC facility with the main accelerator ring and the various injectors used for successively increasing the proton beam energy. The protons used for collision are produced from a hydrogen gas source. Ionized hydrogen atoms are then fed into a chain of subsequent accelerators. A linear accelerator (Linac 2) increases the beam energy to 50 MeV, corresponding to a third of the speed of light. Next, the beam is injected into the Proton Synchrotron Booster (PSB) [93], where it is divided into four packages – one for each of the superimposed rings of the PSB. The kinetic energy of the protons is raised to 1.4 GeV, which translates to ~92 % of the speed of light. The Proton Synchrotron (PS) [94] raises the beam energy further to 25 GeV. At this point the protons are approaching almost the speed of light and the energy increase affects the relativistic momentum rather than the velocity. The final step in the injector chain is the Super Proton Synchrotron (SPS) [95], where the energy of the protons reaches 450 GeV. At this energy, the beam is injected in opposite directions into the two beam pipes of the LHC, to reach the final energy of up to 7 TeV per beam. The protons are packed into bunches. When filled, the LHC ring is designed to hold up to 2808 proton bunches, each containing ~10^{10} particles. Superconductive Radio Frequency (RF) cavities keep the bunches together and accelerate them with an oscillating electric field of 2 MV at a frequency of 400 MHz [96].

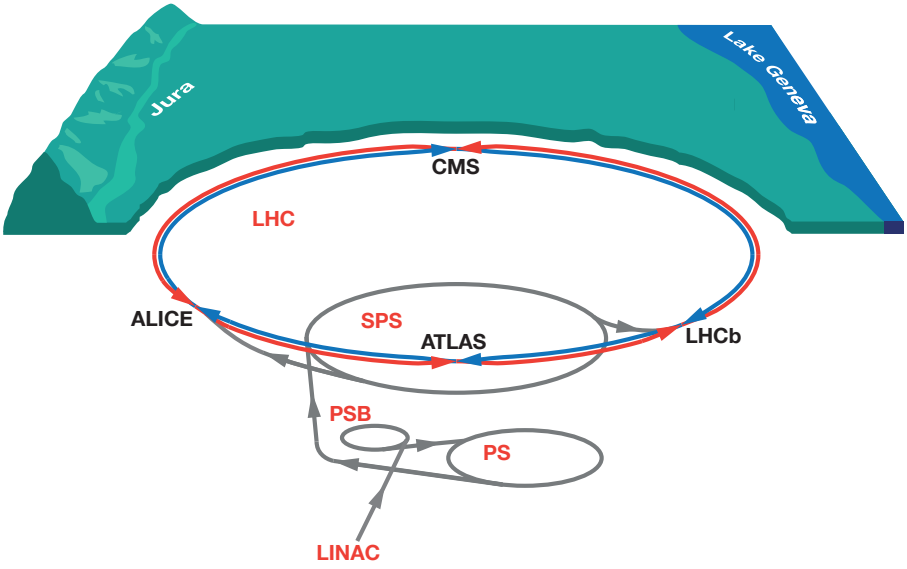

Figure 3.1: Schematic drawing (not to scale) of the Large Hadron Collider (LHC) and all the accelerators used for providing particle beams at up to a center-of-mass energy of 14 GeV. The chain of pre-accelerators includes a linear accelerator (LINAC), the Proton Synchrotron Booster (PSB), the Proton Synchrotron (PS) and the Super Proton Synchrotron (SPS). At the interaction points of the proton beams, the four main experiments are located: ATLAS, CMS, LHCb and ALICE.

Built into the existing tunnel of the old Large Electron-Positron Collider (LEP) 100 m underground, the LHC had to fit the given geometry of eight straight sections and eight arc sections. In the arc sections the protons must be forced on a circular trajectory, which can be achieved by using magnets. Particles with charge q, moving at a velocity $\vec{v}$ in a magnetic field $\vec{B}$ encounter the Lorentz force

$$\vec{F}_{\mathrm{L}} = q \cdot \left[\vec{v} \times \vec{B}\right], \tag{3.1}$$

which always stands perpendicular to the particle's movement, resulting in a circular trajectory. With an effective radius r and the kinetic energy E_{kin} the centripetal force $F = \frac{E_{\mathrm{kin}}}{r}$ can be used to express the required magnetic field as:

$$B = \frac{E_{\mathrm{kin}}}{qvr}. \tag{3.2}$$

At the LHC 1232 dipole magnets of 14.3 m length bend the proton beams on their trajectory. To achieve this for 7 TeV protons with a velocity $v \approx c$ and the given magnet geometry, a magnetic field strength of $B = 8.33\,\mathrm{T}$ is needed. Field intensities of this magnitude can only be accomplished by the use of superconducting magnets. Therefore the coils of dipole magnets are made from Nb-Ti cables that are operated in superfluid helium at 1.9 K [97, 98]. In total 858 quadrupole magnets are used alongside other multipole magnets for focusing the beams. At four points in the LHC ring the proton beams are brought to collision and resulting *events* are recorded by the four main experiments which are situated at those interaction points. One event contains several proton interactions. This overlay is also referred to as *pile-up*.

The two general purpose detectors ATLAS [99] and CMS [100] are designed to provide data for a broad variety of physics analyses. This includes precision measurements of the Standard Model as well as searches for physics that lies beyond it. The ALICE [101] experiment is dedicated to study the strong-

interaction sector of the Standard Model and the physics of the quark-gluon plasma. At LHCb [102] precise measurements of CP violation and rare decays of B hadrons are performed. In addition, there are two smaller experiments: At LHCf [103] the focus of study are neutral particles that are emitted closely to the beam direction at the collision point of ATLAS; The TOTEM [104] detector is situated close to CMS and its purpose is the measurement of the total proton-proton cross-section at LHC.

Next to the center-of-mass energy, the other key parameter to describe the performance of a particle collider is the instantaneous luminosity $\mathcal{L}$. It defines the number of collisions per second N_{event} for a given cross-section σ_{event}:

$$N_{\text{event}} = \sigma_{\text{event}} \cdot \mathcal{L}. \tag{3.3}$$

To discover rare processes that may occur in physics beyond the Standard Model, high event rates are crucial and therefore achieving a high luminosity was one of the main goals when designing the LHC. The instantaneous luminosity can be expressed as:

$$\mathcal{L} = f \cdot \frac{n_{\text{B}} N_1 N_2}{A}, \tag{3.4}$$

where n_{B} is the number of bunches, N_1, N_2 are the numbers of particles in the colliding bunches, f is the collision frequency and A is the effective area cross-section of the beam [105]. Expressed in terms of the commonly used beam parameters ε (emittance) and β^* [106] this equation reads as:

$$\mathcal{L} = f \cdot \frac{n_{\text{B}} N_1 N_2}{4\varepsilon\beta^*}. \tag{3.5}$$

The size of the beam at the interaction point depends on its focusing. As already mentioned the focusing occurs by the use of multipole magnets. The parameter β^* measures the distance from the interaction point to the point where the beam is twice the size as where it is focused. It therefore determines how strongly the beams are squeezed together.

The performance of the LHC could be optimized in its time of operation such that the total integrated luminosity in 2012 increased by a factor of four with respect to 2011, resulting in a delivery of $L = 23.3\,\text{fb}^{-1}$. Of this data, $20.3\,\text{fb}^{-1}$ could be used for physics analysis (see section 3.4.4). The accumulation of data in 2011 and 2012 is shown in figure 3.2, where the delivered luminosity is represented in green and the recorded data by the ATLAS detector in yellow. Along with a revised run plan in 2012, resulting in more data-taking time, the peak luminosity could be raised as well, which was achieved by a smaller β^* and a higher number of protons per bunch [107]. Table 3.1 summarises some key parameters of the accelerator operation in the years 2011 and 2012, along with the respective design values. For the second operational

	2011	2012	design value
$\sqrt{s}$ [GeV]	7	8	14
peak luminosity [$\text{cm}^{-2}\,\text{s}^{-1}$]	3.8×10^{33}	7.7×10^{33}	10^{34}
delivered int. luminosity [fb^{-1}]	5.6	23.3	80 – 120
max. number of bunches	1380	1374	2808
bunch spacing [ns]	50	50	25
protons per bunch	$(1.1 - 1.5) \times 10^{11}$	$(1.1 - 1.7) \times 10^{11}$	1.2×10^{11}
β^* [m]	1 – 1.5	0.6	0.55

Table 3.1: LHC design parameters compared to the respective numbers in operation [92, 107, 108].

run of the LHC, which started in 2015, the center-of-mass energy was increased to $\sqrt{s} = 13\,\text{TeV}$. With the higher energy, beam parameters like β^* and the bunch intensity must be revised. However, it is planned to increase the peak luminosity further. A significant step to achieve this, is operating with a bunch spacing of 25 ns, which was an important goal for the second run [109].

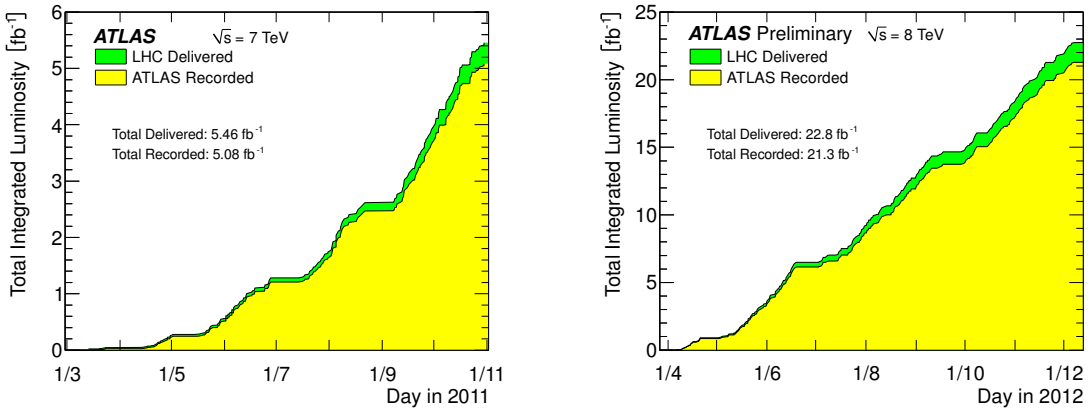

Figure 3.2: Integrated luminosity in 2011 (left) and 2012 (right), delivered by LHC (green) and recorded by ATLAS (yellow) [110].

3.2 The ATLAS Detector

The ATLAS detector is a general-purpose detector that is situated close to the Meyrin site of the CERN facilities. It has a size of 44 m in length, 25 m in height and weighs approximately 7000 t. It symmetrically surrounds the beam pipe of the LHC in a cylindrical design at the point of interaction to cover a solid angle of almost 4π. A schematic view of the whole detector is displayed in figure 3.3. The ATLAS detector is setup in a commonly used layered structure of subdetectors, which serve different purposes. The central region in respect to the direction of the beam pipe is called the *barrel* region. Here, the layers are arranged cylindrically around the beam axis. The barrel region is joined by a so-called *end-cap* region to each side, where the detectors are arranged radially in wheels.

The subdetectors can be categorized by three types. The central detectors are used for measuring the positions of tracks of charged particles together with their transverse momentum. The latter is achieved by placing these detectors in the magnetic field of a solenoid. This part of ATLAS is called the *Inner Detector* (ID). The Inner Detector and the solenoid magnet are surrounded by an electromagnetic calorimeter (ECAL) and a hadronic calorimeter (HCAL). They are used to measure the total energy of electromagnetically interacting particles (ECAL) and hadronically interacting particles (HCAL). The outermost part of ATLAS are the muon spectrometers, which are within the magnetic field of a toroid magnet. All various detector components shall be discussed in further detail in the following.

3.2.1 The ATLAS Coordinate System

Before describing the various subdetectors, it is useful to briefly explain the coordinate system. Its origin is defined as the nominal interaction point. The z-axis runs along the beam direction, while the positive x-axis points towards the center of the LHC ring and the y-axis points upwards. In the x-y-plane the radius $R = \sqrt{x^2 + y^2}$ is used.

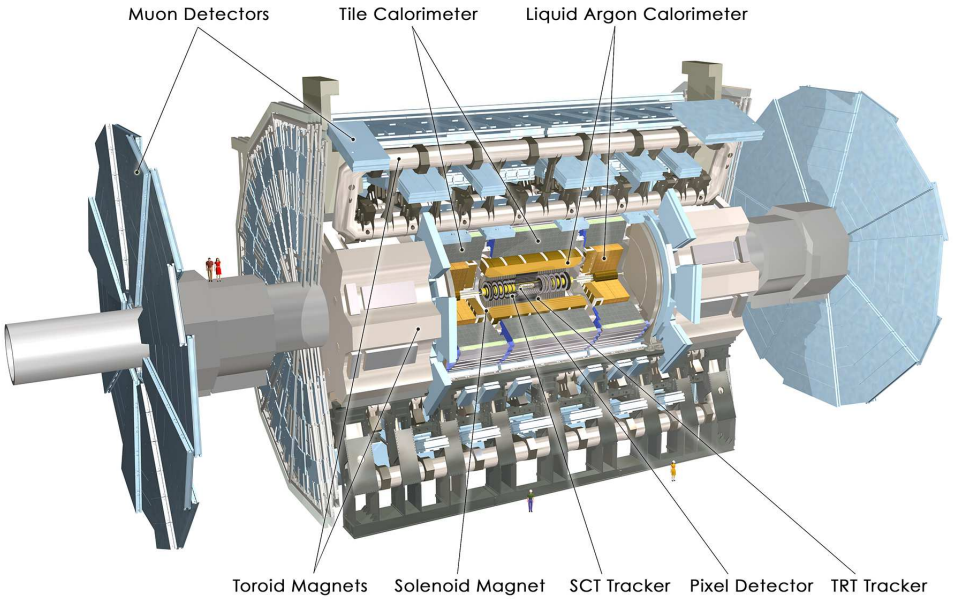

Figure 3.3: Schematic drawing of the ATLAS detector [111].

In this thesis angles are commonly used to refer to coordinates. The azimuthal angle $\phi \in [-\pi, \pi]$ proceeds around the z-axis in the transverse x-y-plane, while the polar angle $\theta \in [0, \pi]$ is measured with respect to the z-axis. For the latter however, it is more convenient to introduce another parameter – the pseudorapidity η. Defined as

$$\eta = -\ln \tan\left(\frac{\theta}{2}\right), \tag{3.6}$$

the difference between two pseudorapidities η_1 and η_2 is invariant under Lorentz transformation. Since in hadron collisions the involved quarks and gluons can have large unknown momenta along the z-axis, the resulting particles occur boosted into that direction. For this reason it is very useful to define a quantity which is easily transformed. With this, we also define a measure for the distance between two objects in the angular space of η and ϕ as

$$\Delta R = \sqrt{\Delta\eta^2 + \Delta\phi^2}. \tag{3.7}$$

The transverse plane of the detector is of particular interest for many aspects of the analysis. This happens for the same reason pseudorapidity was defined. Since the boost from the initial partons is unknown, only the projection of the momentum in the transverse plane

$$p_{\mathrm{T}} = \sqrt{p_x^2 + p_y^2}, \tag{3.8}$$

is regarded and referred to as the *transverse momentum*.

3.2.2 Magnet System

The measurement of the transverse momentum of a charged particle requires deflection within a magnetic field. The direction of the deflection provides the sign of the particle's charge. Since the radius of the track curvature of the particle depends on its momentum for a given magnetic field strength, the momentum can be determined by measuring this bending radius. At ATLAS, four large superconducting magnetic

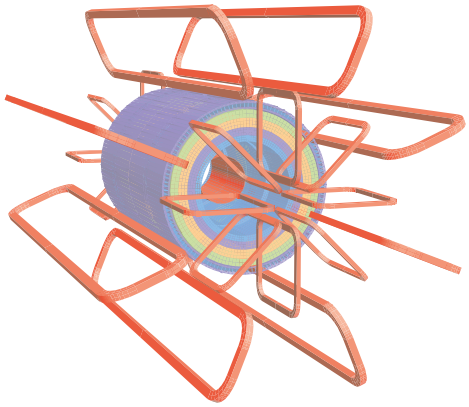

Figure 3.4: Schematic drawing of the ATLAS magnet systems. All magnet coils are displayed in red. Eight barrel toroid coils and eight toroid end-cap coils for each side are visible. Within this structure lies the calorimeter surrounding the central solenoid [99].

systems are used to achieve this, as displayed in figure 3.4. A central solenoid provides the field for the Inner Detector and three toroid systems supply the muon spectrometers.

Solenoid Magnet The central solenoid [112] is 5.8 m long, 2.56 m in diameter and encloses the Inner Detector. It provides a homogeneous 2 T field parallel to the beam axis. It is designed such that the material thickness is minimized, which is crucial for the performance of the calorimeter. In total the solenoid only adds 0.66 radiation length[1] (X_0) to the material budget. This is achieved by using indirectly cooled, aluminum-stabilized superconducting coils, which are operated at a nominal temperatur of 4.5 K.

Toroid Magnet The toroid systems [113, 114] consist of a barrel section and two parts for the end-caps. Each of the parts consists of eight coils aligned cylindrically around the calorimeters as displayed in figure 3.4. The ATLAS toroid system is a massive structure with a total mass of over 1000 t. The barrel coils are 25.3 m in length and the complete structure has a diameter of 20.1 m. The end-cap coils have a length of 5 m with an outer diameter of 10.7 m. These dimensions define the size of the whole detector. The three toroid systems create magnetic fields of 0.2 – 2.5 T in the barrel part and 0.2 – 3.5 T in the end-caps. Within these fields, the muon spectrometers are located.

3.2.3 Tracking at ATLAS

As its name suggests, the Inner Detector [116, 117] is the part of ATLAS closest to the interaction point. It serves the purpose of a measuring particle tracks and consists of three parts[2]: the Pixel Detector, the Semi-Conductor Tracker (SCT) and the Transition Radiation Tracker (TRT). An illustration of the complete Inner Detector is displayed in figure 3.5a. Figure 3.5b shows the barrel part only, which visualizes the dimensions and the layout better. In figure 3.5c a cross-sectional drawing in the R-z-plane is displayed, where each detector part can be seen with its reach in $|\eta|$.

In a distance of only 5 cm from the interaction point the beam pipe is enclosed by the Pixel Detector, which itself is surrounded by the SCT. The outermost part of the Inner Detector is the TRT.

[1] The radiation length X_0 is a measure for the amount of material that is needed to decrease the energy of traversing particles by a factor of $1/e$.

[2] After the first run of the LHC, a fourth detector part, the Insertable B-Layer [118], was installed in the gap between the beam pipe and the rest of the Inner Detector. Since it is not relevant for this thesis, it is left out of discussion.

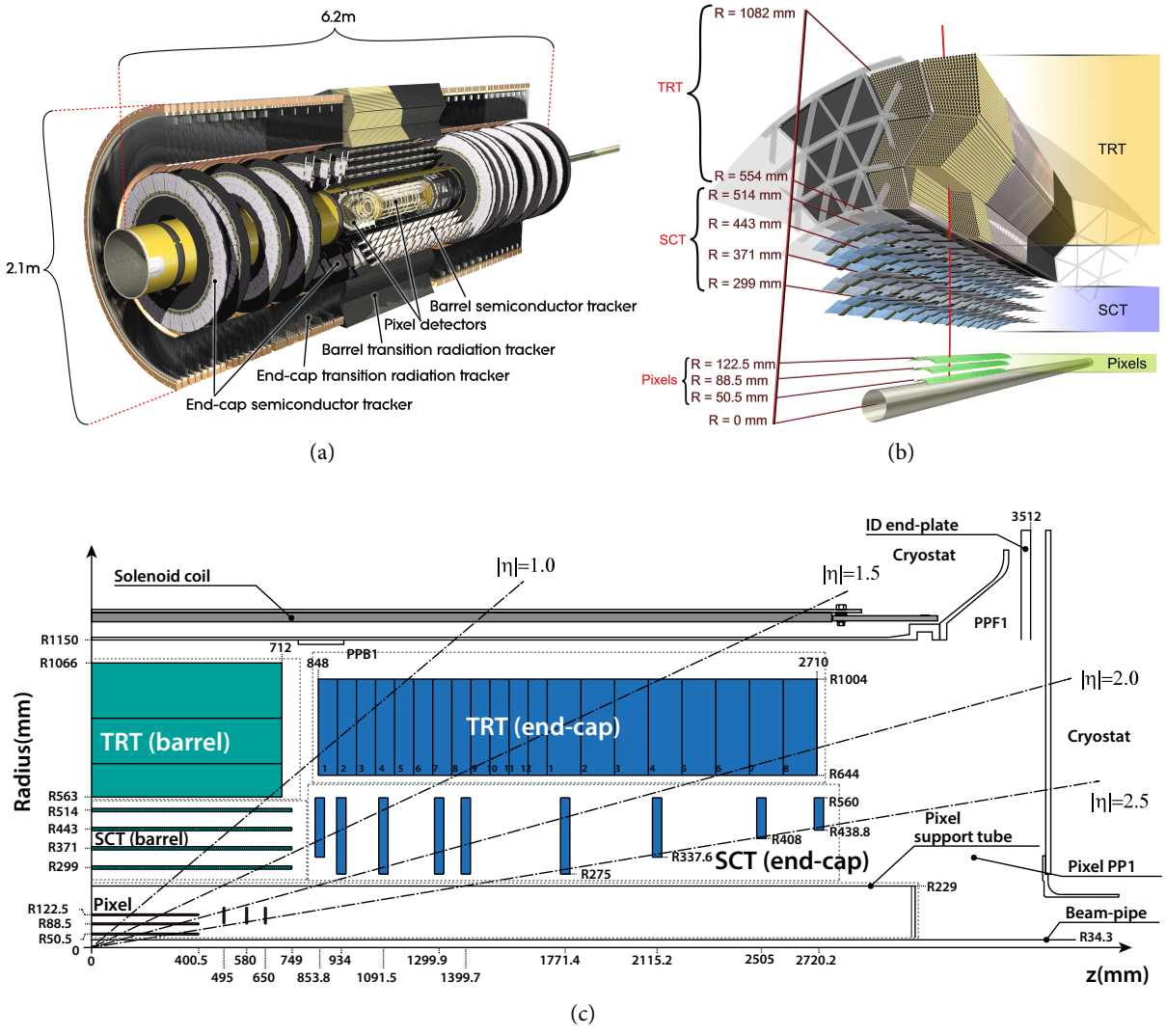

Figure 3.5: Figure (a) displays a cutaway drawing of the complete Inner Detector, while in figure (b) a more descriptive view of the barrel part is displayed [115]. In figure (c) a cross-sectional drawing of the Inner Detector in the R-z plane is displayed which shows the arrangement of all subdetector parts and their reach in $|\eta|$ (adapted from [99]).

Pixel Detector As the innermost part of the tracking system, the Pixel Detector [119, 120] deals with a high track density. It requires a high space-point resolution to separate the large number of particle tracks ($\mathcal{O}(1000)$ per collision) within the small volume of this subdetector. Furthermore, the Pixel Detector must be able to withstand a large radiation dose to achieve a sufficient life-time. The measurement principle used for the Pixel Detector is based on the excitation of valence electrons in a semiconductor material to the conduction band. The resulting electrons and holes are detected by dedicated electronics. The Pixel Detector consists of modules of 250 µm thick silicon wafer with a size of (19×63) mm^2. Each module has 47 232 pixels with a size of (50×400) µm^2. 1744 of these modules are stacked in three layers in the barrel region and three layers in the wheels of the two end-caps, assuring that each particle leaves three space point measurements for reconstructing tracks. This results in a total of 80.4 million readout channels.

With a point resolution of 10 µm in the R-ϕ-plane and 115 µm in z for the barrel region, respectively in R for the end-caps, the Pixel Detector performs the most precise spatial measurements of the various subdetectors.

SCT The SCT [121, 122] is a silicon strip detector and measures particle tracks based on the same detection principle as the Pixel Detector. The silicon strips are 6.4 cm long and daisy-chained in pairs to form one sensor unit. 768 active strips with a 80 µm pitch cover the area of one module where each module consists of two layers of strips. These sets of strips are tilted under an angle of 40 mrad to provide information about the z-coordinate in the barrel, respectively R in the end-caps.

There are four cylindrical layers of detector modules with strips parallel to the beam axis in the barrel region. In the end-caps the silicon strips are arranged radially to the beam axis. Nine wheels of modules are configured such that, together with the barrel modules (compare figure 3.5c), they provide four space point measurements up to $|\eta| = 2.5$.

The SCT consists of 4088 modules, which gives a total of over 6 milion read-out channels. The spatial resolution of the SCT is 17 µm in the R-ϕ-plane and 580 µm in z (barrel) and R (end-caps).

TRT Unlike the other two tracking subdetectors, the TRT [123, 124] is a gaseous detection device. It is built from many polyimide drift (straw) tubes, each 4 mm in diameter. While the tube itself serves as a cathode, a gold plated tungsten anode wire is placed in its center to create a radially symmetric electric field. The tubes are filled with a gas mixture that consists of 70 % Xe, 27 % CO_2 and 3 % O_2. Charged particles traversing the volume of the straw will ionize the gas atoms. The free electrons produced in this ionization drift in the electric field towards the anode wire, where gas amplification occurs. This results in a gain by a factor of 2.5×10^4 for the signal induced at the anode.

In the barrel region, the TRT is divided into three rings, where each ring consists of 32 modules of straws. There are 73 layers of straws, each with a length of 144 cm and arranged parallel to the beam pipe. In the end-caps the straws are arranged radially in 160 planes and their length is 37 cm. This assures a minimum of 36 measurements for each track for particles with $p_T > 0.5$ GeV and $|\eta| < 2.0$, except the so-called transition region with $0.8 < |\eta| < 1.0$, where the number of measurements decreases to 22.

The TRT does not only serve the purpose of a tracking device, but is also used for electron identification (in particular for separation between electrons and pions). The straw layers are interleaved with radiator material that causes relativistic charged particles to emit transition radiation. Photons from this radiation are absorbed by the Xe atoms in the gas mixture within the straws. Since the electron mass is much smaller than the pion mass, an electron will cause a higher signal than a pion of the same momentum. To achieve both track and transition radiation measurement, the TRT signals are discriminated against two thresholds – a lower one for tracking and a higher one for particle identification.

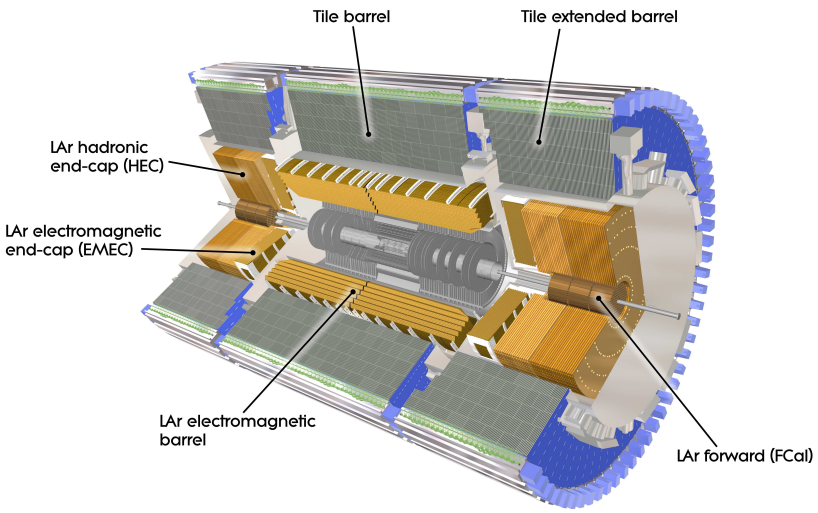

Figure 3.6: Schematic drawing of the ATLAS calorimeters [126].

The TRT consists of 298 304 straws in total. By measuring not only whether a straw was hit or not, but also the drift time of the primary electrons within the gas volume, the TRT reaches a spatial resolution of 118 µm in the R-ϕ-plane for the barrel and 132 µm in z-ϕ for the end-caps. However, the TRT does not provide information about the z coordinate of the tracks in the barrel region.

3.2.4 Calorimetry at ATLAS

Next to the tracking, calometry is the second important type of measurement at large multipurpose detectors. The total energy of a particle can be measured by stopping it in an absorber material. This means that the particle deposits its complete amout of energy in the material while giving rise to a shower of secondary particles. This measuring principle is of particular importance for neutral particles, which can only be detected in this way. In the context of this thesis, the calorimeter system is of special interest for measuring the missing transverse momentum and for identification of hadronically decaying tau leptons.

Calorimeters consist of several alternating layers of absorbers and a detection material, in which the particle showers create a signal. The two calorimeters at ATLAS are designed for different categories of interactions: the Electromagnetic Calorimeter and the Hadronic Calorimeter.

The ECAL aims for the detection of electrons, positrons and photons. Electrons and positrons lose energy mainly due to ionization and bremsstrahlung. For high energetic photons the dominant process is conversion to e^+e^- pairs, while for low energetic photons interactions with the atomic shell occur. Initial high energetic particles of these types create a cascade of secondary shower particles due to the combination of bremsstrahlung and pair-production, until ionization processes take over. The HCAL is designed for detecting interactions of hadrons. While charged hadrons also lose energy due to ionization, the dominant part of the energy loss for both charged and neutral high energetic hadrons comes from inelastic hadronic interaction processes with nuclei. Hadronic interactions also produce cascades of secondary particles. However, these hadronic showers are much more complex than the ones produced by purely electromagnetic interacting particles [125].

At ATLAS the so-called LAr Calorimeter (Liquid Argon Calorimeter) [127] is used for electromagnetic calorimetry, while the hadronic calorimetry is mostly done with the Tile Calorimeter [128] and partly also

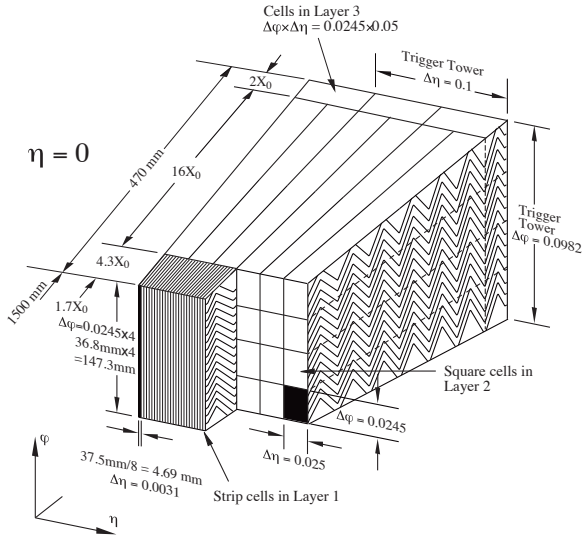

Figure 3.7: Schematic view of an ECAL barrel module [99].

with the LAr Calorimeter. Figure 3.6 shows a cutaway drawing of the calorimeter systems, displaying the LAr Calorimeter in orange and the Tile Calorimeter in blue and grey. The innermost of these detectors is the barrel part of the LAr Calorimeter, which has a range up to $|\eta| < 1.475$. The LAr barrel part is joined by two end-cap parts with a coverage of $1.375 < |\eta| < 3.2$. All three parts are made of accordion shaped modules of alternating lead absorbers and liquid argon as active material. A schematic drawing of a barrel module is displayed in figure 3.7. The accordion geometry assures a full coverage in ϕ. Shower particles ionize the argon atoms and the thereby produced free electrons induce a signal on copper electrodes between the layers.

The end-cap parts of the Electromagnetic Calorimeter are joined by the LAr hadronic end-caps, which measure hadronic showers and the Forward Calorimeter (FCAL), which also uses liquid Argon. All parts of the LAr Calorimeter are cooled down to −180 °C.

The Tile Calorimeter surrounds the LAr Calorimeter. It consists of a central barrel in the region of $|\eta| < 1.0$ and an extended barrel region in $0.8 < |\eta| < 1.7$. The absorbers of the Tile Calorimeter are made of steel.

The active part is built with plastic scintillator tiles. Ionizing shower particles traversing this material produce ultraviolet scintillation light, that is converted to visible light by wavelength-shifting fluors, that the plastic is doped with. Fibre cables at the edges of each tile collect the visible light and lead it to photomultipliers, where the signals are read out.

3.2.5 Muon Systems

The detection principle of muons is based on the fact that they lose very little energy due to interaction with matter. Since muons are about 200 times heavier than electrons, their respective energy loss through bremsstrahlung is much smaller. Below energies of 100 GeV, the energy loss is dominantly due to ionization and excitation. Above this threshold also pair production and bremsstrahlung contribute at a significant level. However, the sum of these interaction effects still remains small, enabling muons to traverse large amounts of material. At ATLAS the minimal energy for muons to escape the calorimeter system is about 4 – 5 GeV [129, 130].

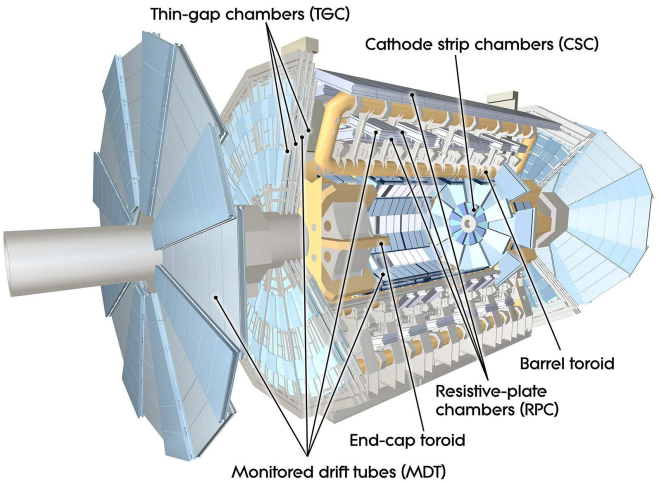

Figure 3.8: Schematic view of the ATLAS muon spectrometer [136].

Since the calorimeters are designed to stop all other particles except neutrinos, the detection of muons can simply be achieved by using a dedicated tracking device surrounding the calorimeter. The ATLAS Muon Spectrometer [131–133], displayed in figure 3.8, uses two technologies for tracking. Monitored Drift Tube chambers (MDTs) [134] cover the range $|\eta| < 2.7$. In the innermost end-cap layer, the range is limited to $|\eta| < 2.0$. Here the rates are so high, that the MDTs have to be replaced by Cathode Strip Chambers (CSCs) [135]. The MDT chambers in the barrel region are arranged in three cylindrical layers around the beam axis, while in each end-cap region they form four wheels, perpendicular to the beam axis. The chambers consist of three to eight layers of aluminum tubes with a diameter of 29.97 mm with gold-plated tungsten wires as anodes. The CSC system is built from two disks of eight chambers. Each chamber has four layers of multiwire proportional chambers with segmented cathodes on both sides.

In addition to the track location measurement, the ATLAS Muon Spectrometer has a trigger system, which provides fast information on muons traversing the detector. This is accomplished with Resistive Plate Chambers (RPCs) [137] in the barrel region ($|\eta| < 1.05$) and Thin Gap Chambers (TGCs) [138] in the end-caps ($1.05 < |\eta| < 2.4$). The RPCs consist of a gas-filled volume with two parallel electrode-plates with a resistive shielding and a distance of 2 mm. Traversing muons create a charge avalanche that induces a signal on the segmented anode plate.

The RPCs provide a spatial resolution of 5 – 10 mm and a time resolution of ~1 ns [139]. The TGCs are multiwire proportional chambers that have a smaller gap between wire and cathodes (1.4 mm) than the distance between each wire (1.8 mm). With high electric fields this assures short drift times and therefore good time resolution.

3.2.6 The ATLAS Trigger System

With a nominal bunch-spacing of 25 ns the proton-proton collision rate at LHC is 40 MHz. Assuming an average event size of 1.6 MB, this would produce 64 TB of data per second. Storing this amount of data is unfeasible and also not necessary. Soft QCD interactions are dominating in proton-proton collisions and therefore most of the events are not interesting for physics analysis. ATLAS uses a three stage trigger system [140–142] that filters for relevant events to reduce the data rate to 200 Hz. These trigger stages are called level 1 (L1), level 2 (L2) and event filter (EF).

Level 1 Trigger The level 1 trigger is hardware-based and selects from resolution-reduced calorimeter and muon trigger chamber information. The L1 calorimeter trigger is able to identify objects like electrons, photons, tau leptons and jets as well as missing transverse momentum. Its decisions are based on clustering algorithms and isolation criteria.

The L1 also provides information about the region of interest, passing the coordinates of relevant objects to the next stage. The L1 reduces the data rate by three orders of magnitude to about 75 kHz.

Level 2 Trigger A further reduction of the event rate to ~3 kHz is reached with the level 2 (L2) trigger. The L2 is software based and uses information from the tracking system as well. It can access the full granularity of the detector. For the selection the L2 trigger only analyzes signals from the region of interest. Each event takes ~40 ms to be processed.

Event Filter As a last step in the trigger chain, the event filter (EF) uses information from L2 to analyze fully reconstructed events. The algorithms for the EF are mostly based on algorithms very similar to those used for offline reconstruction. With a computing time of ~4 s per event, a large computing facility is required. At this stage, the rate has been reduced to the required 200 Hz.

Physics Streams and Trigger Chains The events that have been selected by the trigger system are stored in so-called data streams. These are based on the event types that have been triggered on. There are four data streams for physics analysis: *Egamma*, *Muons*, *JetTauEtmiss* and *MinBias*.

While the first three streams contain events with mostly one type of physics object according to their name, the *MinBias* stream selects events randomly. The physics streams used in this analysis are the *Egamma* stream and the *Muons* stream. Additional streams are used for calibration or Data Quality (DQ) checks.

The whole sequence of trigger decisions defines the so-called *trigger chain*. Trigger chains are what in the analysis is simply referred to as trigger. The trigger chains include various selections of special event categories on event filter level. These are event selections that are of interest for a particular type of physics analysis.

Muon Triggers Muons identified at level 1 [142, 143] need a spatial and temporal coincidence of hits in three RPC layers for the highest p_{T} threshold and a coincidence of hits in two layers for the other thresholds. A coincidence of hits in three TGC layer is needed with an exception for some areas in the lowest threshold. An estimate for the p_{T} of the muon is derived by the deviation of the hits from a muon track with infinite momentum with six thresholds. According to the global trigger the region of interest is passed on to the level 2. This region of interest is typcially the size of $0.1\,\Delta\eta \times 0.1\Delta\phi$ in the RPCs and $0.03\,\Delta\eta \times 0.03\Delta\phi$ in the TGCs.The L1 muon trigger has a geometric coverage of about 99 % in the endcap regions and 80 % in the barrel.

From the region of interest provided by the level 1 trigger, the level 2 trigger processes the reduced amount of data to construct a track using additional information from the MDT chambers. For this a simplified parametrization is used to reduce the computation time. The result is the Level 2 stand-alone-muon which is combined with a matching track from the Inner Detector to receive a weighted average of both objects which is called the level 2 combined muon.

On event filter level muon candidates are constructed by using the muon detector information first and combining them with Inner Detector tracks. If this method does not succeed, muons are searched by extrapolating the Inner Detector tracks to the muon chambers and trying to match them to track segments there. The final trigger considers selection criteria like the minimum p_{T} and the isolation to

other objects. The two muon triggers used in this analysis select single muons and will be further described in section 4.1.4.

Electron Triggers The level 1 electron trigger [142, 144] uses calorimeter information at a reduced granularity. These signals are called trigger towers and cover an area of $0.1\,\Delta\eta \times 0.1\Delta\phi$. For this the cells of the calorimeters are summed up, excluding the fourth layer of the hadronic endcap and barrel-endcap gap scintillators. Using this information EM-clusters are constructed from local maxima in the calorimeter cells.

At level 2, information from the Inner Detector is added. Using the level 1 clusters as basis input, the trigger executes a fast calorimeter reconstruction algorithm. For the Inner Detector data a simplified track reconstruction is performed. The cluster algorithm used at level 2 stage is similar to the one used for offline reconstruction (compare section 3.3) but are performed at a lower resolution. At event filter level the clusters are build using the same granularity as offline.

Three different reference points are established to reject background events. A loose selection is based on selection shower shape variables, hadronic leakage variables and a track-cluster matching. The medium selection adds calorimeter shape cuts, improved track quality and a tighter track-cluster matching. The tight selection has requirements on the ratio of deposited calorimeter energy to the momentum from track reconstruction. Furthermore the particle identification information from the TRT is utilized. The final trigger also considers selection criteria on p_{T} and track isolation (see section 4.1.4).

3.3 Definition of Physics Objects at ATLAS

The particles that are produced by proton collisions or their decay products traverse the detector volume originating from the in the center of the ATLAS detector. The various subdetectors of ATLAS assure that any lepton, hadron or photon leaves traces in the form of electronic signals. Neutrinos alone escape undetected. Assuming that these signals exceed the noise level, the particles can be considered as being detected. However, the detection in one of the subdetectors does not yet provide enough information for identification. Only the combination of all the data from the various subdetectors creates a signature, that can be assigned to a specific particle for example. The procedure of reconstructing physics objects from these signatures will be described in this section. The physics objects are defined in sections 3.3.1-3.3.7 and used throughout the analysis that is described in the following chapters. For the analysis an additional object selection will be applied.

Due to the high instantaneous luminosity of the LHC, reconstruction and identification of objects at ATLAS is a challenging task, that needs fast and efficient algorithms. Objects are either identified directly by the patterns they leave in the detector, or conclusions are drawn from the analysis of their decay products. In both cases there is the possibility of a mis-identification, which leads to the fact that identification is a statistical procedure and does not work for single events separately. While the identification should be as efficient as possible, one wants to minimize mis-identification at the same time. Falsely identified objects are also referred to as *fakes* and the *fake rate* describes the percentage of mis-identified objects of a certain type, e.g. electrons. Studying fakes can be done by using simulated events from theory predictions as well as from well-known processes in data-driven methods. The simulations are crucial to compare the observed data events with the expectations from the SM. The process of generating such simulated events using Monte Carlo methods is described in section 3.4 [145].

Even though neutrinos are not directly detected, an imbalance of the momentum in the transverse plane can be observed. This missing transverse energy is also an important indicator for SUSY processes and will be further described in section 3.3.7.

Since a signature of a physics object in the detector might fulfill all the criteria to be identified as more than one reconstructed analysis object, an overlap removal procedure is used. This discards all but one object as described in section 4.1.2.

3.3.1 Jets

Jets are accumulations of many particles in a comparatively narrow cone, that arise from a single initial high energetic quark or gluon. Also hadronically decaying tau leptons result in particle jets, which is further discussed in section 3.3.6. Since quarks and gluons carry color charge, confinement forces them to hadronize. This means that the initial partons form colorless hadrons together with quarks and antiquarks that are created in pairs in their vicinity from the vacuum.

The jet object that is used in an analysis must be defined by an algorithm. These jet-finding algorithms decide how to group a set of particles into a jet and which properties are assigned to it. Current jet reconstruction at ATLAS relies only on information from the calorimeter, in which the energy of the jet constituents is deposited electromagnetically and hadronically.

There are various approaches for jet finding algorithms. For this thesis, the anti-k_t algorithm is used [146, 147]. The algorithm uses three-dimensional, topological clusters as input. These clusters are defined by summing up calorimeter cell entries. From a seed cell with high energy deposit, iteratively neighboring cells are added and a splitting algorithm finds local minima and maxima to separate the clusters further [145]. The anti-k_t algorithm then defines conical jets by recombining these clusters in a sequential procedure. It defines distances between two objects i and j by

$$d_{ij} = \min\left(k_{Ti}^{2p}, k_{Tj}^{2p}\right) \frac{\Delta R_{ij}^2}{R^2}, \tag{3.9}$$

with $\Delta R_{ij}^2 = \Delta\phi_{ij}^2 + \Delta\eta_{ij}^2$ and k_{Ti}, η_i and ϕ_i are the transverse momentum, pseudorapidity and azimuthal angle of object i. The parameter p defines the impact of the energy versus the geometrical distance, while the radius R controls the size of the jet. Furthermore the distance between an object i and the beam is defined as

$$d_{iB} = k_{Ti}^{2p}. \tag{3.10}$$

From a set of all distances d_{ij} and d_{iB}, the two objects with the smallest distance are merged to one object. This is repeated until the smallest distance is d_{iB}. In this case the object i is defined as a jet, the list is updated, and the procedure starts again. With the parameter R this break condition can be controlled, as it controls the size of d_{ij}. The larger R is chosen, the more objects are added to the final jet. For this analysis it is chosen to be $R = 0.4$. By setting $p = -1$, the anti-k_t algorithm starts merging those objects with high p_{T}. This means that soft radiation does not have a big influence on the shape of the jet.

3.3.2 *b*-jets

Jets originating from b-quarks are of particular interest to control the background contributions in this analysis. These b-jets are identified by using vertex information. Since B-mesons have a life-time of ~1.6 ps, they can travel measurable distances within the detector, before creating a jet featuring a displaced vertex.

In this thesis the MV1 algorithm [148] is used for tagging b-jets. This algorithm is based on a neural network, that uses the output of the JetFitter+IP3D, IP3d and SV1 algorithms as input [149]. The MV1 algorithm offers efficient tagging with a low mistagging rate. For the b-jet identification in this thesis a working point that corresponds to 60 % tagging efficiency is chosen.

3.3.3 Electrons

Electrons leave tracks in the Inner Detector and deposit their energy in the electromagnetic calorimeter, hence entries in those two detector systems are used for the reconstruction algorithm [150, 151]. In the central region of the detector with $\eta < |2.47|$, the reconstruction starts with searching for seed clusters in the calorimeter that have a total transverse energy that exceeds 2.5 GeV. This search is performed with a *sliding window* algorithm. A search window with a size of 3×5 in units of 0.025×0.025 in $(\eta \times \phi)$ moves along the calorimeter cells until the energy threshold is exceeded. The seed cluster is then matched to a track from the Inner Detector.

Tracks with at least four hits in one or both silicon detectors are extrapolated from the point closest to the vertex to the middle of the calorimeter. They have to be within a distance of $\Delta\phi < 0.2$ to the cluster on the side that is bending towards it. If the track bends in the other direction, the criterion is $\Delta\phi < 0.05$.

The tracks are also required to be within $\Delta\eta < 0.05$ with respect to the cluster. If there are less than four silicon hits, the track is considered a TRT-only track. These tracks are extrapolated from the last measurement point and must meet the same requirements for the difference in ϕ. Since the TRT does not provide information about the η coordinate, this requirement is dropped.

Traversing the tracker, electrons lose energy due to bremsstrahlung which causes their trajectory to continuously bend more in ϕ. This energy loss has to be accounted for, which is done by using the Gaussian Sum Filter (GSM) algorithm to refit electron tracks [152]. An electron is reconstructed if at least one track can be matched to the seed cluster. If more than one track matches the cluster, tracks with hits in one or both of the silicon detectors are given priority and the track with the smallest distance ΔR to the seed cluster is selected.

The cluster energy is determined by summing up the measured energy deposit in the cluster with the estimated energy that is missed because it is either deposited outside of the cluster or outside of the calorimeter. For electrons in the central region, the four-momentum is calculated by using both calorimeter and tracking information. The energy is taken from the cluster, while η and ϕ are provided by the track fit. For TRT-only tracks η and ϕ from the cluster are used. In the forward region ($2.5 < |\eta| < 4.9$) no tracking information is available and the reconstruction relies on the calorimeter only.

For the analysis described in this thesis however, only electrons with $|\eta| < 2.47$ are considered. Three different cut-based selections with increasing strictness are defined: *loose*++, *medium*++ and *tight*++.

The *loose*++ selection is based on the shape of the shower in the electromagnetic calorimeter and the size of the hadronic component compared to the energy in the electromagnetic cluster. The *medium*++ selection implements *loose*++ and adds further requirements on the track quality, the shower shape and track-cluster-matching. The *tight*++ selection implements both the *medium*++ and *loose*++ requirements. It further tightens the criterion on $\Delta\phi$ between track and cluster and vetoes electron candidates that match reconstructed photon conversions. In addition, the ratio of the cluster energy to the track momentum is taken into account.

Using a tag-and-probe method on samples of $Z \to e^+e^-$ and $J/\psi \to e^+e^-$ events, the reconstruction and identification efficiency can be measured [153]. A very tight selection is applied on one of the two electrons from the decay, which is used as the *tag*. The second electron passes a looser selection and is used as the *probe* for the efficiency measurement. For background rejection, additional selection criteria like requirements on the invariant mass are applied. Background template fits and combined shape fits are used to estimate the contribution of objects that are falsely identified as electrons in the probe sample. These could for example be hadrons or electrons from photon conversions. This clean probe sample is then used to derive the efficiency of the *loose*++, *medium*++ and *tight*++ selections. These efficiencies are represented in figures 3.9b and 3.9a, as a function of the pseudorapidity and the transverse energy.

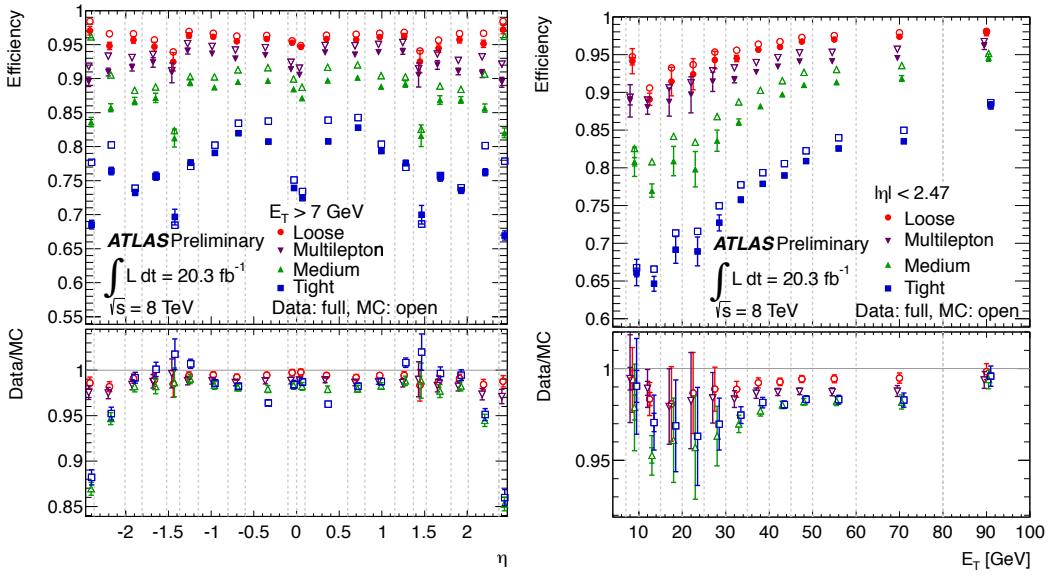

(a) (b)

Figure 3.9: The identification efficiency of electrons as a function of (a) the pseudorapidity and (b) the transverse energy for the different selection points. The measurements were performed with the full 2012 dataset [153].

3.3.4 Photons

Photons are not used for the analysis described in this thesis, nevertheless their reconstruction will also briefly be discussed. The signature of photons in the calorimeter is very similar to the one of electrons. Therefore, the reconstruction [154, 155] of photons uses the same sliding window algorithm to identify electromagnetic clusters. If a photon converts to a e^+e^- pair in the Inner Detector, the two resulting tracks appear with opposite curvatures originating from a single point in the tracking detector. Their tracks can be matched to clusters in the calorimeter. If the photon does not convert, no track will be visible. Furthermore, the shower shape of photons in the calorimeter is narrower compared to the one of electrons. The efficiency of photon identification is measured from $Z \to \ell^+\ell^-\gamma$ decays.

3.3.5 Muons

Since muons are in principle the only detectable particles that surpass the calorimeter, they leave a unique signature in the detector. Their reconstruction and identification [156–158] relies mainly on information from the muon spectrometer. In addition to that, information from the Inner Detector and the calorimeter system is used. According to the available information, four different types of reconstructed muons are defined:

1. *Stand-Alone* (SA) muons are reconstructed only with information from the muon spectrometer.

2. *Combined* (CB) muons are reconstructed independently in the Inner Detector and the muon spectrometer and the two tracks are then merged to one.

3. *Segment-tagged* (ST) muons are reconstructed by extrapolating tracks from the Inner Detector which then can be associated with at least one track segment in the MDT or the CSC chambers. ST

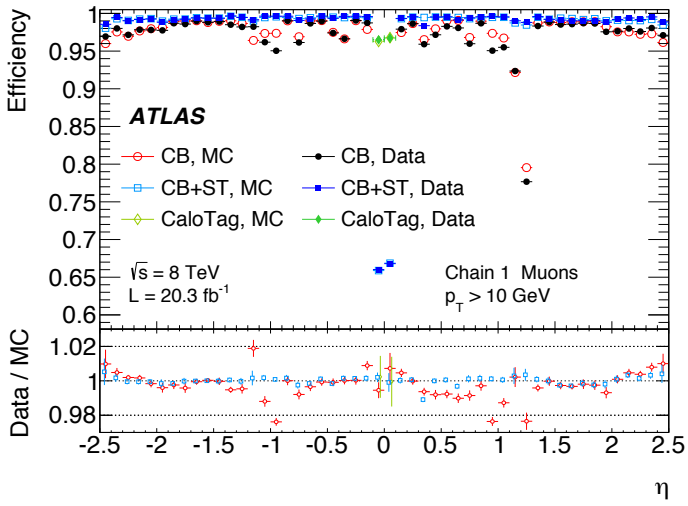

Figure 3.10: The identification efficiency for different muon types with $p_T > 10$ GeV as a function of the pseudorapidity. The measurements were performed in $Z \to \mu\mu$ events with the full 2012 dataset [157].

muons are used to increase the acceptance in case only one of the layers in the muon spectrometer was passed by the muon.

4. *Calorimeter-tagged* (CaloTag) muons are reconstructed from tracks in the Inner Detector that can be associated to calorimeter energy deposits matching a minimum ionizing particle.

The SA, CB and ST muons are reconstructed using two different approaches called the STACO algorithm [159] (also called chain 1) and the MUID algorithm [160] (also called chain 2). Chain 1 performs a statistical combination of the track parameters from the Inner Detector and the muon spectrometer. Chain 2 performs a global refitting of the hits from the two detector systems. For this thesis, the chain 1 muon collection is used. Tracks from the Inner Detector, used for combination, are required to have a minimum number of hits in each of the ID subdetectors.

As for electrons, the reconstruction efficiency of muons is studied with a tag and probe method. These studies are performed in samples of $Z \to \mu\mu$, $J/\psi \to \mu\mu$ and $\Upsilon \to \mu\mu$ decays [157]. In the $Z \to \mu\mu$ events two oppositely charged muons are selected with an invariant mass compatible to that of the Z boson. The *tag* is a CB muon and the *probe* is a CaloTag muon. Figure 3.10 shows the reconstruction efficiency for chain 1 muons as a function of η, measured in $Z \to \mu\mu$ events. For a combination of CB and ST muons the reconstruction efficiency is ~98 % over the whole η range except $\eta \approx 0$. In simulated events, the efficiency is slightly higher than observed in data. This is corrected by a scale factor which is applied to the simulation.

3.3.6 Tau Leptons

The reconstruction and identification of tau leptons is very different from the methods that can be applied to other charged particles. Due to their short life-time of 2.9×10^{-13} s, tau leptons decay before they can be directly observed in the detector. In the case of leptonic decays, there is only very limited possibility of identification. The results will be reconstructed and identified as electrons or muons. The hadronic decays however can be identified to originate from tau leptons, but their jet-like signature in the detector leaves the experimental challenge of distinguishing them from QCD jets. For these reasons, all objects referred to as tau leptons in the context of this analysis are in fact hadronically decaying tau leptons.

Reconstruction of tau jets starts with the anti-k_t algorithm ($R = 0.4$) that has been described in section 3.3.1. Next, particle tracks are associated with the tau candidate if they are in the *core region* with $\Delta R < 0.2$ around the tau candidate direction. More tracks in the *isolation region* with $0.2 < \Delta R < 0.4$ are used for identification. The identification is accomplished with dedicated tau identification algorithms [161–163]. The majority of hadronic tau decays leads to either exactly one or exactly three tracks of charged particles (compare figure 2.12a). These tracks are also referred to as *prongs*. Requiring exactly one or three prongs is one of the most discriminating features to separate tau leptons from QCD jets. Also the comparatively narrow deposition of energy in the calorimeters is an important differentiator.

Many variables are taken into account for the identification and are used in a multi-variate approach based on a boosted decision tree (BDT) [164]. The discriminating variables [163] are listed below. Figure 3.11 shows exemplary distributions for two of those variables.

- *Central energy fraction* f_{cent}: This fraction describes the ratio of transverse energy that is deposited within a cone of $\Delta R < 0.1$ around the tau candidate to all the energy in $\Delta R < 0.2$. It is calculated by summing up all the energy of clusters that have a barycenter that lies within the respective cone.
- *Leading track momentum fraction* f_{track}: This observable is defined as the ratio of the transverse momentum of the highest-p_{T} charged particle in the core region to the total transverse energy sum in the core region.
- *Track radius* R_{track}: This radius describes the distance of the associated tracks to the tau candidate direction, weighted with the transverse momentum and using all tracks in the core and isolation region.
- *Leading track IP significance* $S_{\text{lead. track}}$: This is defined as the distance of closest approach of the highest-p_{T} track in the core region to the primary vertex in the transverse plane, divided by its estimated uncertainty.
- *Number of tracks in the isolation region* $N_{\text{track}}^{\text{iso}}$: The number of tracks that can be associated with the tau candidate in the region $0.2 < \Delta R < 0.4$
- ΔR_{max}: This describes the maxium ΔR between a track that can be associated with the tau candidate and the tau direction.
- *Transverse flight path significance* $S_{\text{T}}^{\text{flight}}$: This significance is defined as the decay length of the secondary vertex in the transverse plane divided by the estimated uncertainty on this length.
- *Track mass* m_{track}: This observable is the invariant mass derived from all tracks of the tau candidate in the core and isolation region.
- *Track-plus-*π^0*-system mass* $m_{\pi^0+3\text{track}}$: The invariant mass of all tracks and π^0 mesons in the core region.
- *Number of* π^0 *mesons*: The number of π^0 mesons in the core region.
- *Ratio of track-plus-*π^0*-system* p_{T}: This is defined as the p_{T} estimated by using the track and the π^0 information divided by p_{T} from calorimeter information only.

The BDT algorithm is trained separately for 1-prong and 3-prong candidates. Three working points with different identification and background rejection powers are defined. These working points are labelled

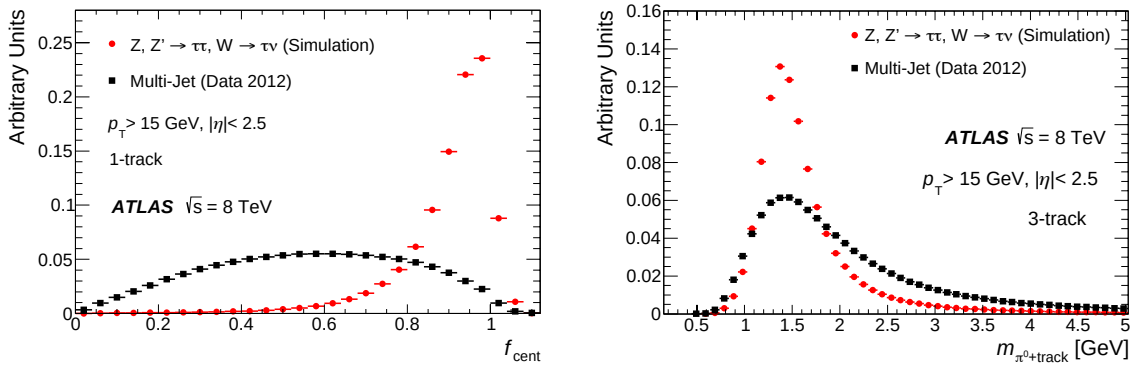

(a) Central energy fraction f_{cent} for 1 prong decays. (b) Track-plus-π^0-system mass $m_{\pi^0+3\text{track}}$ for 3 prong decays.

Figure 3.11: Discriminating variables for tau lepton identification [163]: Displayed are the central energy fraction (a) and the invariant mass of all tracks and π^0 mesons in the core region (b). Both figures show the distribution for simulated $Z \to \tau\tau$ events in red and for background events from data where a dijet selection is applied in black.

loose, *medium* and *tight*, where a tighter selection leads to a lower efficiency but a higher background rejection.

The identification efficiency is displayed in figures 3.12a and 3.12b against the number of primary vertices. The flatness of the distribution indicates robustness against different pile-up (compare section 3.4.5) conditions.

Figures 3.12c and 3.12d display the background rejection power against the tau lepton identification efficiency for different cuts on the BDT output. For the BDT loose working point that is used in this analysis, the efficiency is ~70 %. This corresponds to 10 % unrejected background events for 1-prong candidates, respectively 2 % for 3-prong candidates.

Additionally to the background from QCD jets, electrons and muons can also fake a 1-prong tau signature. Discrimination against light leptons is performed with separate electron and muon vetos. For the electron veto the rejection is achieved using a BDT, while the muon veto uses a cut-based selection.

3.3.7 Missing Transverse Energy

Particles that are not affected by the electromagnetic or the strong force, can escape the detector system without interaction. Neutrinos fall into that category as well as the LSP in case of R-parity conserving SUSY models. However, as there is no initial momentum in the transverse plane, the vector sum of all objects must be zero. Undetected particles therefore appear as an imbalance in the momentum sum.

This imbalance is called missing transverse momentum $E_{\text{T}}^{\text{miss}}$ and it is an important indicator in the search for weakly interacting particles. For the reconstruction of $E_{\text{T}}^{\text{miss}}$ at ATLAS [165, 166] energy deposits in the calorimeters and reconstructed muons are used. The energy deposits are associated with fully reconstructed and calibrated objects. This is done for electrons, photons, jets and muons, carried out in this specific order to avoid overlap. Tau leptons are included in the jet objects. Matching the clusters to physics objects allows for an object-based calibration. All energy deposits that cannot be matched to a particular physics object, are considered as well. The negative vectorial sum of all individual objects, projected onto the transverse plane, provides the total $E_{\text{T}}^{\text{miss}}$.

Mismeasurement of the $E_{\text{T}}^{\text{miss}}$ can be caused by falsely reconstructed or missing objects, calorimeter noise and pile-up. To study the performance of the $E_{\text{T}}^{\text{miss}}$ reconstruction, samples with $Z \to \ell^+\ell^-$ and $W^\pm \to \ell^\pm\nu$ events were analyzed [165]. Due to the absence of neutrinos in $Z \to \ell^+\ell^-$ decays, no $E_{\text{T}}^{\text{miss}}$ is

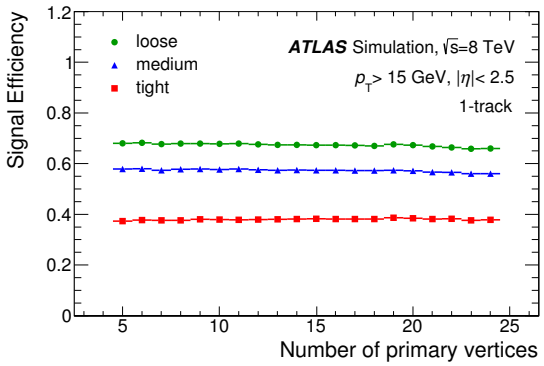

(a) Identification efficiency for 1 prong decays.

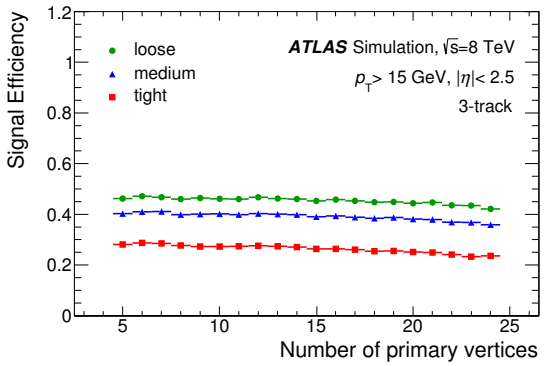

(b) Identification efficiency for 3 prong decays.

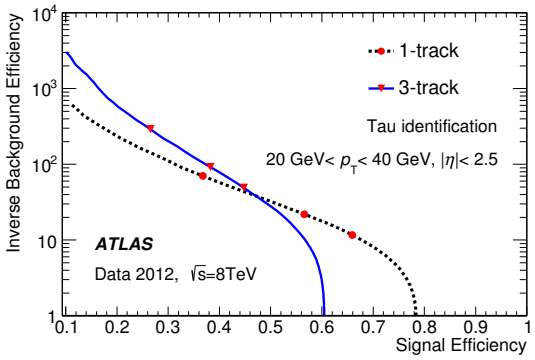

(c) Background rejection vs. identification efficiency.

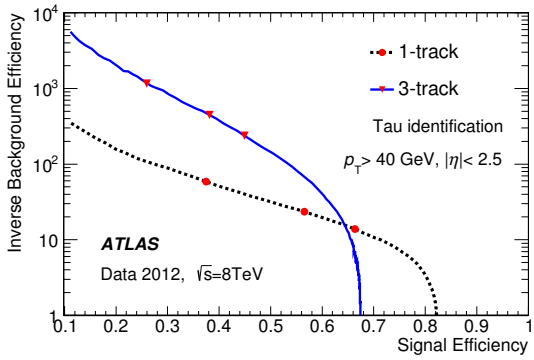

(d) Background rejection vs. identification efficiency.

Figure 3.12: Performance of the tau lepton identification [163]: Displayed are the tau lepton identification efficiency for (a) 1-prong and (b) 3-prong decays at three different working points in dependence of the number of primary vertices. The lower row shows the background rejection versus the signal efficiency for 1-prong and 3-prong decays for (c) $20\,\text{GeV} < p_{\text{T}}^{\tau} < 40\,\text{GeV}$ and (d) $p_{\text{T}}^{\tau} > 40\,\text{GeV}$. The red markers indicate the three working points *loose*, *medium* and *tight*, where *loose* has the best efficiency and tight the worst.

expected in these events. All $E_{\text{T}}^{\text{miss}}$ that is measured must be fake in this case and hence can be considered to show the $E_{\text{T}}^{\text{miss}}$ resolution as displayed in figure 3.13a. In $W^{\pm} \to \ell^{\pm}\nu$ decays however, the neutrino is a source for genuine $E_{\text{T}}^{\text{miss}}$. This can be used for validation studies. Figure 3.13b, as an example for one validation method, shows the $E_{\text{T}}^{\text{miss}}$ linearity which is the difference of reconstructed and true $E_{\text{T}}^{\text{miss}}$, normalized by the true $E_{\text{T}}^{\text{miss}}$ as a function of true $E_{\text{T}}^{\text{miss}}$.

3.4 Simulation, Software and Data Samples

The results of measurements in particle physics are usually only meaningful if they are directly compared to a prediction from theory. In the search for new physics, conclusions are reached by checking the observed data against expectations from the Standard Model background. An overshoot in data events compared to the prediction indicates the presence of new physics processes. Also the expectation on the number of events for various new physics models is important, since this can be used to exclude or validate these models. Hence, simulation of physics events is a crucial ingredient for the analysis. For that purpose, the complete chain of processes in the experiment from the initial proton-proton collisions to particle decays

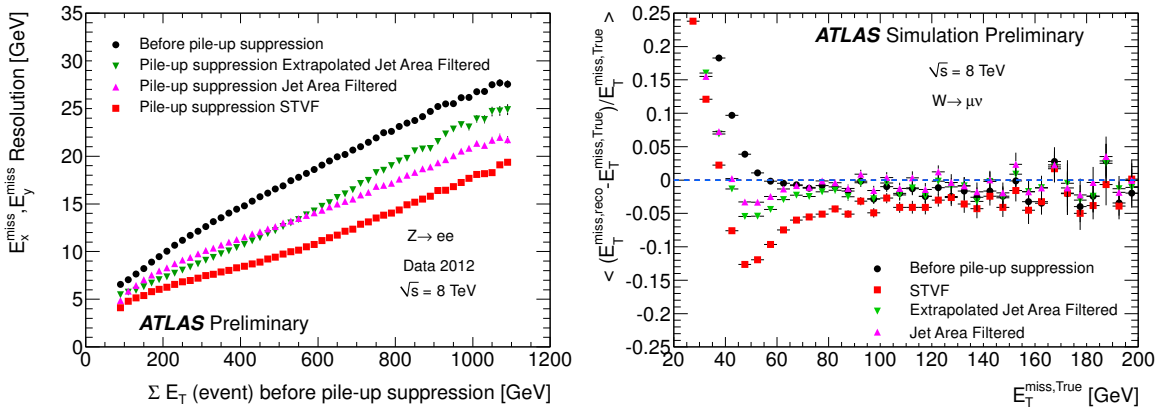

(a) $E_{\mathrm{T}}^{\mathrm{miss}}$ resolution in $Z \to e^+e^-$ events.

(b) $E_{\mathrm{T}}^{\mathrm{miss}}$ linearity in $W^{\pm} \to \mu^{\pm}\nu$ events.

Figure 3.13: Performance studies of the missing transverse momentum [165]: Fake $E_{\mathrm{T}}^{\mathrm{miss}}$ from $Z \to \ell^+\ell^-$ events in 2012 data is used to determine the $E_{\mathrm{T}}^{\mathrm{miss}}$ resolution, plotted against the total transverse energy in the event (a). With real $E_{\mathrm{T}}^{\mathrm{miss}}$ in simulated $W^{\pm} \to \ell^{\pm}\nu$ events the $E_{\mathrm{T}}^{\mathrm{miss}}$ linearity is determined (b).

and the interaction with the ATLAS detector, together with its response, has to be modelled. The simulated detector signals are then picked up by the same reconstruction and identification algorithms that are used for real data as they were described in sections 3.3.1-3.3.7. The complete chain of simulation is achieved with the ATLAS detector simulation [167, 168], which is based on the Athena framework [169].

3.4.1 Event Generation

To account for the fact that processes in quantum field theory are occuring on a random basis according to their probability, the simulation starts with the generation of events using a Monte Carlo (MC) approach. Events are generated with a factorization method, where the occuring processes are split according to their kinematic regime. The different simulation steps include the interaction of the primary partons (hard process), initial and final state radiation, underlying event and hadronization of the color-charged particles. In each of these phases different approximations are used for simulation. Figure 3.14 displays a schematic view of an event as simulated by a generator.

Hard process simulation The first step is the calculation of the hard scattering process, which is the interaction of the primary partons in the proton-proton collision. In figure 3.14 it is indicated by the big dark red circle in the middle of the illustration. The hard process simulation can be performed in fixed order perturbation theory by using matrix elements. The PDFs of the initial protons have to be considered for this step.

Parton showers from Initial and Final State Radiation Initial (ISR) and final state radiation (FSR) in the parton interaction cause additional parton showers. These processes have to be simulated too. Soft and collinear radiation cannot be calculated perturbatively. Therefore the radiation is simulated using parton splitting functions which use simplified kinematics to describe the probability for a parton splitting in two.

Hadronization The output of the showering simulation still only contains color-charged particles, which have to converted to hadrons. This hadronization is marked in green in figure 3.14 and has to be

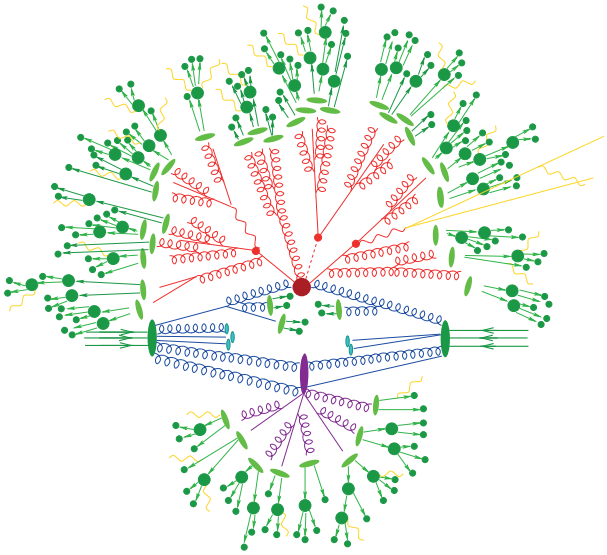

Figure 3.14: Simulation of a proton-proton event at the LHC by an event generator. The big red circle indicates the hard interaction part of the event, which is followed by a decay and additional hard QCD radiation (marked in red). A secondary interaction (underlying event) is marked in purple. The green parts of the figure represent the hadronization and decays of the hadrons [170].

handled with purely phenomenological models such as Lund string fragmentation [171] as for example implemented in Pythia [172]. After the hadronization is completed further decays of the hadrons are computed regarding to their measured branching ratios.

Event Generators The different event generators that are used for the analysis in this thesis are described in the following. Table 3.2 assigns them to the samples they are used for.

- Sherpa [170] is a general purpose leading order (LO) event generator that simulates the full event from the hard interaction to hadronization. Parton showering is performed with Apacic [173]. Tau leptons are simulated directly by the generator. Final state photon radiation is computed with Photos [174] and for hadronization of the color-charged particles a cluster hadronization approach is implemented. The used PDF set is CT10 [175].

- Pythia [172] is like Sherpa a general purpose LO event generator that can perform the simulation of the hard process, the parton showering and the hadronization using the Lund string model. Also here tau leptons are simulated by the generator itself. Pythia is also used used by other generators to include the showering process. The PDF set used is CTEQ6L1 [176].

- Herwig [177–179] is another general purpose LO event generator similar to Sherpa and Pythia. Like Sherpa it is used by other generators to simulate the showering. Tau leptons are simulated with Tauola [180, 181]. The improved version Herwig++ [182] is used for SUSY signal simulation. In this version tau leptons are simulated by the algorithm itself. The used PDF set is CTEQ6L1.

- Alpgen [183] is a LO matrix element generator and creates partons as output, which still have to undergo the showering and hadronization step of the simulation. For that purpose Alpgen is interfaced to Herwig or Pythia. Tau leptons are simulated with Tauola. The PDF set used for Alpgen is CTEQ6L1.

- MC@NLO [184, 185] can calculate matrix elements up to next-to-leading order. Interfaced to Herwig, parton showers and hadronization are simulated. The overlap of higher order calculations with the parton showering algorithm is compensated by assigning negative weights to a fraction of the events [186]. MC@NLO uses CT10 for the PDF set.
- Powheg [187] is another next-to-leading order matrix element generator, which is interfaced to Pythia for parton showering and hadronization. The overlap between higher order calculations and the parton showering algorithm is handled differently than in MC@NLO. In Powheg the hard radiation is simulated first, providing only positively weighted events as output. When using the showering algorithm a veto depending on the p_{T} can be applied as described in more detail in [187]. Also for Powheg tau leptons are simulated with Tauola. For Powheg the used PDF set is CT10.
- AcerMC [188] is a LO generator used to simulate Standard Model backgrounds. Parton showering and hadronization are simulated by Pythia, tau leptons by Tauola. The used PDF set is CTEQ6L1.

3.4.2 Detector Simulation

The event generators provide events as initial sets of particles with the respective four-momentum. To obtain the same information as in real collisions, the interaction of these particles with the magnetic field and the detector material has to be simulated, as well as the signals created as a response by the various detector components. For the simulation of detector interaction the geometry of the detector is translated into a three-dimensional model by use of the Geant4 [189] software. In this model the interactions with all material components and fields are computed. A faster detector simulation uses a parametrization of showers in the calorimeters and the Geant4 approach for the rest of the detector [190]. The output is used by the digitization software to calculate the signals provided by each detector component. These undergo the full reconstruction chain.

3.4.3 User Analysis Software

For this thesis the analysis is performed with the SFM analysis package [191], which is based on the SFrame framework [192]. Both utilize the Root analysis software package [193] to compute results and vizualize them in form of histograms or graphs. Furthermore, they provide tools for management of MC and data samples. Standard object definitions and analysis tools are implemented by the use of version `00-03-14` of the SUSYTools package [194]. This package provides all the common recommendations for object and event cleaning selection as well as event reweighting, application of scale factors and the estimation of the systematic uncertainties.

3.4.4 Proton Collision Data at 8 TeV

The LHC proton-proton collision data were recorded by ATLAS from 12th of April to 6th of December in 2012. Data taking is divided in so-called data taking periods, which consist of runs. These are subdivided into luminosity blocks. The dataset used for this thesis includes the data taking periods A-E, G-J and L. All data delivered by the LHC add up to 23.3 fb^{-1} of which the ATLAS experiment recorded 21.3 fb^{-1}. After applying data quality requirements 20.3 fb^{-1} are left for physics analysis. These requirements are applied by using the so-called Good Runs Lists (GRL), which contains information about usable data based on luminosity blocks. In the process of data taking each subsystem of the ATLAS detector is monitored in the ATLAS Control Room (ACR) to assure they are working within their nominal operating conditions. Furthermore, recorded data are used to perform automated offline checks

Background	Generator for main samples	Generator for alternative samples
W+jets	Sherpa	Alpgen + Herwig
Z+jets	Sherpa	Alpgen + Pythia/Herwig
$t\bar{t}$	Powheg + Pythia	Alpgen
single Top s- and Wt-channel	MC@NLO	—
single Top t-channel	AcerMC	—
Diboson	Sherpa	Powheg + Pythia

Table 3.2: List of SM background processes along with the used MC generator for their simulation and alternative samples used for determining systematic uncertainties.

that flag non-usable data from a particular subsystem. Based on these flags and the comparison of various distributions to nominal values, a final decision about the data quality is made by offline shifters. The collected information about the data quality is stored in the GRL. The GRL used for this analysis is `v61-pro14-02_DQDefects-00-01-00_PHYS_StandardGRL_All_Good`. Data from the *Egamma* stream are used for the $\tau+e$ channel of the analysis and data from the *Muons* stream are used for the $\tau+\mu$ channel (compare section 4.1).

3.4.5 Monte Carlo Background Samples

The various Standard Model processes that add up to the background will be described in section 4.2.1. For analysis of their individual contributions different Monte Carlo (MC) samples are used. A list of utilized generators is compiled in table 3.2. A detailed breakdown of all MC samples can be found in appendix B.1.

These samples are added up to contributions of W+jets, Z+jets, Top Quarks ($t\bar{t}$ and single Top) and Diboson (WW, ZZ and WZ). They are weighted by luminosity such that they represent an equivalent of the used 20.3 fb^{-1}.

Samples with W+jets and Z+jets events, containing up to four jets from matrix elements, are simulated with Sherpa. For top quark pair production backgrounds Powheg interfaced to Pythia is used. These samples are reweighted based on the p_{T} of the $t\bar{t}$ system. The applied weights are based on measurement of the $t\bar{t}$ differential cross-section at $\sqrt{s}$ = 7 TeV as described in [195].

The single top production in s- and Wt-channels is simulated using MC@NLO with Herwig showering, while for the t-channel AcerMC with Pythia showering is used, since it has a better description of particles with forward direction. Diboson events are simulated using the Sherpa generator. For each of these generators, samples with alternative generators are used to evaluate systematic uncertainties (see table 3.2).

Several reweightings and rescalings have to be applied to MC to obtain better agreement between the simulation and data events. Most of these are provided by the SUSYTools package. One important event reweighting has to be applied due to the fact that pile-up conditions at ATLAS change over time. This is accounted for by a reweighting based on the average number of interactions per bunch crossing. Since the efficiencies and fake-rates for b-tagging depend on the choice of tagging algorithm, another weight is applied for events in which b-jets are selected. Also differences in the reconstruction efficiencies of muons, electrons and tau leptons between data and MC as well as differences in the trigger efficiencies are corrected by scale factors. Additional scalings of the MC samples are derived in section 4.3.

3.4.6 Monte Carlo Signal Samples

To draw any conclusions about the origin of possible excesses in data with respect to the expected SM background from simulation, the theory predictions for various SUSY models have to be part of the analysis as well. Furthermore, exclusion limits in the different SUSY scenarios can only be computed when the number of expected signal events in the regarded kinematic regions is known.

Therefore, for each SUSY model signal events are simulated in large sets of samples that cover a variety of different theory parameter combinations. These sets are also referred to as grids where typically two model parameters are varied while the rest of them stays fixed. Each parameter combination can be used as an entry in a two-dimensional plane in which for example exclusion limits are drawn.

The varied parameters in the GMSB grid are Λ and $\tan\beta$ for fixed $M_{\text{mess}} = 250\,\text{TeV}$, $N_5 = 3$, $\mu > 0$ and $C_{\tilde{G}} = 1$. In total 79 samples were generated using Herwig++ for $\Lambda = 40 - 110\,\text{TeV}$ and $\tan\beta = 2 - 62$.

In the nGM model there are two free parameters that are varied: $m_{\tilde{g}} = 400 - 1260\,\text{GeV}$ and $m_{\tilde{\tau}} = 117 - 337\,\text{GeV}$. The grid consists of 70 samples that were generated in Herwig++ as well.

To generate the 125 samples of the bRPV grid the Pythia generator was used. The fixed parameters are $A_0 = -2m_0$, $\tan\beta = 30$ and $\mu > 0$. Varied parameters are $m_0 = 400 - 2200\,\text{GeV}$ and $m_{1/2} = 200 - 800\,\text{GeV}$.

For the mSUGRA grid the varied parameters are $m_0 = 230 - 6000\,\text{GeV}$ and $m_{1/2} = 300 - 1000\,\text{GeV}$. The other parameters are set to $A_0 = -2m_0$, $\tan\beta = 30$ and $\mu > 0$. The set of 322 samples was generated with Herwig++.

Section B.2 contains a detailed breakdown of all signal MC samples with the according cross-sections. The signal cross-sections for all models are calculated at next-to-leading order (NLO) in the strong coupling constant with Prospino 2.1 [196]. Soft gluon emission is considered by resummation at next-to-leading-logarithmic accuracy (NLL) [196–200].

CHAPTER 4

Baseline Selection and Background Estimation

Observations in particle physics are typically interpreted by comparing them to a theoretical expectation. In the search for new physics this expectation consists of various Standard Model processes – denoted as SM background – and a signal. First, the correct description of the SM background contributions has to be studied and validated. Only then conclusions about observations in kinematic regions that might be dominated by SUSY signals can be drawn.

The first part of this chapter describes the baseline selection for the analysis (4.1). After that the SM processes which lead to similar final states are discussed in detail (4.2). For four background types Control Regions are defined to study events of these particular backgrounds (4.3). This allows for applying a correction to the normalization of the background.

Before going into detail about the analysis described in this and the next chapters, this paragraph is intended to give a brief overview of the analysis strategy. The supersymmetric signatures described in section 2.5.6 define the baseline selection including tau leptons and light leptons. The first step of the analyis is defining the physics objects that are used. Only by matching certain requirements a particle enters the selection and is considered in the analysis. Given this, the SM contributions to the baseline selection can be studied. The next step is correcting and validating of the description of data by Monte Carlo simulation. With the correct background description in hand, signal-like selections can be performed. The optimization of these selections are described in the following chapter. The final result is obtained from the background estimates together with an evaluation of the full systematic uncertainties and the data observation.

4.1 Object and Event Selection

The focus of this analysis are events with tau leptons, since they can be a unique signature in the SUSY models that are described in chapter 2. The standard reconstruction of tau leptons however leaves leptonic decay modes disregarded, which make up ~35 % of all decays. Furthermore, some models include both tau leptons and lighter leptons. To account for this, the baseline event selection includes also a light lepton. The analysis is divided into two separate channels. One channel uses electrons ($\tau+e$ channel), the other one muons ($\tau+\mu$ channel). The exact event selection is described in section 4.1.5.

4.1.1 Physics Object Selection

To set the event selection, the definitions of the particle objects themselves must be refined. In section 3.3 the reconstruction and identification of physics objects was described. For the actual analysis however,

physics object	selection criteria
tau lepton	*loose* candidate
	1 or 3 tracks
	$p_{\mathrm{T}}^{\tau} > 20\,\mathrm{GeV}$
	$\lvert\eta\rvert < 2.5$
baseline electron	*medium*++ candidate
	$p_{\mathrm{T}}^{e} > 20\,\mathrm{GeV}$
	$\lvert\eta\rvert < 2.47$
signal electron	*tight*++ electron candidate
	$p_{\mathrm{T}}^{e} > 25\,\mathrm{GeV}$
	$\lvert d_0\rvert < 1\,\mathrm{mm}$, $\lvert z_0 \sin\theta\rvert < 2\,\mathrm{mm}$
	$p_{\mathrm{T}}^{\mathrm{cone20}}/p_{\mathrm{T}}^{e} < 0.1$
baseline muon	combined / segment-tagged muon
	$p_{\mathrm{T}}^{\tau} > 10\,\mathrm{GeV}$
	$\lvert\eta\rvert < 2.4$
	$n_{\text{pixel hits}} + n_{\text{pixel dead}} > 0$
	$n_{\text{SCT hits}} + n_{\text{SCT dead}} > 4$
	$n_{\text{pixel holes}} + n_{\text{SCT holes}} < 3$
	$n_{\text{TRT hits}} > 5$
	for $(0.1 < \lvert\eta\rvert < 1.9)$: $n_{\text{TRT outliers}} < 0.9\, n_{\text{TRT hits}}$
signal muon	$p_{\mathrm{T}}^{\mu} > 25\,\mathrm{GeV}$
	$p_{\mathrm{T}}^{\mathrm{cone20}} < 1.8\,\mathrm{GeV}$
baseline jet	$p_{\mathrm{T}}^{jet} > 20\,\mathrm{GeV}$
	$\lvert\eta\rvert < 2.8$
	jet cleaning
signal jet	$p_{\mathrm{T}}^{jet} > 30\,\mathrm{GeV}$
	$\lvert\eta\rvert < 2.5$
	for $\lvert\eta\rvert < 2.4$, $p_{\mathrm{T}} < 50\,\mathrm{GeV}$: JVF > 0.5

Table 4.1: Summary of the object selection criteria.

additional selection criteria have to be applied to ensure high purity. All physics objects referred to in this thesis have to fulfill the following selection criteria, which are also summarized in table 4.1.

Tau leptons with the *loose* BDT working point (compare section 3.3.6) are chosen for this analysis. The tau jets are required to have exactly one or three tracks and be in the region of $|\eta| < 2.5$. Furthermore, since tau leptons with low transverse momentum show a worse performance in purity and efficiency, the object is required to have $p_{\mathrm{T}} > 20\,\mathrm{GeV}$.

For electrons two types of selections are made: one for a *baseline* object and a second for a *signal* object. Baseline electrons are candidates that pass the *medium*++ selection and are within $|\eta| < 2.47$. As for tau leptons, requiring $p_{\mathrm{T}} > 20\,\mathrm{GeV}$ increases purity and efficiency. The objects used in the final selection however are signal electrons. These have to pass the *tight*++ selection with $p_{\mathrm{T}} > 25\,\mathrm{GeV}$. Furthermore, the distance d_0 of the track to the vertex in the transverse plane has to be less than 1 mm and the distance $|z_0 \cos\theta|$ in the longitudinal plane must be smaller than 2 mm. This suppresses electrons that are the result of a photon conversion. The purity can be further enhanced with a relative isolation requirement: The sum of the p_{T} of all charged tracks in a cone with $\Delta R < 0.2$ around the electron candidate $p_{\mathrm{T}}^{\mathrm{cone20}}$ has to be less than 10 % of the electron p_{T}.

Also for muons both a baseline and a signal object are defined. Baseline muons have to be either combined or segment-tagged muons with $p_T > 10\,\text{GeV}$ and $|\eta| < 2.4$. Furthermore, there are requirements on the tracks. The sum of the number of pixel hits $n_{\text{pixel hits}}$ and the number of crossed dead pixel sensors $n_{\text{pixel dead}}$ must be larger than zero. The sum of the number of SCT hits $n_{\text{SCT hits}}$ and the number of crossed dead SCT sensors $n_{\text{SCT dead}}$ is required to be larger than four. Finally, there must be less than three missing entries in the pixel detector $n_{\text{pixel holes}}$ and the SCT $n_{\text{SCT holes}}$. The total number of hits in the TRT $n_{\text{TRT hits}}$ must be larger than five. For the region of $0.1 < |\eta| < 1.9$ less than 90 % of these hits are allowed to be outliers, meaning hits that can be associated with the track but result in a bad combined fit when extrapolating from the other tracking devices. Signal muons are required to have $p_T > 25\,\text{GeV}$ and fulfill an absolute isolation criterion: the sum of the p_T of all tracks in a cone of $\Delta R < 0.2$ around the muon p_T^{cone20} has to be less than 1.8 GeV.

Jets on baseline level are required to have $p_T > 20\,\text{GeV}$ and be in the region of $|\eta| < 2.8$. To avoid misidentified jets a cleaning is applied as described in [201]. These jets are flagged as *bad jets*. Signal jets need to satisfy $p_T > 30\,\text{GeV}$ and $|\eta| < 2.5$. Futhermore, for jets with $|\eta| < 2.4$ and $p_T < 50\,\text{GeV}$ the jet vertex fraction (JVF) [202] needs to be larger than 0.5. This is the fraction of energy of a jet which originates from the primary vertex.

4.1.2 Overlap Removal

For a given event, objects might be very close together in (ϕ, η) after reconstruction. The distance between these objects has been already defined as ΔR in equation 3.7. These reconstructed particles or jets are very likely to share the same physical origin and hence should be treated as such. Tau leptons for example are with high probability also reconstructed as jets. This means one of the objects needs to be removed in favor of the other. For this overlap removal the baseline level objects are used. The removal procedure is performed in the following order:

1. If the distance between a tau candidate and either a muon or an electron is $\Delta R < 0.2$, the object is considered to be a light lepton and the tau candidate is rejected.

2. If a jet overlaps with a tau lepton or an electron within a distance of $\Delta R < 0.2$, the object is considered to be the lepton and the jet is rejected.

3. If a muon or an electron overlaps with a jet within $0.2 < \Delta R < 0.4$, it is rejected, since it is likely to be a fake or to originate from a heavy flavor decay within the jet, rather than a result of the initial interaction.

4.1.3 Event Cleaning

To ensure the optimal dectector conditions for event reconstruction, a basic preselection is applied. The first step is to use the GRL. The GRL rejects events recorded while the detector was in a state which compromised the data in a way that makes it unsuitable for good reconstruction (compare section 3.4.4). Further requirements are applied offline after the reconstruction of the physics objects:

- No badly reconstructed muons are allowed.
- No cosmic muon candidates are allowed.
- The event must not contain bad jets that remain after overlap removal.
- The selected event is required to have a primary vertex with at least five tracks.

- The event does not contain noise entries in the calorimeters.
- Large $E_{\mathrm{T}}^{\mathrm{miss}}$ in the event is not due to non-operational calorimeter cells from the Tile Calorimeter.

4.1.4 Trigger Selection

Due to the more striking detector signature of muons and electrons compared to the one of tau leptons the obvious choice for triggers are single light lepton triggers. They provide sufficient event rejection to have a reasonable amount of events in terms of storage and computing power. The increasingly high instantaneous luminosities at the LHC demand a regular revision of the tightness of trigger selection criteria. For the 2012 data the triggers with the lowest p_{T} requirements and without prescalings are `EF_e24vhi_medium1` and `EF_mu24i_tight`. Triggers with prescaling reject a certain percentage of the suitable events. They can be used for background studies, but are not used for a search analysis, where the full integrated luminosity is desired. Both triggers require $p_{\mathrm{T}}^{\ell} > 24\,\mathrm{GeV}$. Additionally, both triggers add a requirement on the isolation of the leptons already on event filter stage. For the electron trigger this requirement is $p_T^{\mathrm{cone20}}/p_T < 0.1$ and for the muon trigger $p_T^{\mathrm{cone20}}/p_T < 0.12$. For leptons with higher p_{T} this isolation criterion is dropped by using a logical `OR` with the `EF_e60_medium1` for electrons and `EF_mu36_tight` for muons. As suggested by the name, their p_{T} requirements are $p_{\mathrm{T}} > 60\,\mathrm{GeV}$ and $p_{\mathrm{T}} > 36\,\mathrm{GeV}$ respectively.

The isolation criteria of the two lowest unprescaled triggers are looser or match the offline selection criteria. However, the background estimation technique for Multijet events utilizes the characteristics of looser lepton isolation in this particular event type (compare section 4.4). It therefore requires a selection without any constraint on the isolation. In this case, the unprescaled triggers are not suitable. Instead, the prescaled versions `EF_e24vh_medium1` and `EF_mu24_tight` of the single lepton triggers are used, where the isolation criterion is not part of the selection. During most of the data taking period both triggers had a prescale factor of 10 applied, which means that only 10 % of the events are kept for analysis. This is corrected by calculating the effective integrated luminosity and scaling the samples accordingly by a global factor.

In figure 4.1 the trigger efficiency for the muon triggers used in this analysis are displayed. By requiring $p_{\mathrm{T}}^{\mu} > 25\,\mathrm{GeV}$, one selects muons that are in the plateau region of the trigger efficiency. The efficiency can be obtained with a tag and probe method in $Z \to \mu\mu$ events. For electrons however, the same requirement is not sufficient to reach the efficiency plateau, as can be seen in figure 4.2a. This is considered by applying a p_{T} dependent scale factor, which is obtained with the very precise measurement of the efficiency in $Z \to ee$ events. Figure 4.2b shows the electron trigger efficiency in dependence of η for electrons with $p_{\mathrm{T}} > 25\,\mathrm{GeV}$. The drop in efficiency around $1.37 < |\eta| < 1.52$ is due to the less accurate measurement in the transition region of the calorimeter between the barrel and the end-caps.

4.1.5 Event Selection on Object Level

Aiming for SUSY models with tau-rich final states offers various possibilities for event selection. The analysis described in this thesis covers two of four search channels of a common search for SUSY with tau lepton final states [2]. These two channels are the $\tau+\mu$ channel and the $\tau+e$ channel, which include one light lepton: a muon in the first case and an electron in the latter. The other search channels aim for final states with purely hadronically decaying tau leptons, where one analysis selects exactly one tau lepton and the other one at least two tau leptons. Both of these channels veto light leptons to avoid an overlap with the light lepton channels.

The complete event selection for this analysis is summarized in table 4.2: In addition to the already mentioned event cleaning preselection and the trigger selection, it requires exactly one signal muon in the $\tau+\mu$ channel and exactly one signal electron in the $\tau+e$ channel. In both cases the light lepton of the

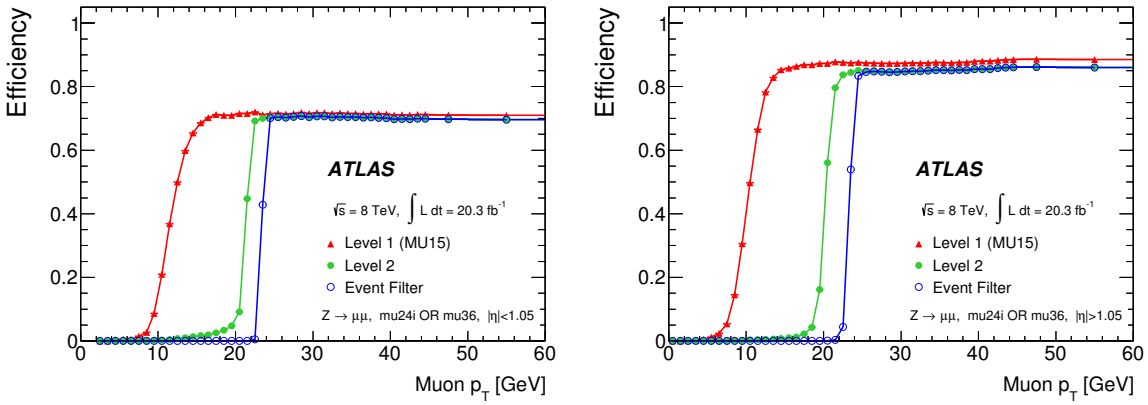

(a) Muon trigger efficiency in the central region.

(b) Muon trigger efficiency in the end-cap region.

Figure 4.1: Muon trigger efficiency in dependence of the transverse momentum for the central region of the detector with $|\eta| < 1.05$ (a) and the end-cap region with $|\eta| > 1.05$ (b) obtained with a tag and probe method in $Z \to \mu\mu$ events [143]. Errors show the statistical uncertainty only.

other flavor is vetoed on the level of the baseline object. This prevents the events in from overlappping with events from the other channel. Furthermore, both channels require at least one tau lepton.

	$\tau+\mu$	$\tau+e$
Physics stream	Muons	Egamma
Preselection	GRL event cleaning	

Trigger	`EF_mu24i_tight`
	`OR`
	`EF_mu36_tight`
		`EF_e24vhi_medium1`
		`OR`
		`EF_e60_medium1`

Physics Objects	$N_\mu^{\text{signal}} = 1$ $N_e^{\text{baseline}} = 0$ $N_\tau \geq 1$	$N_e^{\text{signal}} = 1$ $N_\mu^{\text{baseline}} = 0$ $N_\tau \geq 1$

Table 4.2: The complete event selection for the $\tau+\mu$ and the $\tau+e$ channel.

4.2 Standard Model Background

With the given selection of final states with exactly one light lepton and at least one tau lepton, a large contribution from SM processes is expected while contributions from SUSY processes are negligible. In chapter 5 the final selection will be described, which suppresses background contributions well enough to separate possible signal events. For understanding the remaining background contributions however, the modeling of the SM processes must be validated. This validation is performed in so-called control regions (CR) which add kinematic selection criteria on top of the baseline selection to enrich the events with a specific background type. Yet, these CRs must only have negligible contributions from signal events.

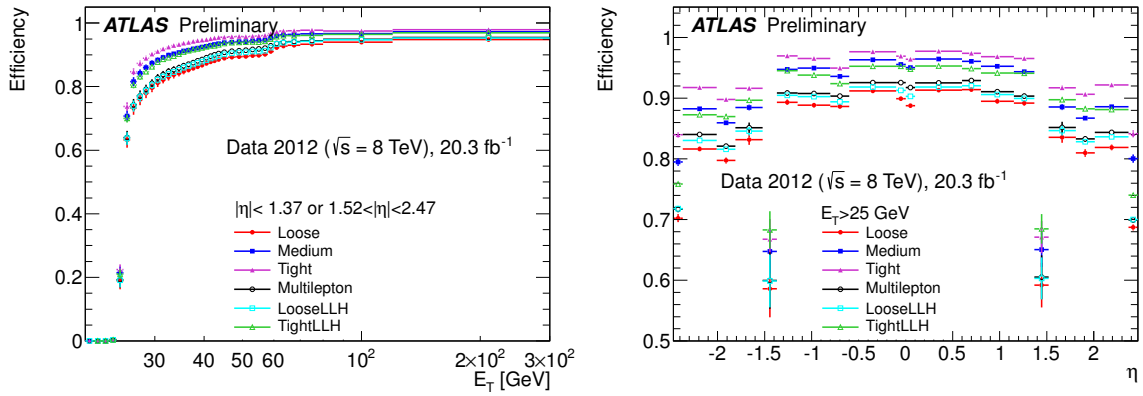

(a) Electron trigger efficiency versus p_{T}.

(b) Electron trigger efficiency versus η.

Figure 4.2: Electron trigger efficiency in the region of $|\eta| < 1.37$ or $1.52 < |\eta| < 2.47$ in dependence of the transverse energy (a) and for $p_{\mathrm{T}} > 25\,\mathrm{GeV}$ against the pseudorapidity (b) measured with a tag and probe method using $Z \to ee$ events [203]. Errors include statistical and systematic uncertainties.

4.2.1 SM Background processes

Considered Standard Model processes include W+jets, Z+jets, Top Quarks, Diboson and Multijet. Figure 4.3 displays exemplary Feynman diagrams of all these processes.

The production of the heavy gauge bosons $W^{\pm}$ and Z^0 is accompanied by jets from quarks and gluons as displayed in figures 4.3a and 4.3b. In case of W+jets, the W decays into a lepton which carries the charge of the gauge boson and a corresponding neutrino of the same flavor. For the majority of these event types, the charged lepton is the selected electron or muon. The selected tau lepton on the other side must be a misidentified gluon or quark jet. For Z+jets events the situation is different. The Z can decay in two charged leptons of the same flavor. If these are tau leptons, one of them might decay hadronically, while the other one decays into an electron or muon.

Top Quarks events are dominated by $t\bar{t}$ processes. Figure 4.3c shows a Feynman diagram for a $t\bar{t}$ process which produces a final state with a real tau lepton and a real light lepton. The top pair decays into two b quarks and two W bosons, of which both decay leptonically – one into a tau lepton and one into the light lepton. In figure 4.3c the same process is displayed with a different final state. Here, one of the W bosons decays hadronically, resulting in jets that can fake the tau lepton signature. The partaking b quarks give rise to b-jets which can be used for identification of such event types.

In Diboson processes two heavy gauge bosons are produced as can be seen in two examples in figures 4.3e and 4.3f. In both displayed examples the final state contains real tau leptons.

Multijet events add large contributions in the control regions. These event types include all events where the selected objects are faked by QCD processes. Light leptons, especially muons, are not very likely mimicked by a jet. However, with the huge cross-section of such events at the LHC, a significant amount of misidentification occurs. Also semileptonic heavy flavor decays of mesons after the hadronization are covered by the Multijet background. Figure 4.4 shows an example with the decay of a B^- into a D^0, a charged light lepton and a neutrino. In this case the light lepton is in fact a real object and identified correctly.

While the estimates for W+jets, Z+jets, Top Quarks and Diboson events are based on MC simulation, the measure for the Multijet background is based on a data-driven method. This method is described in section 4.4.

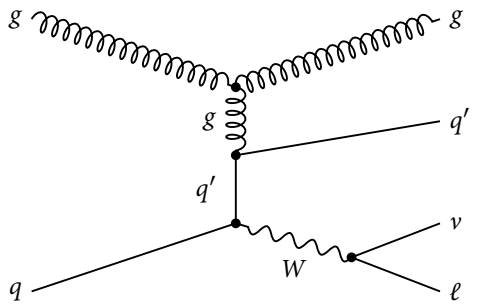

(a) W+jets process

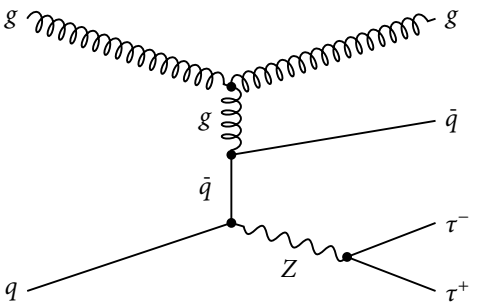

(b) Z+jets process

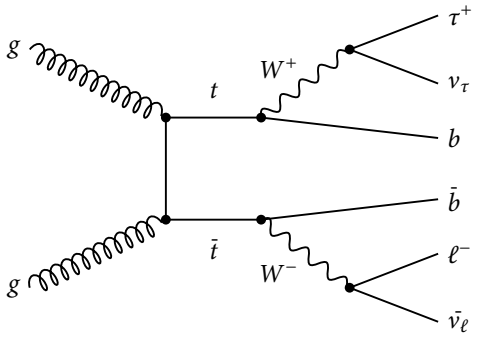

(c) $t\bar{t}$ process with true tau leptons

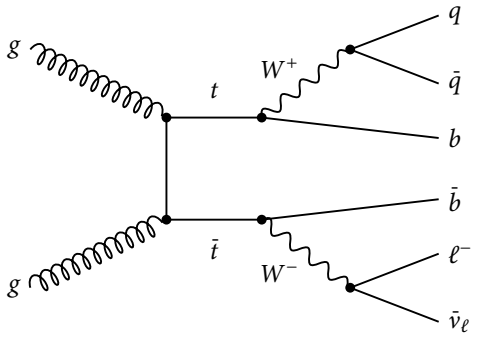

(d) $t\bar{t}$ process with fake tau leptons

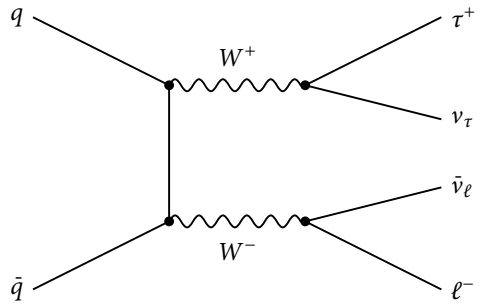

(e) Diboson process

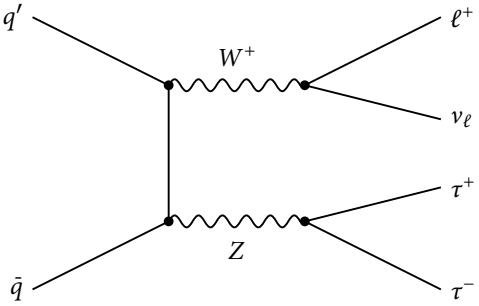

(f) Diboson process

Figure 4.3: Feynman diagram of the various background processes.

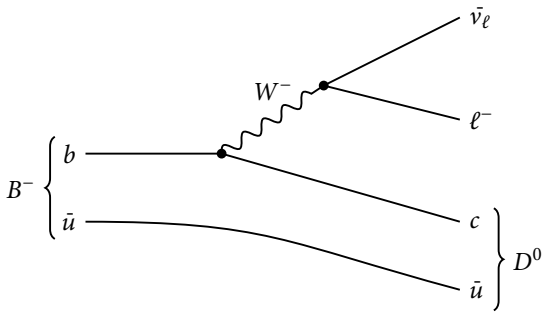

Figure 4.4: Feynman diagram of a semileptonic decay of a B meson.

4.2.2 Relevant kinematic variables

For the definition of control and signal regions a few kinematic variables have to be defined, that will be used throughout the entire analysis. These variables are suited to separate the event types that occur in the various backgrounds from each other. They can also be used to get a signal-enriched event set for the final selection. These variables are listed below:

- The *transverse mass* m_{T}^{ℓ} of the light lepton is a useful quantity to analyze the decay products of a W boson in the event. Since a leptonic decay as displayed in figure 4.3a leaves only the charged lepton as a detectable particle, the W invariant mass can not be measured. Due to energy and momentum conversation however, p_{T}^{ℓ} has a maximum at half of the W mass m_W (*Jacobian Peak*). The fact that the neutrino is the only source of real $E_{\mathrm{T}}^{\mathrm{miss}}$ in this event type can be exploited for the definition of the transverse mass:

$$m_{\mathrm{T}}^{\ell} = \sqrt{2 p_{\mathrm{T}}^{\ell} E_{\mathrm{T}}^{\mathrm{miss}} \left(1 - \cos\left(\Delta\phi\left(\ell, E_{\mathrm{T}}^{\mathrm{miss}}\right)\right)\right)}, \tag{4.1}$$

  where $\Delta\phi(\ell, p_{\mathrm{T}}^{\mathrm{miss}})$ is the azimuthal angle between the lepton and $E_{\mathrm{T}}^{\mathrm{miss}}$. At leading order these two objects should be back to back ($\Delta\phi(\ell, p_{\mathrm{T}}^{\mathrm{miss}}) = \pi$) and $p_{\mathrm{T}}^{\ell} = E_{\mathrm{T}}^{\mathrm{miss}}$. Therefore, the transverse mass has a maximum at $m_{\mathrm{T}}^{\ell} = m_W$.

- The scalar sum of the transverse momenta of the tau, light lepton and two leading signal jets

$$H_{\mathrm{T}} = \sum p_{\mathrm{T}}^{\ell} + \sum p_{\mathrm{T}}^{\tau} + \sum_{i=1,2} p_{\mathrm{T}}^{\mathrm{jet}_i}, \tag{4.2}$$

  is a quantity considered for the separation of background and signal.

- The *effective mass* is defined as the sum of H_{T} and the missing transverse momentum

$$m_{\mathrm{eff}} = H_{\mathrm{T}} + E_{\mathrm{T}}^{\mathrm{miss}}. \tag{4.3}$$

  Just like H_{T} it is a considered observable to define the signal region.

4.2.3 SM Background After Event Selection on Object Level

By considering the expected dominant backgrounds which were described previously, the sum of their predicted contributions can now be compared to the observed data. For this, the transverse masses of both muon and electron and $E_{\mathrm{T}}^{\mathrm{miss}}$ are taken as example control observables. The histograms in figure 4.5 display m_{T}^{ℓ} and $E_{\mathrm{T}}^{\mathrm{miss}}$ directly after the event selection on object level. The 2012 data is indicated by the black dots with black bars representing the statistical uncertainty, while the background contributions are stacked over each other – each background type indicated by a specific color. These are white for Multijet processes, light blue for W+jets, medium blue for Z+jets, light green for Top Quarks and brown for Diboson. The sum of these contributions is marked with a red line which is surrounded by a yellow grid band to indicate the statistical uncertainty on this prediction. The ratio of data to SM prediction is displayed below the histogram. The black dots and bars again represent data and its statistical uncertainty and a yellow band around 1 displays the statistical uncertainty of the predicted SM background.

Comparing the SM background contributions after the baseline selection in figure 4.5a and 4.5b, it can be seen that the background composition is slightly different. Both distributions feature as expected the dominant Jacobian peak of the W+jets background at the mass of the W boson. Also visible is the Z+jets contribution. It is more dominant in the $\tau+e$ channel because electrons are much more likely to fake a tau

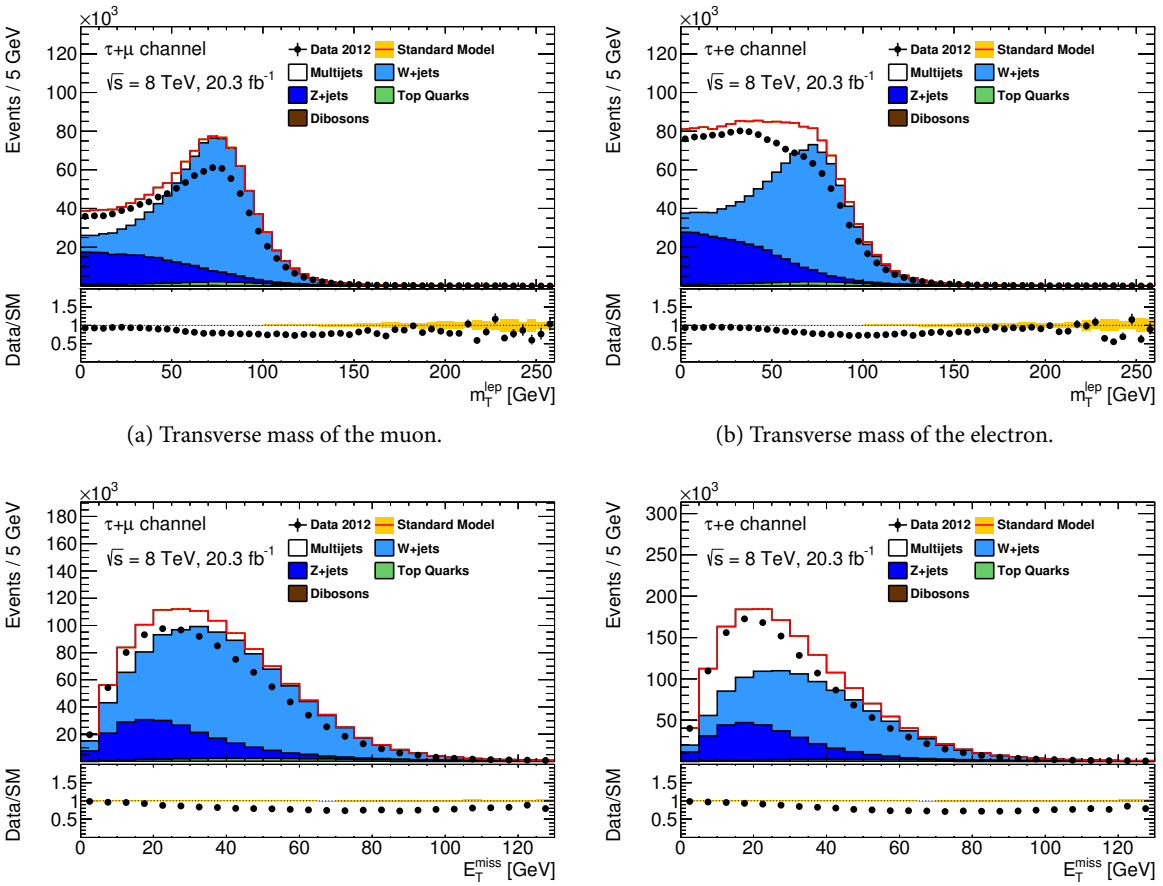

(a) Transverse mass of the muon.

(b) Transverse mass of the electron.

(c) $E_{\mathrm{T}}^{\mathrm{miss}}$ in the $\tau+\mu$ channel.

(d) $E_{\mathrm{T}}^{\mathrm{miss}}$ in the $\tau+e$ channel.

Figure 4.5: Transverse mass of the leptons and the missing transverse momentum after object selection with normalization as predicted by MC and the data-driven Multijet estimate.

candidate. The contribution of the Multijet background is much smaller in the $\tau+\mu$ channel since muons are less likely faked by a QCD jet than electrons. Top Quarks and Diboson contributions are negligible in this kinematic region.

As clearly visible in all distributions displayed in figure 4.5 the sum of the SM process predictions does not match the observed data. This has been shown to be a problem with modeling of the tau lepton fake contribution in the W+jets background. The issue has been studied intensively in [3] and shown to be due to the fact that relevant observables used for tau identification are not correctly modelled in MC. The simulation overpredicts jets that look more tau-like and therefore increases the number of fakes.

To obtain the correct normalization for the various backgrounds, scalings have to be derived and applied.

4.3 Studying the SM Background in Control Regions

To validate the modeling of each background type in detail, their contributions must be studied separately in kinematic regions, that are ideally dominated by one background type completely. The focus will be on W+jets and Top Quarks events, where the Top Quarks background is further separated into events with

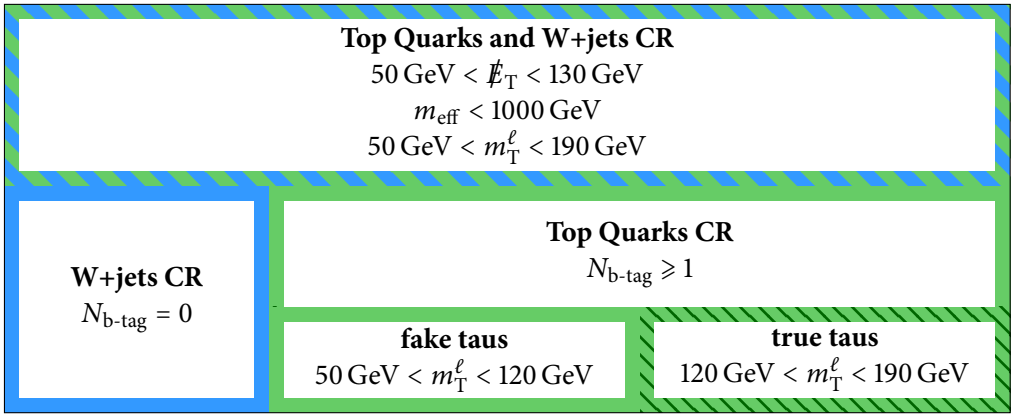

Table 4.3: Kinematic selection criteria for the definition of the control regions for Top Quarks and W+jets backgrounds.

fake tau leptons and true tau leptons. Table 4.3 summarizes all selection criteria used for the definition of the control regions. These selections should be kinematically well separated from the signal region. Since the definition of the signal regions is based on the variables m_{eff} and $E_{\text{T}}^{\text{miss}}$ as described in section 5.1, the control regions are restricted by an upper limit on these variables. Furthermore, the $E_{\text{T}}^{\text{miss}}$ distributions as they are displayed in figure 4.5 show that most of the Multijet events are below $E_{\text{T}}^{\text{miss}}$ = 50 GeV. Therefore, in all control regions only events that satisfy 50 GeV < $E_{\text{T}}^{\text{miss}}$ < 130 GeV and m_{eff} < 1000 GeVare selected.

Both W+jets and Top Quarks events include the decay products of a W boson and separating these event types consequently relies on the physics of a W decay. As explained in section 4.2.2, m_{T}^{ℓ} can be exploited to study the decay products in more detail. For both background types a transverse mass window of 50 GeV<m_{T}^{ℓ} <190 GeV is chosen. It includes the Jacobian peak at $m_{\text{T}}^{\ell} = m_W$. Since Top Quarks events are accompanied by the occurance of b-jets, their presence is vetoed for the W+jets control region. On the contrary, at least one b-jet is required in the Top Quarks control region.

Figures 4.6a and 4.6d display m_{T}^{ℓ} in the W+jets control region. A very high purity of W+jets events can be observed. The overprediction of MC is visible as a constant factor over the considered spectrum of the distribution. The Data/SM ratio already indicates a scaling of ~ 0.7 is needed to compensate the effect.

For the Top Quarks control region m_{T}^{ℓ} is displayed in figures 4.6c and 4.6d. The fraction of Top Quarks events with a real tau lepton is indicated by the hatched dark-green area. As already discussed, fake tau leptons in the Top Quarks background occur in events where one of the two W bosons decays hadronically. This means that only the neutrino of the other W boson's leptonic decay contributes to the real $E_{\text{T}}^{\text{miss}}$. If this is the case, the transverse mass of the lepton is bound by the W mass, which explains the maximum at $m_{\text{T}}^{\ell} = m_W$. In events with true tau leptons however, a second neutrino contributes to the $E_{\text{T}}^{\text{miss}}$ and m_{T}^{ℓ} can exceed the Jacobian peak. This behavior can be seen in figures 4.6e and 4.6f, which show a zoom into the higher mass spectrum with 120 GeV < m_{T}^{ℓ} < 190 GeV. This region is dominated by true tau lepton events and defined as the Top Quarks with true taus control region. The other half of the distribution, namely 50 GeV < m_{T}^{ℓ} < 120 GeV, contains more fake tau events and will be used as the Top Quarks with fake taus control region. Comparing the 2012 data to the SM prediction in Top Quarks events, it can be seen that for both true tau and fake tau events there is only a minor overprediction of data in the MC events visible. The Top Quarks scaling factors thus must be close to 1.

The contribution of true tau lepton events is assessed by matching the reconstructed particles to their truth origin. If the particle overlaps with a tau lepton within a cone of ΔR < 0.2 it is considered a true tau. Accordingly, if the matching particle is a light lepton, a heavy quark jet or a quark originating from a

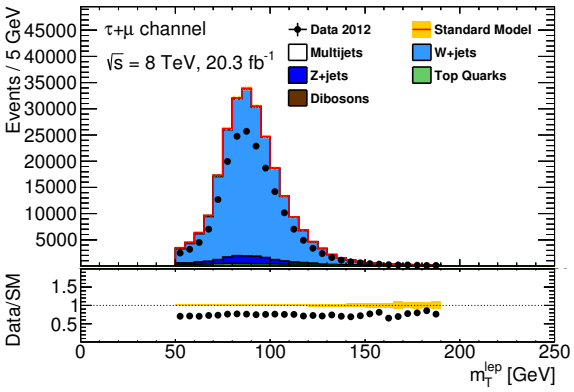

(a) m_{T}^{μ} in the W+jets CR.

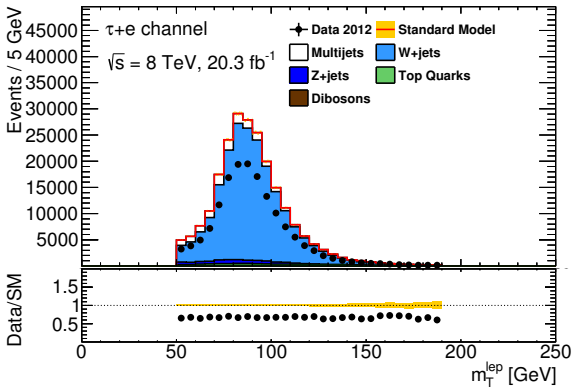

(b) m_{T}^{e} in the W+jets CR.

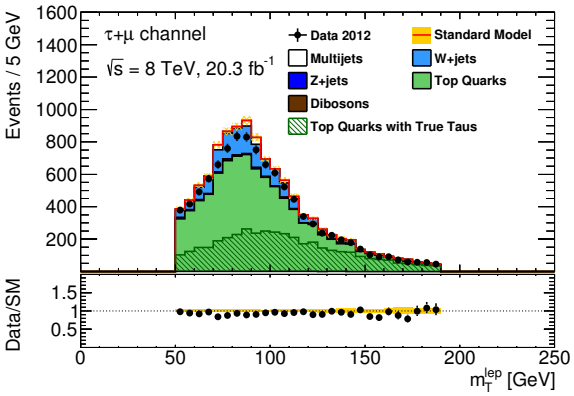

(c) m_{T}^{μ} in the Top Quarks CR.

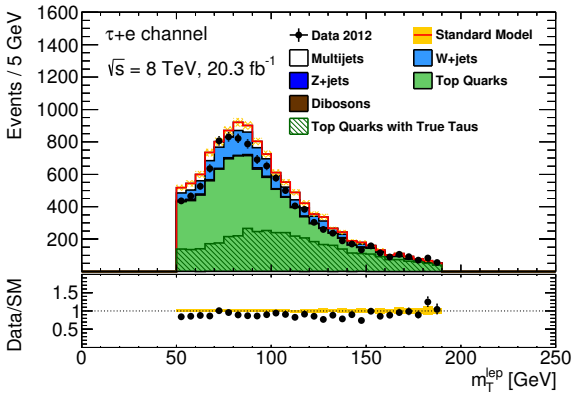

(d) m_{T}^{e} in the Top Quarks CR.

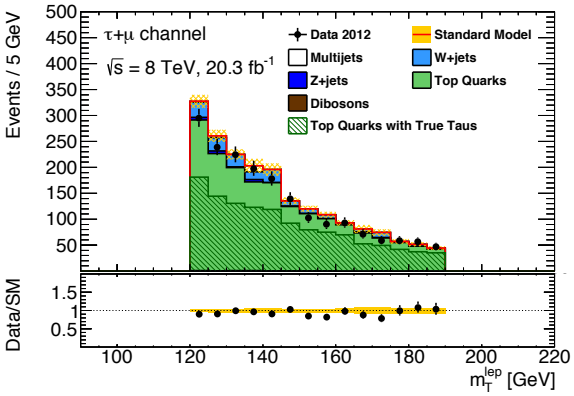

(e) m_{T}^{μ} in the Top Truth CR.

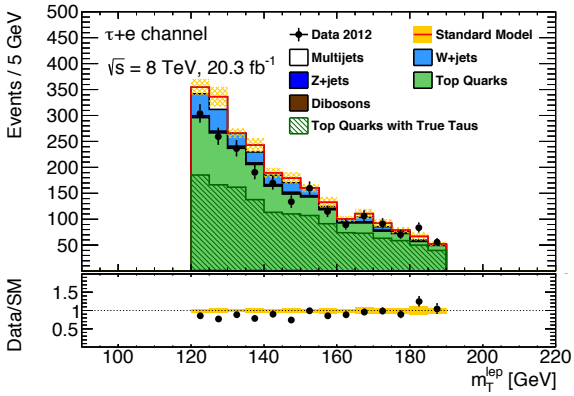

(f) m_{T}^{e} in the Top Truth CR.

Figure 4.6: Transverse mass of the light lepton in the W+jets control region (figures (a) and (b)), and Top Quarks control regions (figures (c) to (f)). The dark-green hatched area in the Top Quarks background indicates the fraction of Top Quarks events with a real tau lepton. Top Quarks events with real tau leptons are dominant towards higher masses, while the fake tau events accumulate around the Jacobian peak.
A disagreement in the normalization between predicted background and observed data is clearly visible in the W+jets control region, while it is less pronounced in the Top Quarks control regions.

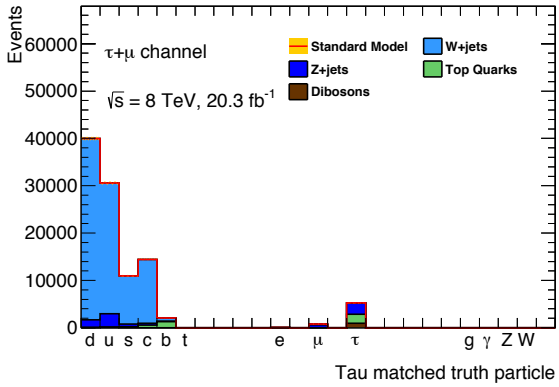

(a) W+jets CR in the $\tau+\mu$ channel.

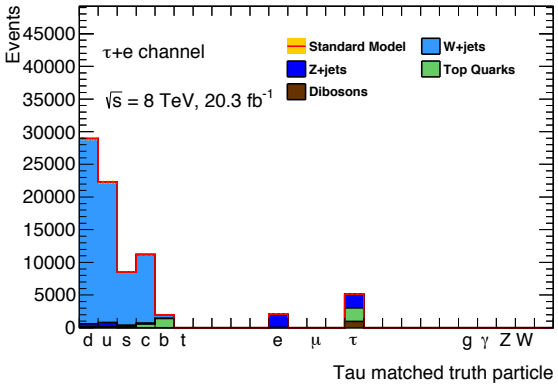

(b) W+jets CR in the $\tau+e$ channel.

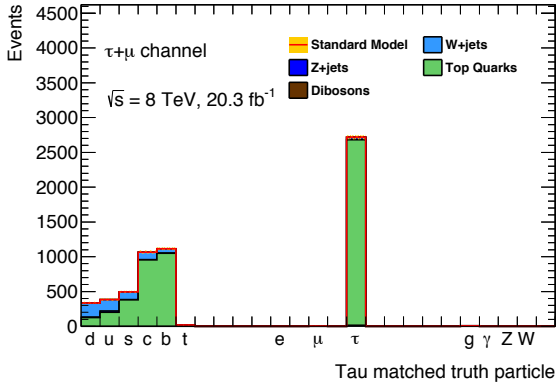

(c) Top Fake CR in the $\tau+\mu$ channel.

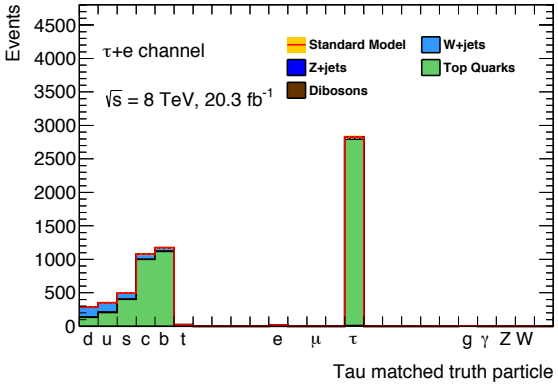

(d) Top Fake CR in the $\tau+e$ channel.

Figure 4.7: Truth origin of the tau candidate in the Top Quarks and W+jets control regions.

W decay, the corresponding object is considered to be the fake tau lepton's true origin. If none of these cases apply, the tau candidate is matched to the highest p_{T} light quark or gluon within a cone of $\Delta R < 0.4$.

The shares of the various truth origins of the tau lepton for the W+jets and the Top Fake control region are displayed in figure 4.7. As can be seen in the distribution of truth matched particles, the majority of the W+jets tau fakes originates from light flavor quarks. The tau fakes in the Top Quarks background however are dominated by heavy flavor quarks. In both background types the number of gluon tau fakes is negligibly small. The difference in the tau lepton's truth composition points at a possible explanation for the origin of the difference in the scale factors between the two background types.

4.3.1 Derivation of Background Scale Factors

Although the enrichment with W+jets and Top Quarks events in their control regions is very efficient, residual events from other background types are inevitable. Moreover, separating between fake and true tau contributions relies on one kinematic variable only and is therefore in fact very inefficent.

The purities and contributions of residual background types are compiled in table 4.4. The numbers of the $\tau+\mu$ and $\tau+e$ channels are compatable. Only the contribution of Multijet events is, as expected, significantly higher in the $\tau+e$ channel. The W+jets CRs have ~90 % purity, while in the Top Truth and

Top Fake control regions ~60 %, respectively ~50 % are reached. The absolute event numbers which are taken as input for the derivation of the scale factors can be found in table B.22.

	$\tau+\mu$ control regions			$\tau+e$ control regions		
	W+jets	Top Truth	Top Fake	W+jets	Top Truth	Top Fake
W+jets events (%)	**92.1**	8.2	16.3	**87.8**	8.9	13.8
Top Truth events (%)	0.8	**61.1**	30.0	1.0	**60.4**	30.1
Top Fake events (%)	1.3	26.8	**50.1**	1.6	25.1	**49.6**
Z+jets events (%)	5.1	1.1	1.1	3.8	1.5	0.9
Diboson events (%)	0.5	0.3	0.2	0.5	0.3	0.2
Multijet events (%)	0.2	2.6	1.5	5.3	3.7	5.5

Table 4.4: Percentages of the various backgrounds for the W+jets, Top Truth and Top Fake control regions. The purities of the CR-specific event type are marked in bold letters. All percentages are derived before applying scalings.

To compute the scale factors for W+jets, Top Truth and Top Fake events, the residual background contributions have to be considered. While Z+jets, Diboson and Multijet backgrounds can simply be subtracted from both data and the total prediction, the overlap of the three scaled backgrounds themselves is accounted for by using a matrix inversion method.

Assuming three different background types α, β and γ with three corresponding control regions A, B and C, the scale factors ω_α, ω_β and ω_γ must be derived. In all three control regions a certain number of events from each background is observed. These nine numbers are denoted as $N^{\alpha,\beta,\gamma}_{\mathrm{A,B,C}}$. In each control region the sum of the scaled event numbers should be equal to the observed data events deducting the events from unscaled backgrounds types $N^{\mathrm{Data}}_{\mathrm{A,B,C}} - N^{\mathrm{BG\,rest}}_{\mathrm{A,B,C}}$. This can be expressed in form of a matrix equation:

$$\underbrace{\begin{pmatrix} N^{\mathrm{Data}}_{\mathrm{A}} - N^{\mathrm{BG\,rest}}_{\mathrm{A}} \\ N^{\mathrm{Data}}_{\mathrm{B}} - N^{\mathrm{BG\,rest}}_{\mathrm{B}} \\ N^{\mathrm{Data}}_{\mathrm{C}} - N^{\mathrm{BG\,rest}}_{\mathrm{C}} \end{pmatrix}}_{\vec{N}_{\mathrm{obs}}} = \underbrace{\begin{pmatrix} N^{\alpha}_{\mathrm{A}} & N^{\beta}_{\mathrm{A}} & N^{\gamma}_{\mathrm{A}} \\ N^{\alpha}_{\mathrm{B}} & N^{\beta}_{\mathrm{B}} & N^{\gamma}_{\mathrm{B}} \\ N^{\alpha}_{\mathrm{C}} & N^{\beta}_{\mathrm{C}} & N^{\gamma}_{\mathrm{C}} \end{pmatrix}}_{M} \underbrace{\begin{pmatrix} \omega_\alpha \\ \omega_\beta \\ \omega_\gamma \end{pmatrix}}_{\vec{\omega}}. \tag{4.4}$$

The vector $\vec{\omega}$ which contains the three scale factors can be obtained by inverting the matrix M and multiplying it with the vector of the observed event numbers $\vec{N}_{\mathrm{obs}}$:

$$\vec{\omega} = M^{-1}\vec{N}_{\mathrm{obs}}. \tag{4.5}$$

In case the rows of M are linearly independent, there is a unique solution to the equation system. This is achieved by designing the control regions such that they are dominated by the favored event type.

Each of the event numbers that enters the calculation has a statistical uncertainty which must be considered. A Toy Monte Carlo method is used to derive the uncertainty on the scale factors from that. In this method, the calculation is repeated multiple times while varying each of the input numbers within their uncertainty arising from limited statistics. The variation is performed following a Gaussian distribution for MC events and following a Poisson distribution for data events.

The results accumulate in a distribution for each scale factor. These three distributions for both $\tau+\mu$ and $\tau+e$ channel are displayed in figure 4.8. Their central values are taken as the scale factor while the width provides the statistical uncertainties.

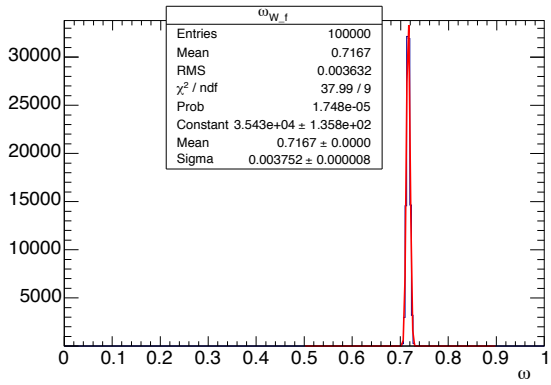

(a) W+jets scaling in the $\tau+\mu$ channel.

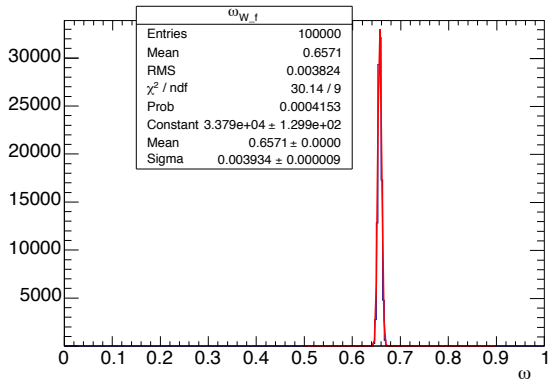

(b) W+jets scaling in the $\tau+e$ channel.

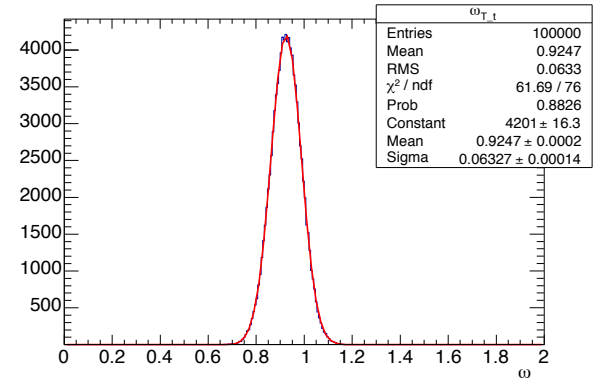

(c) Top Truth scaling in the $\tau+\mu$ channel.

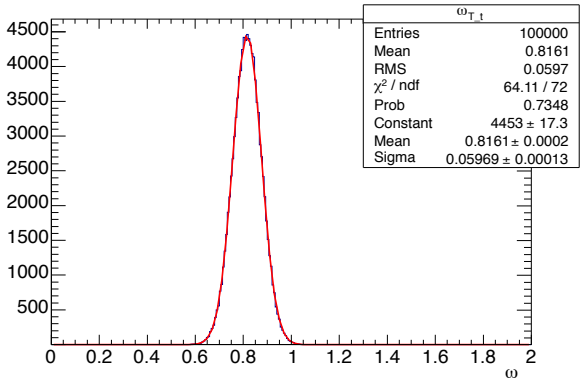

(d) Top Truth scaling in the $\tau+e$ channel.

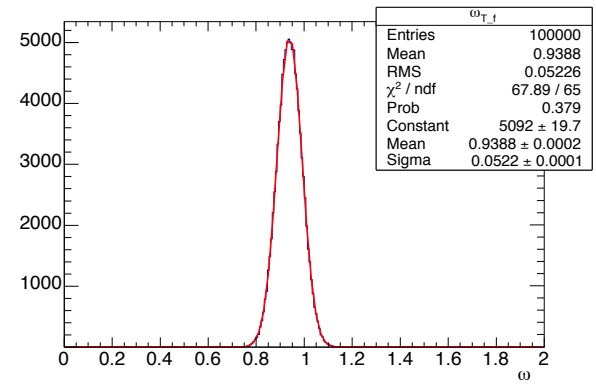

(e) Top Fake scaling in the $\tau+\mu$ channel.

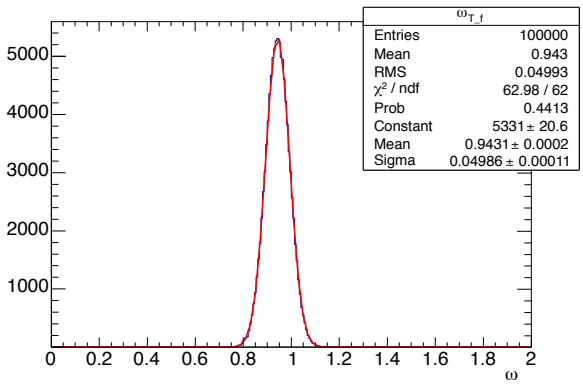

(f) Top Fake scaling in the $\tau+e$ channel.

Figure 4.8: Scale factors for W+jets, Top Truth and Top Fake backgrounds obtained by Toy Monte Carlo using 10 000 randomly generated entries according to the uncertainties of all input numbers and before applying further corrections. The red line indicates the Gaussian fit function which is used to obtain the central value and the width of the distribution.

background	$\tau+\mu$ scaling	$\tau+e$ scaling
W+jets events	$0.72 \pm 0.00^{\text{stat}} \pm 0.14^{\text{syst}}$	$0.66 \pm 0.00^{\text{stat}} \pm 0.12^{\text{syst}}$
Top Truth events	$0.92 \pm 0.06^{\text{stat}} \pm 0.15^{\text{syst}}$	$0.82 \pm 0.06^{\text{stat}} \pm 0.25^{\text{syst}}$
Top Fake events	$0.94 \pm 0.05^{\text{stat}} \pm 0.16^{\text{syst}}$	$0.94 \pm 0.05^{\text{stat}} \pm 0.15^{\text{syst}}$

Table 4.5: Background scale factors for W+jets, Top Truth and Top Fake with statistical and systematic uncertainties.

The scale factor derivation can be performed as well in consideration of systematic uncertainties. The sources of systematic uncertainties are described in detail in section 5.2. The results taking into account both uncertainties are listed in table 4.5. While the scale factors for the Top Quarks background are in fact within their uncertainties close to 1, W+jets events need to be scaled by 0.72 in the $\tau+\mu$ channel and by 0.66 in the $\tau+e$ channel. Differences between both channels are for the Top Quarks background already covered by only statistical uncertainties. The statistical uncertainty on the two W+jets scale factors however is negligibly small. Nevertheless, their difference is covered by the systematic uncertainty. The obtained scale factors are also compatible with the observations from the other two analyses that are part of the common search for SUSY in tau lepton final states as described in [2].

Transverse Momentum Correction of the W+jets Background

After applying the global scalings to the corresponding backgrounds, various kinematic distributions can be checked to validate the background description. Remaining deviations of the prediction from observed 2012 data events must be taken care of.

The only deviation of this kind can be seen for both $\tau+\mu$ and $\tau+e$ channel in the p_{T}^{τ} spectrum of the W+jets background. This is displayed in figure 4.9 in the W+jets control region. The background is still overpredicted in the high p_{T}^{τ} region. As these fake tau leptons are not modelled correctly, as already discussed, it seems coherent that this mismodeling is also visible in an observable like the transverse momentum. A p_{T}^{τ} dependent correction must be applied to account for this bias.

Assuming the other background types are modelled correctly, the wrong shape of the distribution can be simply extracted by comparing the pure W+jets background to the one from data subtracting all other background types in the W+jets control region. The ratio of the residual data and W+jets events in dependence of p_{T}^{τ} is displayed in figure 4.11.

The shape of the distribution can be described by an exponential function of type

$$f(p_{\text{T}}^{\tau}) = \alpha \cdot e^{\beta \cdot p_{\text{T}}^{\tau}} + \gamma. \tag{4.6}$$

This function is used to perform a fit to the distribution. This leads to very similar fit results when comparing the $\tau+\mu$ and $\tau+e$ channels. The parameters α, β and γ are listed in table 4.6.

	$\tau+\mu$	$\tau+e$
α	0.781	0.920
β	0.031	0.029
γ	0.481	0.519

Table 4.6: The derived fit parameters for p_{T}^{τ} corrections in the $\tau+\mu$ and $\tau+e$ channel.

Using the two obtained functions, an event based reweighting can be applied. The global scalings for W+jets, Top Truth and Top Fake backgrounds are then re-derived with the matrix inversion method

(Figure 4.12). The results agree within the statistical uncertainty with the scalings for the in p_{T}^{τ} uncorrected background.

In figure 4.10 the corrected p_{T}^{τ} distribution is displayed. After applying the correction no further deviations from the prediction are observed in data. Control distributions for all various background types are displayed in figures 4.17 to 4.20 at the end of this chapter.

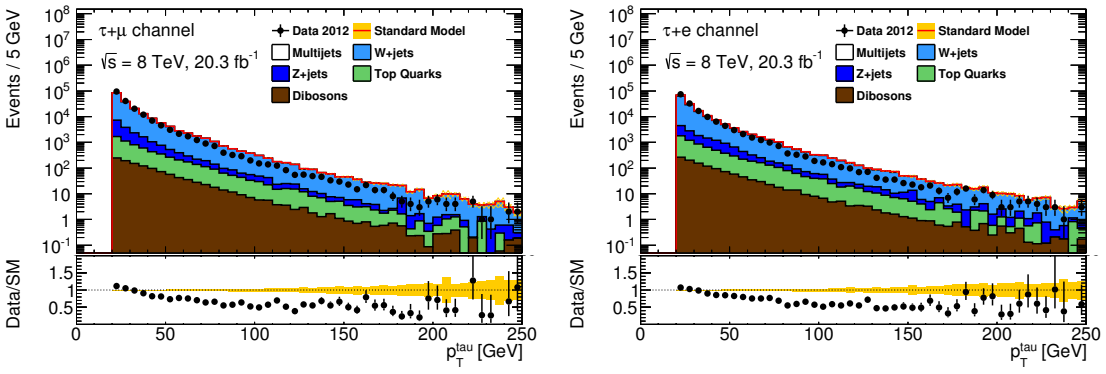

(a) p_{T}^{τ} distribution for the $\tau+\mu$ channel.

(b) p_{T}^{τ} distribution for the $\tau+e$ channel.

Figure 4.9: Deviation of the W+jets background in the p_{T}^{τ} distribution as observed in the W+jets control region.

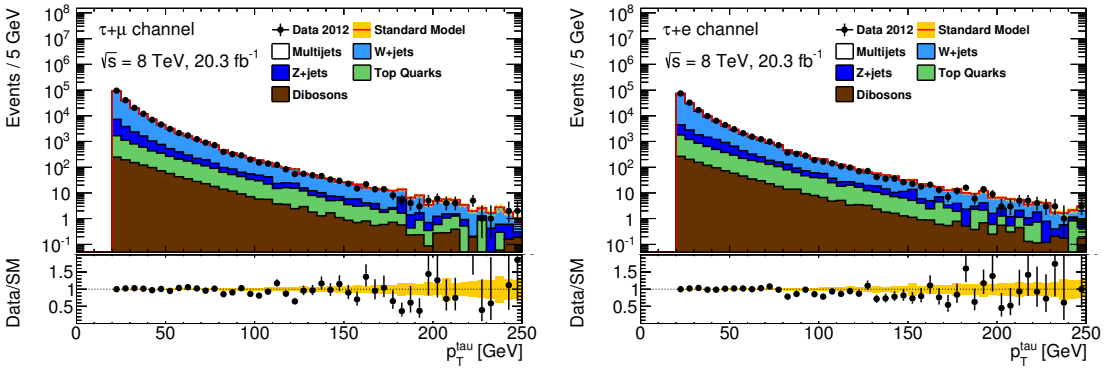

(a) Corrected p_{T}^{τ} distribution for the $\tau+\mu$ channel.

(b) Corrected p_{T}^{τ} distribution for the $\tau+e$ channel.

Figure 4.10: p_{T}^{τ} distribution in the W+jets control region after applying the correction by event reweighting.

4.3.2 Definition of a Z+jets Control Region

To obtain the correct normalization of the predicted background in MC, control regions for two important background types were defined: W+jets and Top Quarks. The choice was motivated by the fact that the overprediction is connected to a mismodeling of fake tau leptons originating from jets, which occur mainly in these two backgrounds. Nevertheless, the Z+jets background is another major part which needs to be validated as well. For this purpose, a Z+jets control region is defined and studied.

The Z^0 boson decays into two tau leptons of opposite sign charge. By selecting events in which the light lepton and the leading p_{T} tau lepton have opposite sign, the Z+jets background is slightly enriched compared to other background types. Furthermore conservation of momentum dictates the tau leptons

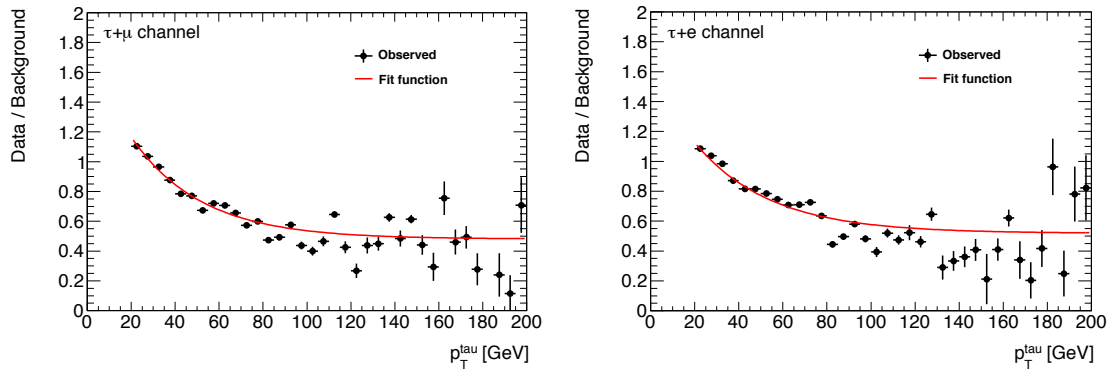

(a) $\tau+\mu$ channel (b) $\tau+e$ channel

Figure 4.11: Ratio of data minus residual backgrounds to W+jets background in the p_{T}^{τ} spectrum. The observed ratio is displayed by the black points. The fit function describing the slope is displayed by the red line.

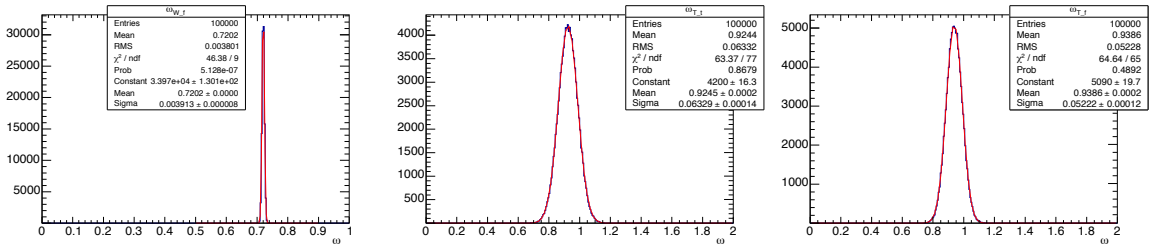

(a) W+jets scaling in the $\tau+\mu$ channel. (b) Top Truth scaling in the $\tau+\mu$ channel.(c) Top Fake scaling in the $\tau+\mu$ channel.

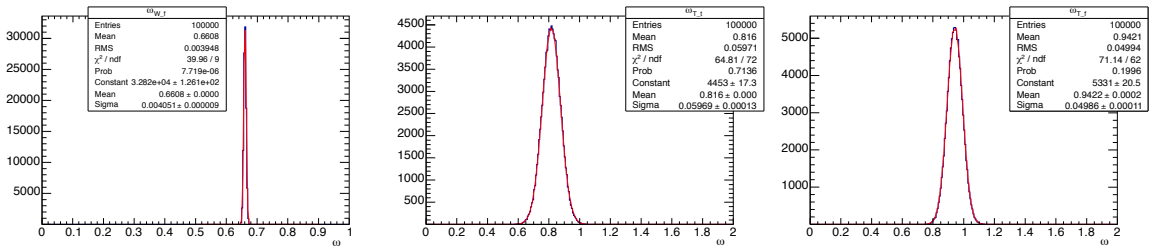

(d) W+jets scaling in the $\tau+e$ channel. (e) Top Truth scaling in the $\tau+e$ channel.(f) Top Fake scaling in the $\tau+e$ channel.

Figure 4.12: Obtained scalings in the various control regions after applying the p_{T}^{τ} correction to W+jets. The results are compatible with the previous scalings within the statical uncertainty.

emerge back-to-back, which is not the case in W+jets or Top Quarks events for example. Since the angle between the reconstructed tau lepton and the light lepton is smeared by the decays of the original physical objects, the requirement on it is chosen to be

$$\Delta\phi(\tau,\ell) > 2.4. \tag{4.7}$$

In the m_{T}^{ℓ} distribution W+jets and Top Quarks backgrounds feature the Jacobian peak at the W mass. The decay chain of the Z^0 boson however possesses three neutrinos as sources for $E_{\mathrm{T}}^{\mathrm{miss}}$ of which two are not directly connected to the light lepton. Resulting from this, most of the Z+jets events are at the lower

masses in the m_{T}^{ℓ} spectrum and the selection criterion therefore is

$$m_{\mathrm{T}}^{\ell} < 40\,\mathrm{GeV}. \tag{4.8}$$

Unfortunately most of the Multijet background accumulates in exactly this kinematic region of the transverse lepton mass distribution as well. To suppress these contributions the requirement on the lepton's transverse momentum needs to be increased (compare figures 4.16e and 4.16f):

$$p_{\mathrm{T}}^{\ell} > 40\,\mathrm{GeV}. \tag{4.9}$$

The hadronic decay of the one tau lepton and the leptonic decay of the other one shift and smear the Z+jets peak in the invariant mass distribution away from the Z^0 mass, since not all of the decay products are visible. However, the distribution is still narrower in Z+jets events than in the other background types. For this reason the following window in the visible mass is selected:

$$50\,\mathrm{GeV} < m_{\mathrm{vis}}(\tau, \ell) < 105\,\mathrm{GeV} \tag{4.10}$$

With these requirements a kinematic region with sufficient enrichment of Z+jets events is selected. The control distributions in figure 4.20 show a good agreement between 2012 data and MC prediction. Both normalization and shapes are well described without any further corrections.

Looking at the truth composition of the Z+jets background as displayed in figure 4.13, an interesting difference between the $\tau+\mu$ and the $\tau+e$ channels can be observed. While the number of truth taus is roughly the same and in both channels the lighter lepton is the main source of misidentified tau leptons, the overall number of fake taus in the $\tau+e$ channel is much higher. In fact, most reconstructed tau leptons in the Z+jets control region of the $\tau+e$ channel originate from electron fakes.

In the $\tau+\mu$ channel the contribution of fake taus is much smaller. However, the fact that electron fakes dominate over real taus is caused by the control region selection itself: The majority of electron fakes arises from $Z^0 \to e^+e^-$ events. Unlike tau leptons, electrons do not decay and therefore appear in a distinct, narrow peak in the invariant mass around the Z^0 mass in the window defined in 4.10.

By choosing this mass window in the defintion of the Z+jets control region, electron fakes are enriched with respect to real tau leptons in the $\tau+e$ channel. The same holds of course for muon fakes, but their occurance is much rarer and hence the effect is not that strong.

In a kinematic region which does not have a specific requirement on the invariant mass, real tau leptons are more common in both channels. Still, the overall fake tau contribution from electrons is higher than the one from muons which leads to the fact that the Z+jets background represents a larger proportion in the $\tau+e$ channel.

4.4 Data-driven Estimate for the Multijets Background

For estimating the background from Multijet events at the LHC, conventional MC predictions are only applicable in a limited number of cases.

With the given event selection, the Multijet background is a pure fake contribution. As already mentioned in section 4.2.1, fake light leptons originating from jets are not very likely. Only the huge cross-section of QCD processes at the LHC causes contributions by a large extent to the total background after baseline event selection and in the control regions.

Due to the rareness of these Multijet fakes, an unfeasible amount of MC would be needed to generate enough statistics and therefore, alternative approaches are commonly used in many analyses. These utilize

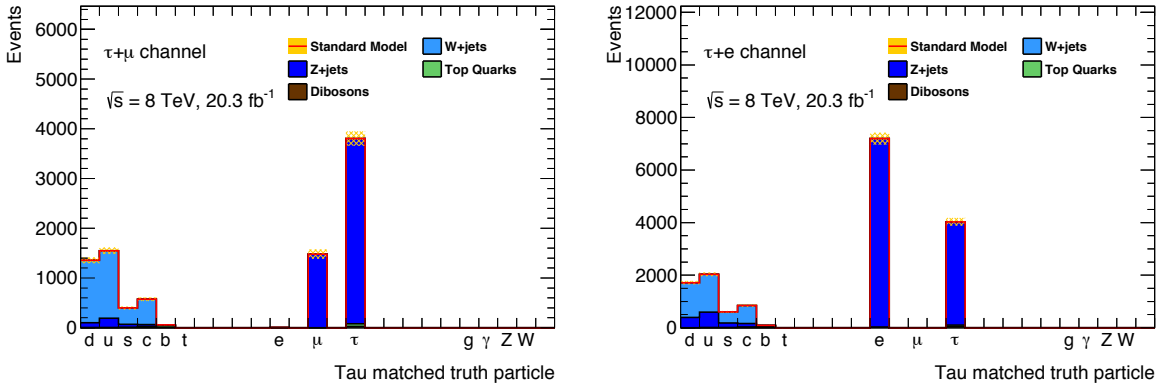

(a) Z+jets CR in the $\tau+\mu$ channel.

(b) Z+jets CR in the $\tau+e$ channel.

Figure 4.13: Truth origin of the tau candidate in the Z+jets control region.

observations from the 2012 data to estimate the Multijet contribution. Depending on the selection of physics objects, various methods have been developed. The technique which is used in this analysis is based on a data-driven approach with a matrix method [204].

This procedure exploits the fact that falsely reconstructed leptons from Multijet events tend to have a weaker isolation than real leptons. For the same reason, the isolation of leptons was also used as an identification criterion in the physics object definition (compare section 4.1.1).

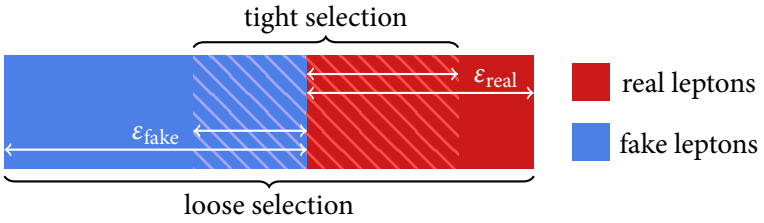

Figure 4.14: Illustration of the matrix method.

The method is illustrated in figure 4.14: The normal selection of signal leptons, as defined in section 4.1.1, shall be denoted as the *tight selection*. It is indicated by the hatched area in the illustration. The tight selection leads to a distinct number of events $N_{\text{T}}^{\text{obs}}$ which is the sum of the number of events with real leptons $N_{\text{T}}^{\text{real}}$ and the number of events where the lepton was a Multijet fake $N_{\text{T}}^{\text{fake}}$:

$$N_{\text{T}}^{\text{obs}} = N_{\text{T}}^{\text{real}} + N_{\text{T}}^{\text{fake}}. \tag{4.11}$$

The latter is the needed background estimate. In figure 4.14 events with fake leptons are represented by the blue area, while events with real leptons are shown in red.

By loosening the selection criteria for leptons, a larger number of events $N_{\text{L}}^{\text{obs}}$ is considered. For this, the baseline selection as defined in section 4.1.1 is used. For this *loose selection*, which is illustrated by the full colored area in figure 4.14, in particular the isolation criterion is dropped. As a result, more fake than real leptons enter the loose selection.

The ratio of the selection efficiency from loose to tight for purely fake lepton events is denoted by $\varepsilon_{\text{fake}}$ and the one for real leptons events by $\varepsilon_{\text{real}}$. The number of observed events in the tight selection can then be written as

$$N_{\text{L}}^{\text{obs}} = N_{\text{L}}^{\text{real}} + N_{\text{L}}^{\text{fake}} = \varepsilon_{\text{real}} N_{\text{T}}^{\text{real}} + \varepsilon_{\text{fake}} N_{\text{T}}^{\text{fake}}. \tag{4.12}$$

If the ratios $\varepsilon_{\text{fake}}$ and $\varepsilon_{\text{real}}$ are known, equations 4.11 and 4.12 are solvable for $N_{\text{T}}^{\text{fake}}$, while depending only on the total observed number of events for the tight and loose selection $N_{\text{T}}^{\text{obs}}$ and $N_{\text{L}}^{\text{obs}}$:

$$N_{\text{T}}^{\text{fake}} = \frac{N_{\text{L}}^{\text{obs}} - N_{\text{T}}^{\text{obs}} \varepsilon_{\text{real}}}{\varepsilon_{\text{fake}} - \varepsilon_{\text{real}}} \tag{4.13}$$

To obtain the ratio $\varepsilon_{\text{real}}$, a tag-and-probe method in a $Z \to \ell^+\ell^-$ control region is used. $\varepsilon_{\text{fake}}$ is measured in a Multijet-enriched control region where residual contributions from other background types are subtracted according to their MC predictions [204].

The measurements are binned in p_{T} and η which allows for obtaining not only the prediction of the total number of fake events with a particular selection, but also information about the correct shape of observables.

As described in section 4.1.4, prescaled triggers are used to account for the fact that the isolation criterion on the light lepton needs to be dropped completely in the loose selection. A possible influence of pile-up effects due to different prescale conditions can be ruled out by comparing the distributions of the average number of interactions per bunch-crossing in both trigger selections. For the τ+e channel, which has larger contributions from Multijet fakes, these distributions are displayed for the three control regions W+jets, Top Truth and Top Fake in figure 4.15. No significant difference is observed with using the prescaled trigger.

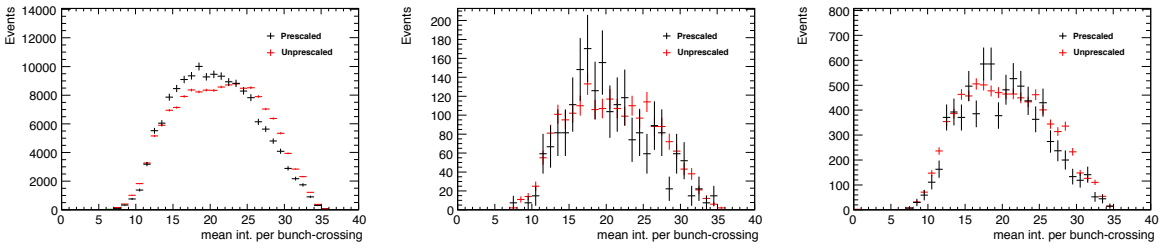

(a) W control region (b) top truth control region (c) top fake control region

Figure 4.15: Distributions of the average number of interactions per bunch-crossing for prescaled and unprescaled triggers in the τ+e analysis.

Control distributions to validate the predictions of the matrix method are displayed in figure 4.16. These distributions are observed after the baseline selection without any further kinematic cuts, because here most of the Multijet background is still passing the selection. Figures 4.16a and 4.16b display the transverse mass distribution which was already used as an example before applying the scale factors in figure 4.5, where most of the Multijet background is found at small masses below the Jacobian peak of the W+jets background. Figures 4.16c and 4.16d show the ratio of $E_{\text{T}}^{\text{miss}}$ and m_{eff}, which are both quantities used for the design of signal regions. The transverse momenta of the muon and the electron are shown in figures 4.16e and 4.16f. Fake leptons from Multijet events are found in the lower part of the p_{T} spectrum. In figures 4.16g and 4.16h the transverse momentum of the highes p_{T} jet is displayed. All kinematic

observables show sufficient agreement between data and the sum of MC and the data-driven Multijet estimate. Small deviations are only visible in single bins of some kinematic distributions.

The Multijet estimate in this analysis is mostly used for small remaining contributions in the control regions. The signal regions will be designed such that there is only a negligible amount of Multijet events left. This remnant is then considered only by setting an upper limit (compare section 5.3.1).

4.5 Background Control Distributions

To validate the accuracy of the background prediction, numerous control distributions are checked on their description of shape and normalization. A few examples of such control distributions are discussed below.

4.5.1 W+jets Background

Examples for the W+jets control region can be found in figure 4.17. In figures 4.17a and 4.17b the transverse momentum of the light lepton is displayed. The lower parts of the distributions are cut off by the selection criterion for signal leptons, but the maximum around half of the W mass at $p_{\mathrm{T}}^{\ell} \approx 40\,\mathrm{GeV}$ is still visible.

Figures 4.17c and 4.17d show the shares of events with negatively and positively charged light leptons. Due to the fact that the colliding protons have two up-quarks, those dominate the production of W bosons at the LHC. Therefore, more positively charged W bosons emerge and consequently also more positively charged light leptons appear with the given event selection.

The angular distance between the light lepton and $E_{\mathrm{T}}^{\mathrm{miss}}$ can be seen in figures 4.17e and 4.17f. The distributions have their maximum at $\phi = \pi$ which is expected since the neutrino from the W decay is the only source of real $E_{\mathrm{T}}^{\mathrm{miss}}$. Finally, as an example of one of the signal region relevant quantities, the effective mass is displayed in figures 4.17g and 4.17h. All distributions show good agreement between prediction and observed data.

4.5.2 Top Truth Background

Example distributions from the Top Truth control region are shown in figure 4.18. The transverse momentum of the tau lepton can be seen in figures 4.18a and 4.18b. The remaining contributions from fake tau leptons appear to be mainly in the low p_{T} region. At high p_{T} real tau leptons dominate the distributions.

In the Top Quarks background real tau leptons can only emerge along with light leptons in $t\bar{t}$ events. The real tau lepton and the light lepton originate from the $t\bar{t}$ pair and therefore appear with opposite sign only. This is displayed in figures 4.18c and 4.18d. The remaining fake tau contributions appear in both opposite and same sign final states.

The same reasoning explains the angular distance between the light lepton and the true tau lepton. Because the top quarks are created almost back-to-back, their decay products appear also well separated as displayed figures 4.18e and 4.18f, where the maximum of the distributions can be seen at $\phi = \pi$. The same holds for the angular distance between the light lepton and $E_{\mathrm{T}}^{\mathrm{miss}}$ in Top Truth events. Here, $E_{\mathrm{T}}^{\mathrm{miss}}$ is dominated by the two neutrinos that appear along with the tau lepton. This can be observed in figures 4.18g and 4.18h.

4.5.3 Top Fake Background

The Top Fake control region distributions are collected in figure 4.19. The number of jets is displayed in figures 4.19a and 4.19b. Top Fake events tend to have an increased jet multiplicity. One additional jet

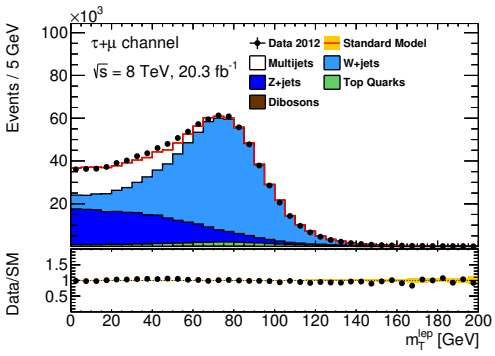

(a) m_{T}^{ℓ} distribution in the $\tau+\mu$ channel.

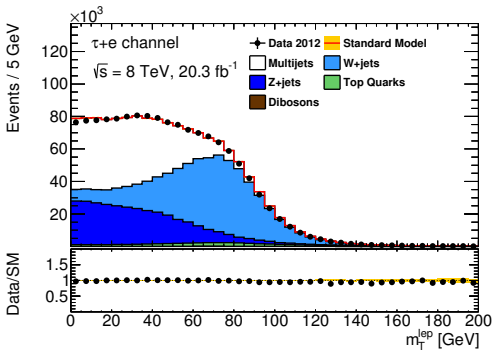

(b) m_{T}^{ℓ} distribution in the $\tau+e$ channel.

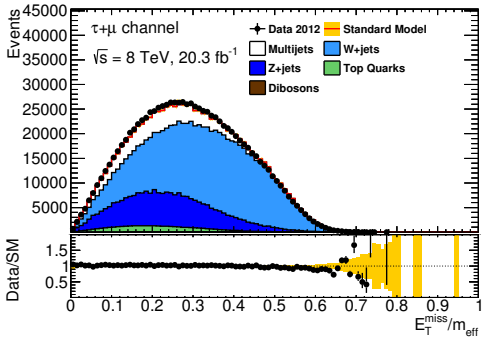

(c) $E_{\mathrm{T}}^{\mathrm{miss}}/m_{\mathrm{eff}}$ distribution in the $\tau+\mu$ channel.

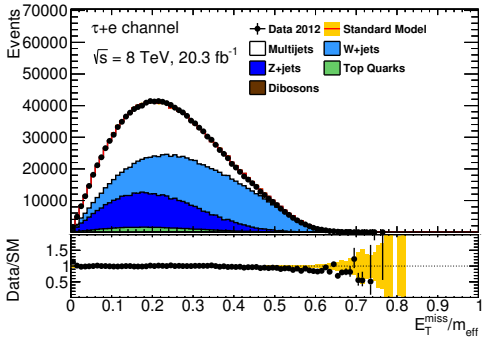

(d) $E_{\mathrm{T}}^{\mathrm{miss}}/m_{\mathrm{eff}}$ distribution in the $\tau+e$ channel.

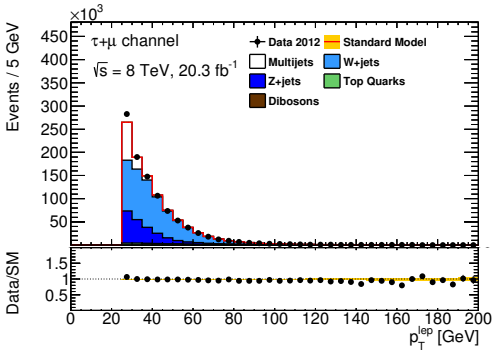

(e) p_{T}^{ℓ} in the $\tau+\mu$ channel.

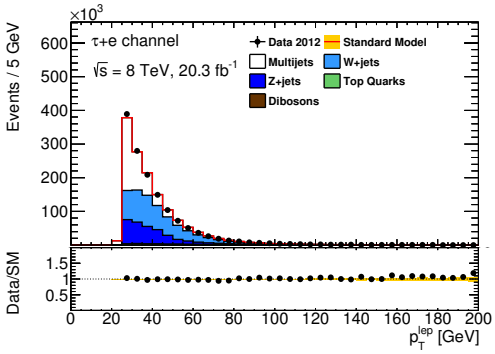

(f) p_{T}^{ℓ} in the $\tau+e$ channel.

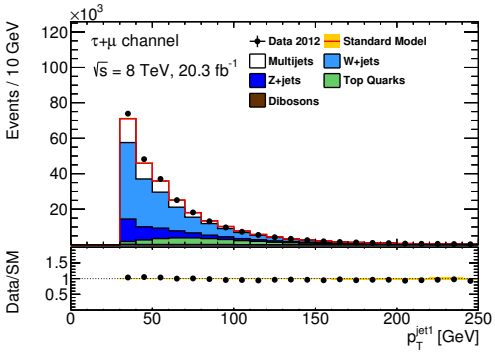

(g) p_{T} of the leading jet in the $\tau+\mu$ channel.

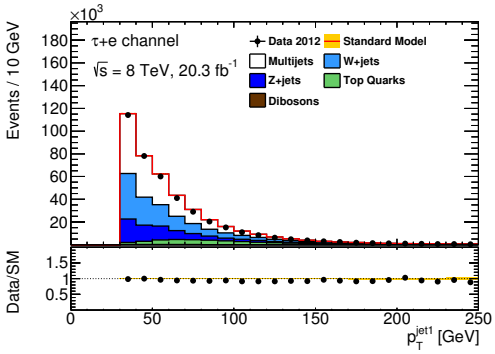

(h) p_{T} of the leading jet in the $\tau+e$ channel.

Figure 4.16: Comparisons between data and background predictions, from scaled Monte Carlo and the data-driven Multijet estimate after object selection.

appears from the hadronic W decay, while another one is identified as the tau lepton. The remaining true tau contributions have a maximum at two jets (which are the two b-jets from the top quark decays). However, for Top Fake events the maximum is in fact shifted by one bin.

Figures 4.19c and 4.19d show the angular distance between the leading jet and $E_{\mathrm{T}}^{\mathrm{miss}}$. The neutrino produced along with the light lepton is the only source of $E_{\mathrm{T}}^{\mathrm{miss}}$, and well separated from the jets originating from the opposite top quark. Consequently, the fake tau also tends to be more separated from $E_{\mathrm{T}}^{\mathrm{miss}}$ as seen in figures 4.19e and 4.19f. Finally, m_{eff} is displayed in figures 4.19g and 4.19h. All Top Quarks background control plots show good agreement between prediction and observed data.

4.5.4 Z+jets Background

In figure 4.20 example distributions for the Z+jets control region can be found. Since the $E_{\mathrm{T}}^{\mathrm{miss}}$ in Z+jets events is dominated by the two neutrinos from the leptonic tau decay, the angular difference tends to be maximal between $E_{\mathrm{T}}^{\mathrm{miss}}$ and the tau lepton as displayed in figures 4.20a and 4.20b. Likewise, the angular difference between $E_{\mathrm{T}}^{\mathrm{miss}}$ and the light lepton tends to be minimal as displayed in figures 4.20c and 4.20d.

The visible mass of the tau and the electron is displayed in figures 4.20e and 4.20f. As already discussed in section 4.3.2, electrons likely fake tau leptons in the τ+e channel. These $Z \to e^+e^-$ show as a distinct peak at the Z mass which appears on top of the smeared and shifted peak from real taus. In the τ+μ channel only the latter peak is visible.

Finally, figures 4.20g and 4.20h display $E_{\mathrm{T}}^{\mathrm{miss}}$. The Z+jets control distributions show overall good agreement between prediction and data. More control distributions for all background types can be found in section A.1 in the appendix.

4.6 Chapter Summary

In this chapter the baseline selection and background estimation techniques were described. After the definition of the used physics objects the event selection and resulting SM background processes were specified. To normalize and validate the background, control regions were introduced for W+jets, Top Quarks and Z+jets events. Scaling factors W+jets, Top Fake and Top Truth events were derived from these control regions with a matrix inversion method.

The contribution of Multijet events was estimated with a matrix method utilizing different efficiencies for fake and real leptons depending on the tightness of the object selection.

The correct description of the background was then validated by comparing the shapes of various control distributions.

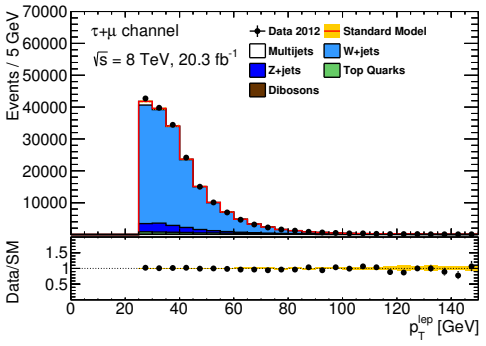

(a) p_{T}^{ℓ} in the $\tau+\mu$ channel

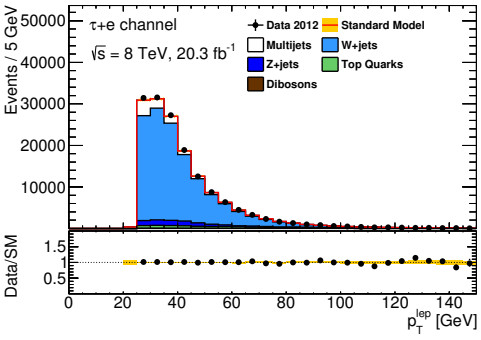

(b) p_{T}^{ℓ} in the $\tau+e$ channel

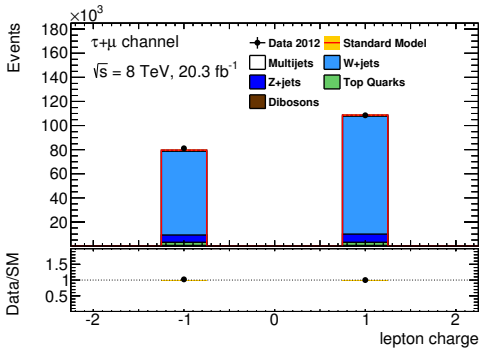

(c) Charge of the in the muon

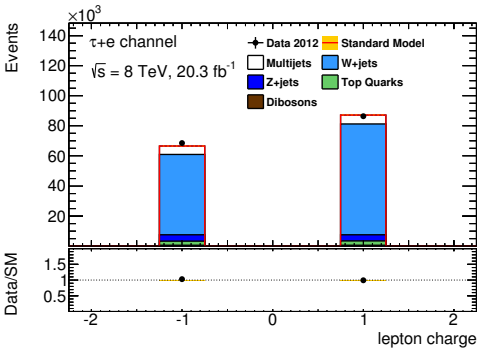

(d) Charge of the in the electron

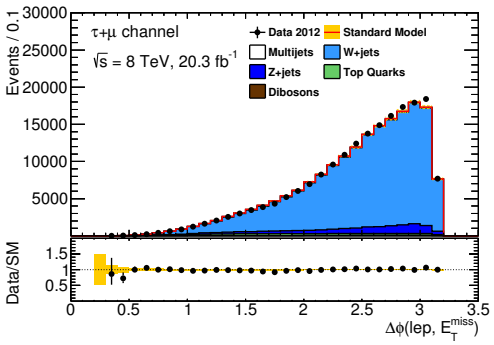

(e) $\Delta\phi(\ell, E_{\mathrm{T}}^{\mathrm{miss}})$in the $\tau+\mu$ channel

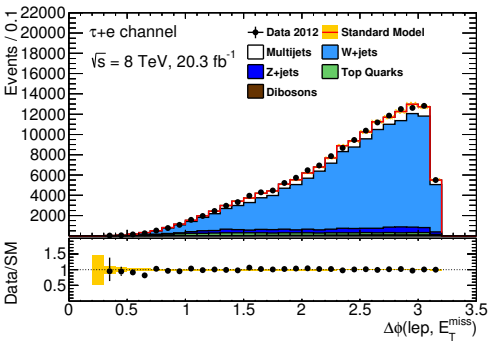

(f) $\Delta\phi(\ell, E_{\mathrm{T}}^{\mathrm{miss}})$in the $\tau+e$ channel

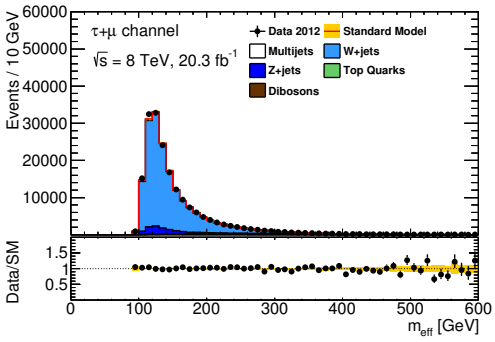

(g) m_{eff} in the $\tau+\mu$ channel

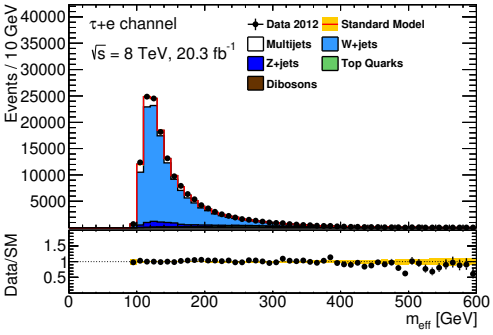

(h) m_{eff} in the $\tau+e$ channel

Figure 4.17: Control distributions in the W+jets control region after applying all background corrections.

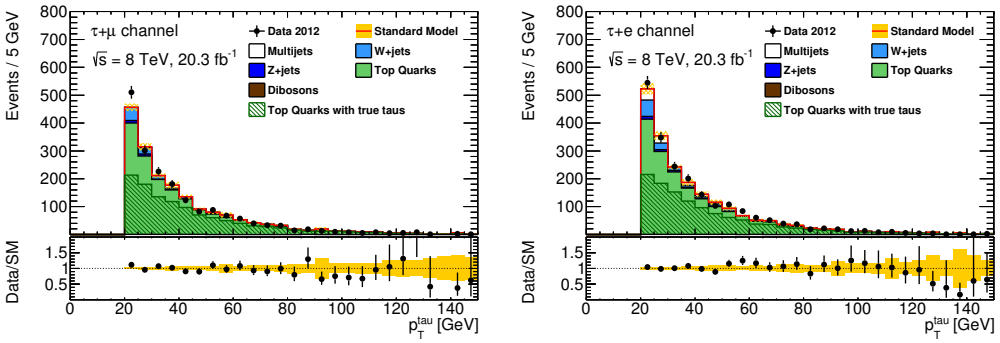

(a) p_{T}^{τ} in the $\tau+\mu$ channel

(b) p_{T}^{τ} in the $\tau+e$ channel

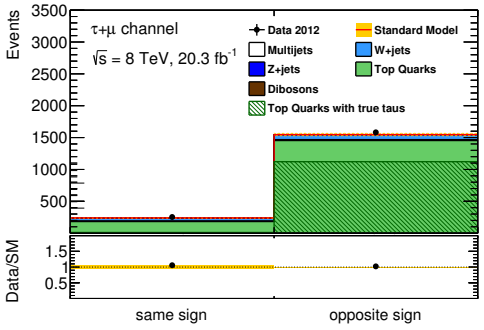

(c) charge of the tau and the muon

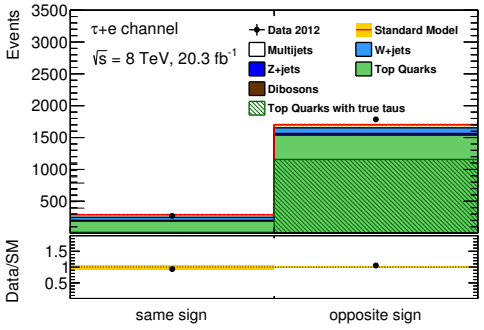

(d) charge of the tau and the electron

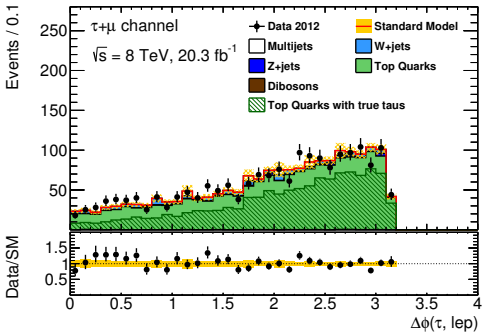

(e) $\Delta\phi(\tau,\ell)$ in the $\tau+\mu$ channel

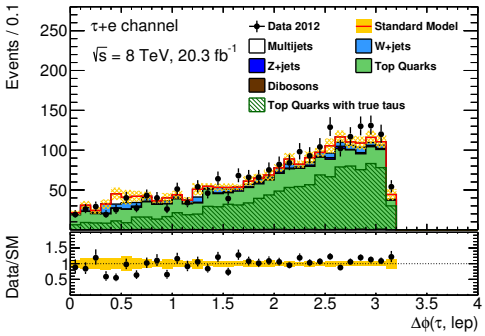

(f) $\Delta\phi(\tau,\ell)$ in the $\tau+e$ channel

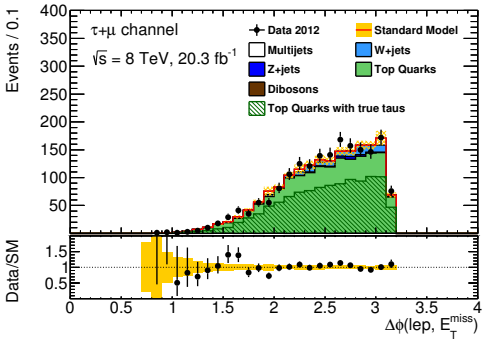

(g) $\Delta\phi(\ell, E_{\mathrm{T}}^{\mathrm{miss}})$ in the $\tau+\mu$ channel

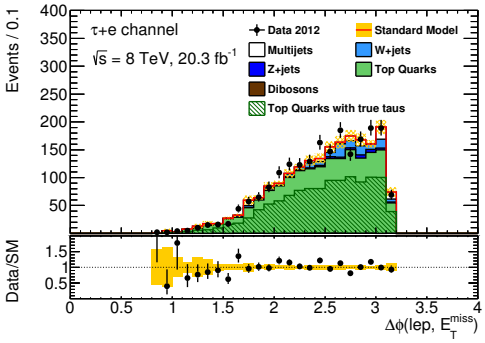

(h) $\Delta\phi(\ell, E_{\mathrm{T}}^{\mathrm{miss}})$ in the $\tau+e$ channel

Figure 4.18: Control distributions in the Top Truth control region after applying all background corrections.

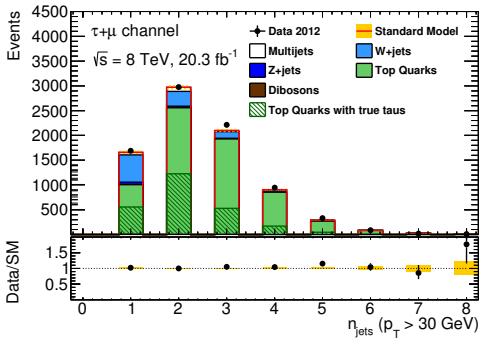

(a) number of jets in the $\tau+\mu$ channel

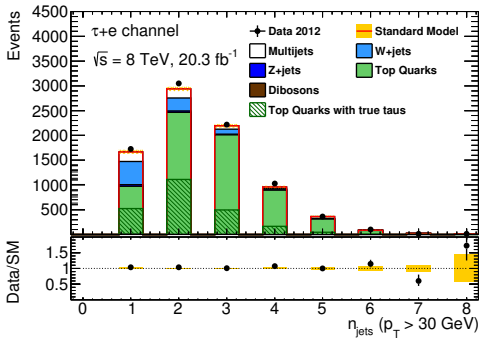

(b) number of jets in the $\tau+e$ channel

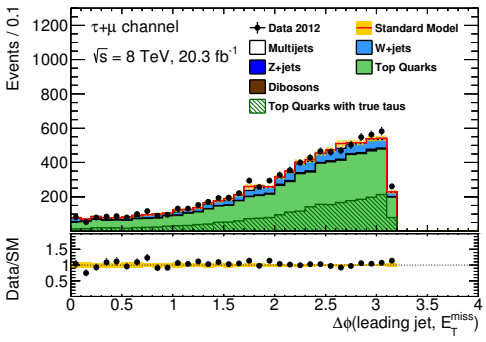

(c) $\Delta\phi(\text{jet}^{\text{lead}}, E_{\text{T}}^{\text{miss}})$ in the $\tau+\mu$ channel

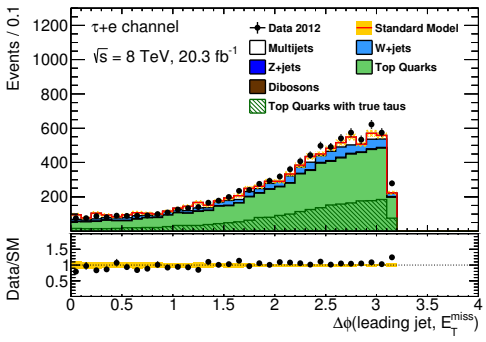

(d) $\Delta\phi(\text{jet}^{\text{lead}}, E_{\text{T}}^{\text{miss}})$ in the $\tau+e$ channel

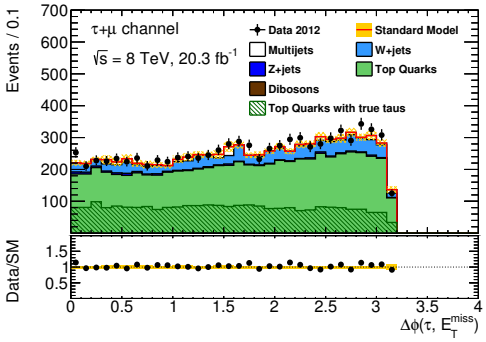

(e) $\Delta\phi(\tau, E_{\text{T}}^{\text{miss}})$ in the $\tau+\mu$ channel

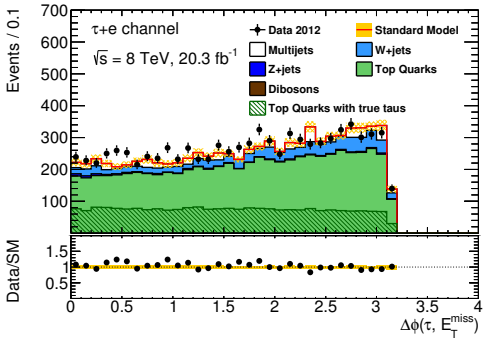

(f) $\Delta\phi(\tau, E_{\text{T}}^{\text{miss}})$ in the $\tau+e$ channel

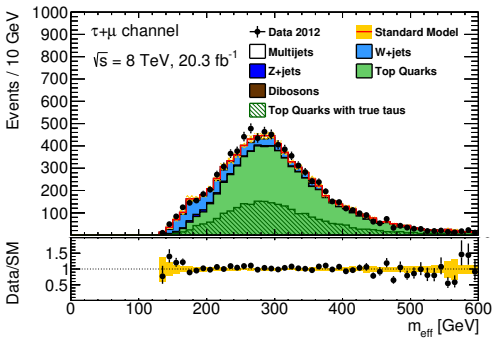

(g) m_{eff} in the $\tau+\mu$ channel

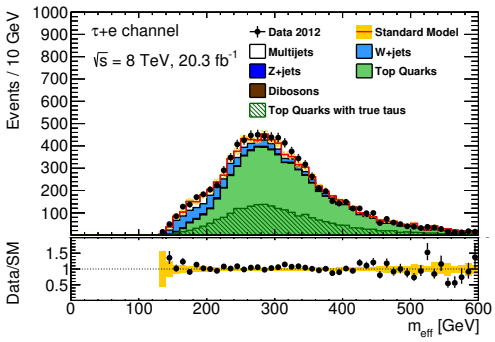

(h) m_{eff} in the $\tau+e$ channel

Figure 4.19: Control distributions in the Top Fake control region after applying all background corrections.

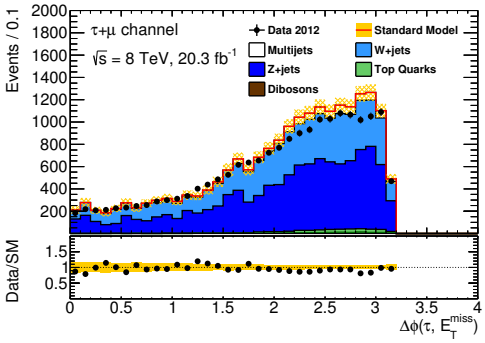

(a) $\Delta\phi(\tau, E_{\mathrm{T}}^{\mathrm{miss}})$ in the $\tau+\mu$ channel

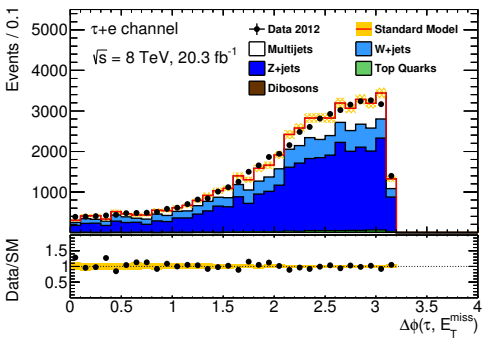

(b) $\Delta\phi(\tau, E_{\mathrm{T}}^{\mathrm{miss}})$ in the $\tau+e$ channel

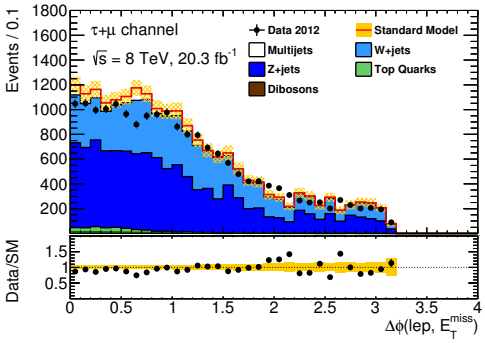

(c) $\Delta\phi(\ell, E_{\mathrm{T}}^{\mathrm{miss}})$ in the $\tau+\mu$ channel

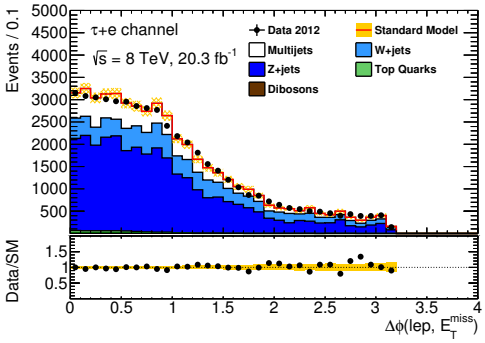

(d) $\Delta\phi(\ell, E_{\mathrm{T}}^{\mathrm{miss}})$ in the $\tau+e$ channel

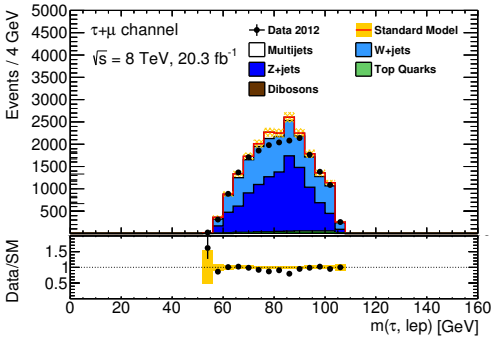

(e) visible mass of the tau and the muon

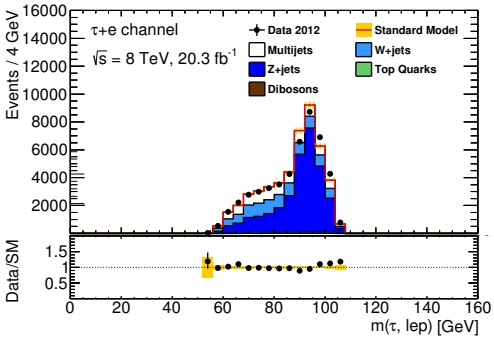

(f) visible mass of the tau and the electron

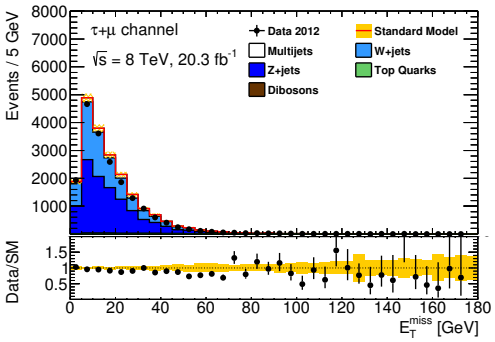

(g) $E_{\mathrm{T}}^{\mathrm{miss}}$ in the $\tau+\mu$ channel

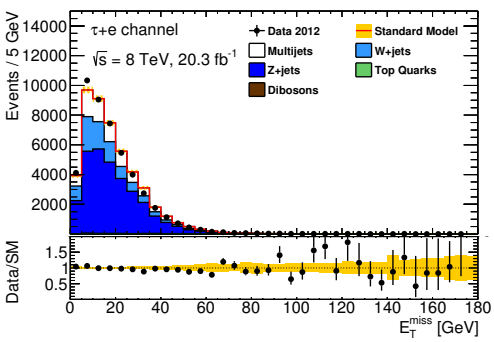

(h) $E_{\mathrm{T}}^{\mathrm{miss}}$ in the $\tau+e$ channel

Figure 4.20: Control distributions in the Z+jets control region.

CHAPTER 5

Search for SUSY Signals

After validating the correct background prediction, events in more specialized kinematic regions can be selected to search for possible SUSY decay modes. In the first part of this section the optimization of the signal regions for the individual SUSY models is described (5.1). After that, the systematic uncertainties on the background predictions in the signal regions are discussed (5.2). In the final part the observed data is compared to expectations from SM contributions and the predicted signals and the results are interpreted with statistical methods (5.5 and 5.6).

5.1 Separation of Signal and Background

With an accurate description of the Standard Model background, the number of expected and observed events can be studied in kinematic regions that are possibly dominated by SUSY signals. For this, the Standard Model background needs to be suppressed heavily while at the same time SUSY events can still pass the selection criteria. For the prediction of the number of SUSY events in the various models signal Monte Carlo samples are used.

To separate SUSY signal events from the Standard Model background the sensitivities of various kinematic variables are studied. Since four different models are taken into account, dedicated signal regions (SR) are designed for each model. In these models large sets of parameter combinations are considered. The impact of varying these parameters must be accounted for as well.

5.1.1 Basic Background Reduction

Before optimizing for each individual SUSY model a basic reduction of the largest background contributions from Multijet, Z+jets and W+jets events can be achieved by selecting events that satisfy

$$m_{\mathrm{T}}^{\ell} > 100\,\mathrm{GeV}.$$

As already discussed in the previous chapter, most of the W+jets events accumulate in the region of the W mass. Furthermore, the huge majority of Multijet events and a large part of Z+jets events lie below the Jacobian peak. A logarithmic scale presentation of the m_{T}^{ℓ} distribution with overlaid events from signal MC for selected benchmark points is displayed in figure 5.1.

All signals show a rather flat behavior in the whole mass spectrum, whereas each of the SM background contributions have their maximum below 100 GeV. Therefore, this requirement on the transverse mass of the light lepton is well suited for a first basic background suppression. For this reason, it will be used in all signal regions.

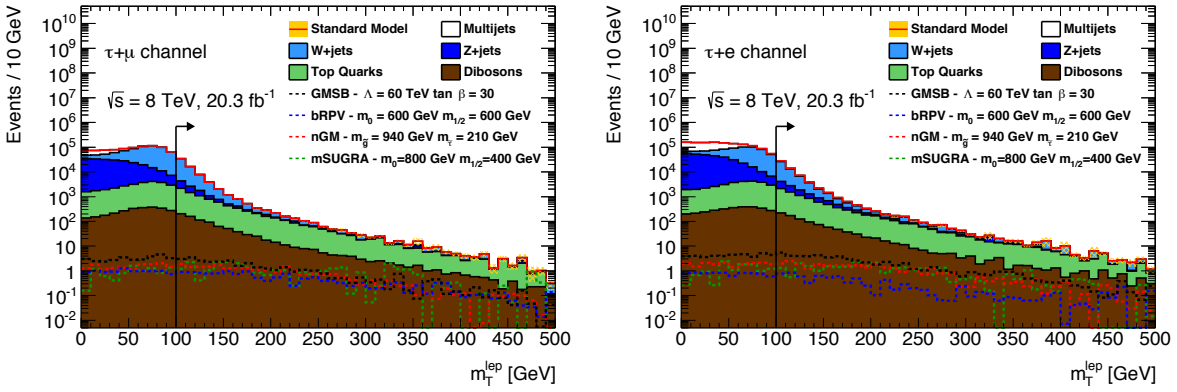

(a) m_{T}^{ℓ} distribution in the $\tau+\mu$ channel.

(b) m_{T}^{ℓ} distribution in the $\tau+e$ channel.

Figure 5.1: The transverse mass of the leptons after baseline selection with overlaid signal events of chosen benchmark points for the four analyzed SUSY models. The black line and arrow indicate the cut at $m_{\mathrm{T}}^{\ell} = 100\,\mathrm{GeV}$.

5.1.2 Signal Region Optimization

For the final optimized signal regions three different kinematic variables are considered: m_{eff}, H_{T} and $E_{\mathrm{T}}^{\mathrm{miss}}$. In addition, the impact of a requirement on the minimal number of jets per event is investigated. The final states of all considered models contain either colorless and chargeless long-lived LSPs or include a larger number of neutrinos. Therefore, one characteristic of the signal is expected to be large $E_{\mathrm{T}}^{\mathrm{miss}}$. Since this analysis aims for SUSY particles produced via the strong interaction, an increased occurance of high energetic jets is expected as well. H_{T} accounts for large hadronic transverse energy of the event. Defined as the sum of $E_{\mathrm{T}}^{\mathrm{miss}}$ and H_{T}, m_{eff} considers both aspects.

The three distributions of the background predictions for $E_{\mathrm{T}}^{\mathrm{miss}}$, H_{T} and m_{eff} are displayed in figure 5.2 after requiring $m_{\mathrm{T}}^{\ell} > 100\,\mathrm{GeV}$. Overlaid are signal benchmark points for the four regarded SUSY models that are at the edge of the sensitive area in the parameterspace for this analysis. A separation between the SM background and the signals can be observed towards higher masses where the signal stays flat while the SM background disappears.

Some SUSY models feature an increased jet multiplicity. In this case an additional requirement on the minimal number of jets in the final state helps to optimize the signal selection.

In figure 5.3 the N_{jet} distribution is displayed after requiring m_{T}^{ℓ} >100 GeV. While the number of events of the SM background decreases when more jets are selected, the signals behave differently. In the GMSB scenario the number of events shows no dependence on N_{jet} for low jet multiplicities. Towards higher jet multiplicities the GMSB signal slightly decreases.

In the other three considered SUSY models the signal shows a different behavior. The nGM model as well as bRPV and mSUGRA feature final states with multiple jets. In all three models the signal does not have a flat behavior but rises up to events with about four jets and then stays relatively flat. This already indicates that an additional jet cut is beneficial for the signal separation in these models.

For the optimization procedure a measure for the optimal separation between signal and background is needed. The *Asimov* significance [205] quantifies the discovery significance for a given number of signal events N_{Sig} and background events N_{BG}:

$$z_{\mathrm{A}} \equiv \sqrt{2\left[\left(N_{\mathrm{Sig}} + N_{\mathrm{BG}}\right)\ln\left(1 + \frac{N_{\mathrm{Sig}}}{N_{\mathrm{BG}}}\right) - N_{\mathrm{Sig}}\right]}. \tag{5.1}$$

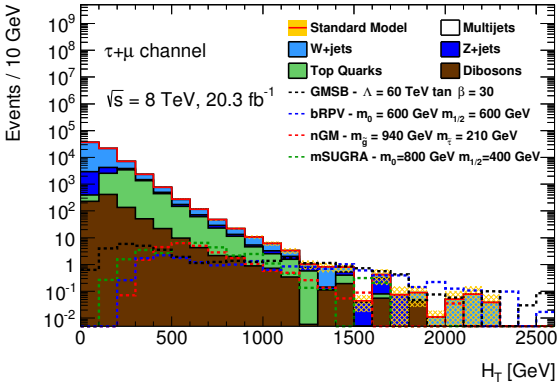

(a) H_{T} in the $\tau+\mu$ channel.

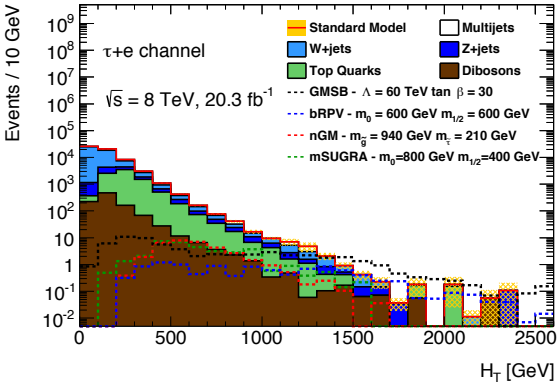

(b) H_{T} in the $\tau+e$ channel.

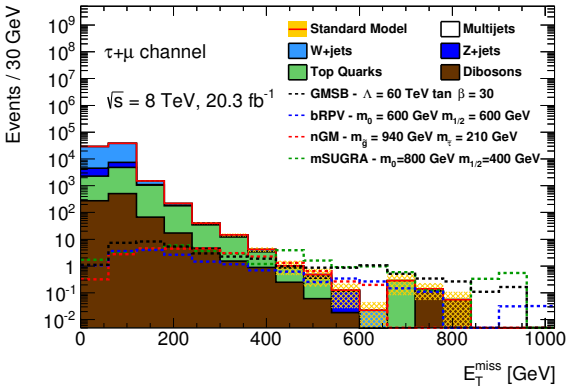

(c) $E_{\mathrm{T}}^{\mathrm{miss}}$ in the $\tau+\mu$ channel.

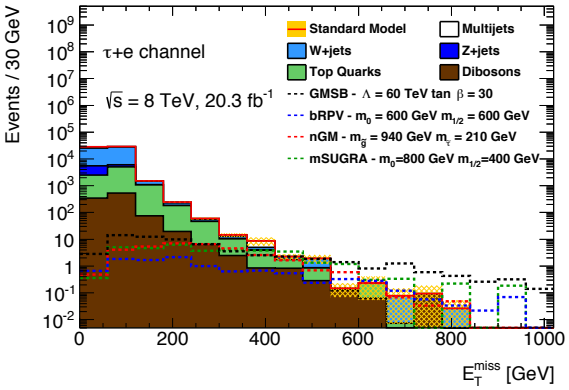

(d) $E_{\mathrm{T}}^{\mathrm{miss}}$ in the $\tau+e$ channel.

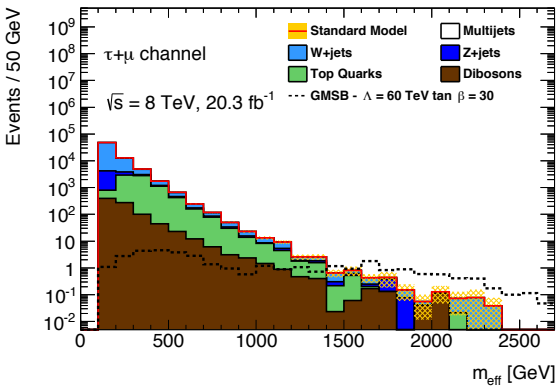

(e) m_{eff} in the $\tau+\mu$ channel.

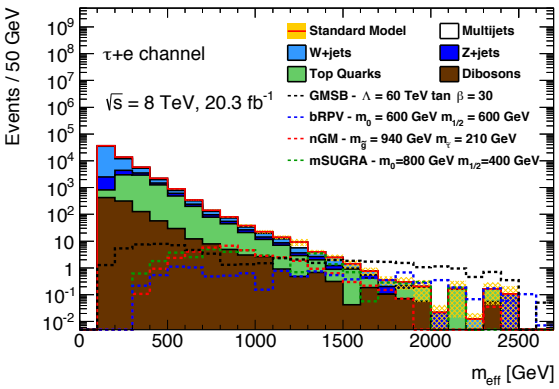

(f) m_{eff} in the $\tau+e$ channel.

Figure 5.2: The signal sensitive kinematic distributions H_{T}, $E_{\mathrm{T}}^{\mathrm{miss}}$ and m_{eff} after requiring m_{T}^{ℓ} >100 GeV. Only the MC predictions are displayed. Chosen signal benchmark points of all four SUSY models, represented by the dashed colored lines, are overlaid.

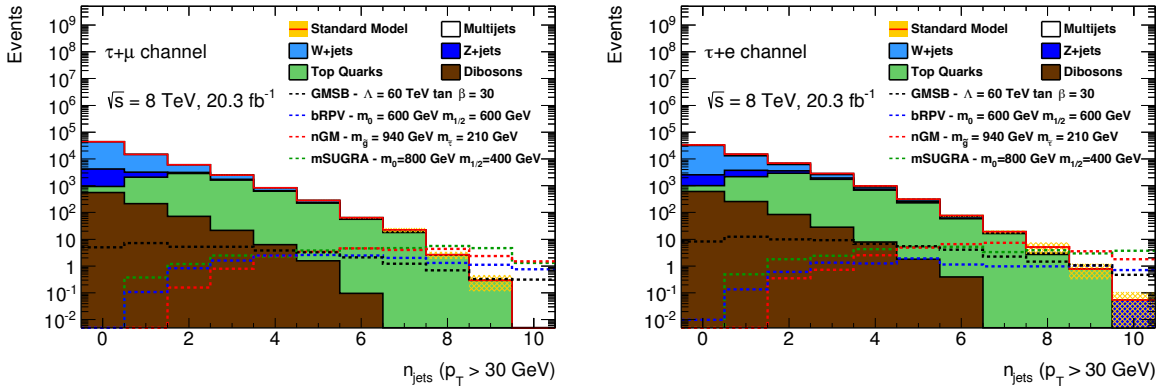

(a) N_{jet} in the $\tau+\mu$ channel.

(b) N_{jet} in the $\tau+e$ channel.

Figure 5.3: The number of jets after requiring m_{T}^{ℓ} >100 GeV. Only the MC predictions are displayed. Chosen signal benchmark points of all four SUSY models are overlaid.

For large statistics this reduces to the more commonly known ratio $N_{\text{Sig}}/\sqrt{N_{\text{BG}}}$. For low statistics however, z_{A} provides the correct description accounting for the underlying Poisson statistics.

A more complex modification of 5.1 considers the uncertainties on the number of signal and background events as well [206]:

$$z_{\text{A}} \equiv \sqrt{2\left\{(N_{\text{Sig}}+N_{\text{BG}})\ln\left[\frac{(N_{\text{Sig}}+N_{\text{BG}})(N_{\text{BG}}+\sigma^2_{N_{\text{BG}}})}{N^2_{\text{BG}}+(N_{\text{Sig}}+N_{\text{BG}})\sigma^2_{N_{\text{BG}}}}\right]-\frac{N^2_{\text{BG}}}{\sigma^2_{N_{\text{BG}}}}\ln\left[1+\frac{N_{\text{Sig}}\sigma^2_{N_{\text{BG}}}}{N_{\text{BG}}(N_{\text{BG}}+\sigma^2_{N_{\text{BG}}})}\right]\right\}}. \quad (5.2)$$

In cases where the uncertainty can not be neglected 5.1 overestimates the discovery significance.

For the optimization these measures are used in so-called significance scans. The significance z_{A} is calculated for all possible cut values in the regarded signal-sensitive distributions. For this, the event numbers of all backgrounds in the bins that lie above the cut value are summed up to N_{BG}. Correspondingly, the signal events are summed up to N_{Sig}. The value of z_{A} computed with these numbers gives one entry in the significance diagram at the currently regarded cut value. This significance scan indicates the cut value with optimal discovery potential at the maximum of the curvature.

5.1.3 GMSB Signal Region

To study the performance of different kinematic cuts in the GMSB model three benchmark signal points are selected from the grid. They cover an area in the parameter space in which the analysis shows different sensitivities. These benchmark points are:

- Λ = 60 TeV, tan β = 30
- Λ = 70 TeV, tan β = 40
- Λ = 80 TeV, tan β = 50

Comparing the maximum of the significances reached with m_{eff}, H_{T} and $E_{\text{T}}^{\text{miss}}$, m_{eff} is determined to be the most sensitive kinematic variable. The corresponding significance scans for the other kinematic variables are collected in section A.2 of the appendix.

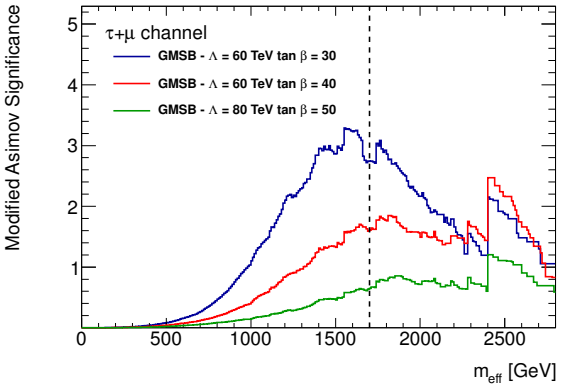

(a) z_A in the $\tau+\mu$ channel.

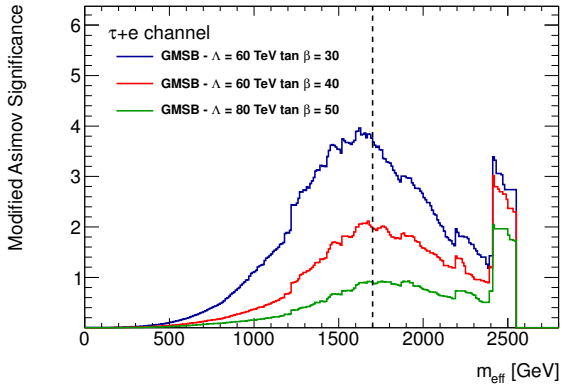

(b) z_A in the $\tau+e$ channel.

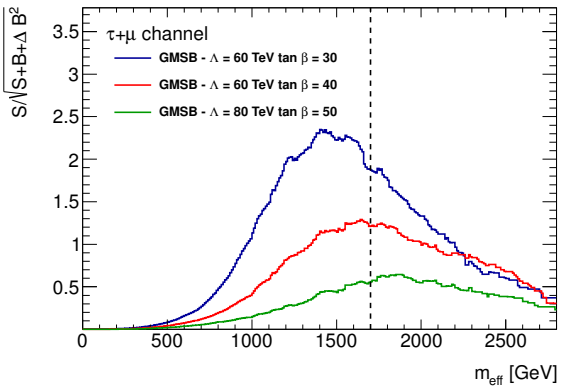

(c) $S/\sqrt{S+B+\Delta B^2}$ in the $\tau+\mu$ channel.

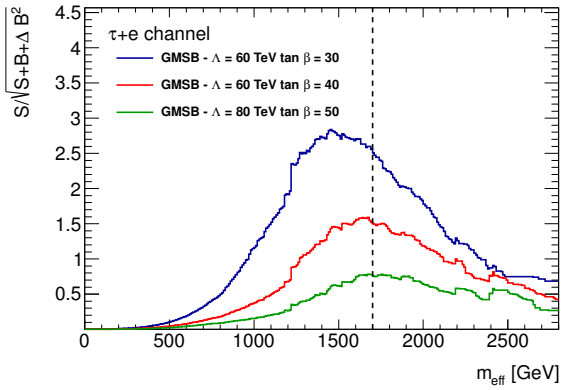

(d) $S/\sqrt{S+B+\Delta B^2}$ in the $\tau+e$ channel.

Figure 5.4: Modified Asimov significance and $S/\sqrt{S+B+\Delta B^2}$ scans for the GMSB signal region in the m_{eff} distribution after requiring m_{T}^{ℓ} >100 GeV for three chosen benchmark points. The dashed black line indicates a cut value at m_{eff} = 1700 GeV.

Figure 5.4 shows two significance scans for each channel. The modified Asimov significance is displayed in figures 5.4a and 5.4b. Figures 5.4c and 5.4d show for comparison the simpler significance measure $N_{\text{Sig}}/\sqrt{N_{\text{Sig}}+N_{\text{BG}}+\Delta N_{\text{BG}}^2}$ (where N_{Sig} and N_{BG} are simply denoted by S and B in the figure).

For the three different benchmark points the maximum of the scans is slightly shifted. The less sensitive the analysis is for a particular point, the higher is the suggested cut value. To account for this in regard of the optimal discovery potential, the medium benchmark point is chosen as a reference since it is at the edge of sensitivity.

The additional plots in section A.2 also include scans where the background shape is fitted to smoothen the curve characteristics. All scans suggest the common optimal cut value for the GMSB signal region for both channels is

$$m_{\text{eff}} > 1700\,\text{GeV} \tag{5.3}$$

as indicated by the dashed black lines in figure 5.4.

To study the performance of an additional cut on the minimal number of jets per event, more significance scans in the N_{jet} distribution are performed. The N_{jet} distribution studied after the previously established requirements of $m_{\text{T}}^{\ell} > 100\,\text{GeV}$ and $m_{\text{eff}} > 1700\,\text{GeV}$.

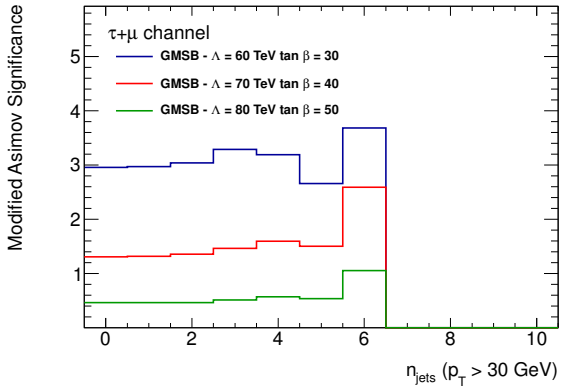

(a) z_A in the $\tau+\mu$ channel.

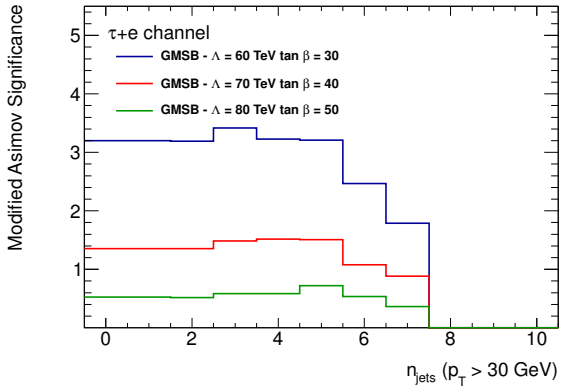

(b) z_A in the $\tau+e$ channel.

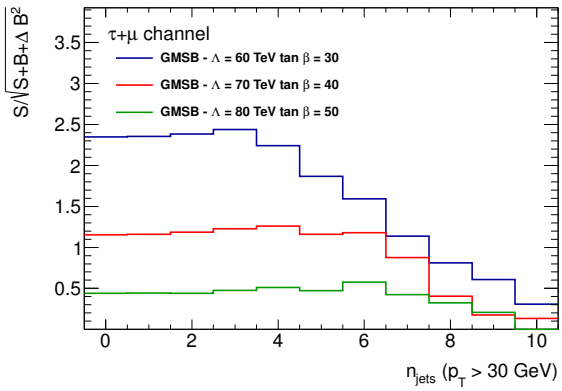

(c) $S/\sqrt{S+B+\Delta B^2}$ in the $\tau+\mu$ channel.

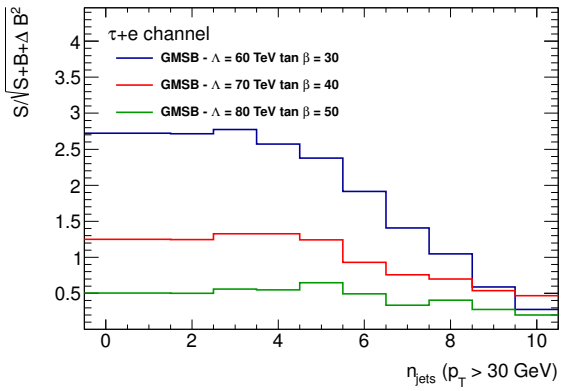

(d) $S/\sqrt{S+B+\Delta B^2}$ in the $\tau+e$ channel.

Figure 5.5: Modified Asimov significance and $S/\sqrt{S+B+\Delta B^2}$ scans for the GMSB signal region in the N_{jet} distribution after requiring $m_{\text{T}}^{\ell} > 100\,\text{GeV}$ and $m_{\text{eff}} > 1700\,\text{GeV}$ for three chosen benchmark points.

The corresponding scans are displayed in figure 5.5. Neither the modified Asimov significance nor the $S/\sqrt{S+B+\Delta B^2}$ scan show a considerable gain in sensitivity by an additonal requirement on N_{jet}. Therefore, the N_{jet} cut is discarded as a selection criterion for the GMSB signal region.

5.1.4 nGM Signal Region

The nGM signal region is also optimized with three chosen benchmark points from the corresponding signal grid. These points are:

- $m_{\tilde{\tau}} = 210\,\text{GeV}$, $m_{\tilde{g}} = 860\,\text{GeV}$
- $m_{\tilde{\tau}} = 210\,\text{GeV}$, $m_{\tilde{g}} = 1020\,\text{GeV}$
- $m_{\tilde{\tau}} = 210\,\text{GeV}$, $m_{\tilde{g}} = 1180\,\text{GeV}$

Since the sensitivity in this grid has been shown to be independent of the stau mass by previous studies [207], the stau mass is fixed for the optimization procedure. The grid points are only varied in the gluino mass. The three considered gluino masses correspond to a region in the parameter space that is expected to contain a possible exclusion limit.

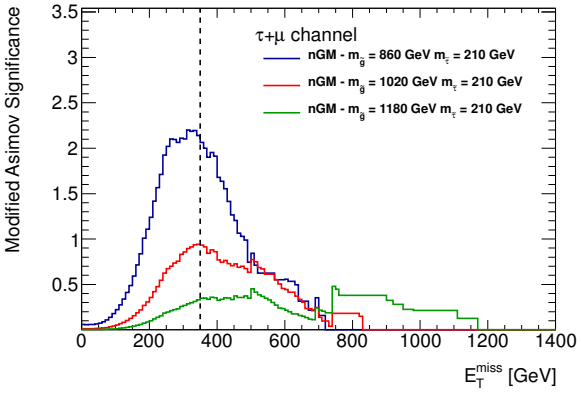

(a) z_A in the $\tau+\mu$ channel.

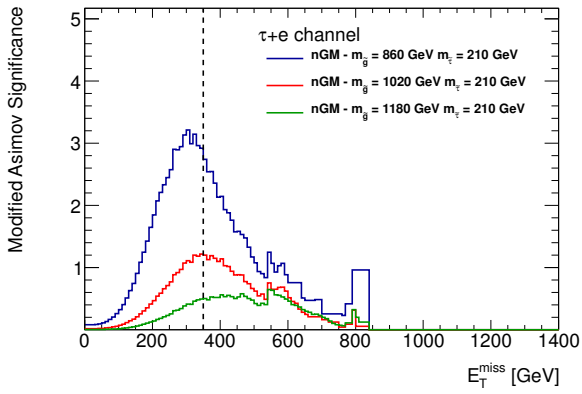

(b) z_A in the $\tau+e$ channel.

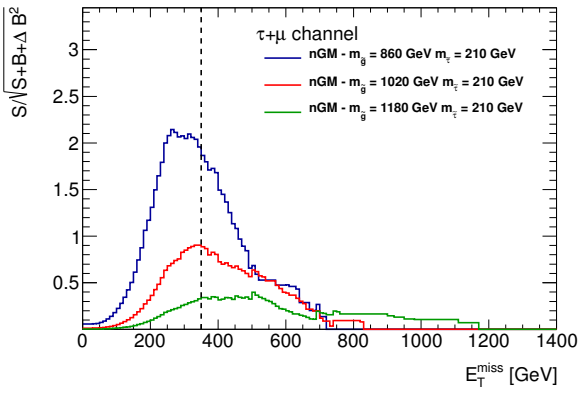

(c) $S/\sqrt{S+B+\Delta B^2}$ in the $\tau+\mu$ channel.

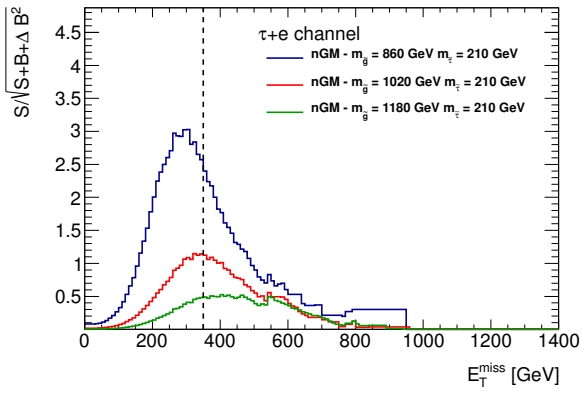

(d) $S/\sqrt{S+B+\Delta B^2}$ in the $\tau+e$ channel.

Figure 5.6: Modified Asimov significance and $S/\sqrt{S+B+\Delta B^2}$ scans for the nGM signal region in the $E_{\mathrm{T}}^{\mathrm{miss}}$ distribution after requiring m_{T}^{ℓ} >100 GeV and $N_{\mathrm{jet}} \geq 3$ for three chosen benchmark points. The dashed black line indicates a cut value at $E_{\mathrm{T}}^{\mathrm{miss}} = 350\,\mathrm{GeV}$.

From the three considered kinematic variables, $E_{\mathrm{T}}^{\mathrm{miss}}$ shows the best separation power for signal and background in the nGM model. The according significance scans for m_{eff} and H_{T} are collected in section A.2.

Figure 5.6 displays two significance scans for both channels similar to the ones used before for the GMSB model. The signal contributions for final states with less than two jets are neglegibly small, as visible in the N_{jet} distributions in figure 5.3. The optimization the $E_{\mathrm{T}}^{\mathrm{miss}}$ distribution is therefore scanned after already requiring $N_{\mathrm{jet}} \geq 3$.

The region in which a possible exclusion is expected lies slightly above the grid points with gluino masses of 860 GeV. The corresponding benchmark point is used as a reference for the cut optimization. The maximum of the significance indicates the optimal cut value is

$$E_{\mathrm{T}}^{\mathrm{miss}} > 350\,\mathrm{GeV}. \tag{5.4}$$

In the significance scans in figure 5.6 this cut is represented by the black dashed line.

Additional significance scans in the N_{jet} distribution are displayed in figure 5.7. The discovery significance rises towards higher jet multiplicities as expected. The increase is highest for the step of selecting

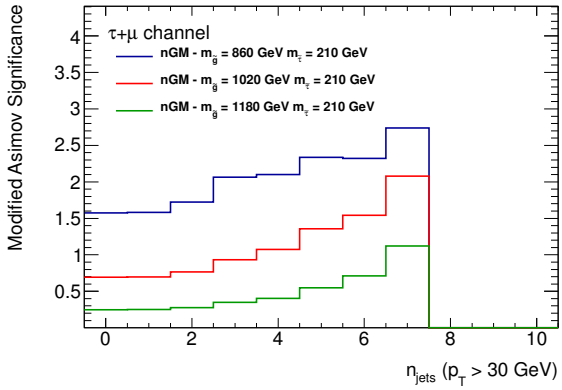

(a) z_A in the $\tau+\mu$ channel.

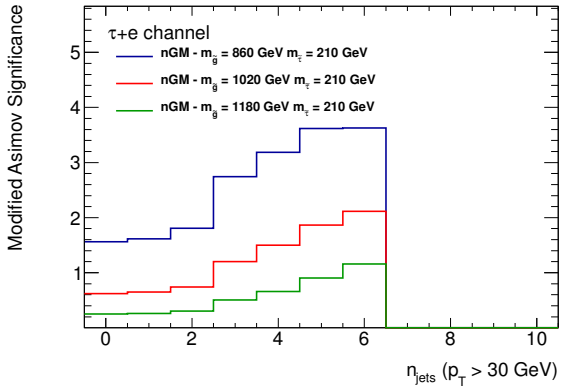

(b) z_A in the $\tau+e$ channel.

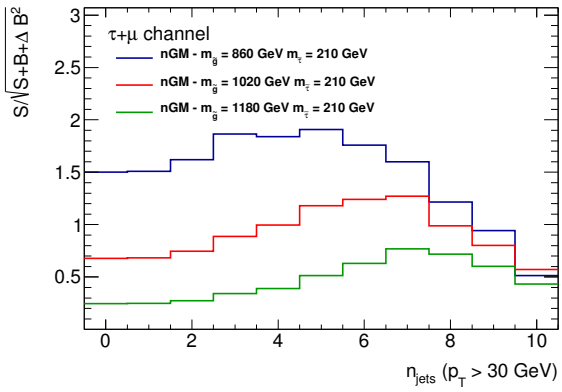

(c) $S/\sqrt{S+B+\Delta B^2}$ in the $\tau+\mu$ channel.

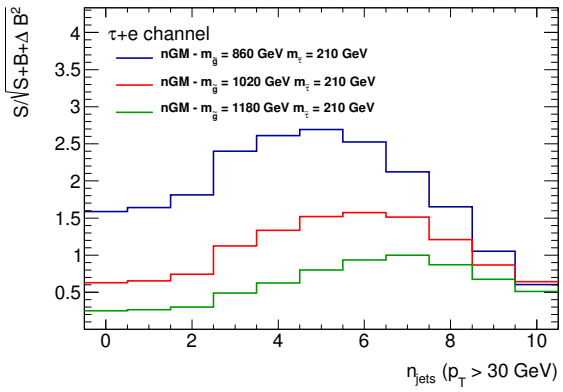

(d) $S/\sqrt{S+B+\Delta B^2}$ in the $\tau+e$ channel.

Figure 5.7: Modified Asimov significance and $S/\sqrt{S+B+\Delta B^2}$ scans for the nGM signal region in the N_{jet} distribution after requiring $m_{\text{T}}^{\ell} > 100\,\text{GeV}$ and $E_{\text{T}}^{\text{miss}} > 350\,\text{GeV}$ for three chosen benchmark points.

three jets. For this reason and for the purpose of keeping enough statistics for a reliable background estimate the previously chosen requirement of $N_{\text{jet}} \geq 3$ is not altered.

5.1.5 bRPV Signal Region

Like before, three grid points are chosen from the bRPV signal grid which are used for optimizing the signal region. These benchmark points are:

- $m_0 = 600\,\text{GeV}$, $m_{1/2} = 600\,\text{GeV}$
- $m_0 = 800\,\text{GeV}$, $m_{1/2} = 500\,\text{GeV}$
- $m_0 = 1000\,\text{GeV}$, $m_{1/2} = 450\,\text{GeV}$

They are chosen with respect to the expected sensitivity in the parameter space of the grid which depends both on m_0 and $m_{1/2}$ as discovered in previously performed studies.

For separation of signal and background m_{eff} shows the best performance of the three considered kinematic variables. Equivalent scans for H_{T} and $E_{\text{T}}^{\text{miss}}$ for comparison are collected in section A.2 in the appendix.

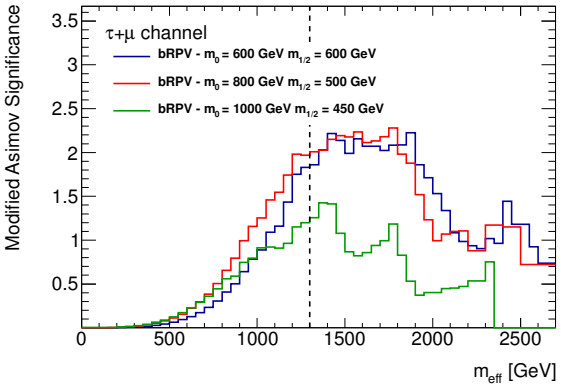

(a) z_A in the $\tau+\mu$ channel.

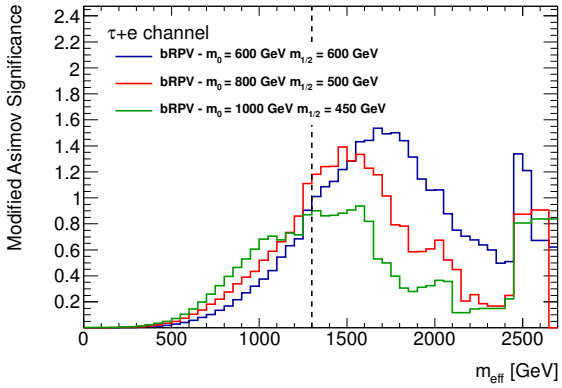

(b) z_A in the $\tau+e$ channel.

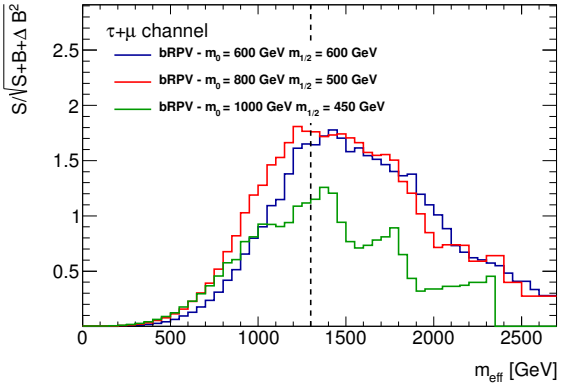

(c) $S/\sqrt{S+B+\Delta B^2}$ in the $\tau+\mu$ channel.

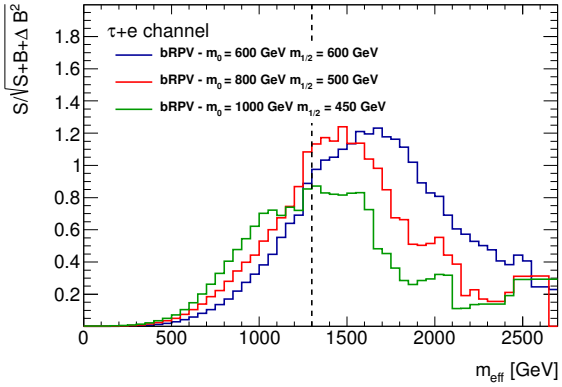

(d) $S/\sqrt{S+B+\Delta B^2}$ in the $\tau+e$ channel.

Figure 5.8: Modified Asimov significance and $S/\sqrt{S+B+\Delta B^2}$ scans for the bRPV signal region in the m_{eff} distribution after requiring m_{T}^{ℓ} >100 GeV for three chosen benchmark points. The dashed black line indicates a cut value at m_{eff} = 1300 GeV.

Figure 5.8 displays the modified Asimov significance and $S/\sqrt{S+B+\Delta B^2}$ for the m_{eff} distribution. A sufficient discovery significance is accomplished with

$$m_{\text{eff}} > 1300\,\text{GeV} \tag{5.5}$$

as indicated by the dashed black lines in the figure.

The benefit of an additional requirement on the jet multiplicity is obvious after regarding the signal shape in figure 5.3. Figure 5.9 displays the relevant significance scans in the N_{jet} distribution. Considering both adequate gain in significance and sufficient remains of statistics for a reliable background description, a requirement of $N_{\text{jet}} \geq 4$ is used.

5.1.6 mSUGRA Signal Region

Finally, three grid points are selected from the mSUGRA grid to optimize the corresponding signal region. These benchmark points are listed below.

- m_0 = 800 GeV, $m_{1/2}$ = 400 GeV

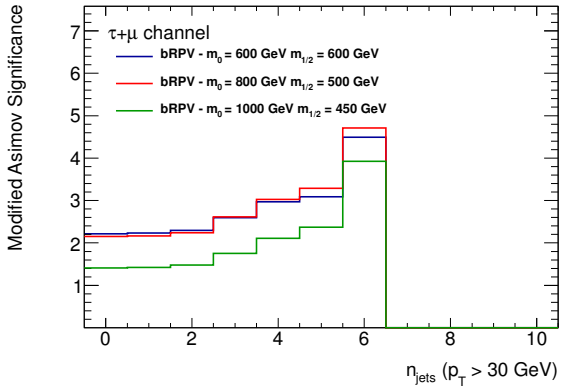

(a) z_A in the $\tau+\mu$ channel.

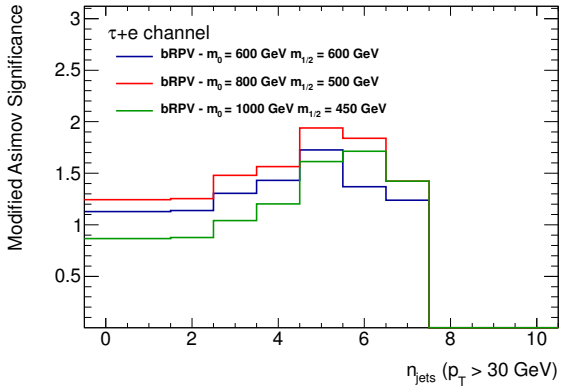

(b) z_A in the $\tau+e$ channel.

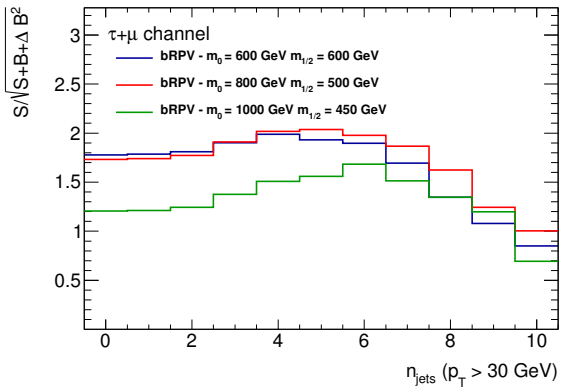

(c) $S/\sqrt{S+B+\Delta B^2}$ in the $\tau+\mu$ channel.

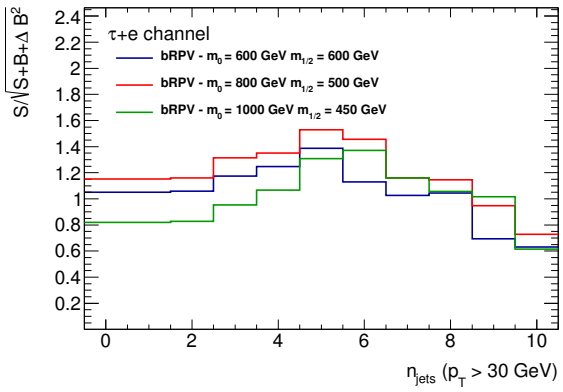

(d) $S/\sqrt{S+B+\Delta B^2}$ in the $\tau+e$ channel.

Figure 5.9: Modified Asimov significance and $S/\sqrt{S+B+\Delta B^2}$ scans for the bRPV signal region in the N_{jet} distribution after requiring $m_{\text{T}}^{\ell} > 100\,\text{GeV}$ and $m_{\text{eff}} > 1300\,\text{GeV}$ for three chosen benchmark points.

- $m_0 = 1800\,\text{GeV}$, $m_{1/2} = 250\,\text{GeV}$
- $m_0 = 3000\,\text{GeV}$, $m_{1/2} = 300\,\text{GeV}$

Sensitivity to the mSUGRA model is expected in the parameter space with low $m_{1/2}$ and in the region with low m_0 and medium $m_{1/2}$.

The most sensitive kinematic distribution for the mSUGRA model is $E_{\text{T}}^{\text{miss}}$. Just as for the other models, the alternative kinematic variables are collected in the appendix, section A.2, for comparison. The significance scans in the $E_{\text{T}}^{\text{miss}}$ distribution are displayed in figure 5.10. All four scans indicate that a requirement of

$$E_{\text{T}}^{\text{miss}} > 300\,\text{GeV} \tag{5.6}$$

yields a good separation of signal and background in all three considered regions of the parameter space.

The significance scans in the N_{jet} distribution are displayed in figure 5.11. The largest gain in significance is accomplished with requiring $N_{\text{jet}} \geq 3$. With these cuts the mSUGRA signal region is very similar to the one defined for the bRPV model.

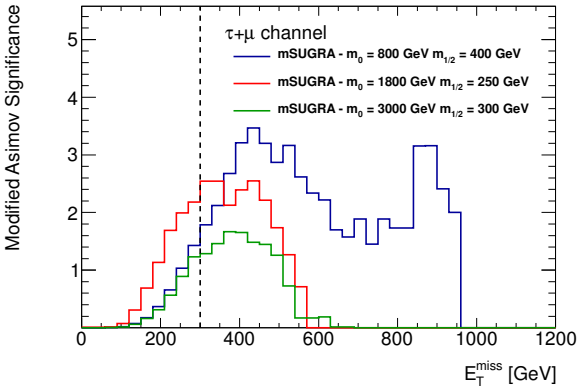

(a) z_A in the $\tau+\mu$ channel.

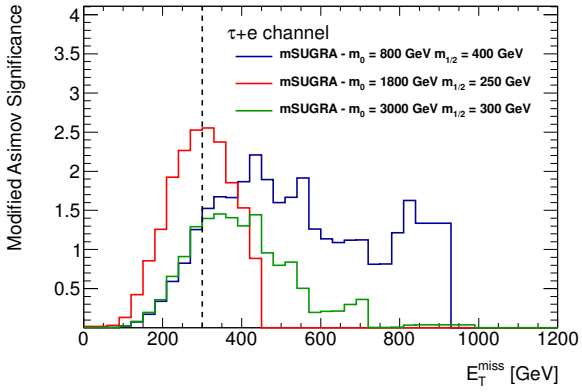

(b) z_A in the $\tau+e$ channel.

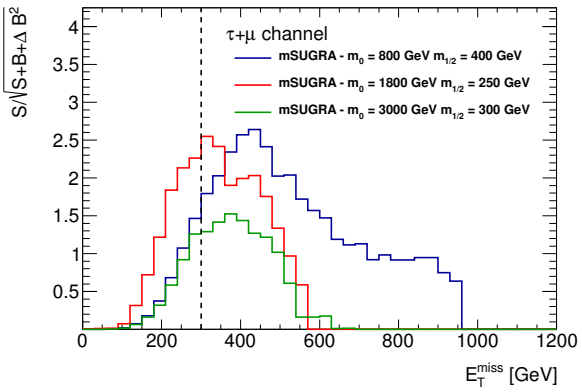

(c) $S/\sqrt{S+B+\Delta B^2}$ in the $\tau+\mu$ channel.

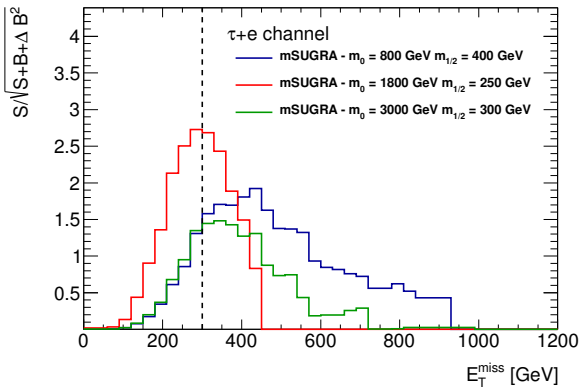

(d) $S/\sqrt{S+B+\Delta B^2}$ in the $\tau+e$ channel.

Figure 5.10: Modified Asimov significance and $S/\sqrt{S+B+\Delta B^2}$ scans for the mSUGRA signal region in the $E_{\mathrm{T}}^{\mathrm{miss}}$ distribution after requiring m_{T}^{ℓ} >100 GeV for three chosen benchmark points. The dashed black line indicates a cut value at $E_{\mathrm{T}}^{\mathrm{miss}}$ = 300 GeV.

5.1.7 Summary of the signal region selection

Considering both the $\tau+\mu$ and the $\tau+e$ channel, eight signal regions in total were defined for the four studied SUSY models. These signal regions use a common cut of $m_{\mathrm{T}}^{\ell} > 100$ GeV. The other requirements utilize m_{eff} or $E_{\mathrm{T}}^{\mathrm{miss}}$ to isolate the signal. Additional cuts on the minimal number of jets are used for further background reduction if beneficial.

The selection criteria are equivalent in the two channels. A summary of all the selection criteria is shown in table 5.1.

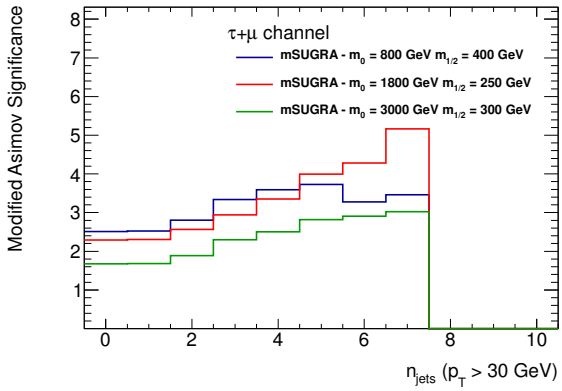

(a) z_A in the $\tau+\mu$ channel.

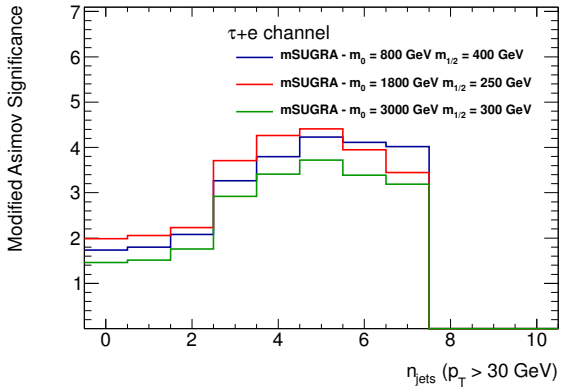

(b) z_A in the $\tau+e$ channel.

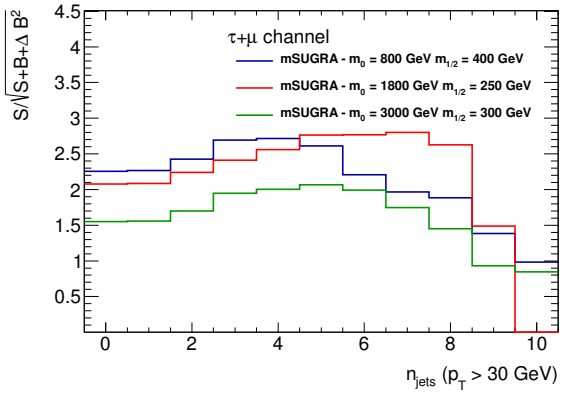

(c) $S/\sqrt{S+B+\Delta B^2}$ in the $\tau+\mu$ channel.

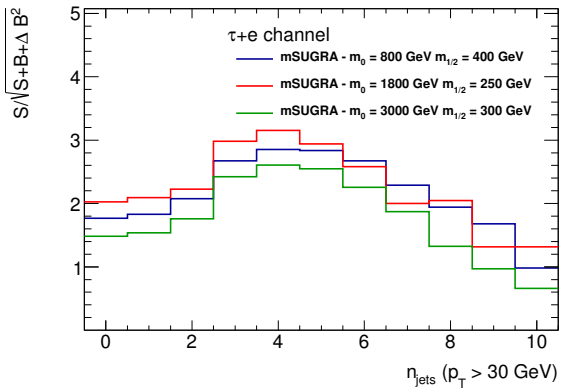

(d) $S/\sqrt{S+B+\Delta B^2}$ in the $\tau+e$ channel.

Figure 5.11: Modified Asimov significance and $S/\sqrt{S+B+\Delta B^2}$ scans for the mSUGRA signal region in the N_{jet} distribution after requiring $m_{\text{T}}^{\ell} > 100\,\text{GeV}$ and $E_{\text{T}}^{\text{miss}} > 300\,\text{GeV}$ for three chosen benchmark points.

Signal Region Selection				
observable	GMSB SR	nGM SR	bRPV SR	mSUGRA SR
m_{T}^{ℓ}	$> 100\,\text{GeV}$			
N_{jets}	—	≥ 3	≥ 4	≥ 3
$E_{\text{T}}^{\text{miss}}$	—	$> 350\,\text{GeV}$	—	$> 300\,\text{GeV}$
m_{eff}	$> 1700\,\text{GeV}$	—	$> 1300\,\text{GeV}$	—

Table 5.1: Summary of the kinematic requirements on the transverse mass, the number of jets, $E_{\text{T}}^{\text{miss}}$ and m_{eff} for the four signal regions.

5.2 Systematic Uncertainties

A measurement in physics can only be performed within a limited precision. This precision is determinated by several factors. In case of a statistical process the number of measurements imposes the statistical uncertainty. Additional systematic uncertainties arise from the method of measuring itself. In a very complex setup such as the ATLAS experiment there are many sources for systematic uncertainties that have to be considered and evaluated.

Estimates for the systematic uncertainties are needed in the signal regions and affect the number of background events as well as the number of signal events. However, their influence is also present in the control regions. By computing the background scalings in the control regions this transfers to the signal region as well.

The sources of uncertainties include for instance the measurement of identification and trigger efficiencies, energy scales of the calorimeter response, pile-up corrections or the event modeling in the MC generator.

To account for the detector response effects each MC event is re-evaluated while varying the critical quantity which might cause a possible deviation. This re-evaluation is performed according to the prescriptions that are provided by various ATLAS subgroups, responsible for measuring the quantity in question and its uncertainty.

For each systematic uncertainty all MC samples have to be processed again under variation of the according quantity. An uncertainty which only affects the overall normalization would be partly absorbed by the computation of background scale factors in the control regions. To account for this effect, the scale factors for W+jets, Top Truth and Top Fake events are re-calculated in the according control regions for each systematic. These scale factors are applied before comparing the deviation of the event yields to the ones obtained by using the central values of the critical observable.

5.2.1 Detector Specific Uncertainties

All uncertainties related to the reconstruction or measurement performance of detector related quantities are derived with the software packages that are provided by the various ATLAS performance groups as implemented in SUSYTools. Table B.23 in the appendix contains a summary of those packages and the version numbers used.

Jet Energy Scale The signals of the calorimeters are interpreted as jet energies. However, the relation between the energy and the obtained signals – the jet energy scale (JES) – is only measured within a limited precision. The uncertainty is determined in MC studies in dependence of the p_{T} and the flavor of the jet, as a function of the pseudorapidity, for different pile-up conditions and taking into account the influence of close-by jets [201, 208].

The modifications of the jet energies are propagated to the modified missing transverse momentum $E_{x,y}^{\mathrm{miss}\prime}$ by

$$E_{x,y}^{\mathrm{miss}\prime} = E_{x,y}^{\mathrm{miss}} + \sum_{\mathrm{jets}} p_{x,y} - \sum_{\mathrm{jets}} p_{\mathrm{x,y}}. \tag{5.7}$$

Since these corrections are applied before overlap removal, they also affect objects which are identified as tau leptons. These tau objects however, are treated as jets in the definition of $E_{\mathrm{T}}^{\mathrm{miss}}$ which is used in this analysis.

Jet energy scale and tau energy scale are treated as uncorrelated. There is no significant overlap expected in these two quantities because the energy scale calibrations are derived with very different methods.

Jet Energy Resolution The energy resolution of the jet reconstruction (JER) is also only simulated with a finite precision. The uncertainty on JER is estimated by different in situ, techniques which are described in [209]. The observed discrepancies are of the order of 10 %. This is considered by a Gaussian resmearing of the jets after their reconstruction which is performed in dependency of η and p_{T}.

The changes in the jet energy are propagated to $E_{\mathrm{T}}^{\mathrm{miss}}$ by equation 5.7. Again, the corrections are applied before overlap removal and therefore also affect tau candidates.

Tau energy scale The uncertainty on the tau energy scale (TES) is evaluated in MC truth studies. The largest impact on the total uncertainty is due to the modeling of hadronic showers. All techniques and results are described in [210]. The uncertainty depends on p_{T}, η and n_{prong} and has a size of 2 – 4 %.

Since not the tau objects themselves but instead their seed jets are considered in the $E_{\mathrm{T}}^{\mathrm{miss}}$ definition, the tau energy scaling is not propagated to $E_{\mathrm{T}}^{\mathrm{miss}}$.

Tau identification The tau identification efficiency is subject to a systematic uncertainty as well. It is studied with a tag and probe method in $Z \to \tau\tau$ and $W \to \tau\nu$ events. Depending on the working point and n_{prong} the uncertainties are about 2 – 5 %. All studies on these measurements are documented in [210]. To evaluate the impact on the signal region yields, the MC events are re-weighted according to the measured uncertainty for each tau candidate that can be matched to a truth object.

Altering only the event weights however is mostly compensated by scaling the background in the control regions. Therefore the tau identification uncertainties have only little impact on this analysis.

Missing transverse momentum Systematic uncertainties for the missing transverse momentum depend on variations of the jet and lepton energies (excluding tau leptons) that are considered in the calculation of $E_{\mathrm{T}}^{\mathrm{miss}}$.

Additionally, so-called *soft terms* (ST) uncertainties have to be taken into account. These relate to energy contributions in the calorimeters which are below the reconstruction thresholds and are not identified to be part of any physics object in the event. Those objects must be considered with an energy scale and a resolution uncertainty

Pile-Up Uncertainties Pile-up re-weighting of the events is another source of systematic uncertainties. To account for a potential mismodeling of the pile-up conditions the nominal value of the average number of interactions per bunch-crossing is altered by 10 %.

The signal jet definition requires a cut on the jet vertex fraction (JVF). This cut helps separating jets from additional pile-up activity. The systematic uncertainty introduced with the cut choice is considered by varying the cut value on JVF.

B-Tag efficiencies The identification efficiencies of jets originating from b and c quarks as well as the misidentification rate are considered and varied for the overall uncertainty related to b-tagging. Since b-tagging is used for separation of the W+jets and Top Quarks background in the control regions, its influence propagates to the signal region via the derivation of the background scale factors.

Muon Related Systematic Uncertainties There are a number of uncertainties related to muon identification. Their impact on the overall uncertainty is rather small, but they are nevertheless taken into account for the $\tau+\mu$ channel.

For uncertainties on the muon energy scale (MSCALE) the p_{T} of the muons is scaled up and down. The energy resolution has two components – one for the Muon Spectrometer (MMS) and one for the Inner

Detector (MID). To evaluate the uncertainties, the p_{T} is smeared for both components individually. More details on the measurements of these uncertainties can be found in [211].

Furthermore, the identification efficency (MEFF) and the trigger efficiencies (MTRIG) are included as sources for uncertainties. These efficiencies are considered in the event weights, which are scaled up and down.

Electron Related Systematic Uncertainties The energy scale uncertainty has four different components. The scale uncertainty from the energy calibration using the Z boson mass (EGZEE), the uncertainty due to the calorimeter material (EGMAT), the scale uncertainty for the presampler energy measurement (EGPS) and an additional uncertainty for low p_{T} electrons, resulting from a deficit of passive material in simulation. The energies of the electrons are scaled up and down within the uncertainties for these four components.

The uncertainty on the energy resolution (EGRES) of electrons is quantified by applying a gaussian smearing to the energy that is dependent on p_{T} and η.

Identification efficiency (EEFF) and trigger efficiency (ETRIG) are considered by scaling the according event weights up and down. All measurements and systematics are described in more detail in [212].

5.2.2 Theory Uncertainties

Generator Uncertainties For each of the background contributions that are estimated using Monte Carlo only, an alternative event generator is used to assess the systematic uncertainty from event modeling. Table 3.2 lists these samples. For W+jets and Z+jets the nominal Sherpa samples are compared to Alpgen. The Powheg $t\bar{t}$ samples are checked against alternative Alpgen samples. Sherpa Diboson is compared to Powheg.

The alternative samples undergo the same scaling procedure in the control regions as the nominal samples. Figures 5.12 and 5.13 show the m_{eff} and the $E_{\mathrm{T}}^{\mathrm{miss}}$ distributions after requiring $m_{\mathrm{T}}^{\ell} > 100\,\mathrm{GeV}$.

The overall shape of these distributions agrees well for all alternative generators with the one in the nominal sample. However, the tails of the distributions are exposed to larger deviations. This is not only due to the fact that these are extreme kinematic regions, which are difficult to model, but in many cases also because of very limited statistics. Especially the alternative samples are affected by this. For some of the backgrounds a part of the signal regions leaves not a single event in the alternative samples for comparison.

In a relative conservative approach the systematic uncertainty in these cases is assumed to be 100 %. This is maintainable since the deviations are also rather large even with sufficient statistics.

Signal MC Uncertainties All signal samples are weighted according to their cross-section and taking into account the luminosity. This is performed with NLO accuracy for electroweak production and at NLO+NLL level for strong production processes. In doing so, not only the overall sample normalization is correct but also the individual processes are weighted properly.

However, there are uncertainties on the cross-sections that have to be considered. These uncertainties include variations of the PDFs and variations of theory parameters. Taking into account these variations the cross-sections are calculated again to assess the overall uncertainty on the signal cross-section.

5.2.3 Discussion of the Systematic Uncertainties

The total systematic uncertainty is derived treating the two-sided variations as correlated. They are summed up with the other uncertainties quadratically. As discussed before, overall scale variations mostly cancel

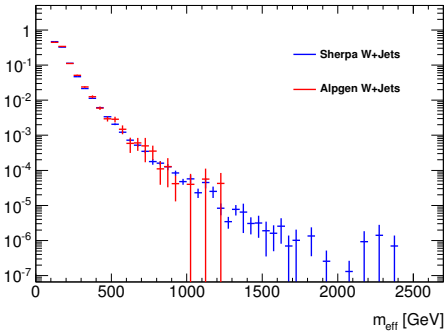

(a) W+jets samples in the $\tau+\mu$ channel.

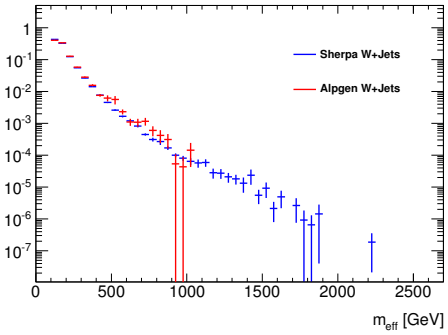

(b) W+jets samples in the $\tau+e$ channel.

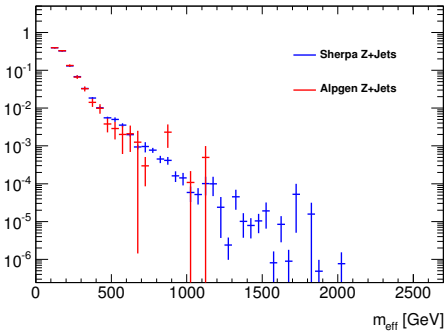

(c) Z+jets samples in the $\tau+\mu$ channel.

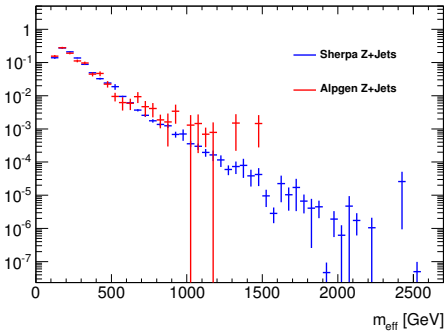

(d) Z+jets samples in the $\tau+e$ channel.

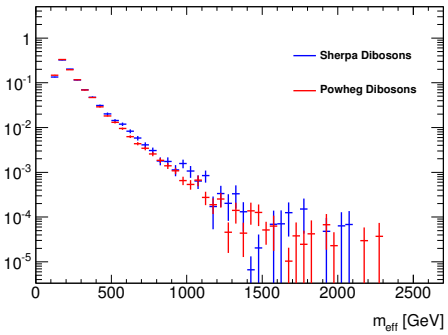

(e) Diboson samples in the $\tau+\mu$ channel.

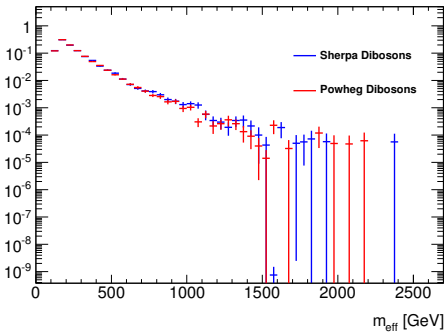

(f) Diboson samples in the $\tau+e$ channel.

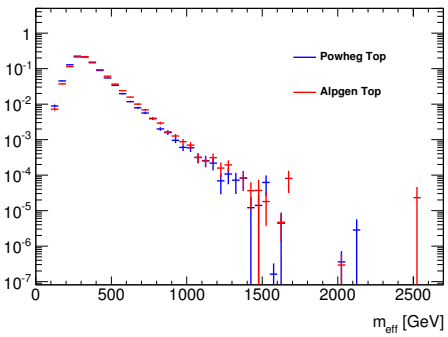

(g) Top Quarks samples in the $\tau+\mu$ channel.

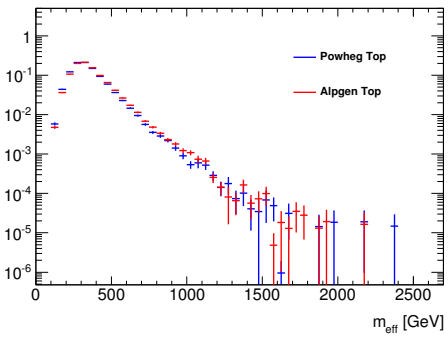

(h) Top Quarks samples in the $\tau+e$ channel.

Figure 5.12: Generator comparison for W+jets, Z+jets, Diboson and Top Quarks in the m_{eff} distribution after requiring $m_{\text{T}}^{\ell} > 100\,\text{GeV}$.

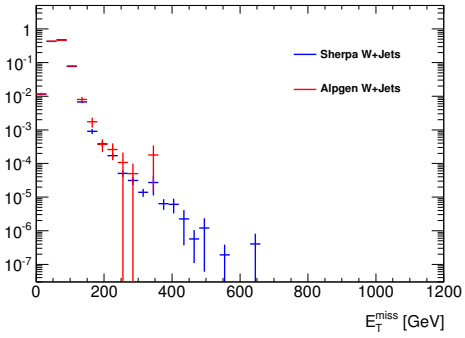

(a) W+jets samples in the $\tau+\mu$ channel.

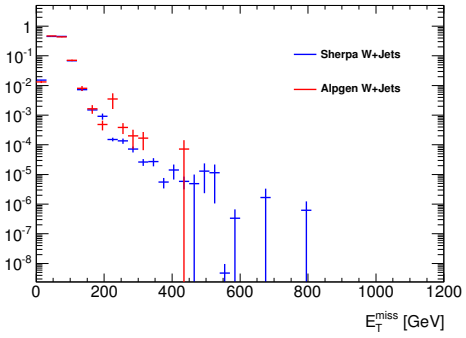

(b) W+jets samples in the $\tau+e$ channel.

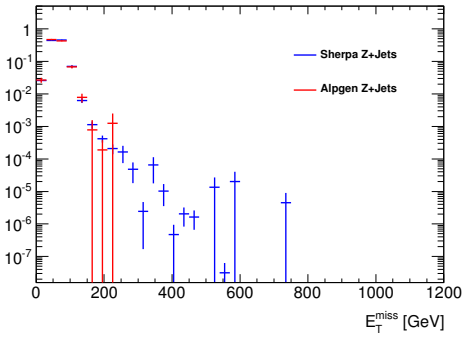

(c) Z+jets samples in the $\tau+\mu$ channel.

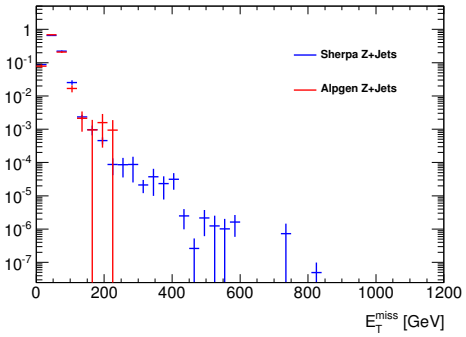

(d) Z+jets samples in the $\tau+e$ channel.

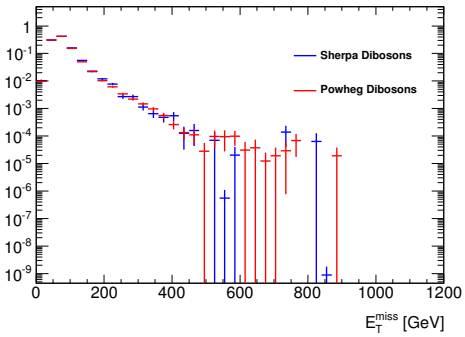

(e) Diboson samples in the $\tau+\mu$ channel.

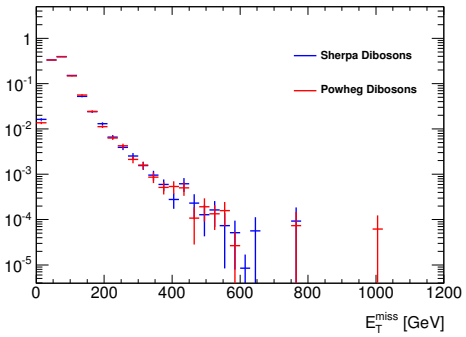

(f) Diboson samples in the $\tau+e$ channel.

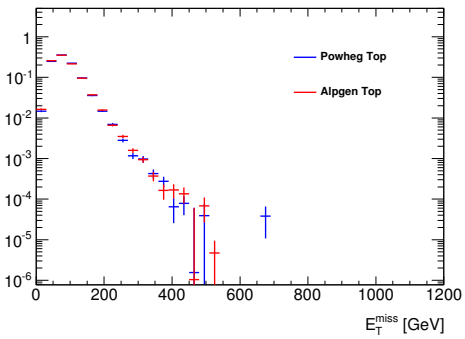

(g) Top Quarks samples in the $\tau+\mu$ channel.

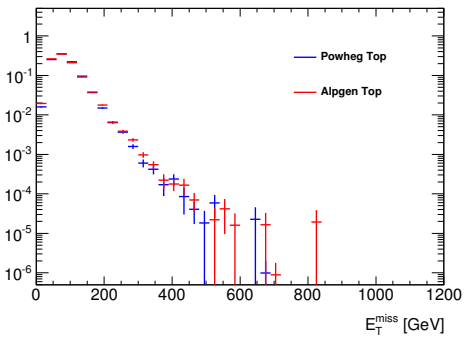

(h) Top Quarks samples in the $\tau+e$ channel.

Figure 5.13: Generator comparison for W+jets, Z+jets, Diboson and Top Quarks in the $E_{\mathrm{T}}^{\mathrm{miss}}$ distribution after requiring $m_{\mathrm{T}}^{\ell} > 100\,\mathrm{GeV}$.

Source of uncertainty	$\tau+e$ GMSB	$\tau+e$ nGM	$\tau+e$ bRPV	$\tau+e$ mSUG.	$\tau+\mu$ GMSB	$\tau+\mu$ nGM	$\tau+\mu$ bRPV	$\tau+\mu$ mSUG.
Generator uncertainties	47 %	46 %	7 %	28 %	3 %	25 %	26 %	32 %
Jet energy resolution	7 %	5 %	9 %	3 %	5 %	6 %	8 %	3 %
Jet energy scale	5 %	9 %	7 %	12 %	7 %	13 %	10 %	13 %
Tau energy scale	7 %	2 %	8 %	1 %	8 %	8 %	4 %	4 %
Pile-up reweighting	3 %	2 %	1 %	0 %	2 %	3 %	1 %	1 %
Total syst.	60 %	48 %	32 %	30 %	36 %	34 %	41 %	33 %

Table 5.2: Examples for some of the main systematic uncertainties and the total systematic uncertainty on the total background expectation for the eight different signal regions used in this analysis. The total systematic uncertainty includes the complete set of systematic uncertainties as listed in section B.4 in the appendix.

out due to the background scaling procedure. Other systematic uncertainties, such as the energy scale variations, have an influence on the shape of some relevant distributions. They therefore have a larger impact on the total systematic uncertainty.

Table 5.2 lists some of the main systematic uncertainties and the total systematic uncertainty on the total background expectation for all four signal regions and both channels. A detailed breakdown of all uncertainties can be found in tables B.24 to B.31 in the appendix.

In the $\tau+e$ channel total uncertainty varies between 30 % for the mSugra signal region and 60 % for the GMSB signal region. In the $\tau+\mu$ channel it varies between 33 % for the mSugra signal region and 41 % for the bRPV signal region. The biggest impact in all signal regions comes from the generator uncertainty.

5.2.4 Uncertainties on the Signal Prediction

For the predicted number of selected SUSY signal events the luminosity uncertainty of 2.8 % for 2012 data is taken into account as well as detector uncertainties and process cross-section uncertainties. The full detector uncertainties and the cross-section uncertainties for the various signal grids are displayed in figure 5.14 for the $\tau+\mu$ channel and in figure 5.14 for the $\tau+e$ channel.

5.3 Background Expectation in the Signal Regions

For the background estimation in the signal regions the Monte Carlo is scaled and corrected according to the observation in the control regions. The background expectations are validated by comparison to observed data in validation regions before comparing to signal region observations.

5.3.1 Final Estimate for the Multijet Background

Multijet events are estimated with an upper limit since the contributions are negligibly small and the statistics are too low to obtain an estimate provided directly by the matrix method in these kinematic regions. Figure 5.16 shows the m_{eff} and the $E_{\text{T}}^{\text{miss}}$ distributions for the total background from MC simulation overlaid with the expectation for Multijet events provided by the matrix method. A log-likelihood fit is used to extrapolate the shape of the distribution in the tails.

The Multijet background distribution declines either more steeply or comparable to the rest of the SM background. Therefore, a conservative approach can be used to estimate the contribution of Multijet events in the signal regions: From the ratio of Multijet events to total MC in a lower region of the distributions

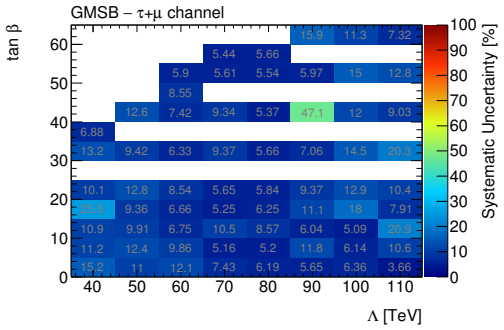

(a) Systematic uncertainty for GMSB.

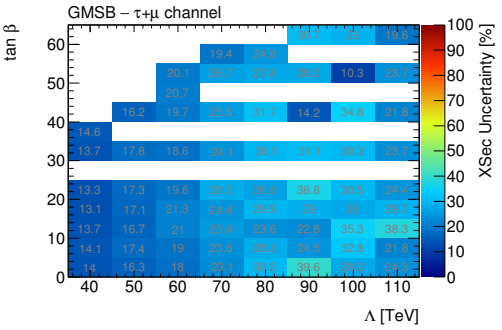

(b) Cross-section uncertainty for GMSB.

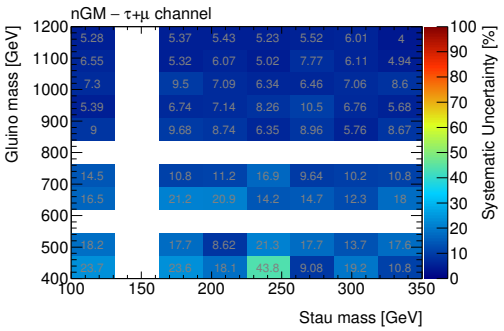

(c) Systematic uncertainty for nGM.

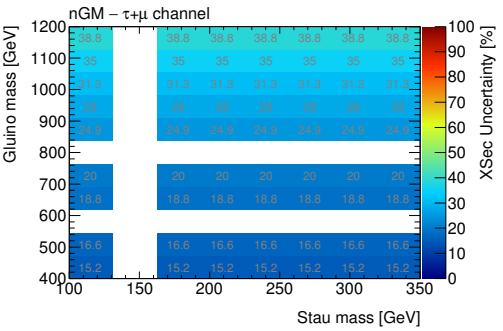

(d) Cross-section uncertainty for nGM.

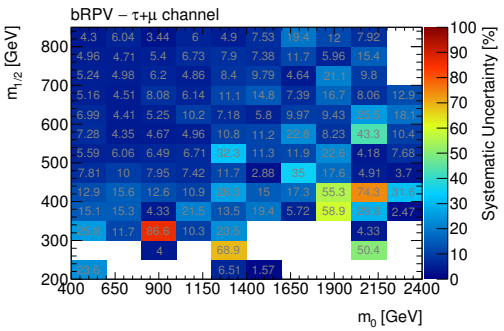

(e) Systematic uncertainty for bRPV.

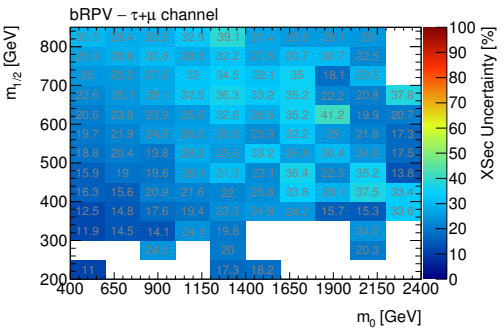

(f) Cross-section uncertainty for bRPV.

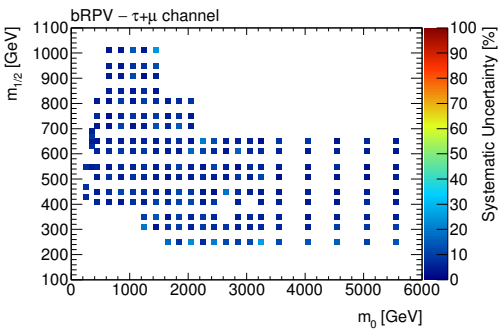

(g) Systematic uncertainty for mSUGRA.

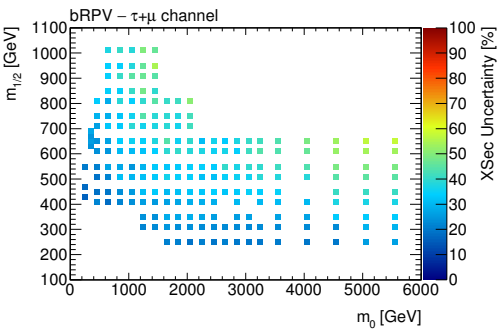

(h) Cross-section uncertainty for mSUGRA.

Figure 5.14: Systematic detector uncertainty and cross-section uncertainty for the signal grids in the $\tau+\mu$ channel.

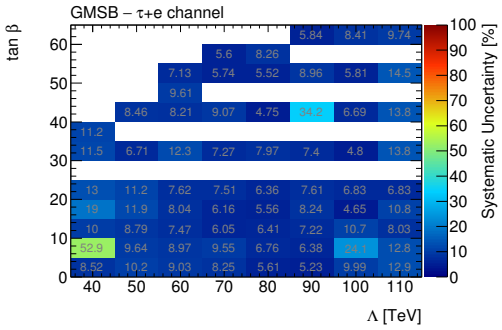

(a) Systematic uncertainty for GMSB.

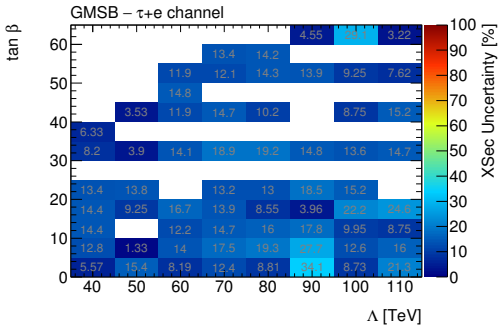

(b) Cross-section uncertainty for GMSB.

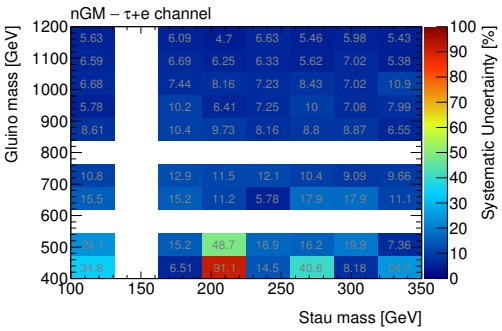

(c) Systematic uncertainty for nGM.

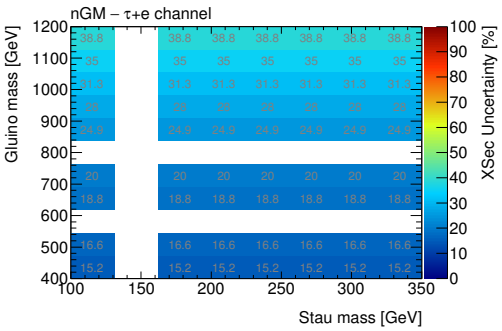

(d) Cross-section uncertainty for nGM.

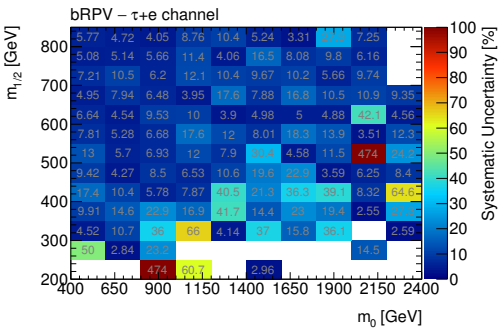

(e) Systematic uncertainty for bRPV.

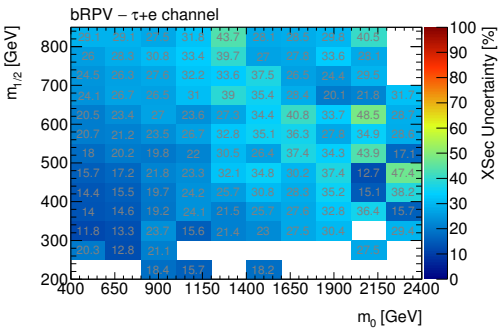

(f) Cross-section uncertainty for bRPV.

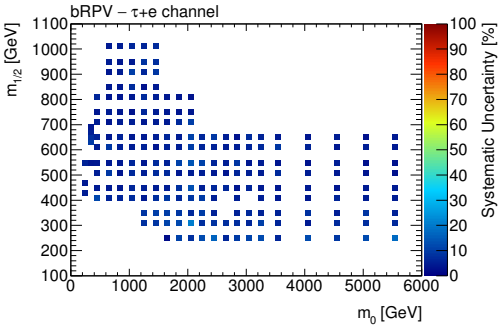

(g) Systematic uncertainty for mSUGRA.

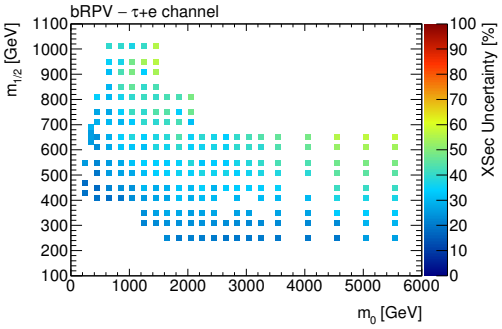

(h) Cross-section uncertainty for mSUGRA.

Figure 5.15: Systematic detector uncertainty and cross-section uncertainty for the various signal grids in the $\tau+e$ channel.

that has more statistics, a simple extrapolation to the signal region is performed. Under the assumption this ratio stays constant, an upper limit on the final Multijet estimate is derived by applying the ratio to the total number of MC events in the signal region. Since this method is not expected to provide an accurate result, the uncertainty on the number is set to 100 %.

The upper limits are found to be 0.01 – 0.04 events for the $\tau+\mu$ channel and 0.1 – 0.4 events for the $\tau+e$ channel. Their impact on the final results can be therefore considered to be almost negligible, when compared to the rest of the background as listed in tables 5.4 to 5.6. Nevertheless, the numbers are taken into account as a contribution to the final number of background events for the calculation of exclusion limits.

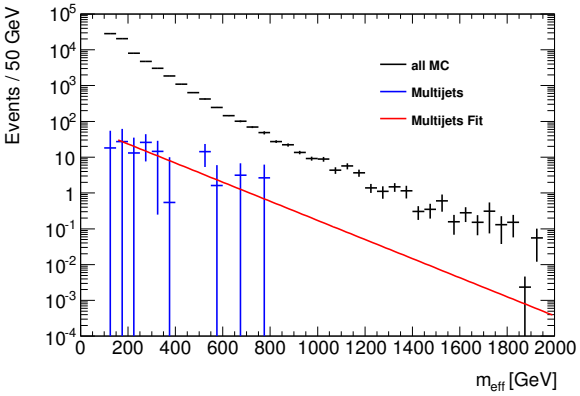

(a) m_{eff} in the $\tau+\mu$ channel.

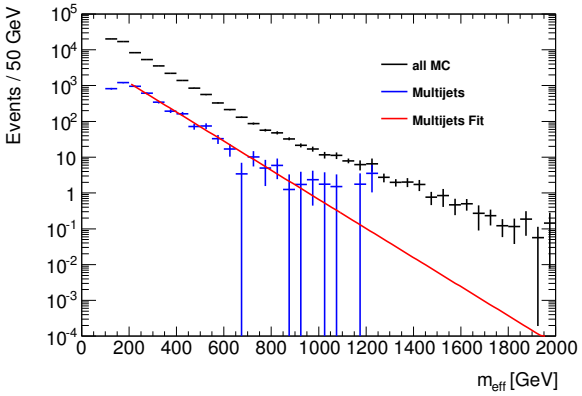

(b) m_{eff} in the $\tau+e$ channel.

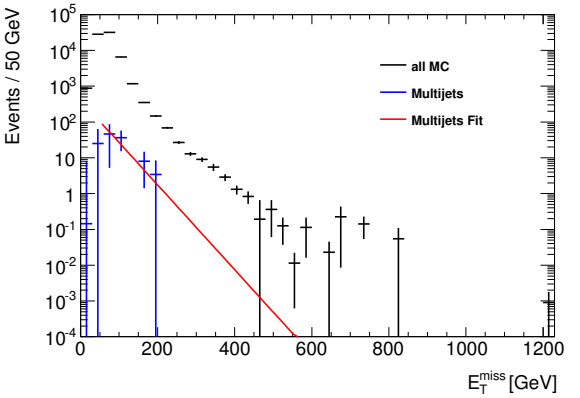

(c) $E_{\text{T}}^{\text{miss}}$ in the $\tau+\mu$ channel.

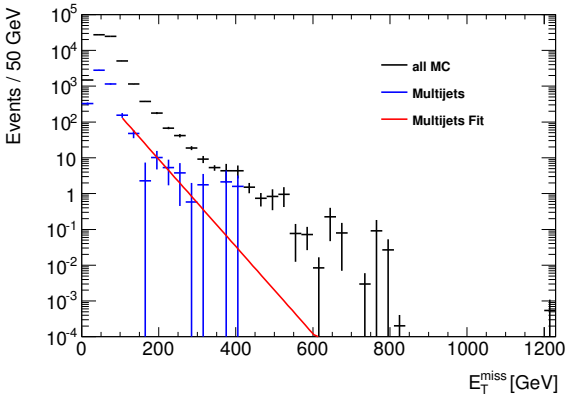

(d) $E_{\text{T}}^{\text{miss}}$ in the $\tau+e$ channel.

Figure 5.16: Shape comparison of the Multijet background and the rest of the SM background in m_{eff} and $E_{\text{T}}^{\text{miss}}$ after requiring $m_{\text{T}}^{\ell} > 100$ GeV. The Multijet background is extrapolated with a exponential log-likelihood fit in the tails of the distributions.

5.3.2 Final Estimate for the Total SM Background

The total number of background events events can be found in table 5.3 for the various signal regions. In this notation, the uncertainties are listed separately, where the first number gives statistical and the second number gives the systematic uncertainty.

The number of expected background events for one signal region is comparable among the $\tau+\mu$ and the $\tau+e$ channel. The expectations range from ~1 in the GMSB signal region to ~10 in the mSugra signal region.

Tables 5.4 to 5.6 list a detailed breakdown of event numbers for various selection-steps until the final signal region selection, split into W+jets, Z+jets, Top Quarks, Diboson and Multijet contributions. Furthermore, event predictions for one signal benchmark point for the relevant signal models are listed.

signal region	total background estimate in SR	
	$\tau+\mu$ channel	$\tau+e$ channel
GMSB	$0.98 \pm 0.31 \pm 0.35$	$1.34 \pm 0.33 \pm 0.80$
nGM	$3.6 \pm 0.9 \pm 1.2$	$4.3 \pm 0.9 \pm 2.0$
bRPV	$2.5 \pm 0.6 \pm 1.0$	$4.0 \pm 0.8 \pm 1.3$
mSugra	$9.9 \pm 1.5 \pm 3.3$	$10.0 \pm 1.4 \pm 3.0$

Table 5.3: Total background estimates for the four signal regions in $\tau+\mu$ and $\tau+e$ channel including statistical (first number) and systematic (second number) uncertainty.

Just as the total background estimates the individual background contributions are overall compatible for the two channels. Observed deviations can be explained with the different performance of object identification for muons and electrons. To check the impact of a higher fake rate in the electron identification the truth matched particles for muons, electrons and tau leptons are studied using the example of the GMSB signal region.

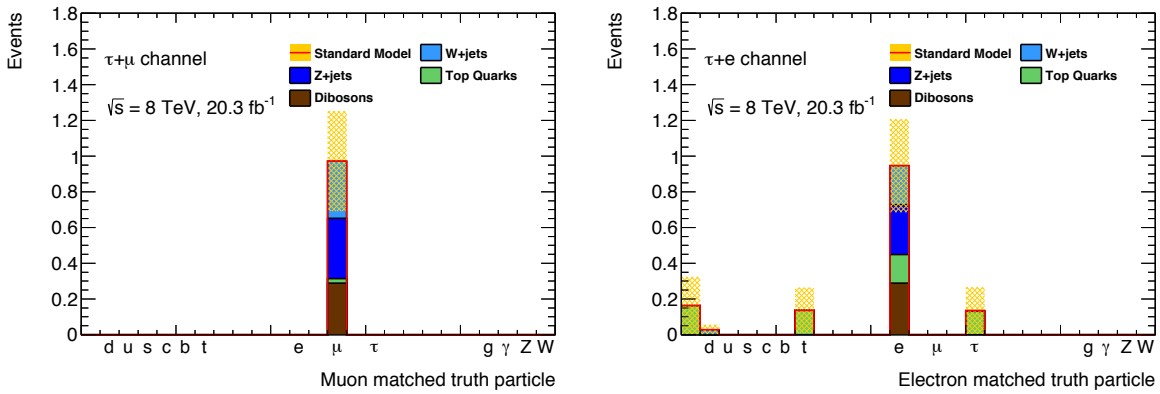

(a) Lepton truth content in the $\tau+\mu$ channel.

(b) Lepton truth content in the $\tau+e$ channel.

Figure 5.17: Light lepton truth content after requiring $m_{\mathrm{T}}^{\ell} > 100\,\mathrm{GeV}$ and $m_{\mathrm{eff}} > 1700\,\mathrm{GeV}$.

Figure 5.17 shows the truth matched particles for the light leptons in this region. The truth matching is performed similar to the method used for tau leptons as described in section 4.3. The unlabeled first bin of the distributions contains particles that could not be matched to a truth object with this method.

For muons all reconstructed objects are matched to a truth muon object. Reconstructed electrons however, are faked by quark jets and tau leptons with a proportion of ~ 25 %. Compared to the expected fake rate for electrons this is a relatively large fraction. The kinematic regions used for electron performance measurements are however not comparable to the ones that are used as signal regions in this analysis.

Statistics are very limited in the signal regions and serve as one explanation for the differences in the event yields. This becomes apparent when comparing the background contributions for the truth matched leptons only. Nonetheless, the electron fake contributions can explain the big difference that is observed for the Top Quarks background.

The truth particles matched to the tau objects are displayed in figure 5.18. Also here the statistical significance of the distribution should be treated with care. A tendency of more faked tau leptons due to electrons is expected and can be observed in the distribution. Additionally, fake tau leptons from quark jets contribute in both channels.

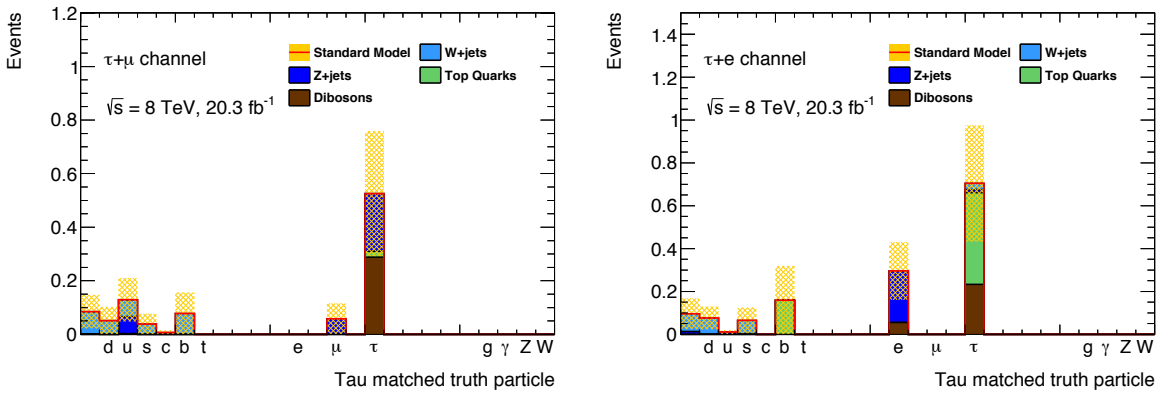

(a) Tau truth content in the $\tau+\mu$ channel.

(b) Tau truth content in the $\tau+e$ channel.

Figure 5.18: Tau truth content after requiring $m_{\mathrm{T}}^{\ell} > 100$ GeV and $m_{\mathrm{eff}} > 1700$ GeV.

Some divergence between the two channels might originate from the trigger and identification efficiencies for muons and electrons. All discrepancies are covered by the systematic uncertainty on the final background estimate.

$\tau+\mu$ channel	GMSB 60/30	Diboson	Multijet	Top Quarks	W+jets	Z+jets
object selection	65 ± 2	3472 ± 16	124 371 ± 735	33 518 ± 106	581 254 ± 1361	212 231 ± 1033
$m_{\mathrm{T}}^{\ell} > 100\,\mathrm{GeV}$	34.5 ± 1.3	871 ± 8	110 ± 62	7549 ± 48	56 034 ± 389	4801 ± 110
$m_{\mathrm{eff}} > 600\,\mathrm{GeV}$	17.9 ± 1.0	27.7 ± 1.4	2.45 ± 5.09	272 ± 8	133 ± 6	30.5 ± 2.2
$m_{\mathrm{eff}} > 800\,\mathrm{GeV}$	13.7 ± 0.9	9.23 ± 0.80	—	52 ± 3	34.5 ± 2.5	8.06 ± 0.90
$m_{\mathrm{eff}} > 1000\,\mathrm{GeV}$	12.1 ± 0.9	3.78 ± 0.51	—	13.5 ± 1.7	11.0 ± 1.4	2.45 ± 0.49
$m_{\mathrm{eff}} > 1200\,\mathrm{GeV}$	10.1 ± 0.8	1.41 ± 0.30	—	3.21 ± 0.75	2.51 ± 0.43	0.95 ± 0.30
$m_{\mathrm{eff}} > 1400\,\mathrm{GeV}$	8.26 ± 0.69	0.54 ± 0.18	—	0.72 ± 0.31	1.05 ± 0.24	0.56 ± 0.25
$m_{\mathrm{eff}} > 1600\,\mathrm{GeV}$	6.16 ± 0.59	0.46 ± 0.16	—	0.06 ± 0.04	0.51 ± 0.17	0.38 ± 0.24
$m_{\mathrm{eff}} > 1700\,\mathrm{GeV}$	4.34 ± 0.48	0.29 ± 0.13	< 0.01	0.02 ± 0.02	0.32 ± 0.13	0.33 ± 0.24

$\tau+e$ channel	GMSB 60/30	Diboson	Multijet	Top Quarks	W+jets	Z+jets
object selection	97 ± 2	3933 ± 17	511 792 ± 1056	36 316 ± 107	513 118 ± 1207	295 939 ± 1235
$m_{\mathrm{T}}^{\ell} > 100\,\mathrm{GeV}$	57 ± 2	989 ± 8	4537 ± 110	7852 ± 46	43 062 ± 313	4098 ± 81
$m_{\mathrm{eff}} > 600\,\mathrm{GeV}$	30.2 ± 1.4	33.6 ± 1.5	55 ± 11	335 ± 9	161 ± 7	80 ± 3
$m_{\mathrm{eff}} > 800\,\mathrm{GeV}$	22.7 ± 1.3	13.5 ± 1.0	19.7 ± 6.4	78 ± 4	41.2 ± 3.3	22.6 ± 1.7
$m_{\mathrm{eff}} > 1000\,\mathrm{GeV}$	20.0 ± 1.2	5.54 ± 0.63	8.47 ± 4.10	21.2 ± 2.3	14.6 ± 1.5	6.31 ± 0.63
$m_{\mathrm{eff}} > 1200\,\mathrm{GeV}$	16.4 ± 1.1	2.00 ± 0.36	3.42 ± 2.52	5.98 ± 1.14	5.64 ± 0.87	2.15 ± 0.36
$m_{\mathrm{eff}} > 1400\,\mathrm{GeV}$	13.1 ± 0.9	0.83 ± 0.23	—	2.21 ± 0.64	2.21 ± 0.59	0.80 ± 0.19
$m_{\mathrm{eff}} > 1600\,\mathrm{GeV}$	9.72 ± 0.82	0.48 ± 0.17	—	0.75 ± 0.31	0.46 ± 0.16	0.42 ± 0.14
$m_{\mathrm{eff}} > 1700\,\mathrm{GeV}$	8.06 ± 0.75	0.29 ± 0.13	< 0.2	0.52 ± 0.26	0.25 ± 0.11	0.28 ± 0.12

Table 5.4: Cutflow table showing the individual background contributions and predicted number of events for one signal benchmark point for cuts up to the GMSB signal region in the $\tau+\mu$ channel (upper table) and $\tau+e$ channel (bottom table). The signal benchmark points are GMSB (Λ = 60 TeV, $\tan\beta$ = 30). The given uncertainties are from limited statistics in the according samples.

$\tau+\mu$ channel	nGM 940/210	mSUGRA 800/400	Diboson	Multijet	Top Quarks	W+jets	Z+jets
object selection	39.9 ± 1.2	41.6 ± 3.6	3472 ± 16	124 371 ± 735	33 518 ± 106	581 254 ± 1361	212 231 ± 1033
$m_{\mathrm{T}}^{\ell} > 100\,\mathrm{GeV}$	24.6 ± 0.9	32.3 ± 3.2	871 ± 8	110 ± 62	7549 ± 48	56 034 ± 389	4801 ± 110
$N_{\mathrm{jet}} \geq 3$	24.4 ± 0.9	30.8 ± 3.2	29.8 ± 1.4	31.6 ± 17.4	2532 ± 26	1010 ± 26	130 ± 9
$E_{\mathrm{T}}^{\mathrm{miss}} > 100\,\mathrm{GeV}$	22.7 ± 0.9	27.9 ± 3.0	15.7 ± 1.0	—	726 ± 14	86 ± 6	6.89 ± 1.66
$E_{\mathrm{T}}^{\mathrm{miss}} > 200\,\mathrm{GeV}$	15.2 ± 0.7	13.6 ± 2.0	3.90 ± 0.53	—	61 ± 4	5.16 ± 0.80	0.46 ± 0.16
$E_{\mathrm{T}}^{\mathrm{miss}} > 300\,\mathrm{GeV}$	7.72 ± 0.53	13.6 ± 2.0	0.72 ± 0.21	< 0.08	8.36 ± 1.40	0.75 ± 0.20	0.07 ± 0.03
$E_{\mathrm{T}}^{\mathrm{miss}} > 350\,\mathrm{GeV}$	5.24 ± 0.43	10.5 ± 1.7	0.32 ± 0.14	< 0.04	2.80 ± 0.83	0.39 ± 0.15	0.06 ± 0.03

$\tau+e$ channel	nGM 940/210	mSUGRA 800/400	Diboson	Multijet	Top Quarks	W+jets	Z+jets
object selection	54 ± 1	46.8 ± 3.6	3933 ± 17	511 792 ± 1056	36 316 ± 107	513 118 ± 1207	295 939 ± 1235
$m_{\mathrm{T}}^{\ell} > 100\,\mathrm{GeV}$	34.1 ± 1.1	35.1 ± 3.1	989 ± 8	4537 ± 110	7852 ± 46	43 062 ± 313	4098 ± 81
$N_{\mathrm{jet}} \geq 3$	33.8 ± 1.1	32.8 ± 3.0	38.7 ± 1.7	377 ± 32	2702 ± 26	895 ± 23	293 ± 9
$E_{\mathrm{T}}^{\mathrm{miss}} > 100\,\mathrm{GeV}$	30.9 ± 1.1	30.0 ± 2.8	18.5 ± 1.1	29.3 ± 10.5	780 ± 14	80 ± 6	8.69 ± 1.86
$E_{\mathrm{T}}^{\mathrm{miss}} > 200\,\mathrm{GeV}$	10.3 ± 0.6	14.1 ± 1.9	4.17 ± 0.52	4.49 ± 3.60	61 ± 4	4.48 ± 0.62	0.65 ± 0.20
$E_{\mathrm{T}}^{\mathrm{miss}} > 300\,\mathrm{GeV}$	10.3 ± 0.6	14.1 ± 1.9	1.47 ± 0.30	< 0.04	7.43 ± 1.31	0.96 ± 0.22	0.15 ± 0.07
$E_{\mathrm{T}}^{\mathrm{miss}} > 350\,\mathrm{GeV}$	6.37 ± 0.48	10.8 ± 1.6	0.73 ± 0.21	< 0.1	2.98 ± 0.82	0.45 ± 0.14	0.11 ± 0.06

Table 5.5: Cutflow table showing the individual background contributions and predicted number of events for two signal benchmark points for cuts up to the nGM and the mSUGRA signal regions in the $\tau+\mu$ channel (upper table) and $\tau+e$ channel (bottom table). The signal benchmark points are nGM ($m_{\tilde{g}}$ = 940 GeV, $m_{\tilde{\tau}}$ = 210 GeV) and mSUGRA (m_0 = 800 GeV, $m_{1/2}$ = 400 GeV). The background is dominated by Top Quarks events. The given uncertainties are from limited statistics in the according samples.

$\tau+\mu$ channel	bRPV 600/600	Diboson	Multijet	Top Quarks	W+jets	Z+jets
object selection	25.8 ± 1.1	3472 ± 16	124 371 ± 735	33 518 ± 106	581 254 ± 1361	212 231 ± 1033
$m_{\mathrm{T}}^{\ell} > 100\,\mathrm{GeV}$	16.2 ± 0.9	871 ± 8	110 ± 62	7549 ± 48	56 034 ± 389	4801 ± 110
$N_{\mathrm{jet}} \geq 4$	13.8 ± 0.8	8.04 ± 0.77	13.2 ± 10.4	923 ± 16	240 ± 13	34.9 ± 3.9
$m_{\mathrm{eff}} > 600\,\mathrm{GeV}$	11.5 ± 0.8	2.97 ± 0.48	2.43 ± 3.60	109 ± 5	25.5 ± 2.4	6.22 ± 0.75
$m_{\mathrm{eff}} > 800\,\mathrm{GeV}$	9.30 ± 0.72	1.45 ± 0.32	—	27.1 ± 2.3	8.89 ± 1.21	2.34 ± 0.45
$m_{\mathrm{eff}} > 1000\,\mathrm{GeV}$	7.74 ± 0.67	0.92 ± 0.26	—	8.49 ± 1.32	2.55 ± 0.56	0.62 ± 0.19
$m_{\mathrm{eff}} > 1200\,\mathrm{GeV}$	6.46 ± 0.61	0.32 ± 0.14	—	1.80 ± 0.54	0.99 ± 0.33	0.31 ± 0.13
$m_{\mathrm{eff}} > 1300\,\mathrm{GeV}$	5.55 ± 0.52	0.20 ± 0.11	< 0.04	1.22 ± 0.46	0.82 ± 0.32	0.29 ± 0.13

$\tau+e$ channel	bRPV 600/600	Diboson	Multijet	Top Quarks	W+jets	Z+jets
object selection	18.2 ± 1.0	3933 ± 17	511 792 ± 1056	36 316 ± 107	513 118 ± 1207	295 939 ± 1235
$m_{\mathrm{T}}^{\ell} > 100\,\mathrm{GeV}$	10.1 ± 0.7	989 ± 8	4537 ± 110	7852 ± 46	43 062 ± 313	4098 ± 81
$N_{\mathrm{jet}} \geq 4$	8.05 ± 0.69	10.2 ± 0.9	117 ± 18	985 ± 16	216 ± 11	81 ± 4
$m_{\mathrm{eff}} > 600\,\mathrm{GeV}$	6.84 ± 0.65	3.92 ± 0.56	8.01 ± 4.95	125 ± 5	32.3 ± 3.7	14.5 ± 1.2
$m_{\mathrm{eff}} > 800\,\mathrm{GeV}$	5.82 ± 0.62	1.65 ± 0.37	5.97 ± 3.62	34.6 ± 2.6	10.6 ± 1.8	5.06 ± 0.67
$m_{\mathrm{eff}} > 1000\,\mathrm{GeV}$	5.20 ± 0.58	0.85 ± 0.26	1.64 ± 1.78	10.4 ± 1.4	4.05 ± 0.81	1.64 ± 0.33
$m_{\mathrm{eff}} > 1200\,\mathrm{GeV}$	4.40 ± 0.50	0.36 ± 0.15	—	3.87 ± 0.94	2.20 ± 0.60	0.36 ± 0.12
$m_{\mathrm{eff}} > 1300\,\mathrm{GeV}$	4.03 ± 0.48	0.22 ± 0.12	< 0.3	1.99 ± 0.59	1.61 ± 0.54	0.20 ± 0.09

Table 5.6: Cutflow table showing the individual background contributions and predicted number of events for one signal benchmark point for cuts up to the bRPV signal region in the $\tau+\mu$ channel (upper table) and $\tau+e$ channel (bottom table). The signal benchmark points are bRPV (m_0 = 600 GeV, $m_{1/2}$ = 600 GeV). The given uncertainties are from limited statistics in the according samples.

5.3.3 Truth Content in Signal Monte Carlo

The distributions that were shown above for background simulation, can also be studied for signal Monte Carlo. Figure 5.19 shows the GMSB signal for the lepton's truth matched particle. The tau truth content is displayed in figure 5.20. Tau leptons are rarely faked in both channels. A significant difference is observed for the light lepton. While muon fakes are also rare, a large fraction of the reconstruted electrons are mimicked by tau leptons.

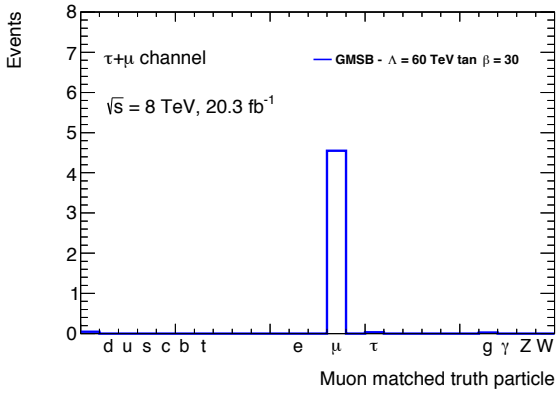

(a) Light lepton truth content in the $\tau+\mu$ channel.

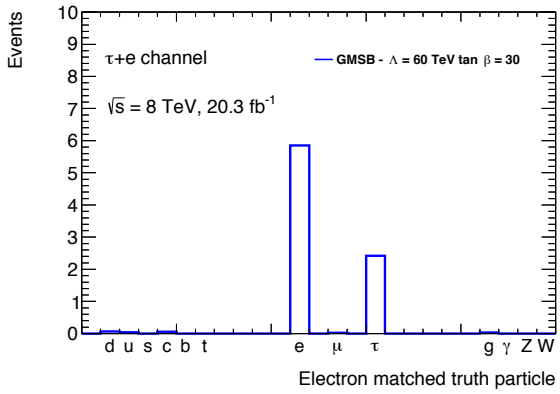

(b) Light lepton truth content in the $\tau+e$ channel.

Figure 5.19: Light lepton truth content after requiring $m_{\mathrm{T}}^{\ell} > 100\,\mathrm{GeV}$ and $m_{\mathrm{eff}} > 1700\,\mathrm{GeV}$.

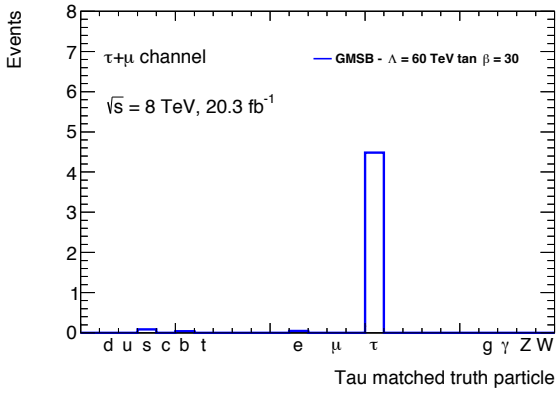

(a) Tau truth content in the $\tau+\mu$ channel.

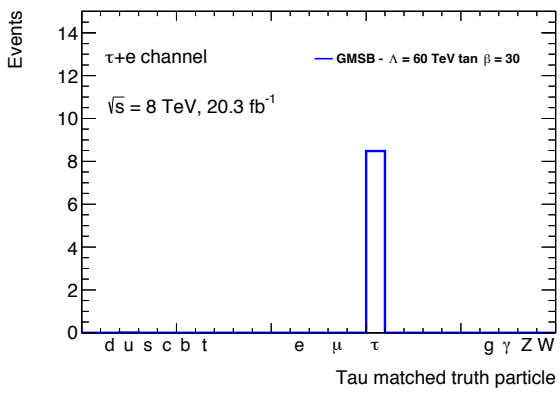

(b) Tau truth content in the $\tau+e$ channel.

Figure 5.20: Tau lepton truth content after requiring $m_{\mathrm{T}}^{\ell} > 100\,\mathrm{GeV}$ and $m_{\mathrm{eff}} > 1700\,\mathrm{GeV}$.

5.3.4 Validation of the SM Background

The correct modeling of the shapes of the final distributions determines the right expected number of events in the signal regions. The expected shapes from MC simulation should be therefore compared to data. To avoid bias however, a blind analysis is performed. This means all data events that are kinematically close to or in the signal regions should be only observed once the analysis is finite.

The MC expectation can be compared to data in validation regions (VR). These can be the lower parts of the final distributions which have an adequate distance to the signal region. Yet, this only gives access to a small part of the full distribution. To study the full spectrum of the m_{eff} and $E_{\text{T}}^{\text{miss}}$ distributions, the requirement on m_{T}^{ℓ} is inverted and five validation regions are defined as summarized in table 5.7.

Validation Region Selection					
observable	VR1	VR2	VR3	VR4	VR5
m_{T}^{ℓ}	< 100 GeV				
$N_{\text{b-jets}}$	≥ 0			≥ 1	
N_{jets}	≥ 0	≥ 3	≥ 4	≥ 0	≥ 4

Table 5.7: Summary of the kinematic requirements on the transverse mass, the number of jets, $E_{\text{T}}^{\text{miss}}$ and m_{eff} for the validation regions.

VR1 and VR2 relate to the GMSB and bRPV signal region respectively. VR3 is used to validate the distributions for nGM and mSugra signal regions. A comparison of data and MC in the $E_{\text{T}}^{\text{miss}}$ and m_{eff} distributions in these validation regions is displayed in figure 5.21. In all six distributions the shape is modeled very well over the full spectrum of the observable.

The N_{jet} distributions are observed in VR1 which does not use any requirement on the jet multiplicity. A good agreement between data and MC is observed as shown in figure 5.22.

VR4 and VR5 require at least one b-jet to select mostly Top Quarks events. These validation regions are used to study the impact of the correction of the Top Quarks background based on the p_{T} of the $t\bar{t}$ system as already mentioned in section 3.4.5. The according distributions are collected in figures A.13 to A.15 in the appendix.

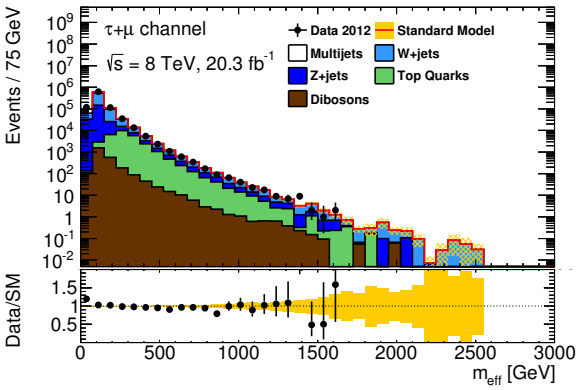

(a) VR1: m_{eff} in the $\tau+\mu$ channel.

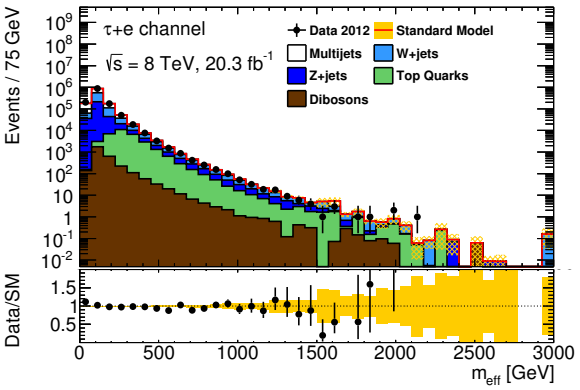

(b) VR1: m_{eff} in the $\tau+e$ channel.

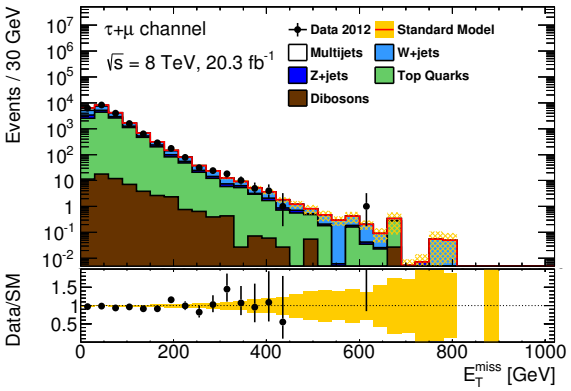

(c) VR2: $E_{\text{T}}^{\text{miss}}$ in the $\tau+\mu$ channel.

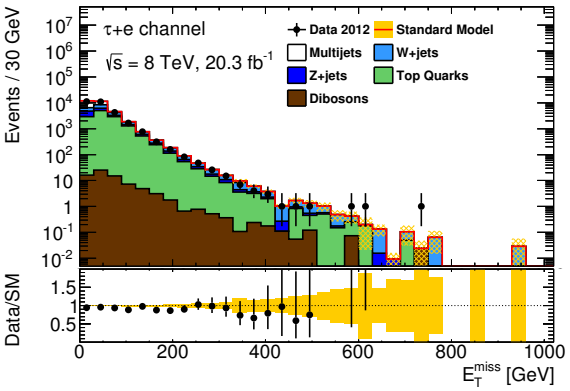

(d) VR2: $E_{\text{T}}^{\text{miss}}$ in the $\tau+e$ channel.

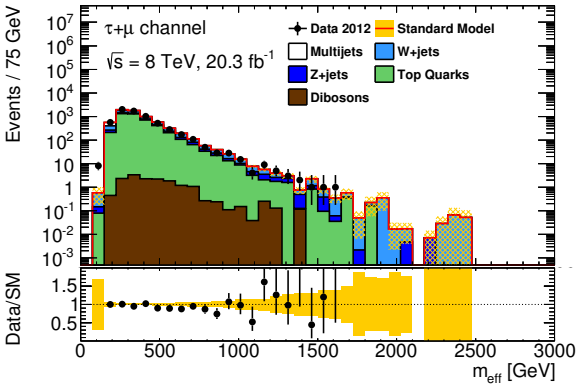

(e) VR3: m_{eff} in the $\tau+\mu$ channel.

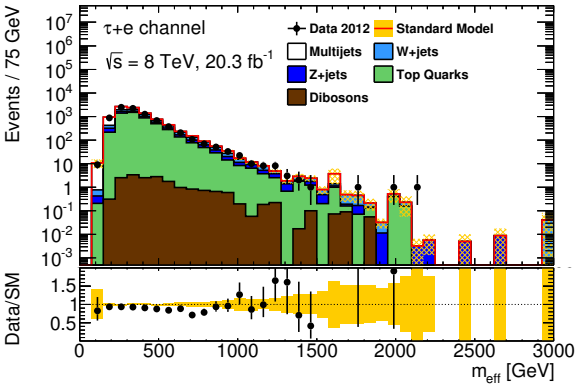

(f) VR3: m_{eff} in the $\tau+e$ channel.

Figure 5.21: Comparison of data and SM expectation for m_{eff} and $E_{\text{T}}^{\text{miss}}$ in the validation regions VR1, VR2 and VR3, accessing the tails of the distribution. The selection is orthogonal to the signal region by requiring $m_{\text{T}}^{\ell} < 100$ GeV.

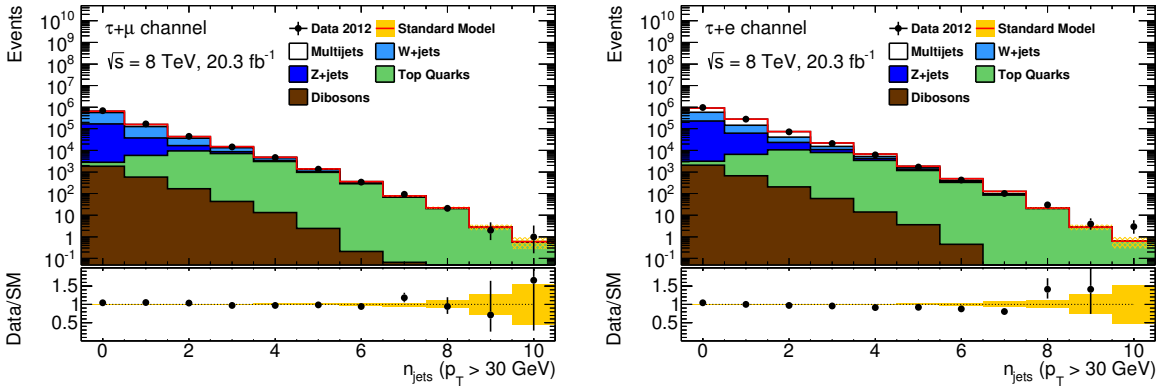

(a) in the $\tau+\mu$ channel.

(b) in the $\tau+e$ channel.

Figure 5.22: Comparison of data and SM expectation for the N_{jet} distribution in the validation region VR1. The selection is orthogonal to the signal region by requiring $m_{\text{T}}^{\ell} < 100\,\text{GeV}$.

5.4 Signal Grid Characteristics

5.4.1 GMSB model

In figure 5.23 details on various characteristics of the GMSB signal model are compiled. The number of signal events is displayed in figures 5.23a and 5.23b for the individual grid points. Figures 5.23c and 5.23d show the statistical uncertainty on these numbers.

The signal points with high event numbers accumulate in the low Λ region of the grid and fall off to higher energies as expected from the cross-sections. The statistical uncertainty rises towards high Λ points because the statistics are very low in this region. It ranges from 8 % to 50 %.

Comparing the event numbers, a significant difference between the $\tau+\mu$ and the $\tau+e$ channel is observed due to the electron fake contributions that were already observed in figure 5.19b.

This is also visible in the acceptance×efficiency distribution in figures 5.23e and 5.23f. The acceptance is defined as the fraction of events that contain all necessary objects that could pass the given event selection. The efficiency is defined as the proportion of events within the acceptance that are reconstructed such that they pass the selection. The product of both is the fraction of reconstructed events which pass the selection from all analyzed events.

The individual plots for acceptance and efficiency are collected in section **??**. The large amount of electron fakes leads to efficiencies larger than 100 %. For both channels the product of acceptance and efficiency has a maximum between $\Lambda = 60$ TeV and $\Lambda = 70$ TeV and for $\tan\beta > 15$ of ~ 0.4 % in the $\tau+\mu$ channel and ~ 0.6 % in the $\tau+e$ channel.

In figures 5.23g and 5.23h the signal contamination in the combined W+jets and Top Quarks control region is displayed. The fraction of signal events in this kinematic region is with < 0.1 % negligibly small.

5.4.2 nGM Model

The same distributions for the nGM model are displayed in figure 5.24. High event numbers accumulate in the region with low gluino masses, but independently of the stau mass as displayed in figures 5.24a and 5.24b. With increasing gluino mass the cross-section and therefore the number of events drops. The statistical uncertainties (figures 5.24c and 5.24d) range between 5 % and 76 %.

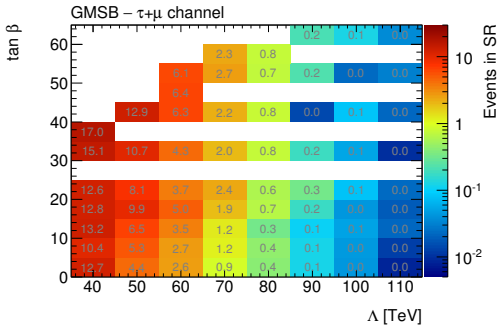

(a) Events in SR in the $\tau+\mu$ channel.

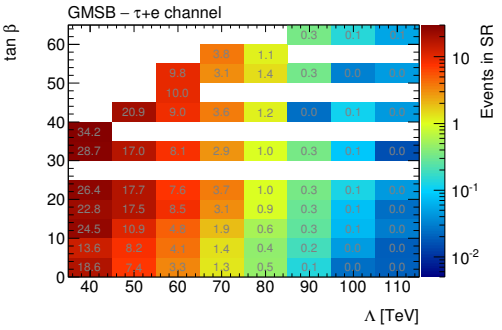

(b) Events in SR in the $\tau+e$ channel.

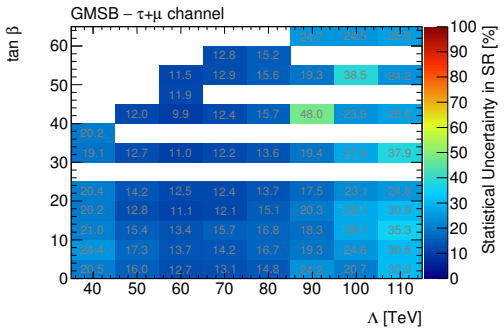

(c) Stat. uncertainty in SR in the $\tau+\mu$ channel.

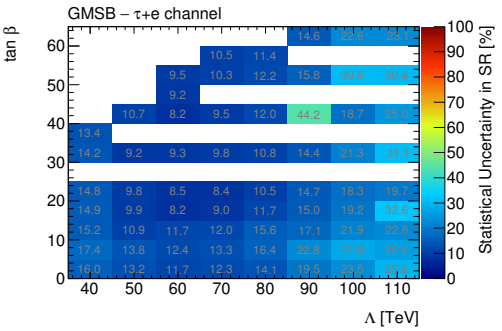

(d) Stat. uncertainty in SR in the $\tau+e$ channel.

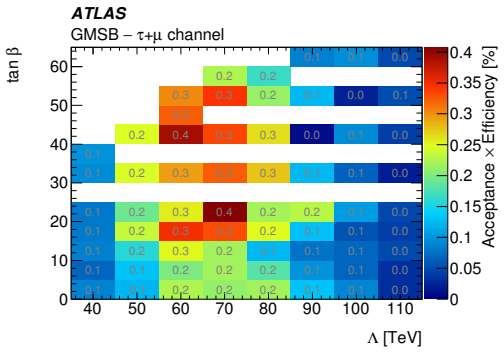

(e) Acceptance × efficiency in the $\tau+\mu$ channel [2].

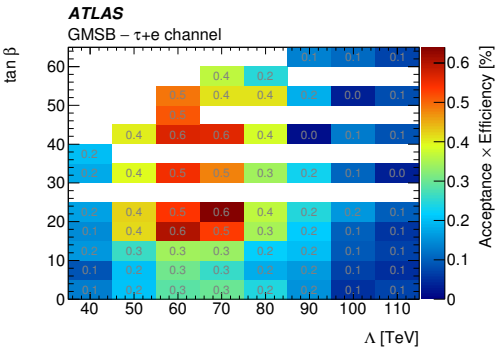

(f) Acceptance × efficiency in the $\tau+e$ channel [2].

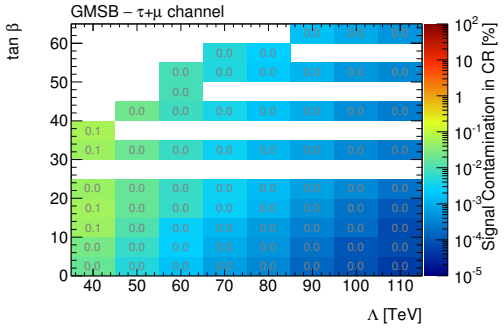

(g) Signal contamination in CR in the $\tau+\mu$ channel.

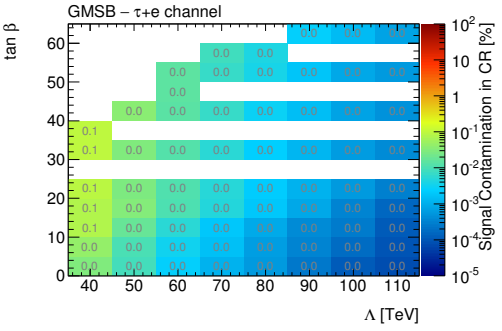

(h) Signal contamination in CR in the $\tau+e$ channel.

Figure 5.23: Details on the GMSB signal grid.

The product of acceptance and efficiency is shown in figures 5.24e and 5.24f and reaches a maximum for grid points with large gluino masses. Also in this model, the fake contribution for selected electrons leads to higher event numbers and efficiencies over 100 % in the $\tau+e$ channel.

The signal contamination of the control region is below 0.02 % for most of the grid points. For the two lowest gluino masses, the contamination (figures 5.24g and 5.24h) ranges between 1 % and 8 %.

5.4.3 bRPV Model

For the bRPV model the grid characteristics are displayed in figure 5.25. For low m_0 and low $m_{1/2}$ high event numbers are observed as displayed in figures 5.25a and 5.25b. The statistical uncertainty (figures 5.25d and 5.25c) reaches from 7 – 8 % in the low m_0 and high $m_{1/2}$ space to 100 % at low $m_{1/2}$.

The product of acceptance and efficiency is displayed in figures 5.25e and 5.25f. It has its maximum for low m_0 and high $m_{1/2}$. Signal contamination from bRPV events in the control region is negligibly small between 0.5 % and less than 0.1 % for the majority of grid points, as seen in figures 5.25g and 5.25h.

5.4.4 mSugra grid

Figure 5.26 displays the various signal grid plots for the mSugra model. Grid points with high numbers of events are found for low $m_{1/2}$ as shown in figures 5.26a and 5.26b. The statistical uncertainty is between 6 % and 100 % (figures 5.26c and 5.26d).

The product of acceptance and efficiency has a maximum for low m_0 and high $m_{1/2}$ as seen in figures 5.26e and 5.26f. Signal contamination in the control region is at most 0.03 % (figures 5.26g and 5.26h) and therefore negligibly small.

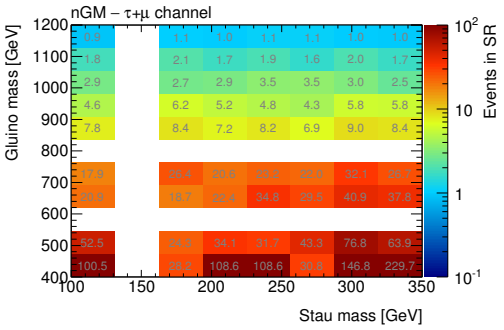

(a) Events in SR in the $\tau+\mu$ channel.

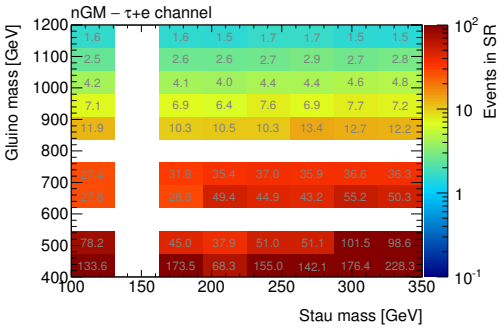

(b) Events in SR in the $\tau+e$ channel.

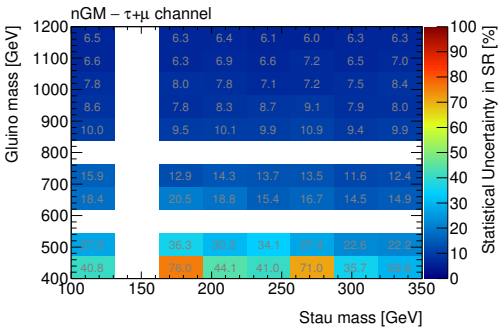

(c) Stat. uncertainty in the $\tau+\mu$ channel.

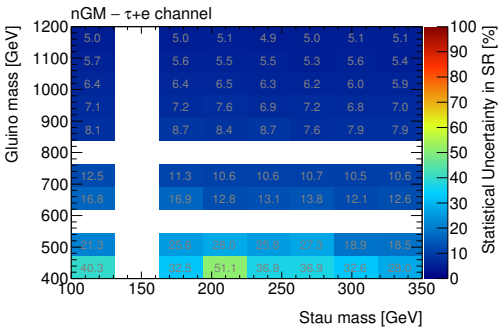

(d) Stat. uncertainty in the $\tau+e$ channel.

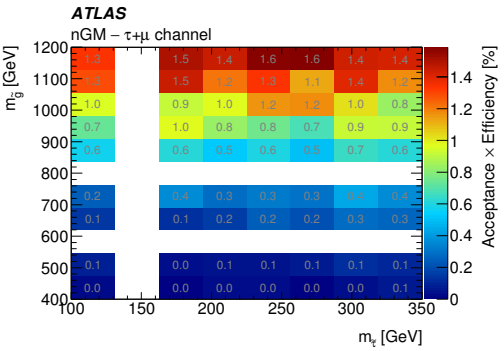

(e) Acceptance × efficiency in the $\tau+\mu$ channel [2].

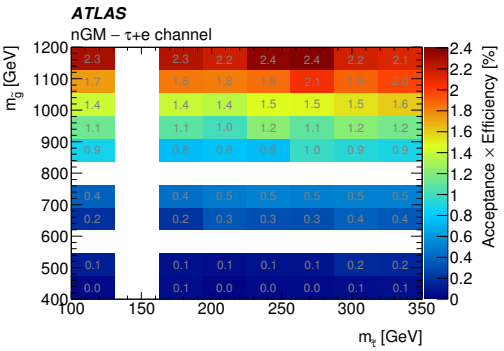

(f) Acceptance × efficiency in the $\tau+e$ channel [2].

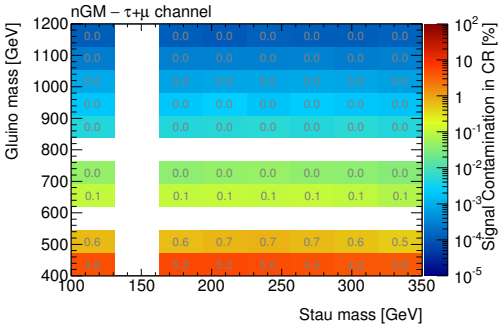

(g) Signal contamination in CR in the $\tau+\mu$ channel.

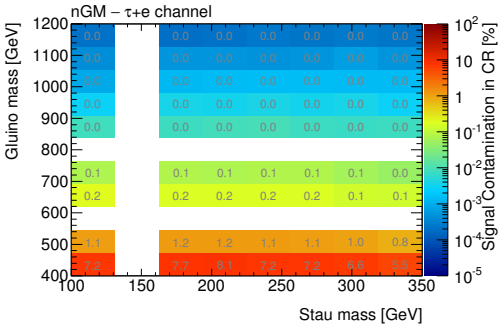

(h) Signal contamination in CR in the $\tau+e$ channel.

Figure 5.24: Details on the nGM signal grid.

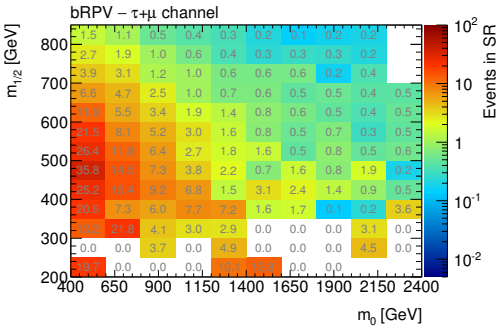

(a) Events in SR in the $\tau+\mu$ channel.

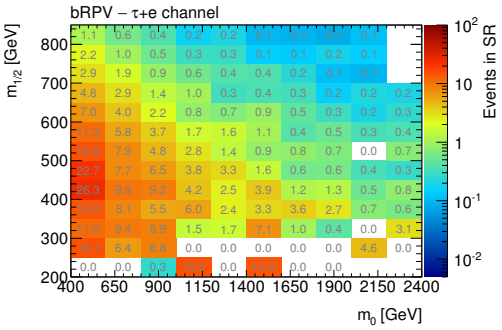

(b) Events in SR in the $\tau+e$ channel.

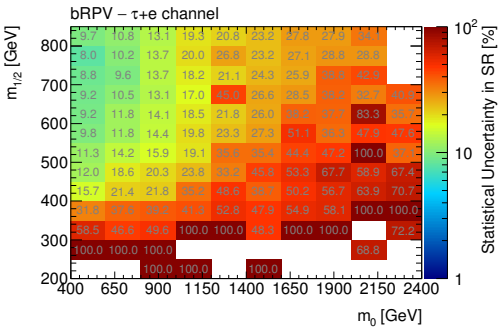

(c) Stat. uncertainty in the $\tau+e$ channel.

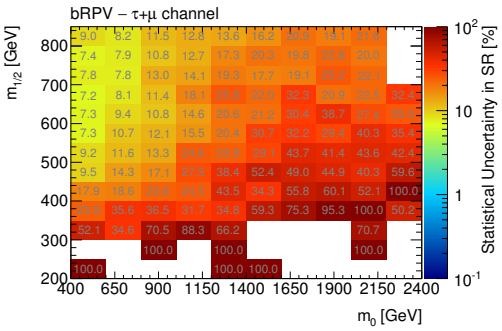

(d) Stat. uncertainty in the $\tau+\mu$ channel.

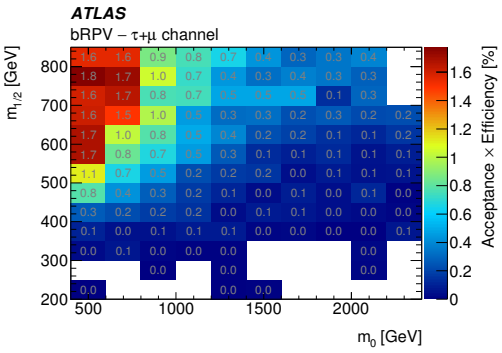

(e) Acceptance × efficiency in the $\tau+\mu$ channel [2].

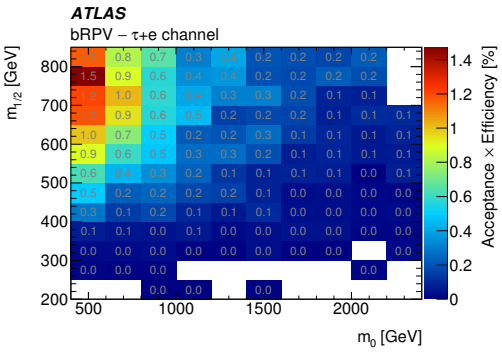

(f) Acceptance × efficiency in the $\tau+e$ channel [2].

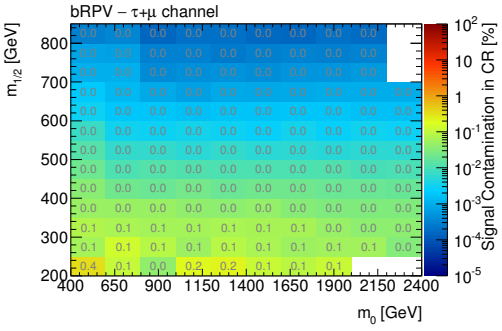

(g) Signal contamination in CR in the $\tau+\mu$ channel.

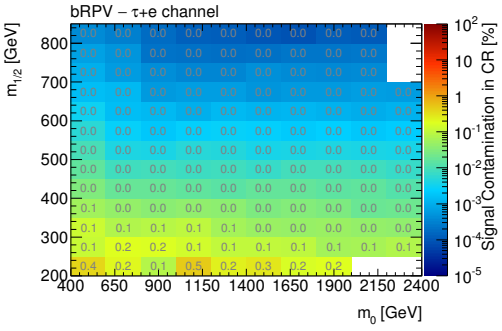

(h) Signal contamination in CR in the $\tau+e$ channel.

Figure 5.25: Details on the bRPV signal grid.

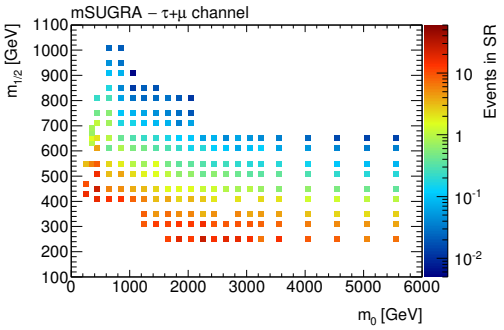

(a) Events in SR in the $\tau+\mu$ channel.

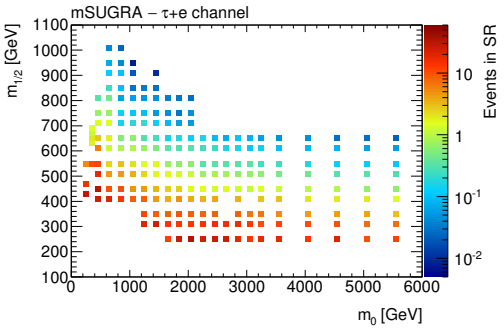

(b) Events in SR in the $\tau+e$ channel.

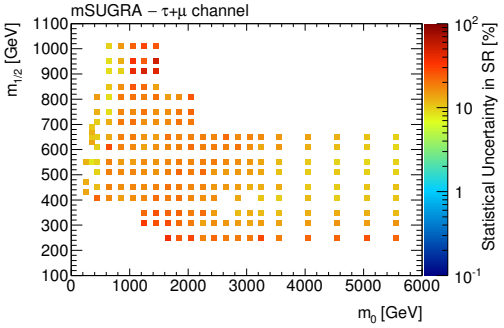

(c) Stat. uncertainty in the $\tau+\mu$ channel.

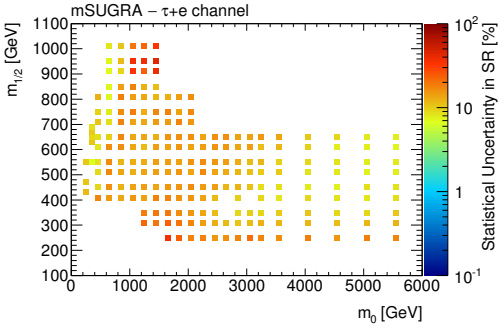

(d) Stat. uncertainty in the $\tau+e$ channel.

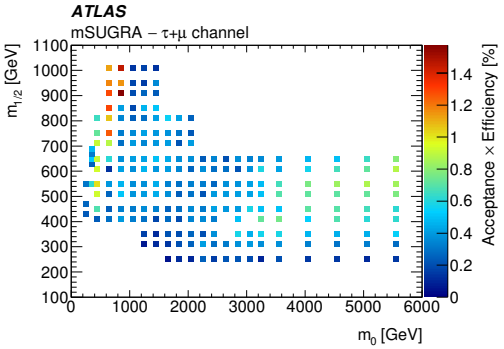

(e) Acceptance × efficiency in the $\tau+\mu$ channel [2].

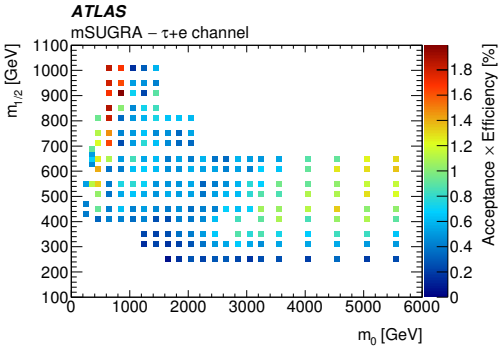

(f) Acceptance × efficiency in the $\tau+e$ channel [2].

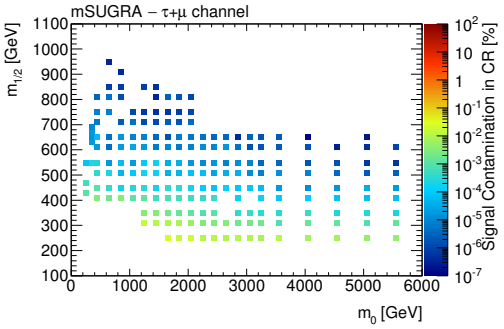

(g) Signal contamination in CR in the $\tau+\mu$ channel.

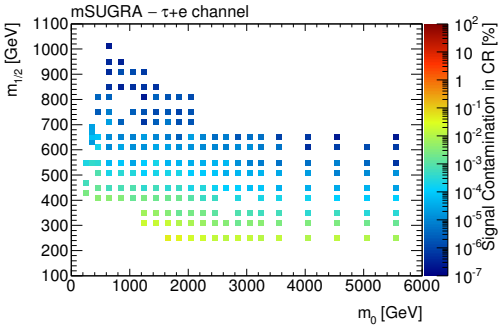

(h) Signal contamination in CR in the $\tau+e$ channel.

Figure 5.26: Details on the mSugra Signal Grid.

5.5 Observation in the Signal Regions

After careful validation of the background estimates and calculation of the full uncertainties for the signal regions, the theory expectation can be compared to observed events in 2012 data. A significant excess in data events can be interpreted as a sign for new physics. Good agreement with the Standard Model expectation can be used to set exclusion limits.

5.5.1 Comparison of Expected SM background and Data Observation

Table 5.8 shows a comparison of expected background events with statistical and systematic uncertainty.

signal region	exp. background	obs. events
$\tau+\mu$ GMSB	$0.98 \pm 0.31^{\text{stat}} \pm 0.35^{\text{syst}}$	2
$\tau+\mu$ nGM	$3.6 \pm 0.9^{\text{stat}} \pm 1.2^{\text{syst}}$	2
$\tau+\mu$ bRPV	$2.5 \pm 0.6^{\text{stat}} \pm 1.0^{\text{syst}}$	7
$\tau+\mu$ mSugra	$9.9 \pm 1.5^{\text{stat}} \pm 3.3^{\text{syst}}$	9
$\tau+e$ GMSB	$1.34 \pm 0.33^{\text{stat}} \pm 0.80^{\text{syst}}$	1
$\tau+e$ nGM	$4.3 \pm 0.9^{\text{stat}} \pm 2.0^{\text{syst}}$	8
$\tau+e$ bRPV	$4.0 \pm 0.8^{\text{stat}} \pm 1.3^{\text{syst}}$	3
$\tau+e$ mSugra	$10.0 \pm 1.4^{\text{stat}} \pm 3.0^{\text{syst}}$	14

Table 5.8: Breakdown of all signal regions with the numbers of expected and observed events.

In the nGM signal region of the $\tau+e$ channel and in the bRPV signal region of $\tau+\mu$ channel a mentionable overshoot of data events is observed. All other signal regions show reasonable agreement between prediction and observation considering the uncertainties. All observations are discussed in more detail below.

5.5.2 Final Distributions

Figure 5.27 displays the data-unblinded m_{eff} distribution after requiring $m_{\text{T}}^{\ell} > 100\,\text{GeV}$ for both channels which includes the GMSB signal region. Overlaid is the GMSB signal for $\Lambda = 60\,\text{GeV}$ and $\tan\beta = 30$. The yellow uncertainty band only includes the statistical uncertainty. Up to $m_{\text{eff}} = 1000\,\text{GeV}$ both distributions show reasonable agreement between data and MC. Above $m_{\text{eff}} = 1000\,\text{GeV}$ the data distribution in the $\tau+e$ channel is well-described by the MC prediction. In the $\tau+\mu$ channel single bins show large discrepancies in the same region. However, bins with a large overshoot in data are accompanied by empty data bins. The discrepancies can therefore merely be interpreted as statistical fluctuations. The integrated number of data events in the $\tau+\mu$ channel for $m_{\text{eff}} > 1200\,\text{GeV}$ is 22. The expected number of background events in that region is $17.5 \pm 1.7^{\text{stat}}$. Assuming an uncertainty of the same order as derived for the signal region, the agreement between observation and background expectation is acceptable.

The m_{eff} distributions after requiring $m_{\text{T}}^{\ell} > 100\,\text{GeV}$ and at least four jets per event include the bRPV signal regions. The according plots are displayed in figure 5.28. Overlaid is the signal for $m_0 = 600\,\text{GeV}$ and $m_{1/2} = 600\,\text{GeV}$.

Also in this case the same overshoot in data events is observed in the $\tau+\mu$ channel. Since the selection criteria only differ in the requirements on the jet multiplicity, an overlap between both signal regions is expected. In the region above $m_{\text{eff}} = 1200\,\text{GeV}$, $3.4 \pm 0.7^{\text{stat}}$ events are expected while 7 events are observed in data. The same seven events are observed in the $\tau+\mu$ bRPV signal region which requires

m_{eff} = 1300 GeV and therefore contains even less expected events from MC. However, since the analysis was performed data-blinded, the MC contributions in the region of 1200 – 1300 GeV are disregarded for the limit setting. The observed excess is noteworthy, but not significant enough to be regarded as anything more than a statistical fluctuation (compare section 5.6).

Figure 5.29 displays the $E_{\text{T}}^{\text{miss}}$ distributions after requiring at least three jets, which contains both the nGM and the mSugra signal regions. The distributions are depicted twice such that the overlaid signal for the nGM grid point at $m_{\tilde{g}}$ = 940 GeV and $m_{\tilde{\tau}}$ = 210 GeV and for the mSugra grid point at m_0 = 800 GeV and $m_{1/2}$ = 400 GeV are better distinguishable. For both the $\tau+\mu$ and $\tau+e$ channels the agreement between expected SM background and observed data is reasonable over the full spectrum of the distribution.

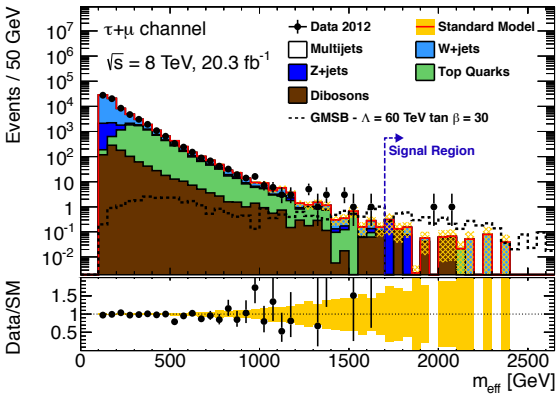

(a) m_{eff} distribution for the $\tau+\mu$ channel.

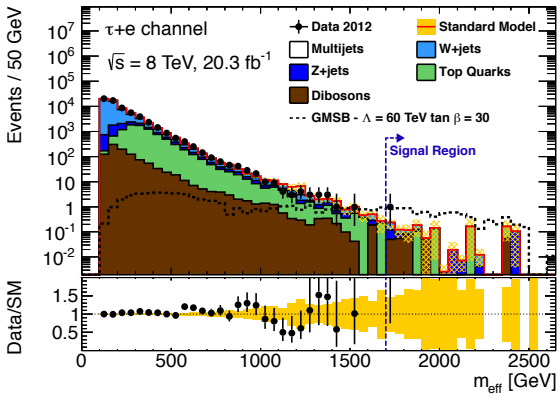

(b) m_{eff} distribution for the $\tau+e$ channel.

Figure 5.27: Final m_{eff} distributions after requiring $m_{\text{T}}^{\ell} > 100$ GeV for the GMSB model. The unblinded GMSB signal regions can be seen in the tail of the distributions for $m_{\text{eff}} > 1700$ GeV as indicated by the dahsed blue line.

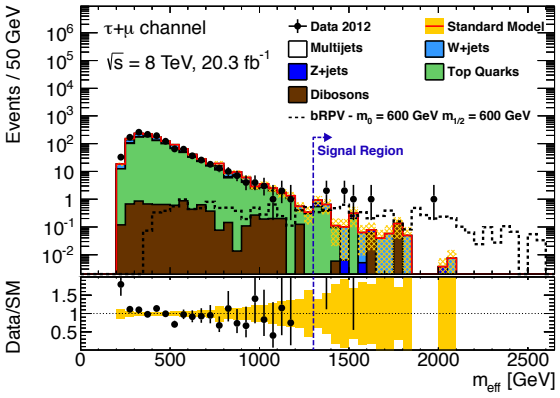

(a) m_{eff} distribution for the $\tau+\mu$ channel.

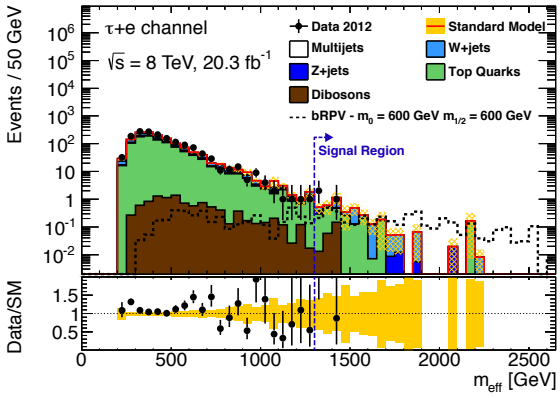

(b) m_{eff} distribution for the $\tau+e$ channel.

Figure 5.28: Final m_{eff} distributions after requiring $m_{\text{T}}^{\ell} > 100$ GeV and $N_{\text{jet}} \geq 4$ for the bRPV model. The unblinded bRPV signal regions can be seen in the tail of the distributions for $m_{\text{eff}} > 1300$ GeV as indicated by the dashed blue line.

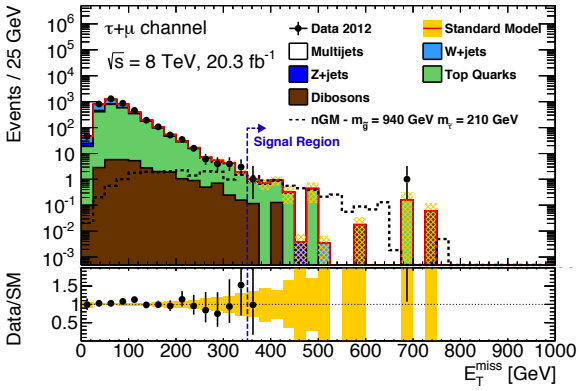

(a) $E_{\mathrm{T}}^{\mathrm{miss}}$ distribution for the $\tau+\mu$ channel.

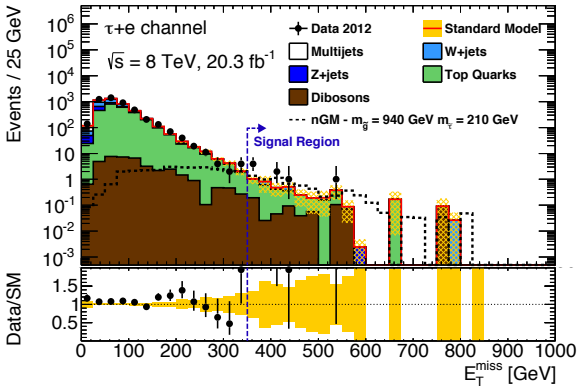

(b) $E_{\mathrm{T}}^{\mathrm{miss}}$ distribution for the $\tau+e$ channel.

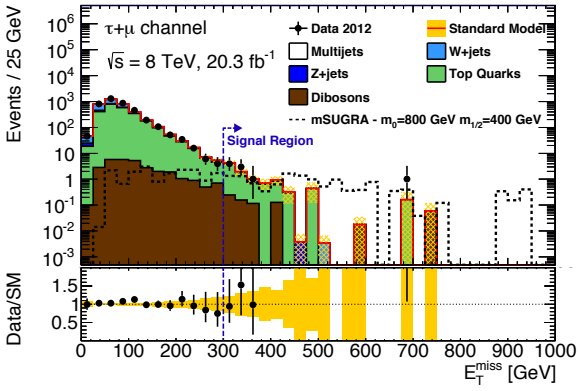

(c) $E_{\mathrm{T}}^{\mathrm{miss}}$ distribution for the $\tau+\mu$ channel.

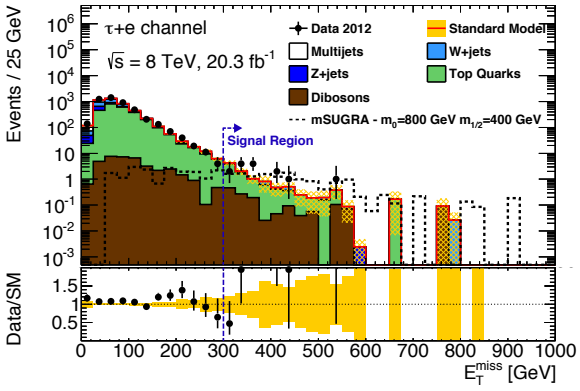

(d) $E_{\mathrm{T}}^{\mathrm{miss}}$ distribution for the $\tau+e$ channel.

Figure 5.29: Final $E_{\mathrm{T}}^{\mathrm{miss}}$ distributions for the nGM and the mSugra models after requiring $m_{\mathrm{T}}^{\ell} > 100$ GeV and $N_{\mathrm{jet}} \geq 3$. The unblinded signal regions are indicated by the dashed blue lines.

5.5.3 Event properties

Two graphical representations of exemplary signal region events are shown in figure 5.30. Displayed are cross-sections of the detector in the $R-\phi$-plane and in the $x-z$-plane with physics objects overlaid. Additionally, the physics objects are displayed in the $\eta-\phi$-plane with their transverse momentum.

An event from the $\tau+\mu$ channel can be seen in figure 5.30a. This event was recorded in run 213951 with the event number 83829742 and satisfies the requirements of the mSugra signal region. The direction of the 310 GeV of $E_{\mathrm{T}}^{\mathrm{miss}}$ is indicated by the red arrow. The two leading jets are displayed by the red (407 GeV) and the green cone (155 GeV).

The leading tau jet has a p_{T} of 90 GeV and is displayed by the light gray cone. The muon with $p_{\mathrm{T}} = 29$ GeV is indicated by the red bar. The orange, cyan and magenta cones represent three additional jets. The blue bar indicates a b-jet.

Figure 5.30a shows an event display for the $\tau+e$ channel. This event is part of the mSugra and the nGM signal regions. It was recorded in run 209269 with the event number 24045925. Also here the direction of the $E_{\mathrm{T}}^{\mathrm{miss}}$ (362 GeV) is illustrated by the red arrow. The leading jets have tranverse momenta of 318 GeV and 87 GeV and are represented by the red and the light gray cone. The tau lepton has a p_{T} of 24 GeV and is displayed by the magenta cone. The electron, indicated by the green bar, has a p_{T} of 121 GeV. The

orange, cyan and yellow cones represent three additional jets. Breakdowns of the event properties, listing the transverse momenta of the leptons and the leading jets, $E_{\mathrm{T}}^{\mathrm{miss}}$, m_{eff} and the product of the charges of tau and light lepton can be found in tables 5.9 and 5.10.

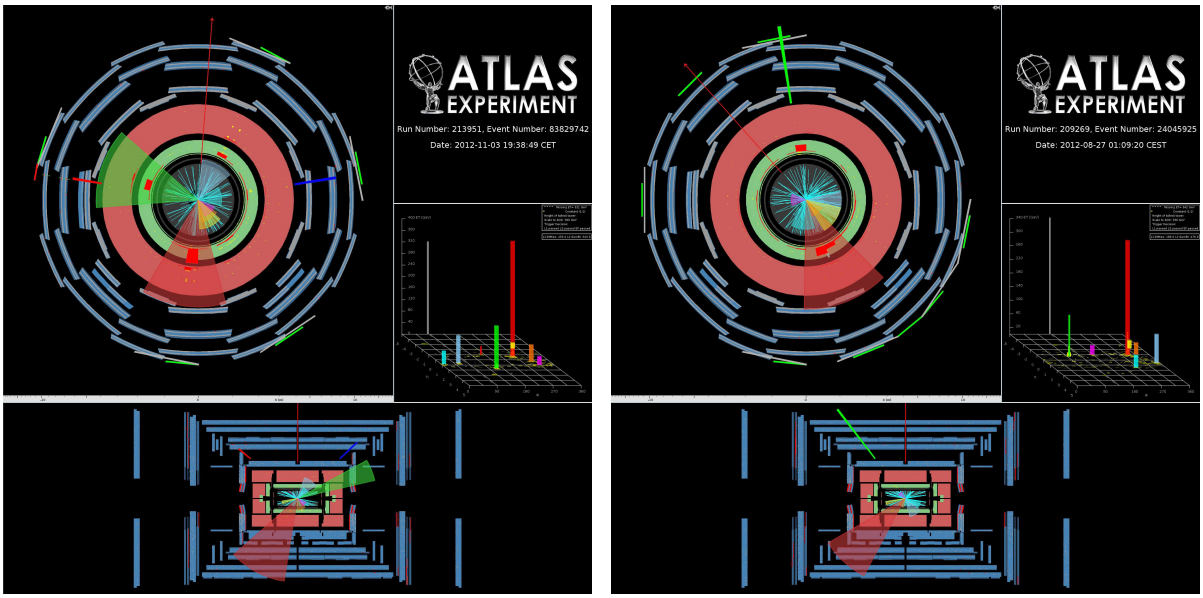

(a) $\tau+\mu$ channel: event 83829742 from run 213951.

(b) $\tau+e$ channel: event 24045925 from run 209269.

Figure 5.30: Two exemplary event displays from chosen signal region events in both channels. The ATLAS detector is displayed in two cross-sectional illustrations in the $R-\phi$ and $x-z$ planes. The Inner Detector in dark grey is surrounded by the two calorimeters represented in green and red. The muon chambers are displayed in blue and grey.

Run	Event	Signal Region	$p_{\mathrm{T}}^{\mathrm{jet1}}$ [GeV]	$p_{\mathrm{T}}^{\mathrm{jet2}}$ [GeV]	p_{T}^{τ} [GeV]	$p_{\mathrm{T}}^{\mathrm{lep}}$ [GeV]	$m_{\mathrm{T}}^{\mathrm{lep}}$ [GeV]	$E_{\mathrm{T}}^{\mathrm{miss}}$ [GeV]	m_{eff} [GeV]	$q^{\mu} \cdot q^{\tau}$
201289	3300658	GMSB	954	613	27	372	124	122	2087	1
215464	216667831	GMSB/bRPV	949	832	27	41	111	128	1977	-1
207447	163926187	bRPV	722	338	23	399	111	13	1494	1
210308	271548868	bRPV	714	245	89	67	109	173	1364	-1
209995	49619930	bRPV	448	256	27	567	124	99	1398	1
212172	172908508	bRPV	793	683	29	105	127	39	1649	-1
213539	320463566	bRPV	693	630	25	103	119	35	1485	1
203336	58164158	bRPV/mSug/nGM	641	121	28	57	308	688	1535	-1
207046	57612181	mSug/nGM	219	136	23	42	130	352	773	-1
203739	33194340	mSug	321	220	21	33	199	300	894	1
204668	70953452	mSug	177	68	29	123	387	325	723	-1
212172	114636438	mSug	462	267	34	58	254	310	1130	-1
212144	190315273	mSug	161	118	22	59	102	325	686	-1
214758	141441810	mSug	319	57	27	68	204	302	773	1
213951	83829742	mSug	407	154	90	29	130	310	990	-1
215433	41374888	mSug	439	149	62	30	197	337	1018	-1

Table 5.9: Event properties for the signal region events in the $\tau+\mu$ analysis.

Run	Event	Signal Region	$p_{\mathrm{T}}^{\mathrm{jet1}}$ [GeV]	$p_{\mathrm{T}}^{\mathrm{jet2}}$ [GeV]	p_{T}^{τ} [GeV]	$p_{\mathrm{T}}^{\mathrm{lep}}$ [GeV]	$m_{\mathrm{T}}^{\mathrm{lep}}$ [GeV]	$E_{\mathrm{T}}^{\mathrm{miss}}$ [GeV]	m_{eff} [GeV]	$q^{e} \cdot q^{\tau}$
203876	178440178	GMSB	760	520	47	297	102	83	1707	-1
213702	77177364	bRPV	723	207	29	303	249	57	1320	1
214651	32875104	bRPV	674	546	72	42	107	76	1412	1
201556	69096769	mSug/nGM	301	116	20	89	341	367	892	1
204910	76173552	mSug/nGM	606	81	37	162	280	424	1310	-1
206409	33967346	mSug/nGM	378	172	41	59	285	359	1009	-1
207221	75207305	mSug/nGM	209	102	22	194	507	361	889	-1
207397	10625286	mSug/nGM	247	177	63	65	269	432	984	-1
208126	14078728	mSug/nGM	262	232	25	28	240	542	1089	-1
209269	24045925	mSug/nGM	318	87	24	121	114	362	910	1
214523	41728226	mSug/nGM	368	76	21	108	418	407	980	1
207044	33093025	mSug	328	46	125	128	407	333	960	-1
207982	62842451	mSug	170	71	29	186	484	336	793	-1
207934	89656078	mSug	135	130	34	31	197	323	653	-1
212172	92733315	mSug	393	175	68	141	300	325	1102	-1
212144	183067656	mSug	202	93	82	107	378	335	819	-1
213486	60952244	mSug	311	202	34	136	126	339	1021	1

Table 5.10: Event properties for the signal region events in the $\tau+e$ analysis.

5.6 Interpretation of the Results

Meaningful conclusions about the observations made in the signal regions are drawn by a statistical interpretation of the results. Since no significant excess in data events over the expected Standard Model background is observed, this is done in the form of exclusion limits for the regarded signal models or in a model independent limit.

In the first part of this section the statistical methods as they are used by the ATLAS and the CMS collaborations are summarized. A more detailed description of the procedures can be found in [213]. After this, the final results are presented in form of exclusion limits in the parameter spaces of the four signal models and as model-independent limits.

5.6.1 Methods of Statistics

The occurrence of physical processes of statistic nature can be described by *probability density functions* (PDFs) based upon the according theoretical model. Consider a general random variable x in dependence of an additional parameter μ, described by the PDF $P(x, \mu)$. For observed data x^0 in an experiment the dependence is reduced to μ only and $\mathcal{L}(\mu) = P(x^0, \mu)$ is called the *likelihood function*.

For the limit setting procedure utilized in this thesis, a simple cut-and-count approach is chosen. In this approach only the total number of signal (S) and background (B) events, observed events (N) and their statistical and systematic uncertainties are used. The underlying statistics are described by a *Poisson* distribution

$$P(N, \lambda) = \frac{\lambda^N}{N!} e^{-\lambda}, \tag{5.8}$$

with $\lambda = B\left(\vec{\theta}\right) + \mu S\left(\vec{\theta}\right)$, assuming the presence of both signal and background. The number of signal events is scaled by a parameter μ which is the signal strength. The contributions of background and signal are modified to account for a number of M relative systematic uncertainties σ_k and enter the likelihood function in form of

$$B\left(\vec{\theta}\right) = B \prod_{k=1}^{M} \left(1 + \theta_k \sigma_k^B\right) \qquad \text{and} \qquad S\left(\vec{\theta}\right) = S \prod_{k=1}^{M} \left(1 + \theta_k \sigma_k^S\right), \tag{5.9}$$

The impact of the systematic uncertainties is parametrized by the nuisance parameters θ_k. An additional constraint for each systematic uncertainty is applied in form of Gaussian distributions $\frac{1}{\sqrt{2\pi}} e^{-\theta_k^2/2}$. Their product is multiplied with the Poisson distribution which provides the full considered likelihood function:

$$\mathcal{L}\left(\mu, \vec{\theta}\right) = \frac{1}{N!} \left(B\left(\vec{\theta}\right) + \mu S\left(\vec{\theta}\right)\right)^N e^{-\left(B\left(\vec{\theta}\right)\right) + \mu S\left(\vec{\theta}\right)} \times \prod_{k=0}^{M} \frac{1}{\sqrt{2\pi}} e^{-\theta_k^2/2}. \tag{5.10}$$

The hypothesis of a signal plus background scenario is then tested [214] by considering the logarithmic likelihood ratio which is defined as

$$q(\mu) = -2 \ln \left[\frac{\mathcal{L}\left(\mu, \vec{\theta}'\right)}{\mathcal{L}\left(\mu'', \vec{\theta}''\right)} \right]. \tag{5.11}$$

The nuisance parameters $\vec{\theta}''$ and the signal strength μ'' in the denominator of this ratio are both free and used to maximize the likelihood function with $0 \leq \mu'' \leq \mu$. The lower constraint is motivated by physics since the signal strength cannot be negative. The upper constraint ensures that an upward fluctuation

is not interpreted as evidence against the signal hypothesis. In the numerator of 5.11 $\vec{\theta}'$ maximizes the likelihood for a fixed signal strength μ.

In the next step toy Monte Carlo pseudo-data is generated to obtain the PDFs $f(q;\mu,\vec{\theta}'_\mu)$ for a signal-plus-background scenario and $f(q;0,\vec{\theta}'_0)$ for the background-only hypothesis. θ'_μ and θ'_0 are fixed values obtained from the parametrization. With these PDFs the p-values for signal+background and background-only hypotheses are defined as

$$p_\mu = \int_{q_\mu^{\text{obs}}}^{\infty} f\left(q;\mu,\vec{\theta}'_\mu\right) dq \qquad \text{and} \qquad 1-p_{\text{B}} = \int_{q_\mu^{\text{obs}}}^{\infty} f\left(q;\mu,\vec{\theta}'_0\right) dq \tag{5.12}$$

These probabilities are used to calculate the confidence level for the signal hypothesis which is defined as

$$\text{CL}_{\text{S}} = \frac{p_\mu}{1-p_{\text{B}}}. \tag{5.13}$$

For $\text{CL}_{\text{S}} \leq \alpha$ a hypothesis is excluded at $1-\alpha$ confidence level. The 95 % confidence level upper limit on μ is observed when $\text{CL}_{\text{S}} = 0.05$ is reached by varying μ.

The toy MC computation in the described procedure is very demanding in CPU time and in this form only used to calculate the model-independent limits. For the exclusion limits in the various signal model parameter spaces the Asimov approximation method [205] is used.

For the limit setting procedure the HistFitter [215] software package is used. It provides functionality for all necessary calculations and statistical methods.

5.6.2 Exclusion Limits for the Various Signal Models

GMSB The exclusion limits for the GMSB model are displayed in figure 5.31. The red line indicates the observed exclusion limit and the dashed, black line the expected limit. For the expected limit pseudo-data is used, where the observed values are set to the background expectation. The observed exclusion line in the $\tau+e$ channel is very close to the expected exclusion. In the $\tau+\mu$ channel the observed limit is weaker than expected since the number of expected background events is lower than the number of observed events. Nevertheless, the observed limit is in good agreement within the uncertainties of the expectation.

The blue contour shows the combined exclusion line of all hadronic and leptonic channels of an earlier 7 TeV analysis [1] for comparison. Both $\tau+\mu$ and $\tau+e$ channel individually outmatch the old combined limit. In the $\tau+e$ channel the exclusion reaches up to $\Lambda = 70$ TeV which corresponds to a gluino mass larger than 1500 GeV.

nGM The nGM model exclusion limits are displayed in figure 5.32. As expected from the distribution of the event numbers observed in this grid the limit has no strong dependence on the stau mass. In both channels the observed limits are within the uncertainty compatible with the expected limit which is at $m_{\tilde{g}} \approx 950$ GeV in both cases. In the $\tau+\mu$ channel the observed limit reaches up to $m_{\tilde{g}} \approx 1000$ GeV and in the $\tau+e$ channel up to $m_{\tilde{g}} \approx 900$ GeV.

bRPV For the bRPV model the exclusion limits are shown in figure 5.33. In both channels the expected limits reach up to $m_0 \approx 1000$ GeV in the parameter space at $m_{1/2} \approx 400$ GeV. Due to the overfluctuation in data, the observed limit in the $\tau+\mu$ analysis reaches the lower edge of the uncertainty band and is not completely covered by it in parts of the grid. For the $\tau+e$ analysis the observed limit is close to the expected exclusion contour line.

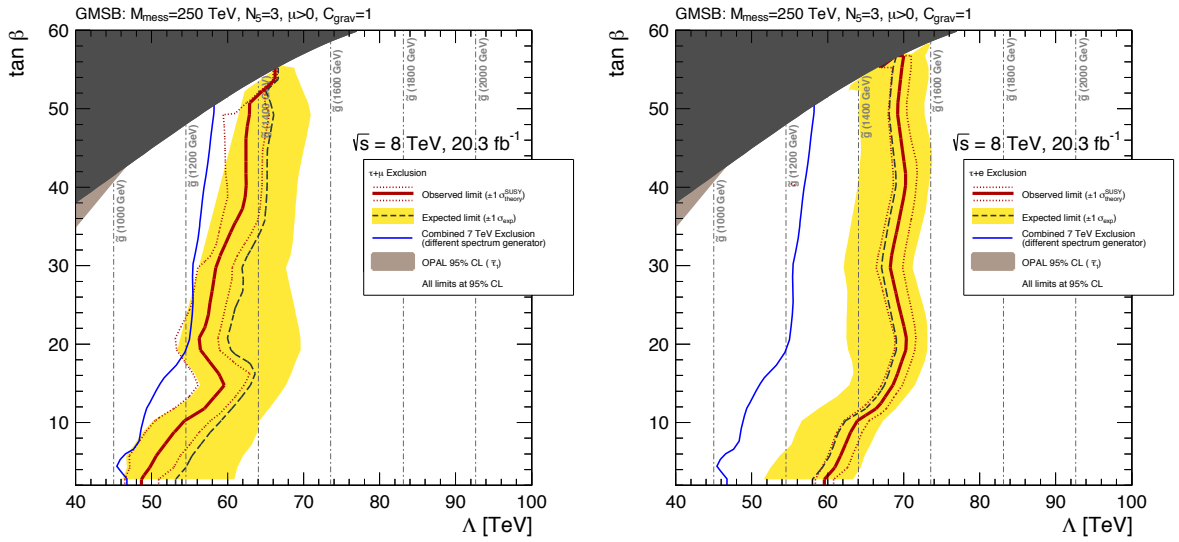

(a) GMSB limit in the $\tau+\mu$ channel.

(b) GMSB limit in the $\tau+e$ channel.

Figure 5.31: Expected (black dashed line) and observed limit (red line) at 95% CL for the GMSB model in the parameters Λ and $\tan\beta$. The blue line indicates the combined observed limit from the 7 TeV analysis.

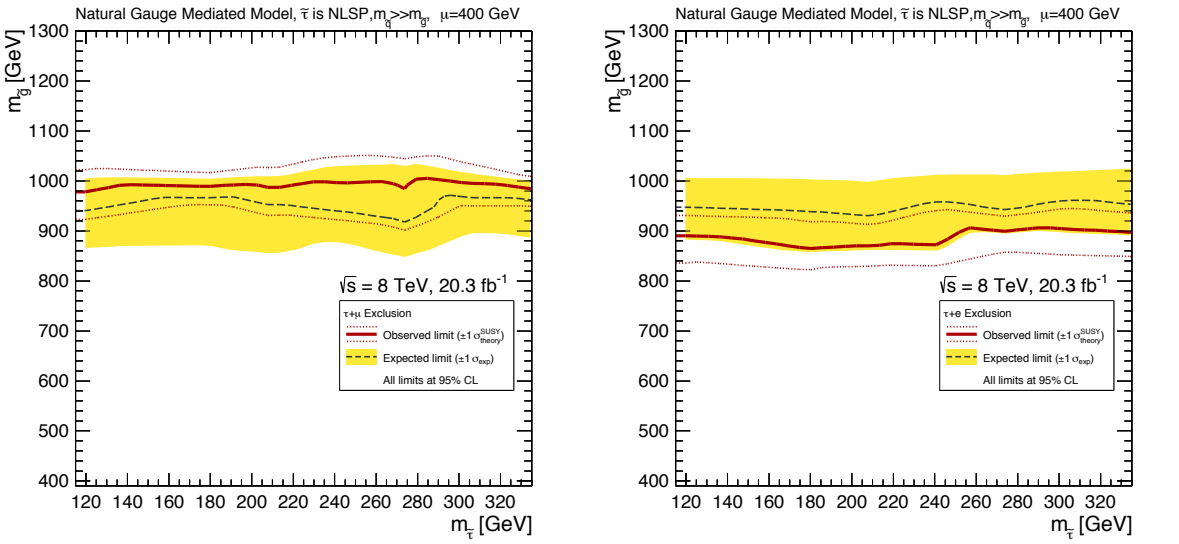

(a) nGM limit in the $\tau+\mu$ channel.

(b) nGM limit in the $\tau+e$ channel.

Figure 5.32: Expected (black dashed line) and observed limit (red line) at 95% CL for the nGM model in the parameters $m_{\tilde{\tau}}$ and $m_{\tilde{g}}$.

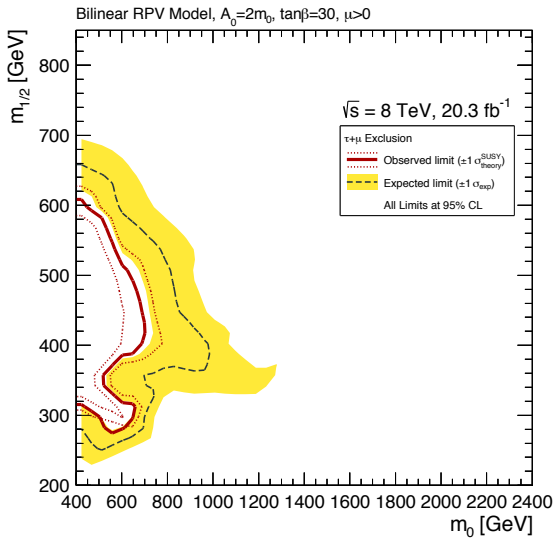

(a) bRPV limit in the $\tau+\mu$ channel.

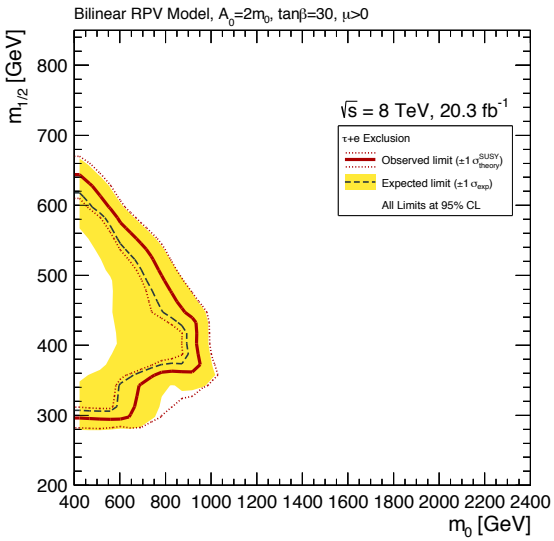

(b) bRPV limit in the $\tau+e$ channel.

Figure 5.33: Expected (black dashed line) and observed limit (red line) at 95% CL for the bRPV model in the parameters m_0 and $m_{1/2}$.

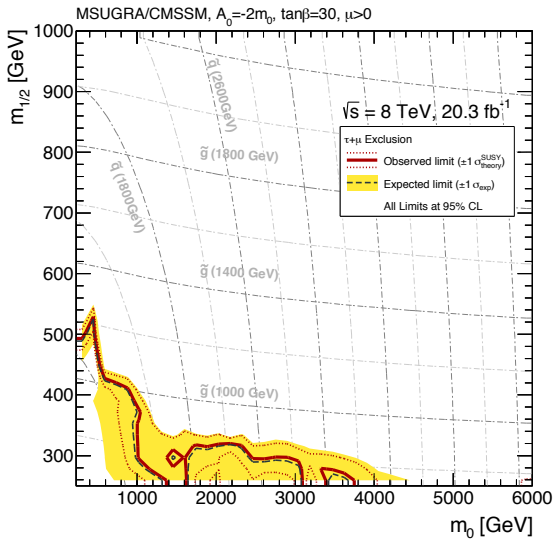

(a) mSUGRA limit in the $\tau+\mu$ channel.

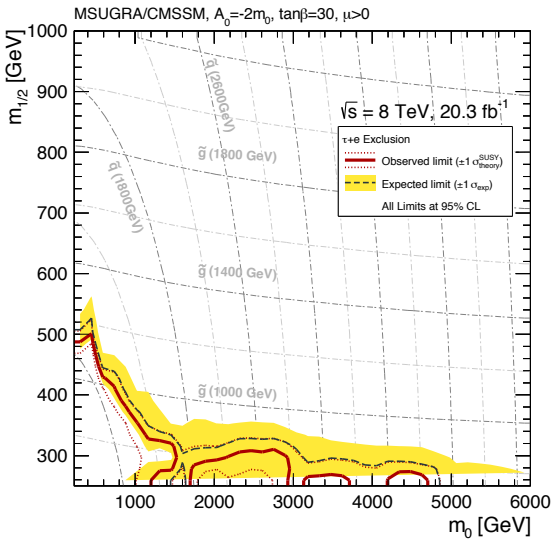

(b) mSUGRA limit in the $\tau+e$ channel.

Figure 5.34: Expected (black dashed line) and observed limit (red line) at 95% CL for the mSUGRA model in the parameters m_0 and $m_{1/2}$.

Signal channel	$\langle\varepsilon\sigma\rangle^{95}_{\text{obs}}$[fb]	S^{95}_{obs}	S^{95}_{exp}	CL_B	$p(s=0)$
GMSB $\tau+e$	0.20	4.1	$4.2^{+1.7}_{-0.4}$	0.41	0.50
nGM $\tau+e$	0.56	11.4	$8.3^{+2.8}_{-2.0}$	0.87	0.15
bRPV $\tau+e$	0.26	5.3	$6.0^{+2.2}_{-1.1}$	0.30	0.50
mSugra $\tau+e$	0.72	14.6	$11.7^{+4.1}_{-3.2}$	0.78	0.24
GMSB $\tau+\mu$	0.26	5.3	$4.0^{+1.6}_{-0.2}$	0.80	0.22
nGM $\tau+\mu$	0.23	4.6	$5.6^{+2.1}_{-1.5}$	0.31	0.50
bRPV $\tau+\mu$	0.52	10.6	$6.1^{+2.6}_{-1.0}$	0.95	0.04
mSugra $\tau+\mu$	0.49	9.9	$10.0^{+3.6}_{-2.7}$	0.49	0.50

Table 5.11: Left to right: 95% CL upper limits on the visible cross-section ($\langle\varepsilon\sigma\rangle^{95}_{\text{obs}}$) and on the number of signal events (S^{95}_{obs}). The third column (S^{95}_{exp}) shows the 95% CL upper limit on the number of signal events, given the expected number (and $\pm1\sigma$ excursions on the expectation) of background events. The last two columns indicate the CL_B value, i.e. the confidence level observed for the background-only hypothesis, and the discovery p-value ($p(s=0)$).

mSugra Finally the exclusion limits for the mSugra model are displayed in figure 5.34. The expected exclusion is at low m_0. At low $m_{1/2}$ it reaches up to $m_0 \approx 500$ GeV in both analyses. The observed limit in the $\tau+\mu$ analysis is almost congruent to the expected limit. In the $\tau+e$ analysis the observed limit is a bit weaker than expected, but well covered by the uncertainty band.

5.6.3 Model Independent Interpretation

The four signal regions designed for this analysis are not only of interest for the particular model they have been optimized for, but can also exclude other signal models. For this reason, model independent exclusion limits on the number of BSM events are derived. To do this, only the expected background and the uncertainty on it, together with the number of observed events in the various signal regions are used.

By setting the number of signal events to 1, the 95 % confidence level on the signal strength μ provides a model-independent result. Normalizing to the integrated luminosity of the data sample an upper limit on the visible cross-section of new physics can be derived.

The calculations are performed by using 5000 toy MC events. The results are listed in table 5.11. The observed excess in the $\tau+\mu$ bRPV signal region is reflected in a discovery p-value of 4 %. However, an observation of 2 σ excess is statistically not a relevant hint for any BSM physics.

5.6.4 Statistical Combination with Other Channels

The results of the two channels presented in this thesis are published together with the two other channels mentioned before. These channels select one and two or more hadronically decaying tau leptons. Since the object selections of all four channels are orthogonal to each other, a statistical combination of the results in representation of one single exclusion limit is possible.

To combine the individual results of all channels the product of all likelihood functions is used. Systematic uncertainties that are shared among all channels are treated by the same nuisance parameters and the same constraining Gauss distribution. In figure 5.35 the combined expected and observed exclusion limits are displayed.

The impact of the light lepton channels on the combined exclusion limits is visible in some parts of the parameter space. For the combined GMSB exclusion contour in figure 5.35a the influence is noticeable

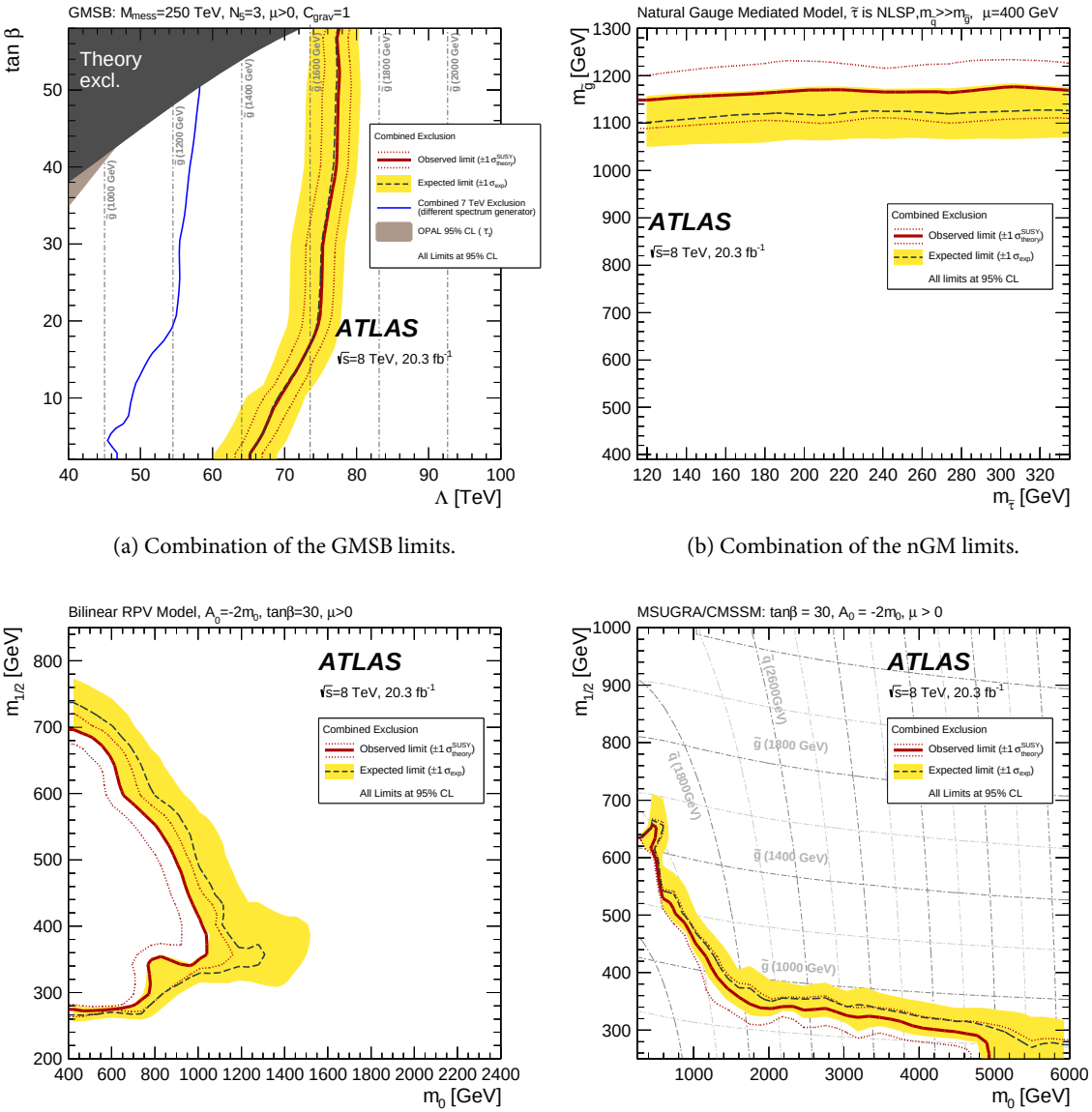

(a) Combination of the GMSB limits.

(b) Combination of the nGM limits.

(c) Combination of the bRPV limits.

(d) Combination of the mSugra limits.

Figure 5.35: Statistical combination of the exclusion limits of $\tau+\mu$, $\tau+e$, 1τ and 2τ channels [2].

in the region below $\tan\beta = 30$. Here, the shape of the combined limit is pushed by the $\tau+e$ channel. The higher sensitivity of the light lepton channels in that region can be explained by the smaller mass difference between stau and the light sleptons, resulting in decays including more prompt light leptons.

In the nGM scenario the two light lepton channels do not have a big impact on the combined exclusion line which is driven by the 2τ analysis as seen in figure 5.35b.

The bRPV limit (figure 5.35c) is pushed by the $\tau+e$ channel in the region of $m_{1/2} \approx 360\,\text{GeV}$ to $m_0 \approx 1000\,\text{GeV}$. The combined expected exclusion exceeds the observed limit as a consequence of the excess observed in the $\tau+\mu$ channel in the according signal region.

Finally in figure 5.35d the combined mSugra limit is displayed. In this scenario light lepton channels are relevant in the low $m_{1/2}$ region, where the combination with the 1τ channel leads to a smooth contour and uncertainty band.

5.7 Chapter Summary

In this chapter a search for new physics beyond the Standard Model was described. The behavior of simulated background and signal samples in four different SUSY models was studied, optimizing four kinematic regions that reject most Standard Model events and select SUSY signal events. These kinematic regions are shared by the two search channels.

The final background estimates were presented along with a detailed description of the impact of systematic uncertainties from theory and arising from various detector measurements relevant for the selection.

After comparing the expectation to data no statistically relevant excess was observed. The results could then be interpreted model-independently and in terms of exclusion limits in the parameter spaces of the four considered SUSY models.

CHAPTER 6

Improving the Limits

In the last chapter of this thesis a brief study on an improved analysis strategy is presented. For future analyses this alternative approach promises a higher sensitivity to signals and stronger exclusion limits.

In the previous chapter exclusion limits were presented which were derived by utilizing the HistFitter framework. However, these limits were based on the total number of signal and background events only. In this chapter a different approach is studied where also the shape of the final distribution is considered. In addition to that, the ability of the HistFitter framework for normalizing the background in control regions is used instead of calculating the scaling factors with the matrix method as described in 4.3.1. Since the purpose of this study is to provide an outlook for possible improvements only the GMSB model in the $\tau+e$ channel is considered.

6.1 Background Normalization in Control Regions

By making use of the full functionality of HistFitter, all three control regions and the signal region are modelled by separate PDFs combined into a single fit which shares the PDF parameters. The control regions are the same that were defined in section 4.3. Instead of using the total event count, three histograms are chosen from those control regions.

Systematic uncertainties are considered in the fit as histograms too. This means that the input consists of three control region distributions and one signal region distribution for each of the six background types (W+jets, Z+jets, Top Truth, Top Fake, Diboson and Multijet), data, and 79 signal grid points. Considering the full set of 40 different $\tau+e$ related systematic uncertainties this leads to ~ 14 000 input histograms. These can be generated dynamically from cuts and weights by HistFitter itself using TTrees. However, the analysis presented in this thesis generates only histogram output. To reduce the number of histograms and thereby simplify the book-keeping only some of the dominating systematic uncertainties are considered. These are the jet energy resolution (JER), the jet energy scale (JES), the tau energy scale (TES) and the pile-up uncertainty.

The correct normalization of the background samples is obtained by constructing PDFs using HistFactory [216] and performing a likelihood fit to the observed data. The PDF used for normalization only describes the background. To extrapolate the fit result into the signal region the total PDF describing all regions has to be deconstructed and reconstructed incorporating the fit results including errors and the covariance matrix. A more detailed description of this process can be found in [215].

The corresponding distributions before and after the fit are displayed in figure 6.1. A large systematic uncertainty on the W+jets background is observed before normalization in figure 6.1a. This uncertainty affects mostly the overall normalization of the distribution and therefore decreases by a large factor after

the fit as seen in figure 6.1b. For Top Truth and Top Fake a decrease in the uncertainty is observed as well, but less prominently.

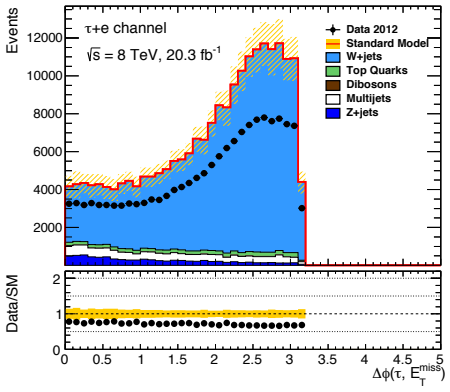

(a) W+jets control plot before normalization.

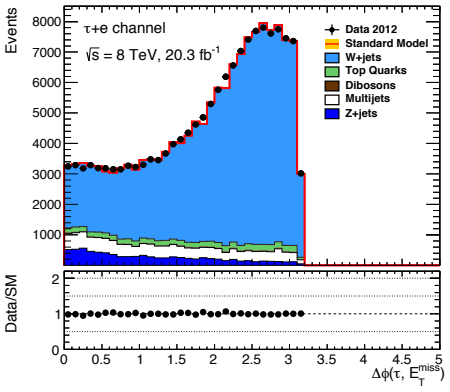

(b) W+jets control plot after normalization

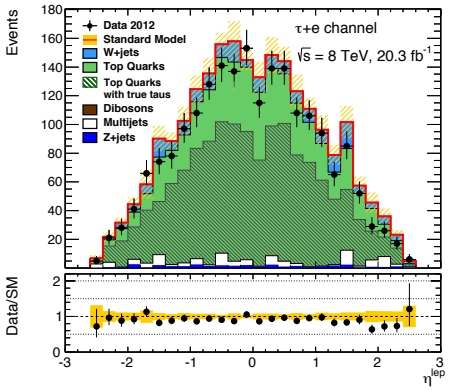

(c) Top Truth control plot before normalization

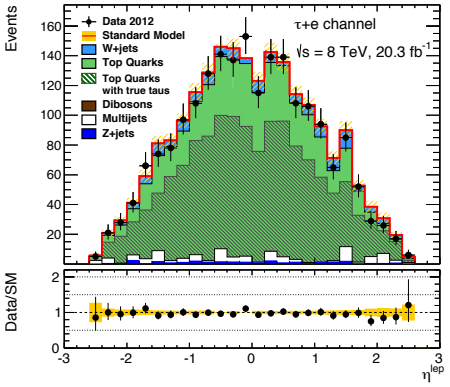

(d) Top Truth control plot after normalization

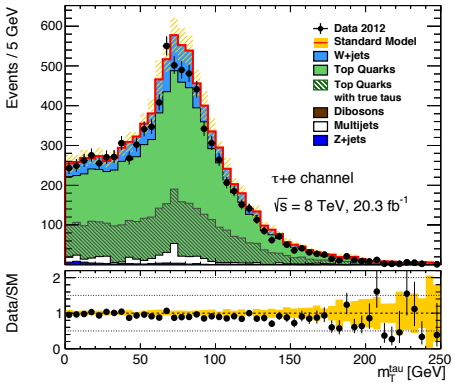

(e) Top Fake control plot before normalization

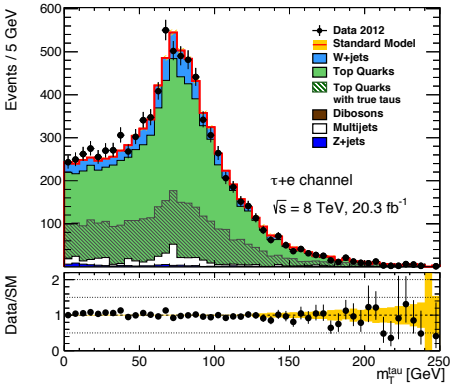

(f) Top Fake control plot after normalization

Figure 6.1: Control distributions for W+jets, Top Truth and Top Fake before (left) and after (right) simultaneous fitting for normalization.

6.2 Signal Region Shape Fit

In the next step the benefit of a shape fit in a modified GMSB signal region is investigated. The signal region is based on m_{eff} as in the regular analysis, but instead of considering just the total event count above a relatively strict cut, a more complex PDF is constructed from multiple bins of the signal region distribution.

The likelihood function used is similar to 5.10. It is extended by incorporating signal region and control regions as the product of PDFs based on Poisson statistics which also consider the shape information provided by every single bin of the input distributions:

$$\mathcal{L}\left(\mu, \vec{\theta}\right) = P_{\text{SR}} \times P_{\text{CR}} \times C_{\text{Syst}}. \tag{6.1}$$

The constraining term for the systematic uncertainty is denoted as C_{Syst} in this case. A more detailed description of this procedure can be found in [216].

Additonal separation power is expected due to the different shapes of signal and background. Aside from that, the tight selection criteria for the cut-and-count approach are optimized for a special set of signal points. The shape fit on the other hand can improve the sensitivity for other grid points or signal models by using a larger phase space.

An optimization of the signal region is performed by comparing different lower m_{eff} cuts and by varying the bin width. For this, a benchmark signal point of the GMSB grid at $\Lambda = 60$ TeV, $\tan\beta = 30$ is chosen. Figure 6.2a displays the expected limits on the signal strength parameter μ_{Sig} in dependence of the bin width for a fixed lower m_{eff} cut at 900 GeV. Figure 6.2b displays the dependence of the limit on the lower cut on m_{eff}. For this the bin width is fixed at 150 GeV. A stronger limit is observed both for smaller bins and for a wider range of the distribution.

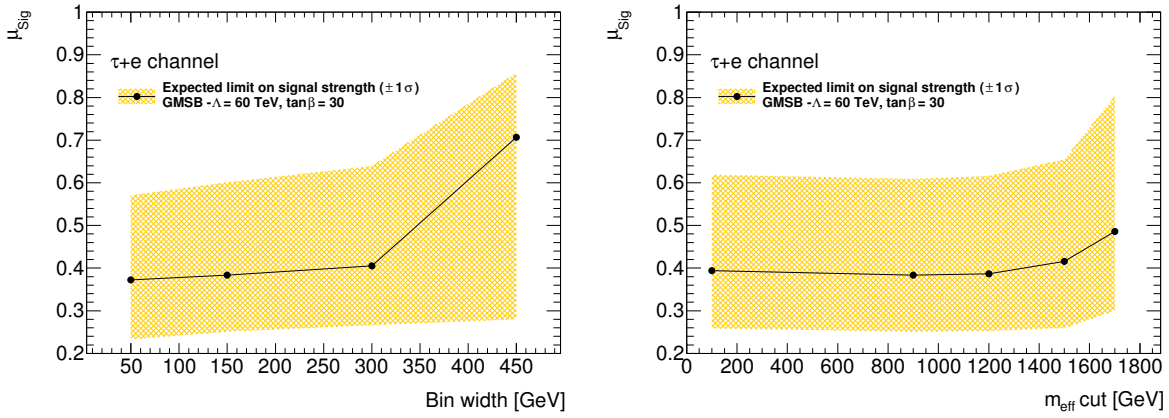

(a) Expected limit for various bin width in m_{eff}.

(b) Expected limit for various m_{eff} cuts.

Figure 6.2: The expected limit on the signal strength parameter μ_{Sig} for the GMSB benchmark signal point $\Lambda = 60$ TeV, $\tan\beta = 30$ in dependence on various bin widths and different lower cuts in the distribution.

To study the effect of a shape fit on the exclusion limit in the parameter space of the signal grid the bin width is fixed to 150 GeV with a lower cut of $m_{\text{eff}} = 900$ GeV as displayed in figure 6.3. The background is normalized according to the background fit and two signal points at $\Lambda = 60$ TeV, $\tan\beta = 30$ and $\Lambda = 70$ TeV, $\tan\beta = 30$ are overlayed.

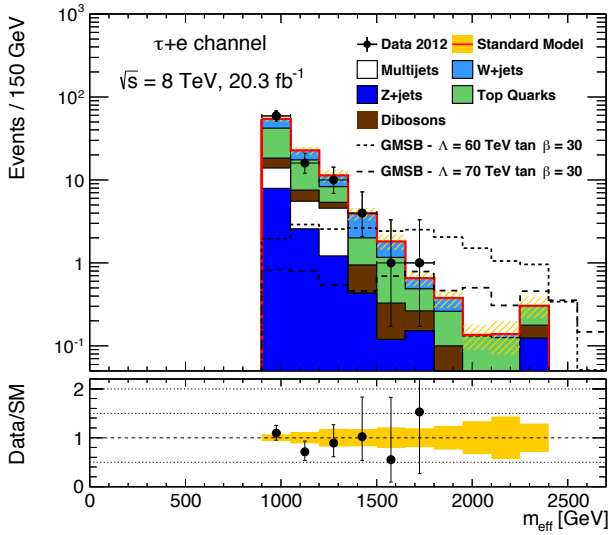

Figure 6.3: Signal region for the GMSB in the $\tau+e$ channel binned in m_{eff}.

A hypothesis test is performed as described in section 5.6.1. To visualize the result in dependence of Λ and $\tan\beta$ it is convenient to consider the significance that was approximated before in equation 5.1. In this case the precise value is used. It is defined as

$$z_0 = \Phi^{-1}(1 - \text{CL}_\text{S}), \tag{6.2}$$

where Φ^{-1} is the quantile function of the normal distribution. A CL_S-value of 0.05 at the exclusion limit corresponds to $z_0 = 1.65$.

Figure 6.4 shows two-dimensional distributions for a cut-and-count approach with $m_{\text{eff}} > 1700\,\text{GeV}$ (top) and the shape fit approach (bottom). Both make use of the same background fit and consider the reduced number of systematic uncertainties. The exclusion limit at $\text{CL}_\text{S} = 0.05$ is indicated by a red line in both plots.

The exclusion limit improves by a 3 – 5 TeV. In the case of the GMSB model the gain in exclusion power is relatively small due to the fact that signal and background shapes are very similar in the tail of m_{eff} and for grid points close to the cut-and-count limit.

For smaller values of Λ a larger gain in significance can be observed. As discussed before, the sensitivity improvement in this case is due to the fact that the tight m_{eff} requirement in the cut-and-count approach discards a large phase space in which the signal is already dominant over the background. This becomes apparent when comparing the signals for $\Lambda = 60\,\text{TeV}$, $\tan\beta = 30$ and $\Lambda = 70\,\text{TeV}$, $\tan\beta = 30$ in figure 6.3. Because of the almost linear dependece of limit strength and m_{eff} requirement the exclusion is not further expanded by the observed sensitivity improvement in any parts of the parameter space. Only signal models with a more complex dependence on the discriminant variable can benefit from this.

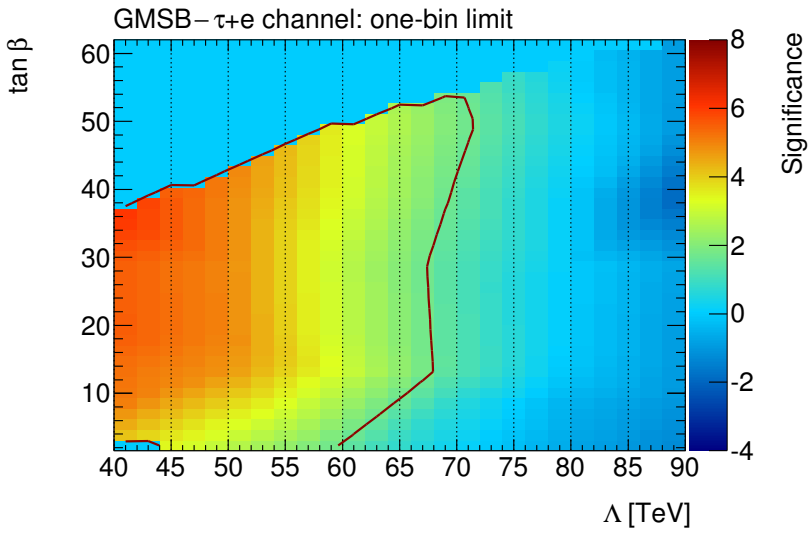

(a) Single-bin approach

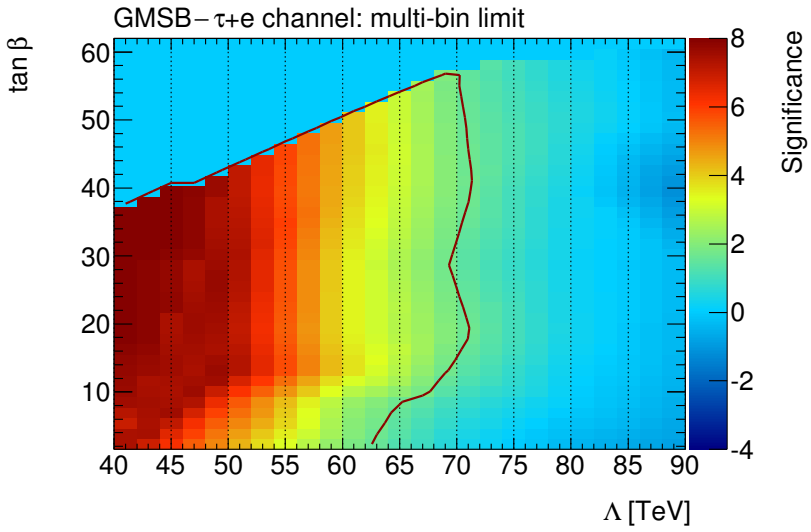

(b) Multi-bin approach

Figure 6.4: Two-dimensional significance distributions for a single-bin (a) and multi-bin (b) SR. The red line indicates the exclusion limit at a significance level of 1.65 which is equivalent to a CL_S-value of 0.05.

CHAPTER 7

Conclusions

"'Would you tell me, please, which way I ought to go from here?' 'That depends a good deal on where you want to get to,' said the Cat. 'I don't much care where –' said Alice. 'Then it doesn't matter which way you go,' said the Cat. '– so long as I get SOMEWHERE*,' Alice added as an explanation. 'Oh, you're sure to do that,' said the Cat, 'if only you walk long enough.'"*

—Lewis Carroll, Alice's Adventures in Wonderland

7.1 Summary

The Standard Model of particle physics has proved itself as a successful theory by delivering a reliable description of elementary particles and their interactions over several orders of magnitude in energy. Yet, in many aspects, it is a theory with limitations. More fundamental theories like supersymmetry can provide solutions to some of the issues of the Standard Model which is why the search for supersymmetric particles is one of the primary objectives in the LHC physics program.

At the LHC, supersymmetric particles potentially emerge from proton-proton collisions at center-of-mass energies of presently up to $\sqrt{s}$ = 13 TeV. Their decay products appear in unique signatures that can feature large missing transverse momentum, high energetic jets and leptons. In many models the stau is the the lightest supersymmetric particle, resulting in final states with multiple tau leptons. These models are targeted by the analysis presented in this thesis. It was performed on the 20 fb^{-1} 8 TeV data delivered by the LHC in 2012. The baseline selection requires at least one tau lepton and exactly one additional light lepton. For practical reasons the analysis is split into two channels – one for muons ($\tau+\mu$) and one for electrons ($\tau+e$).

Standard Model processes that result in similar final states are W+jets, Z+jets, Top Quarks, Diboson and Multijet. Their contributions to the background are estimated by Monte Carlo simulation and data-driven methods. The W+jets and Top Quarks backgrounds are normalized in kinematic regions that are dominated by these particular event types. The Multijet background is derived data-driven with a matrix method.

In both channels four signal regions are considered. Each of them aims at a specific SUSY model: GMSB, nGM, bRPV and mSugra. The signal region selection is based on the kinematic variables m_{T}^{ℓ}, $E_{\text{T}}^{\text{miss}}$ and m_{eff}, as well as on the minimal number of jets. The choice of these kinematic requirements is optimized for model specific benchmark points in the model parameter space.

Systematic uncertainties on the number of expected background events in the signal regions are calculated by re-evaluating the event counts under variation of various detector-specific variables. Furthermore, theory uncertainties are considered by comparing different Monte Carlo generators and applying cross-section uncertainties for the signal Monte Carlo.

The number of observed events in 8 TeV data is compared to the expected number of background events. None of the eight signal regions shows a significant excess in data over the number of expected events. The largest deviation from the Standard Model expectation is observed in the $\tau+\mu$ bRPV signal region with $2.5 \pm 0.6 \pm 1.0$ expected and 7 observed events, which corresponds to $\sim 2\sigma$.

The non-observation of new physics can be interpreted in terms of exclusion limits in the parameter space of the four different SUSY scenarios. In the GMSB model the analysis excludes the parameter space up to $\Lambda \approx 62$ TeV for the $\tau+\mu$ channel and $\Lambda \approx 70$ TeV for the $\tau+e$ channel. This corresponds to gluino masses of $m_{\tilde{g}} \approx 1.4$ TeV and $m_{\tilde{g}} \approx 1.5$ TeV, respectively. For the nGM model the parameter space for gluino masses $m_{\tilde{g}} \lesssim 1$ TeV in the $\tau+\mu$ channel and $m_{\tilde{g}} \lesssim 0.9$ TeV in the $\tau+e$ channel can be excluded independently of the stau mass. The interpretation in the bRPV model excludes a part of the parameter space with low m_0 which reaches up to $m_0 \approx 650$ GeV in the $\tau+\mu$ channel and $m_0 \approx 1000$ GeV in the $\tau+e$ channel for $m_{1/2} \approx 400$ GeV. For mSugra parts of the parameter space with low $m_{1/2}$ can be excluded. For low m_0 the exclusion limits of both channels reach up to $m_{1/2} \approx 500$ GeV.

Exploiting the shape information of the m_{eff} distribution as discriminant between signal and background, an improvement of sensitivity for the exclusion limit is observed. While the gain of the exclusion limit itself is relatively small, the limit on the visible cross-section for the lower mass range is improved significantly.

7.2 Critical Review and Outlook

To isolate events that match the kinematic properties of supersymmetric decay chains, variables like m_{eff} are utilized. In the high energetic tails of these distributions Standard Model contributions are low, while the amount of SUSY events is reasonably high. This approach requires a reliable prediction of expected Standard Model events. Large MC statistics are needed as well as a correct modeling of these rare processes. While the influence of the statistical limitations is considered in the optimization procedure, there is only a restricted possibility to validate the correct Monte Carlo modeling as described in section 5.3.4. This should be regarded critically considering the corrections that are applied to the Monte Carlo samples. While these corrections deliver an accurate description of the Standard Model background in the control regions, there is no possibility to guarantee that this also holds for the signal regions.

In the light of this, the mis-modeling of fake tau leptons is one of the largest limitations of the analysis. However, the impact on the final results is considered to be small enough to be covered by the systematic uncertainties. Improvement in the modeling of tau-like jets in the Monte Carlo samples is in any case desirable.

Further improvements of the analysis could be achieved by gaining more control over the various background contributions and enhancing the signal region sensitivity. Promising results were obtained as part of a bachelor thesis [217] by the definition of a Diboson control region and exploiting the possibility of two-dimensional Asimov significance scans.

For a combined fit approach as described in chapter 6, a Z+jets and a Diboson control region can be implemented in addition to the existing control regions. In the signal region improved statistics can help to enhance sensitivity and reduce uncertainties. The use of binned signal regions is an attractive possibility to increase the sensitivity of the analysis in a larger parameter space of the signal grid. Depending on the difference in shapes of signal and background contributions, also much stronger exclusions limits can be accomplished.

Updated results of search efforts for supersymmetry with tau leptons at 13 TeV with 3.2 fb^{-1} have been published recently [218]. In this iteration only hadronically decaying tau leptons are considered. The combined analysis extends the exclusion limit in the GMSB model up to 107 TeV for large values of $\tan\beta$. In this publication also a so-called simplified model is considered. These models focus on a small set of

particles with a particular decay chain. This can then be interpreted in a variety of SUSY scenarios. For the next iteration with more integrated luminosity it is planned to include the channels with leptonically decaying tau leptons again. Furthermore, the use of binned signal regions will likely be exploited.

All search efforts for supersymmetric particles at the LHC have been without success so far. But even though the parameter space for SUSY is getting smaller, there is still a lot of room for this theory to hide. Theoretical implications like dark matter remain a strong motivation to search for physics beyond the Standard Model and as mentioned in section 2.7 the pMSSM is even leads to slightly better global fits of experimentally observations than the Standard Model. The near future will shed light on the question whether the LHC will be able to reveal new physics or not.

APPENDIX A

Additional Figures

A.1 Additional Control Distributions

This section contains additional control distributions from the four regarded control regions. All distributions are regarded after applying the corrections described in chapter 4. All plots show reasonable agreement between the background prediction from simulation and data-driven estimation and the observed data.

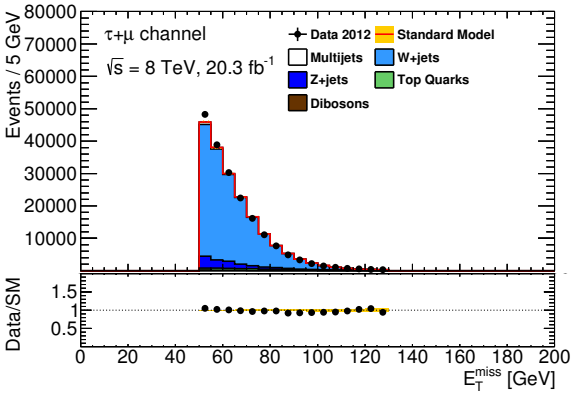

(a) $E_{\mathrm{T}}^{\mathrm{miss}}$ in the $\tau+\mu$ channel.

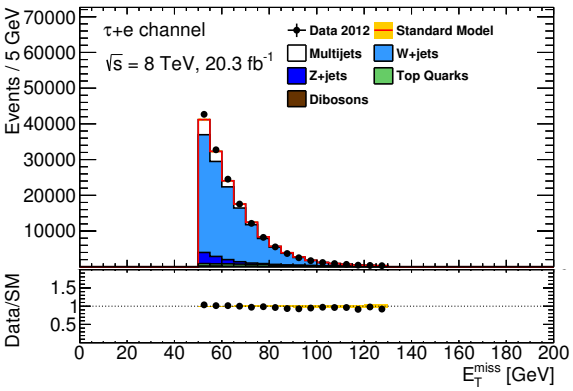

(b) $E_{\mathrm{T}}^{\mathrm{miss}}$ in the $\tau+e$ channel.

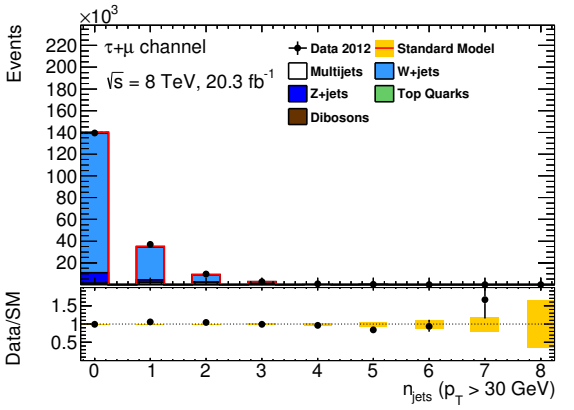

(c) N_{jet} in the $\tau+\mu$ channel.

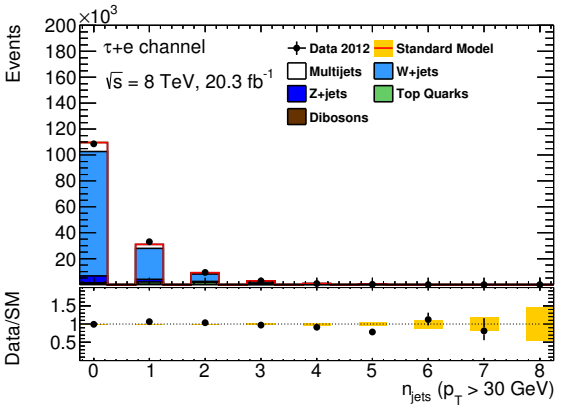

(d) N_{jet} in the $\tau+e$ channel.

Figure A.1: Additional control distributions for the W+jets control region.

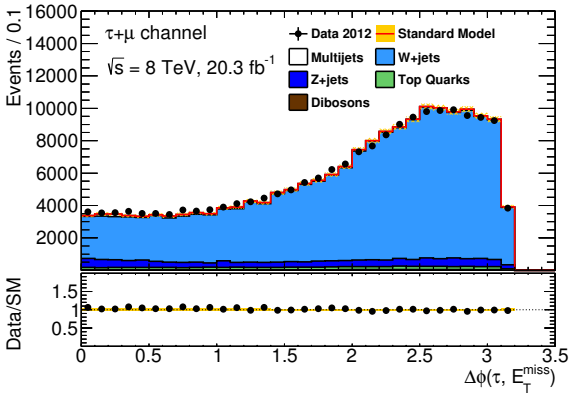

(a) $\Delta\phi(\tau, E_{\mathrm{T}}^{\mathrm{miss}})$in the $\tau+\mu$ channel.

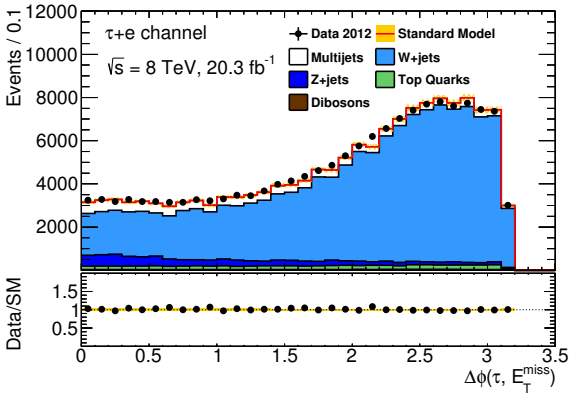

(b) $\Delta\phi(\tau, E_{\mathrm{T}}^{\mathrm{miss}})$in the $\tau+e$ channel.

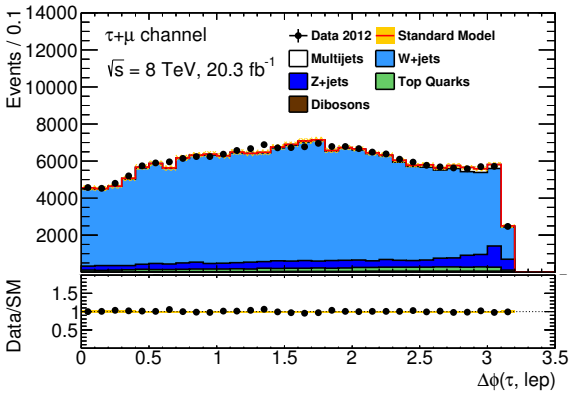

(c) $\Delta\phi(\tau, \ell)$in the $\tau+\mu$ channel

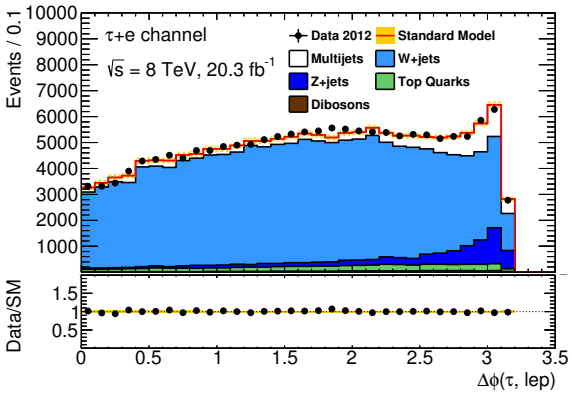

(d) $\Delta\phi(\tau, \ell)$in the $\tau+e$ channel

Figure A.2: Additional control distributions for the W+jets control region.

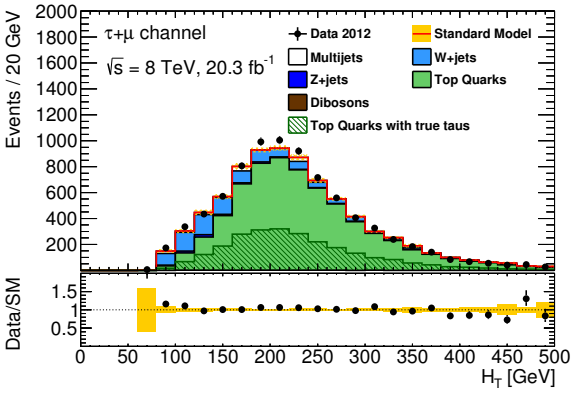

(a) H_{T} in the $\tau+\mu$ channel.

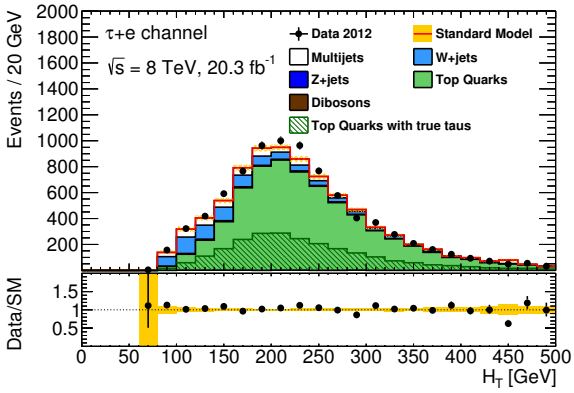

(b) H_{T} in the $\tau+e$ channel.

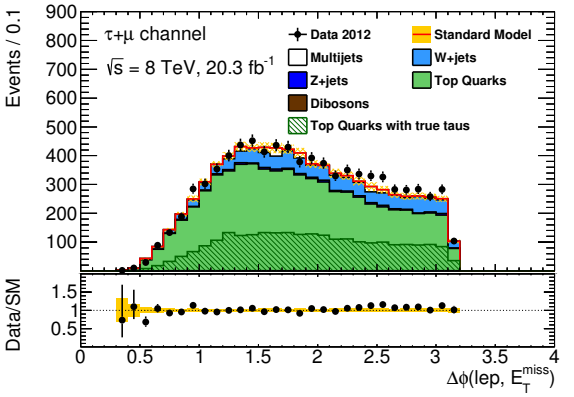

(c) $\Delta\phi(\ell, E_{\mathrm{T}}^{\mathrm{miss}})$ in the $\tau+\mu$ channel.

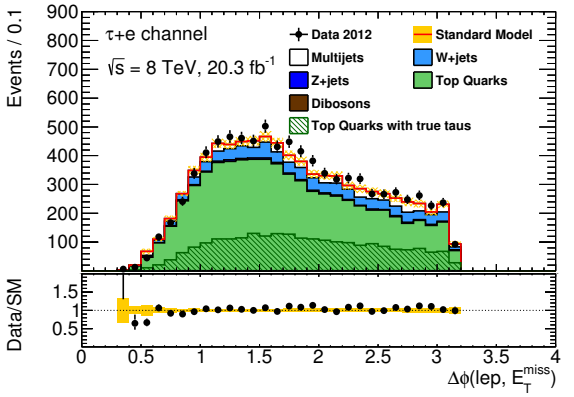

(d) $\Delta\phi(\ell, E_{\mathrm{T}}^{\mathrm{miss}})$ in the $\tau+e$ channel.

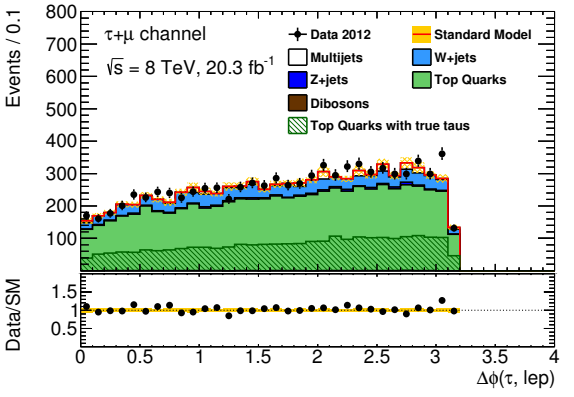

(e) $\Delta\phi(\tau, E_{\mathrm{T}}^{\mathrm{miss}})$ in the $\tau+\mu$ channel.

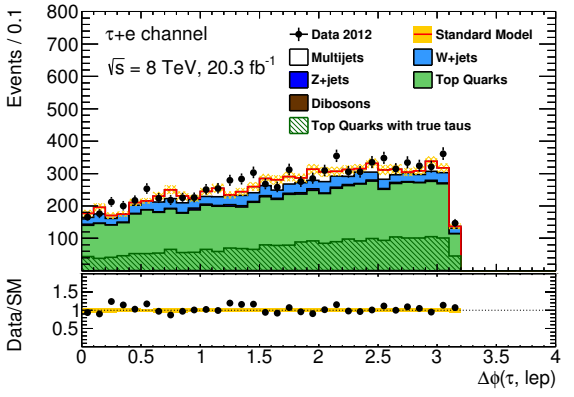

(f) $\Delta\phi(\tau, E_{\mathrm{T}}^{\mathrm{miss}})$ in the $\tau+e$ channel.

Figure A.3: Additional control distributions for the Top Fake control region.

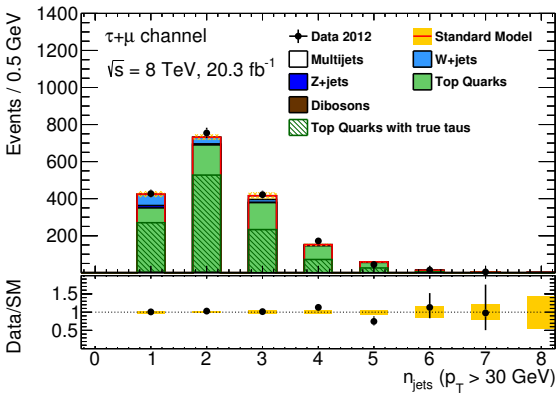

(a) N_{jet} in the $\tau+\mu$ channel.

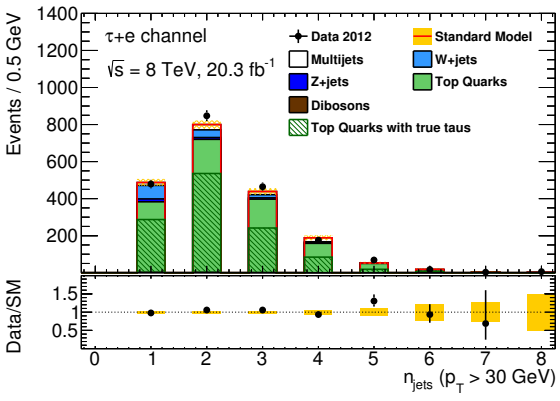

(b) N_{jet} in the $\tau+e$ channel.

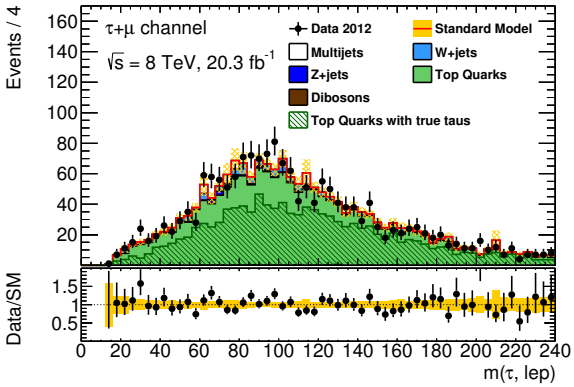

(c) m_{T}^{ℓ} in the $\tau+\mu$ channel.

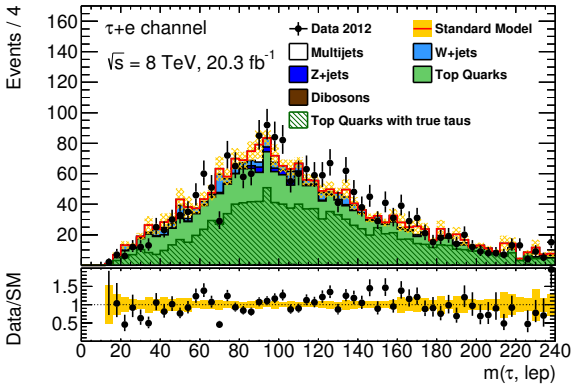

(d) m_{T}^{ℓ} in the $\tau+e$ channel.

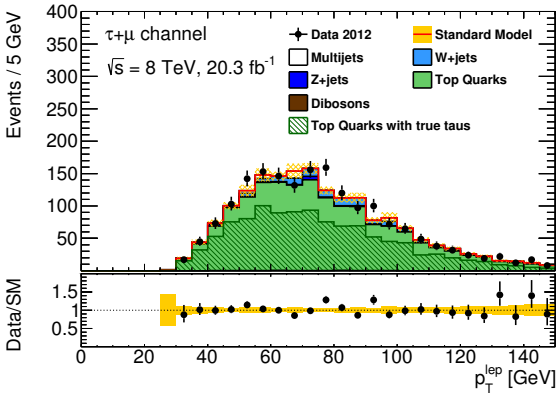

(e) p_{T}^{ℓ} in the $\tau+\mu$ channel.

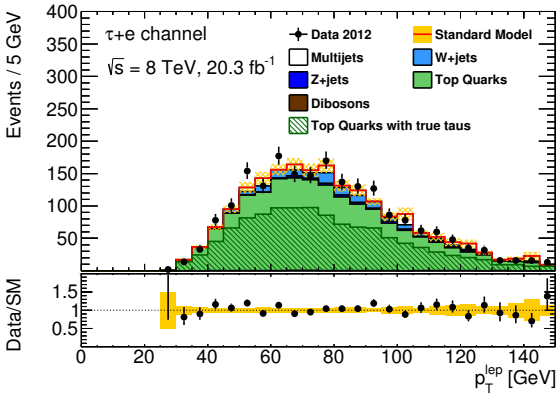

(f) p_{T}^{ℓ} in the $\tau+e$ channel.

Figure A.4: Additional control distributions for the Top Truth control region.

A.2 Additional Significance Scans

This section contains additional Asimov significance scans for the signal region optimization. From the three considered kinematic observables m_{eff}, $E_{\text{T}}^{\text{miss}}$ and H_{T}, those that are not chosen for the final signal region cuts, are displayed here for comparison.

Furthermore, supplementary scans show the unmodified Asimov significance where the background shape is fitted with an exponential function to smoothen the shape of the curvature.

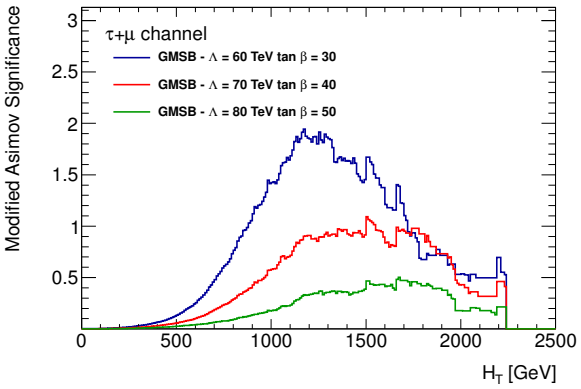

(a) z_{A} in the $\tau+\mu$ channel.

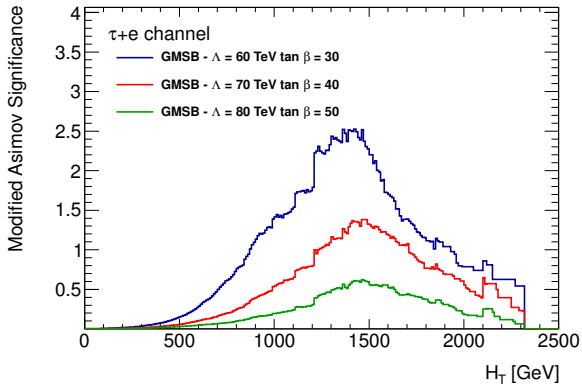

(b) z_{A} in the $\tau+e$ channel.

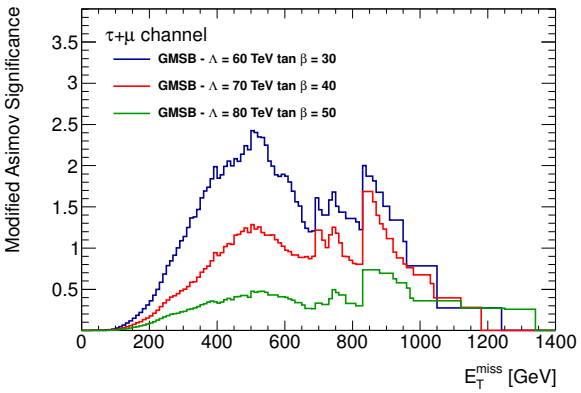

(c) z_{A} in the $\tau+\mu$ channel.

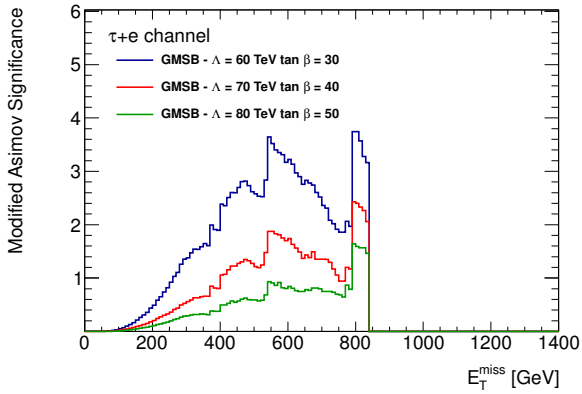

(d) z_{A} in the $\tau+e$ channel.

Figure A.5: Additional significance scans for the GMSB signal region after requiring $m_{\text{T}}^{\ell} > 100\,\text{GeV}$.

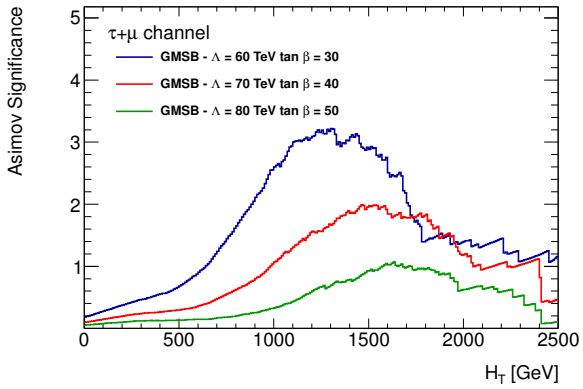

(a) z_A in the $\tau+\mu$ channel.

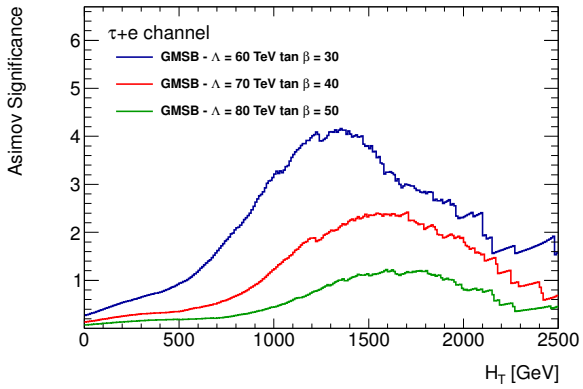

(b) z_A in the $\tau+e$ channel.

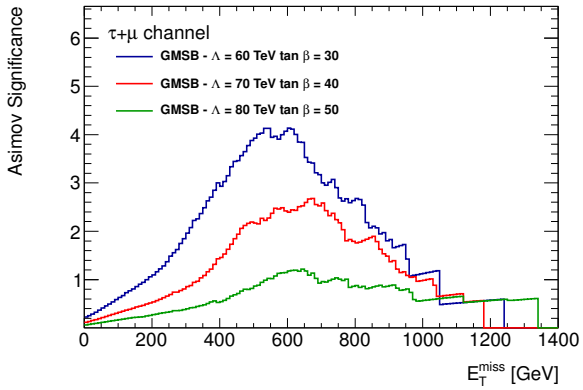

(c) z_A in the $\tau+\mu$ channel.

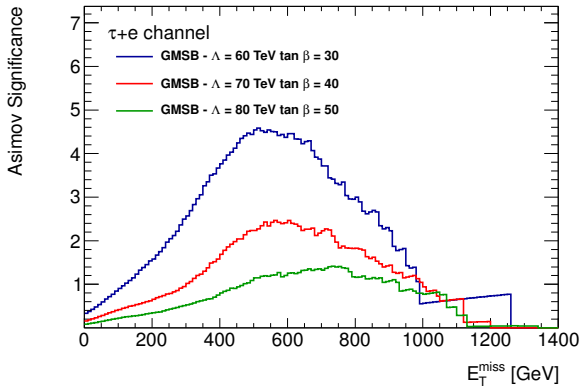

(d) z_A in the $\tau+e$ channel.

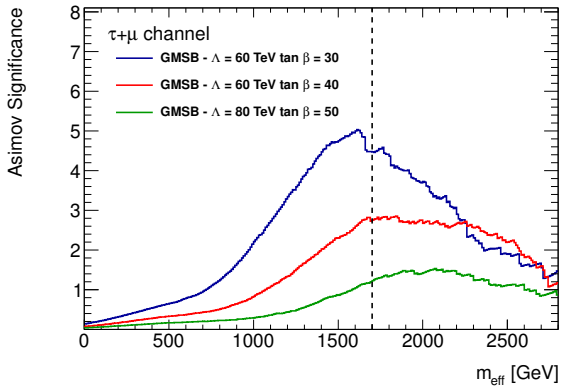

(e) z_A in the $\tau+\mu$ channel.

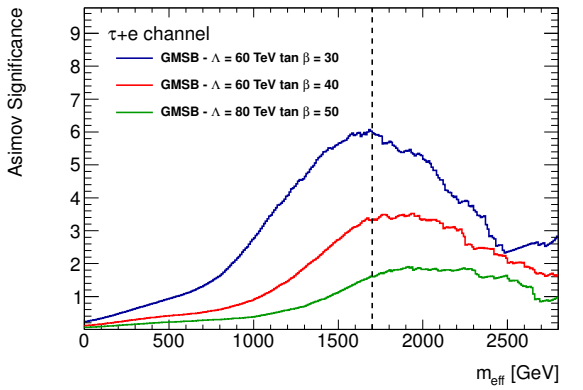

(f) z_A in the $\tau+e$ channel.

Figure A.6: Additional significance scans for the GMSB signal region after requiring $m_T^\ell > 100\,\text{GeV}$. The SM background for these scans was fitted to smoothen the shape of the distribution.

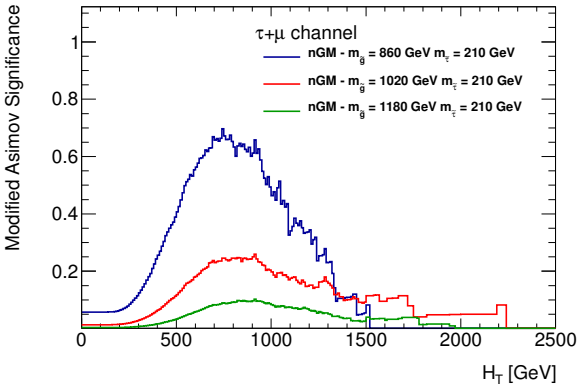

(a) z_A in the $\tau+\mu$ channel.

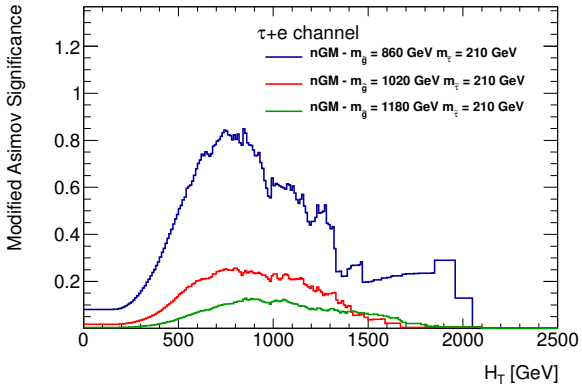

(b) z_A in the $\tau+e$ channel.

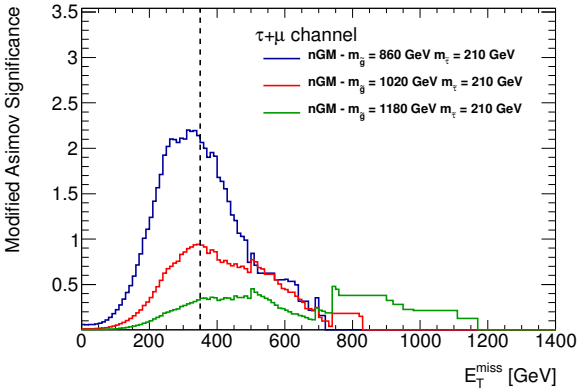

(c) z_A in the $\tau+\mu$ channel.

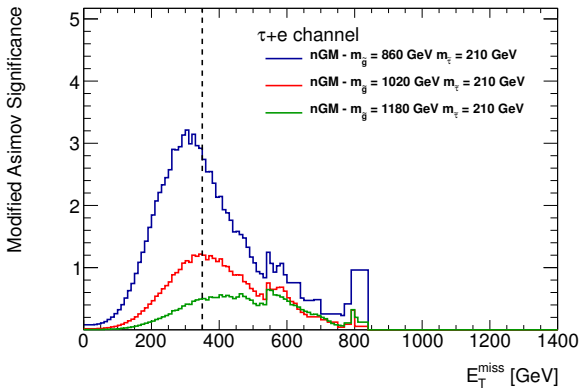

(d) z_A in the $\tau+e$ channel.

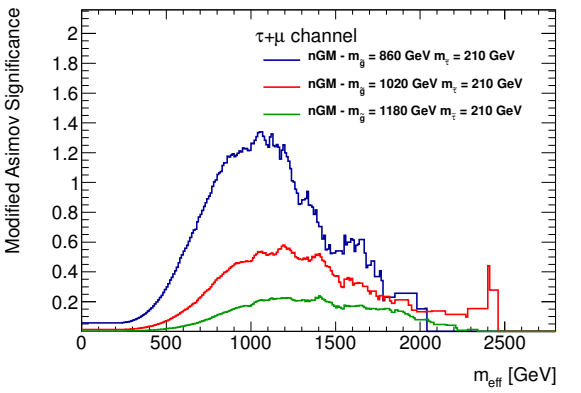

(e) z_A in the $\tau+\mu$ channel.

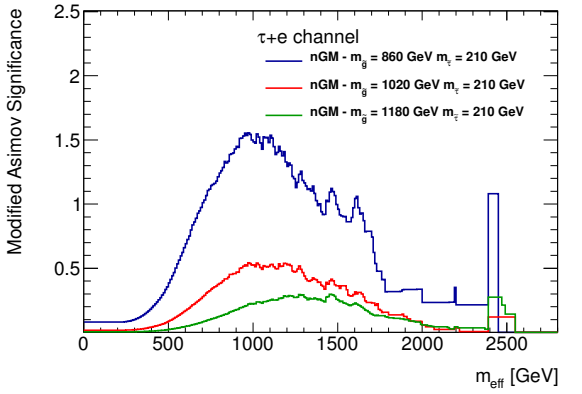

(f) z_A in the $\tau+e$ channel.

Figure A.7: Additional significance scans for the nGM signal region after requiring $m_T^\ell > 100\,\text{GeV}$ and $N_{\text{jet}} \geq 3$.

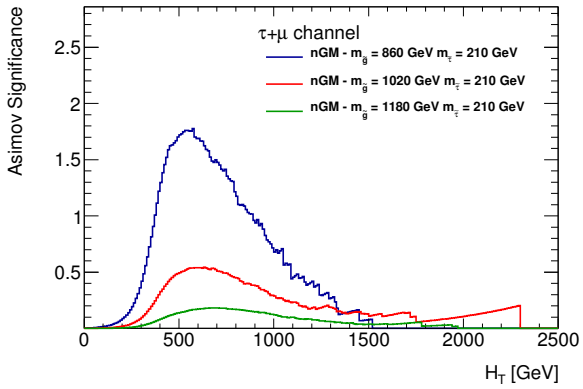

(a) z_A in the $\tau+\mu$ channel.

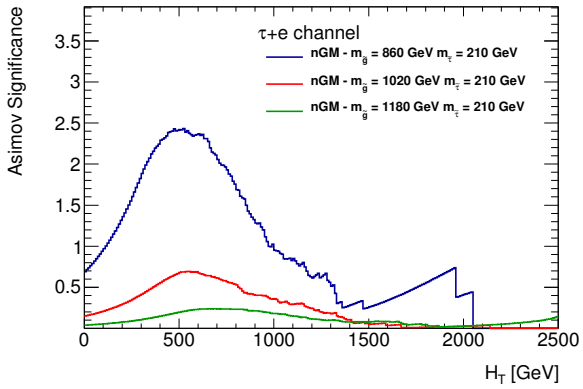

(b) z_A in the $\tau+e$ channel.

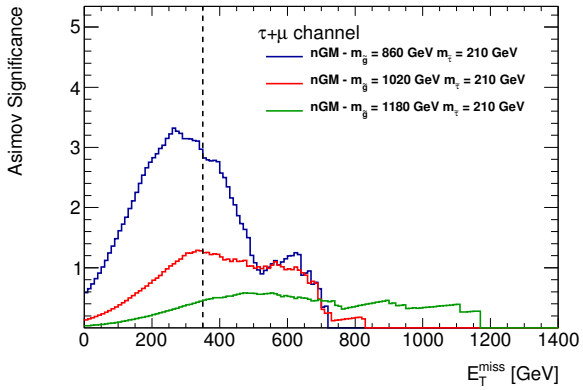

(c) z_A in the $\tau+\mu$ channel.

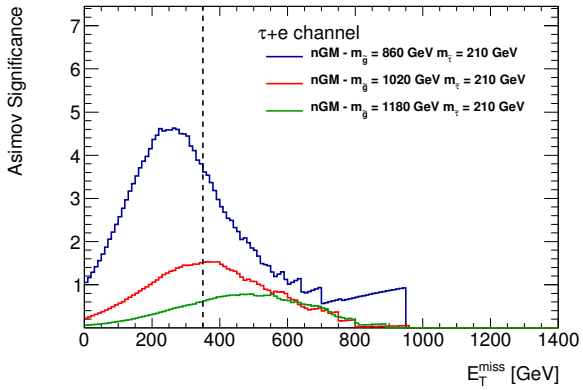

(d) z_A in the $\tau+e$ channel.

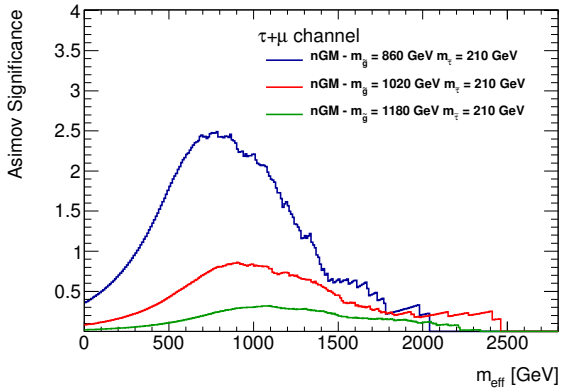

(e) z_A in the $\tau+\mu$ channel.

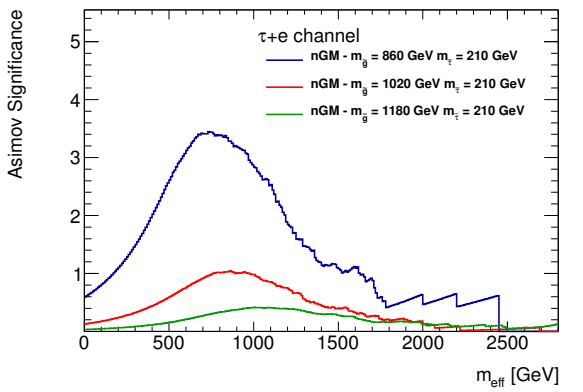

(f) z_A in the $\tau+e$ channel.

Figure A.8: Additional significance scans for the nGM signal region $m_T^\ell > 100$ GeV and $N_{jet} \geq 3$. The SM background for these scans was fitted to smoothen the shape of the distribution.

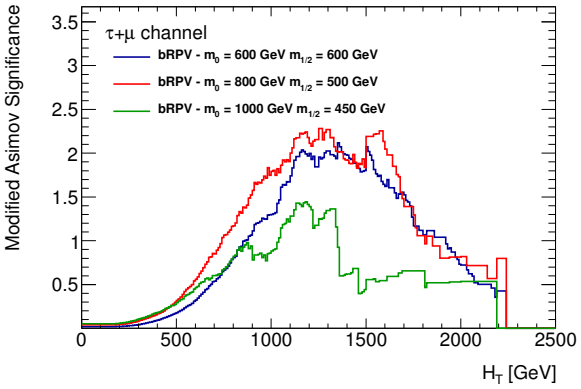

(a) z_A in the $\tau+\mu$ channel.

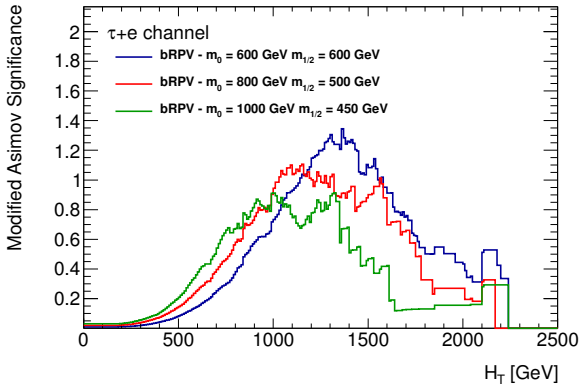

(b) z_A in the $\tau+e$ channel.

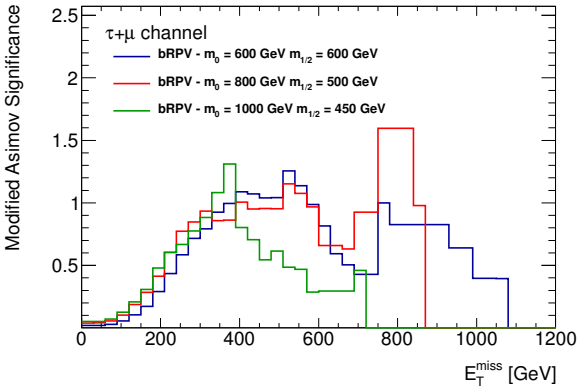

(c) z_A in the $\tau+\mu$ channel.

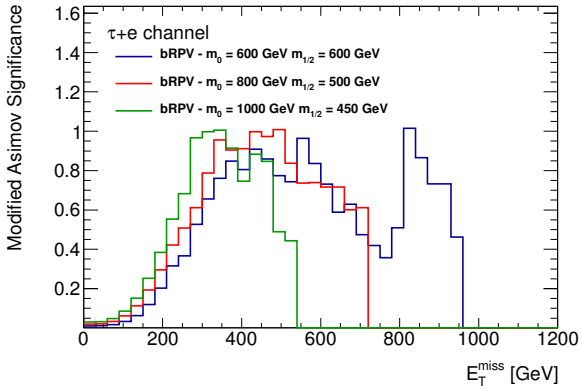

(d) z_A in the $\tau+e$ channel.

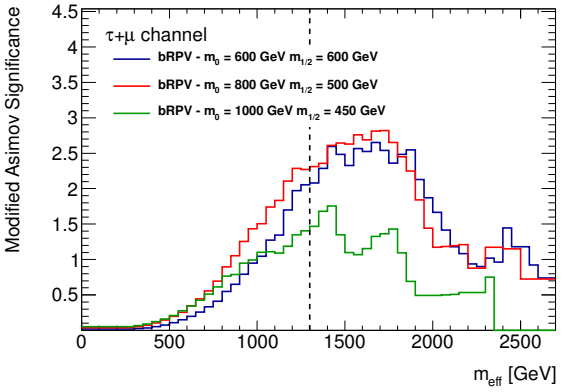

(e) z_A in the $\tau+\mu$ channel.

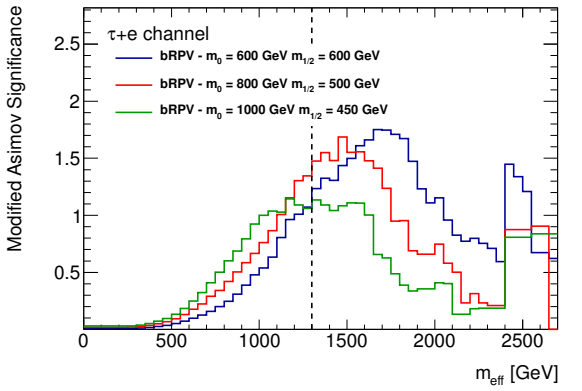

(f) z_A in the $\tau+e$ channel.

Figure A.9: Additional significance scans for the bRPV signal region after requiring $m_T^\ell > 100\,\text{GeV}$ and $N_{\text{jet}} \geq 4$.

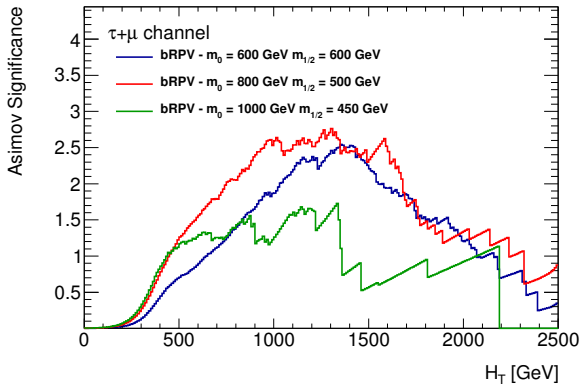

(a) z_A in the $\tau+\mu$ channel.

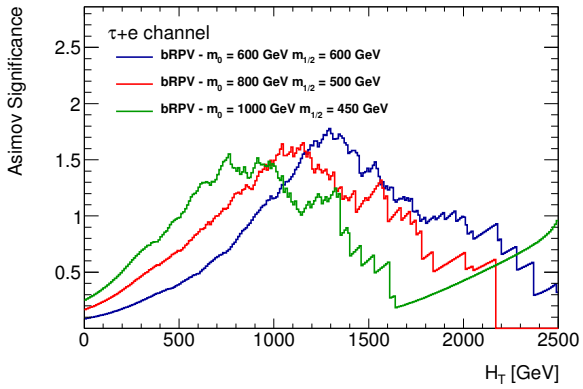

(b) z_A in the $\tau+e$ channel.

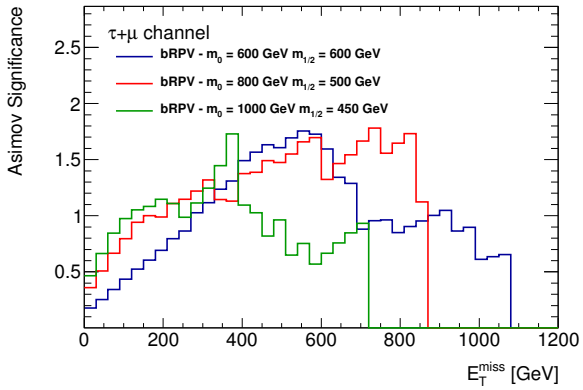

(c) z_A in the $\tau+\mu$ channel.

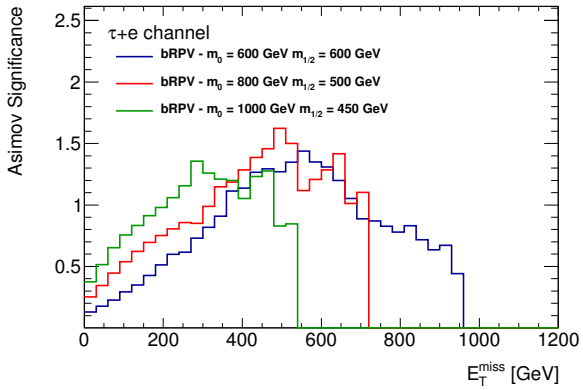

(d) z_A in the $\tau+e$ channel.

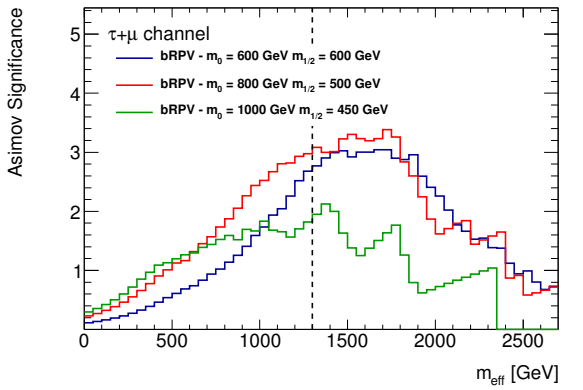

(e) z_A in the $\tau+\mu$ channel.

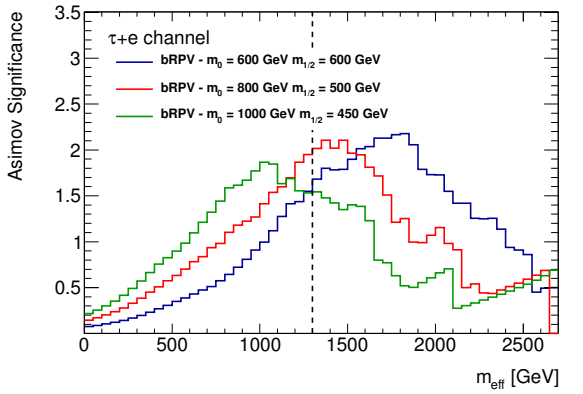

(f) z_A in the $\tau+e$ channel.

Figure A.10: Additional significance scans for the bRPV signal region $m_T^{\ell} > 100\,\text{GeV}$ and $N_{\text{jet}} \geq 4$. The SM background for these scans was fitted to smoothen the shape of the distribution.

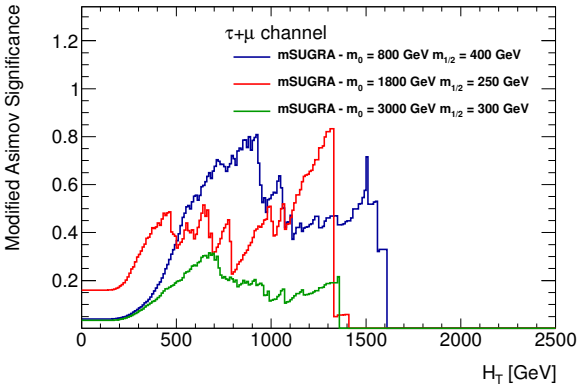

(a) z_A in the $\tau+\mu$ channel.

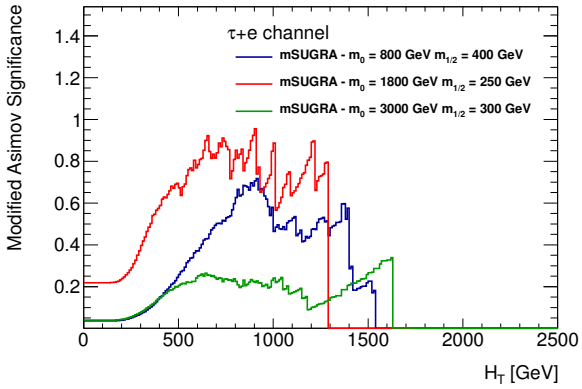

(b) z_A in the $\tau+e$ channel.

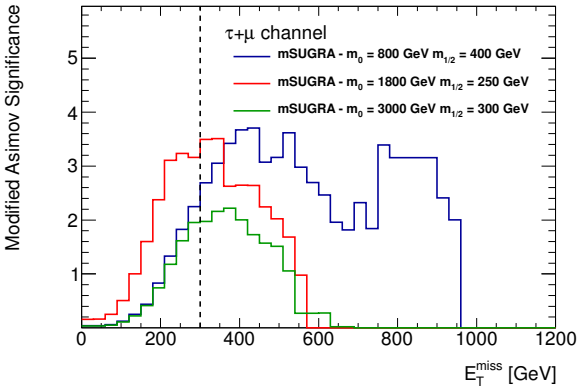

(c) z_A in the $\tau+\mu$ channel.

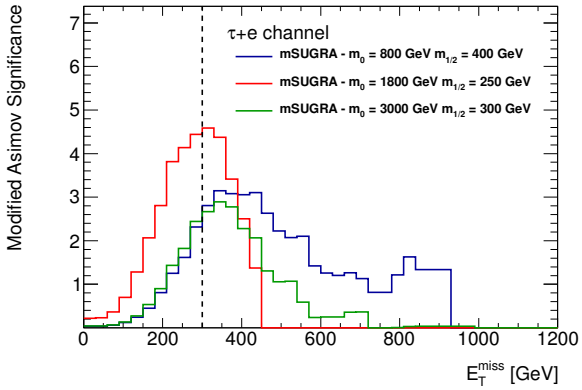

(d) z_A in the $\tau+e$ channel.

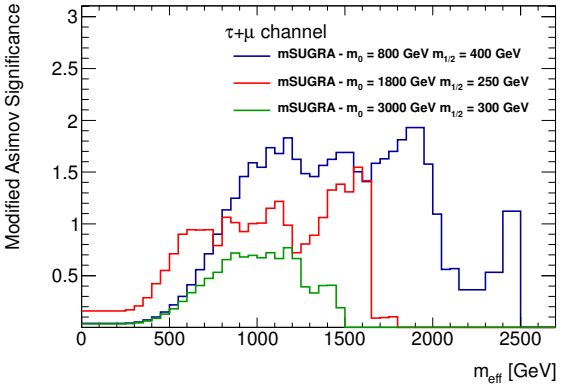

(e) z_A in the $\tau+\mu$ channel.

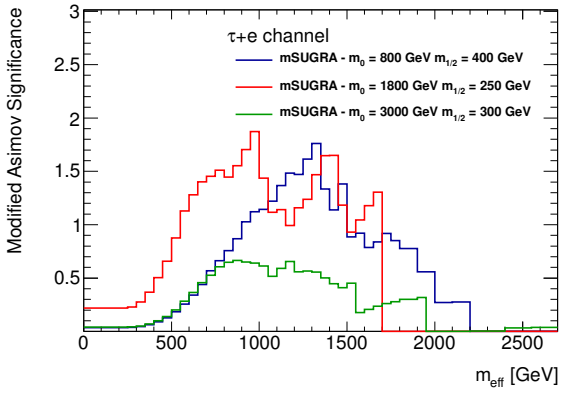

(f) z_A in the $\tau+e$ channel.

Figure A.11: Additional significance scans for the msugra signal region after requiring $m_T^\ell > 100\,\text{GeV}$ and $N_{\text{jet}} \geq 3$.

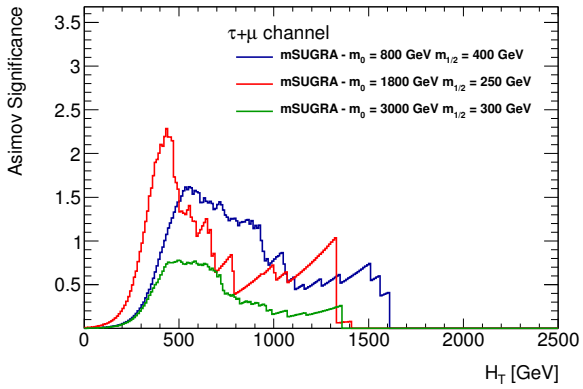

(a) z_A in the $\tau+\mu$ channel.

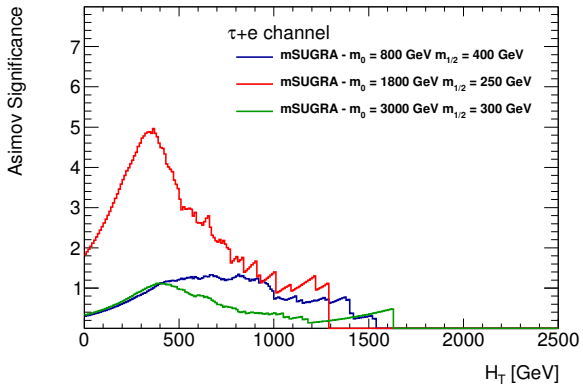

(b) z_A in the $\tau+e$ channel.

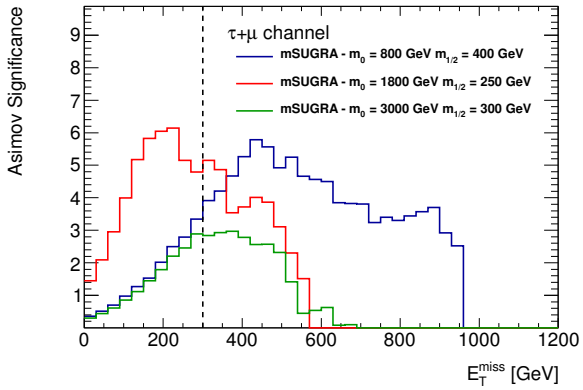

(c) z_A in the $\tau+\mu$ channel.

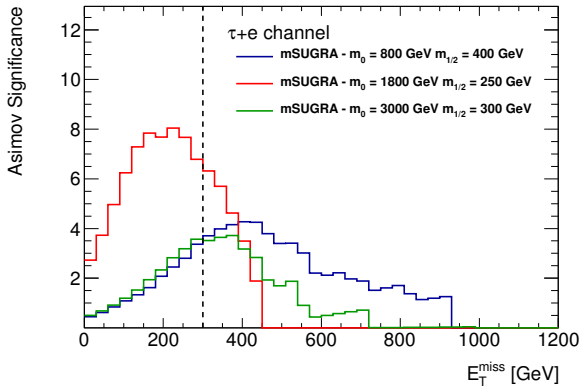

(d) z_A in the $\tau+e$ channel.

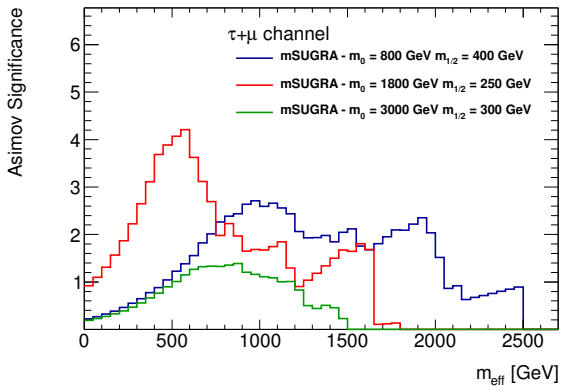

(e) z_A in the $\tau+\mu$ channel.

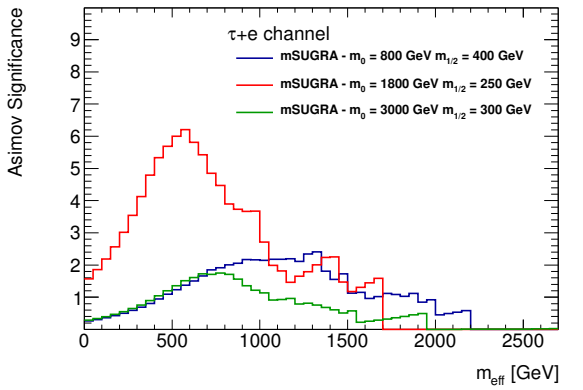

(f) z_A in the $\tau+e$ channel.

Figure A.12: Additional significance scans for the mSugra signal region $m_T^{\ell} > 100\,\text{GeV}$ and $N_{\text{jet}} \geq 3$. The SM background for these scans was fitted to smoothen the shape of the distribution.

A.3 Validation of the Top Quarks Correction

This section contains additional control distributions from the validation regions VR4 and VR5. These validation regions are used to ensure the correct description of the Top Quarks background after applying the correction on the p_T of the $t\bar{t}$ system as described in section 3.4.5. Displayed are E_T^{miss} and m_{eff} in figure A.13 and the transverse momenta of the tau lepton and the light lepton for VR4 in figure A.14. Figure A.15 displays E_T^{miss} and the transverse momenta of tau and light lepton for VR5. All distributions show good agreement between simulation and data.

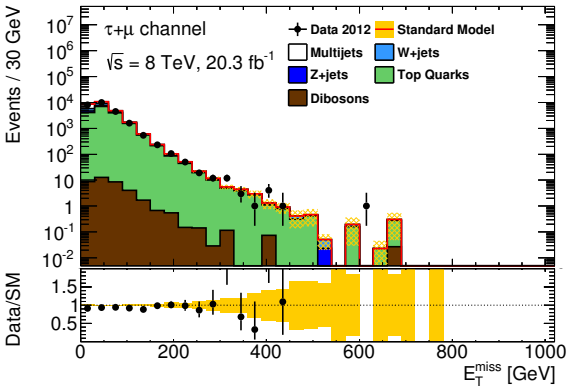

(a) E_T^{miss} in the $\tau+\mu$ channel.

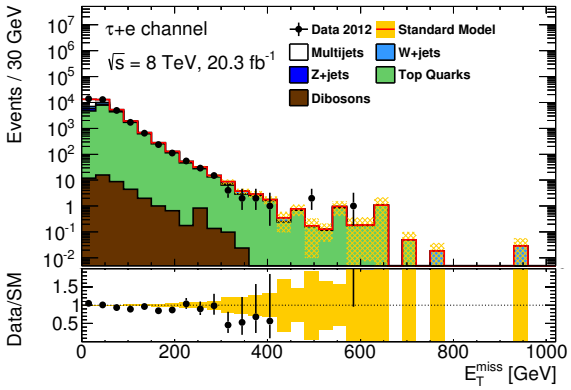

(b) E_T^{miss} in the $\tau+e$ channel.

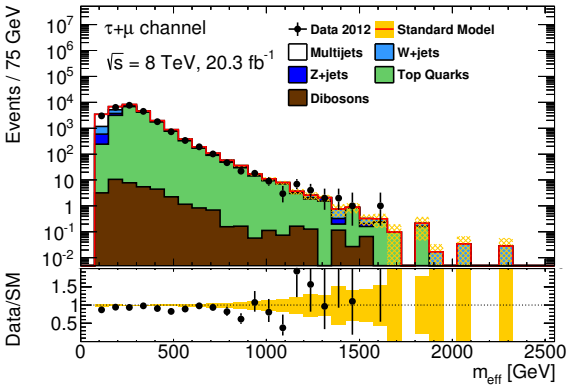

(c) m_{eff} in the $\tau+\mu$ channel.

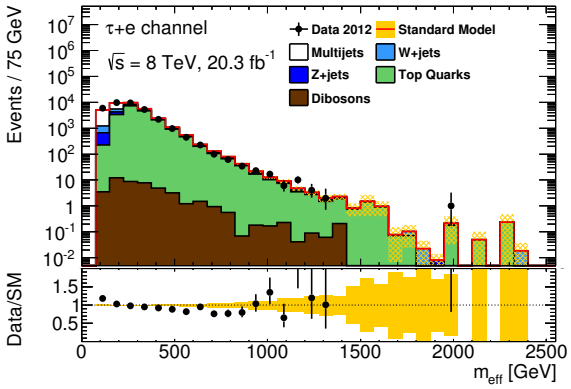

(d) m_{eff} in the $\tau+e$ channel.

Figure A.13: Control distributions in the Validation Region 4.

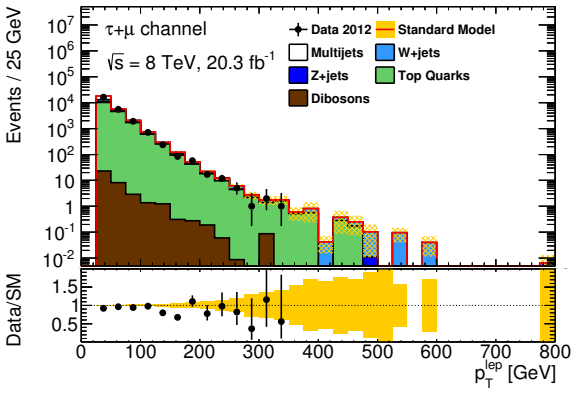

(a) p_{T}^{ℓ} in the $\tau+\mu$ channel.

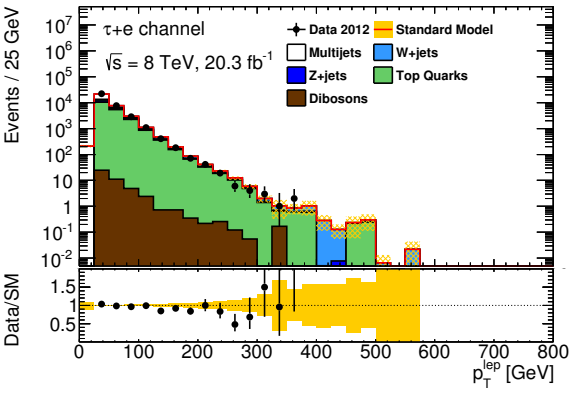

(b) p_{T}^{ℓ} in the $\tau+e$ channel.

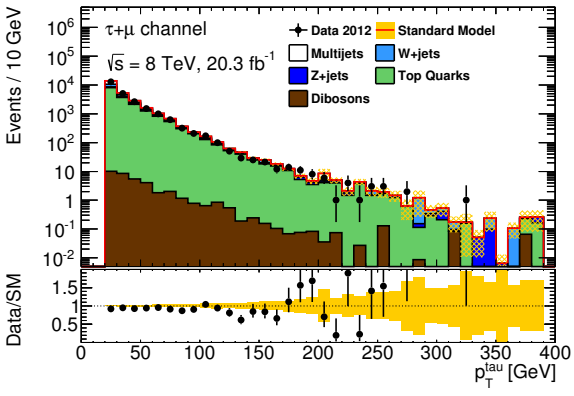

(c) p_{T}^{τ} in the $\tau+\mu$ channel.

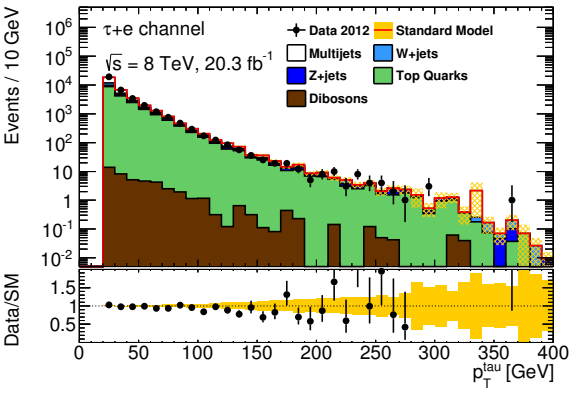

(d) p_{T}^{τ} in the $\tau+e$ channel.

Figure A.14: Control distributions in the Validation Region 5.

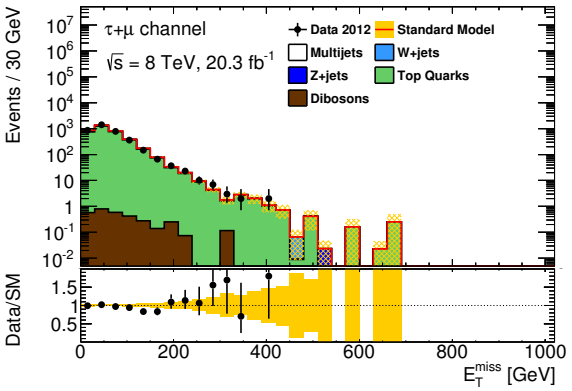

(a) $E_{\mathrm{T}}^{\mathrm{miss}}$ in the $\tau+\mu$ channel.

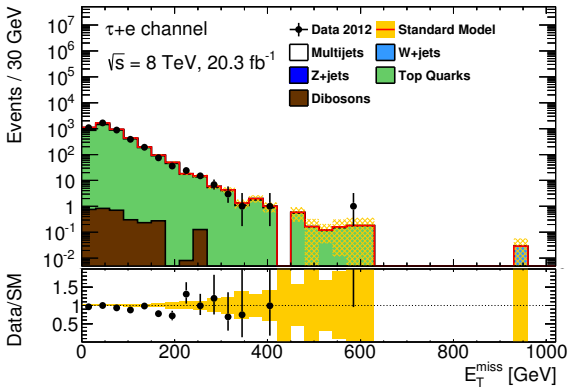

(b) $E_{\mathrm{T}}^{\mathrm{miss}}$ in the $\tau+e$ channel.

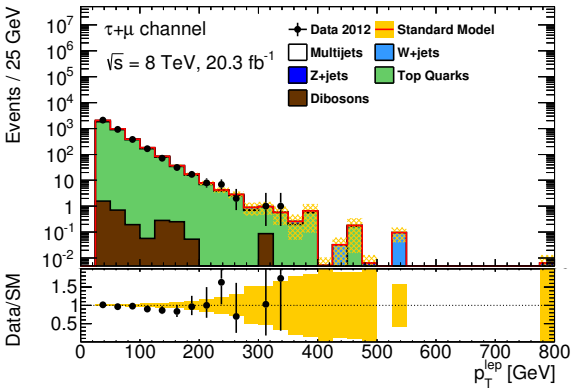

(c) p_{T}^{ℓ} in the $\tau+\mu$ channel.

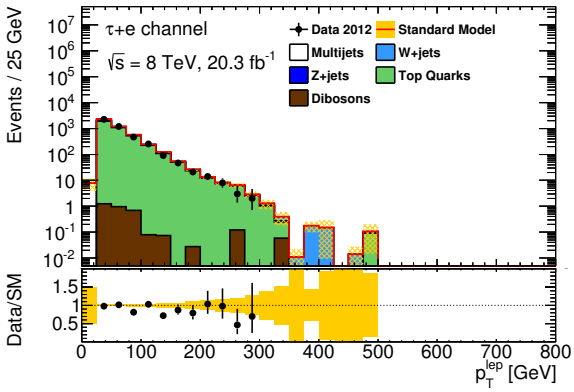

(d) p_{T}^{ℓ} in the $\tau+e$ channel.

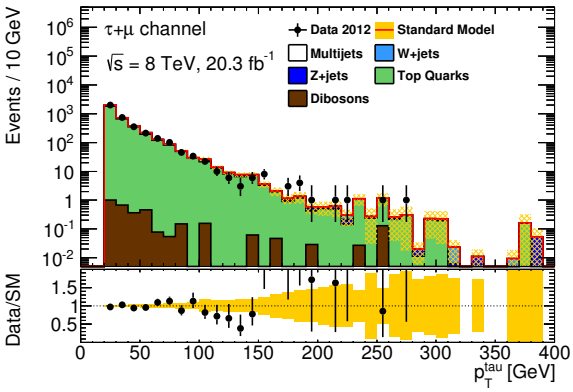

(e) p_{T}^{τ} in the $\tau+\mu$ channel.

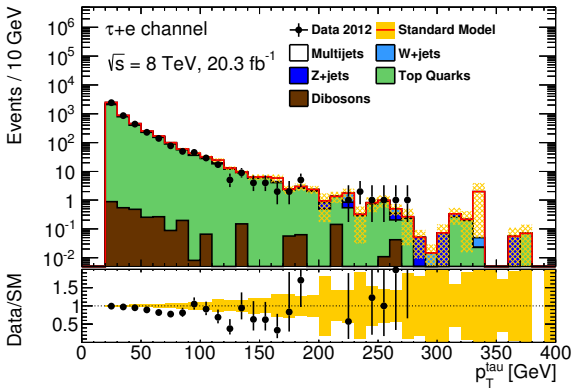

(f) p_{T}^{τ} in the $\tau+e$ channel.

Figure A.15: Control distributions in the Validation Region 5.

A.4 Additional Characteristics of the Signal Grids

This section contains additional signal grid distributions. Figures A.16 and A.17 display the expected and observed CLs for the four different SUSY scenarios. In figures A.18 and A.19 the values for acceptance and efficiency are shown.

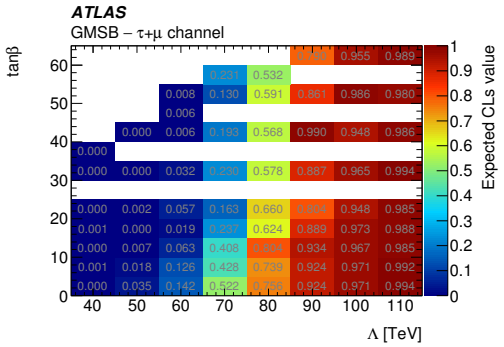

(a) Expected CLs for GMSB.

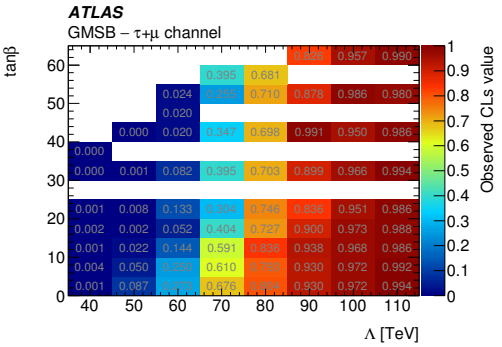

(b) Observed CLs for GMSB.

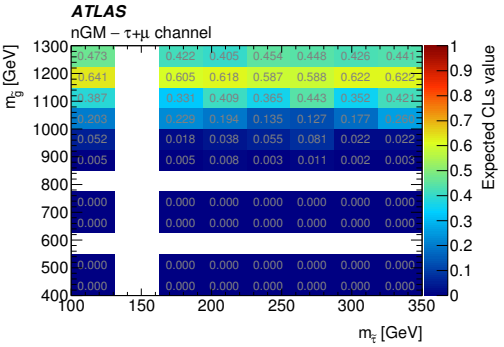

(c) Expected CLs for nGM.

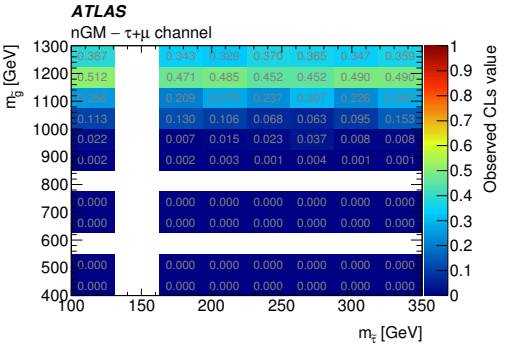

(d) Observed CLs for nGM.

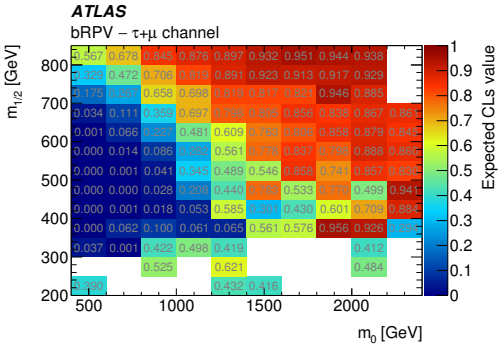

(e) Expected CLs for bRPV.

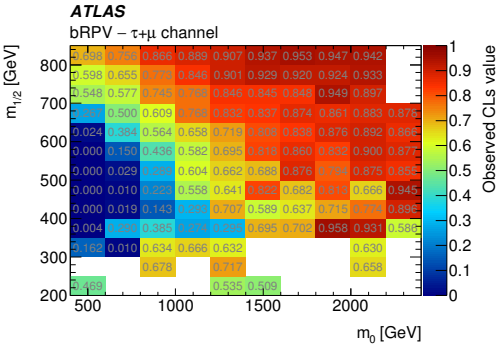

(f) Observed CLs for bRPV.

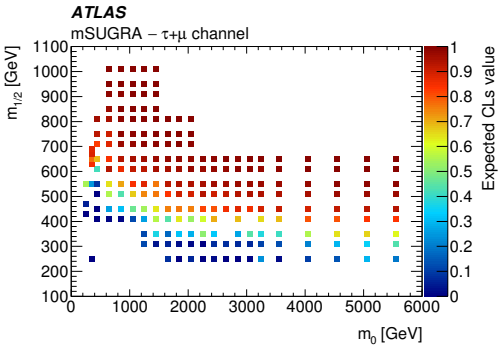

(g) Expected CLs for mSugra.

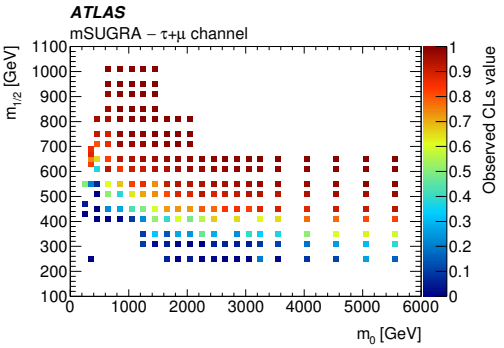

(h) Observed CLs for mSugra.

Figure A.16: Expected and observed CLs values for the various signal grids in the $\tau+\mu$ channel [2].

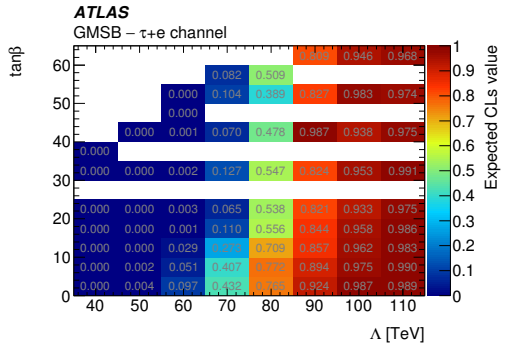

(a) Expected CLs for GMSB.

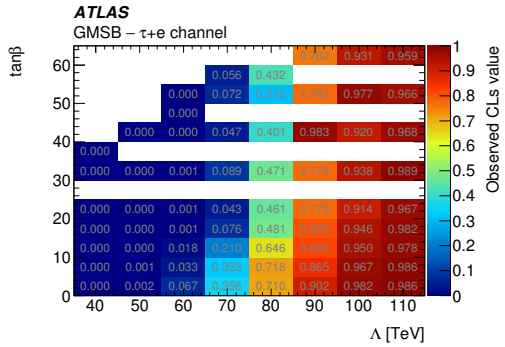

(b) Observed CLs for GMSB.

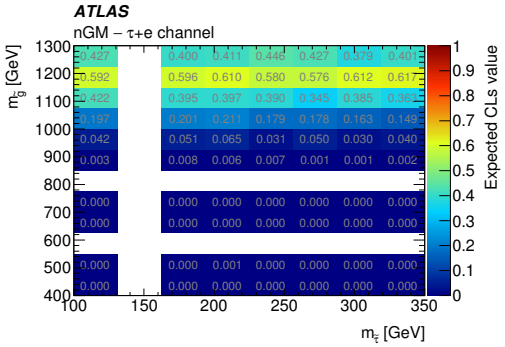

(c) Expected CLs for nGM.

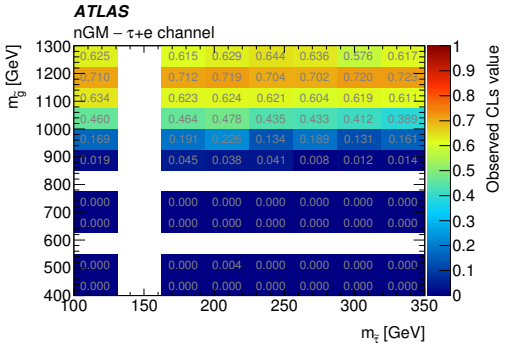

(d) Observed CLs for nGM.

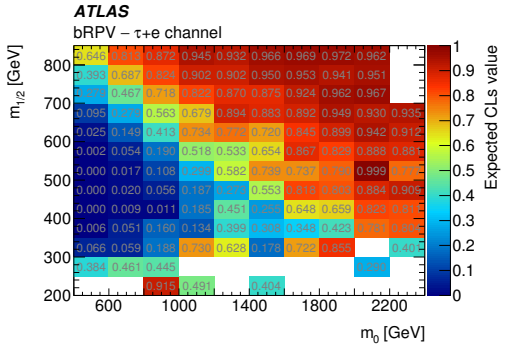

(e) Expected CLs for bRPV.

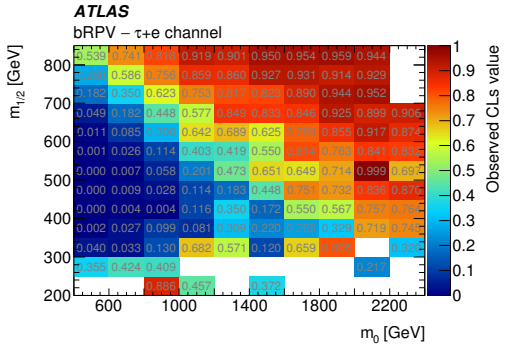

(f) Observed CLs for bRPV.

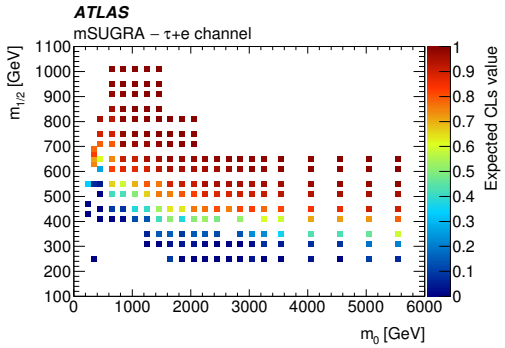

(g) Expected CLs for mSugra.

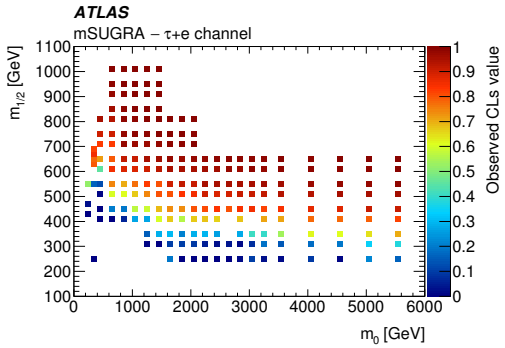

(h) Observed CLs for mSugra.

Figure A.17: Expected and observed CLs values for the various signal grids in the $\tau+e$ channel [2].

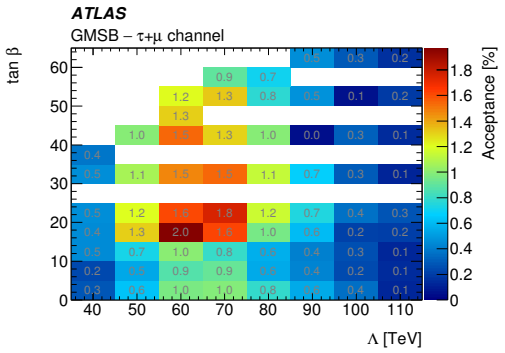

(a) Signal acceptance for the GMSB channel.

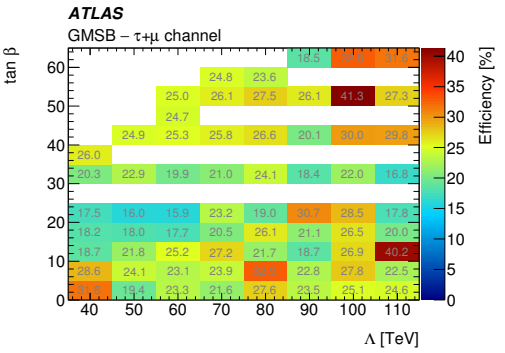

(b) Signal efficiency for the GMSB channel.

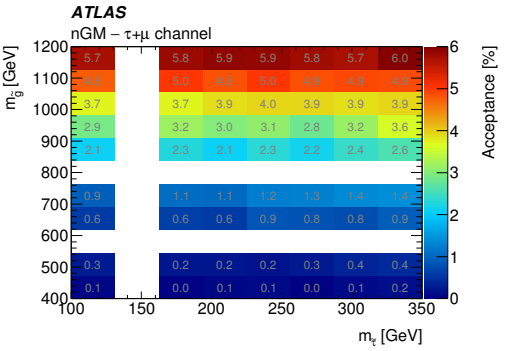

(c) Signal acceptance for the nGM channel.

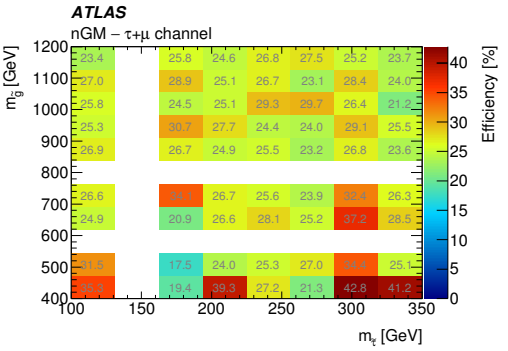

(d) Signal efficiency for the nGM channel.

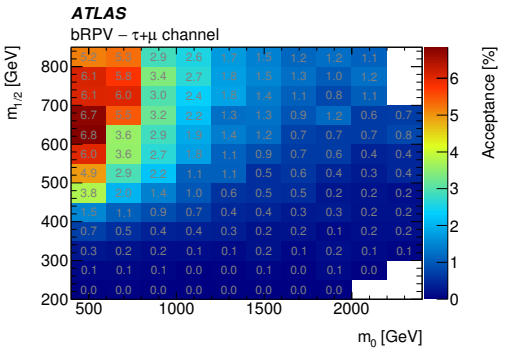

(e) Signal acceptance for the bRPV channel.

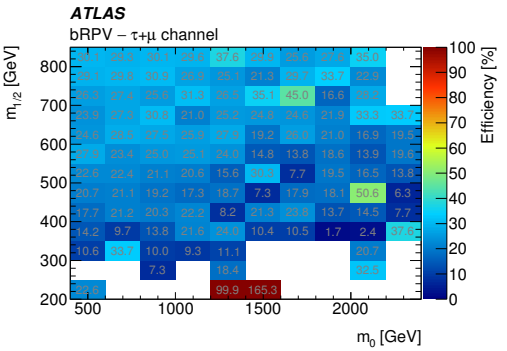

(f) Signal efficiency for the bRPV channel.

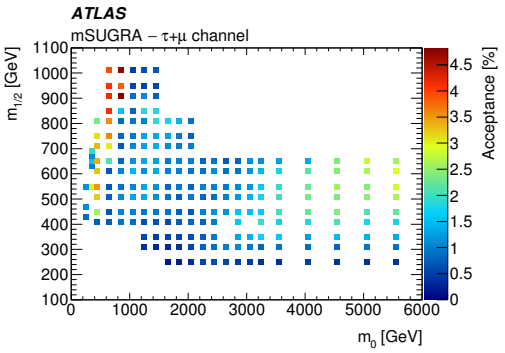

(g) Signal acceptance for the mSugra channel.

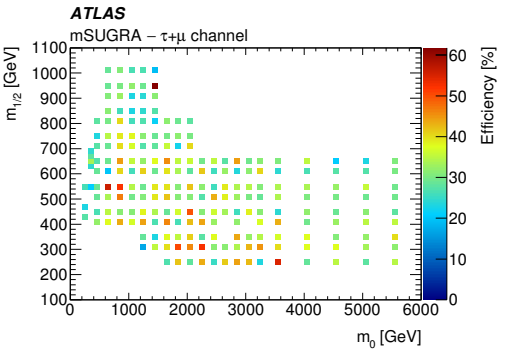

(h) Signal efficiency for the mSugra channel.

Figure A.18: Acceptance and efficiency for the various signal grids for the $\tau+\mu$ channel.

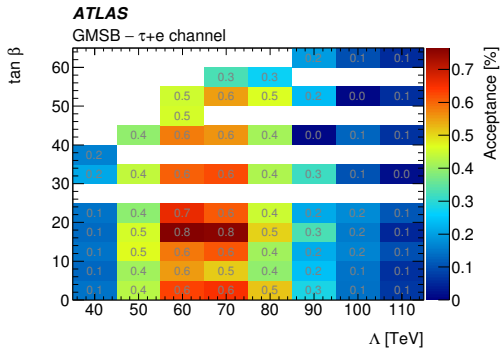

(a) Signal acceptance for the GMSB channel.

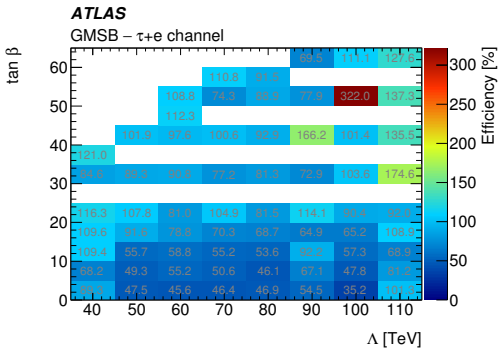

(b) Signal efficiency for the GMSB channel.

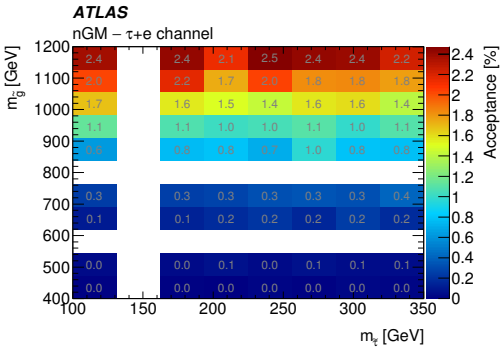

(c) Signal acceptance for the nGM channel.

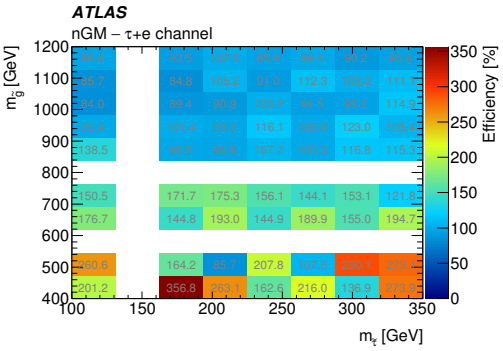

(d) Signal efficiency for the nGM channel.

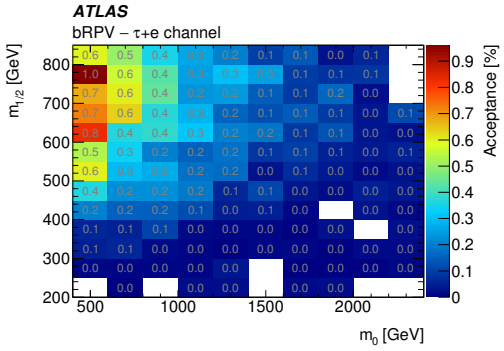

(e) Signal acceptance for the bRPV channel.

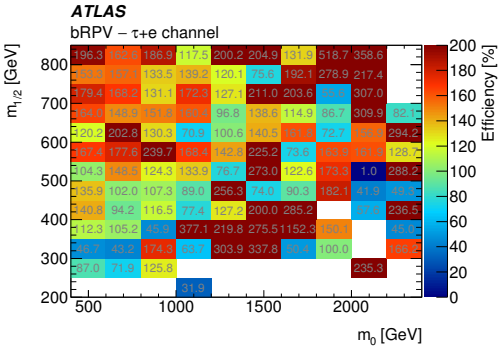

(f) Signal efficiency for the bRPV channel.

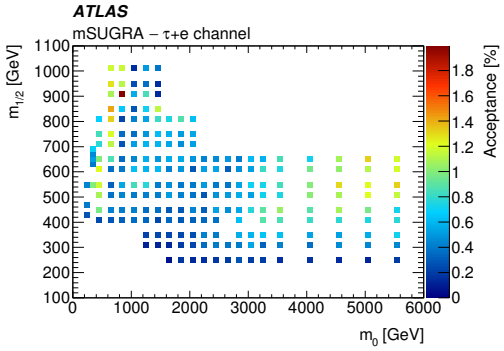

(g) Signal acceptance for the mSugra channel.

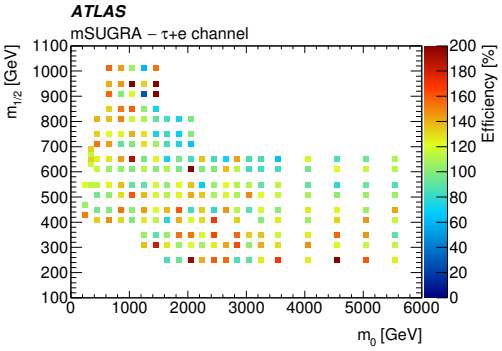

(h) Signal efficiency for the mSugra channel.

Figure A.19: Acceptance and efficiency for the various signal grids for the $\tau+e$ channel.

APPENDIX B

Additional Tables

B.1 Monte Carlo Samples

Sample ID	Name	Generator	xsec [pb]	k-factor	filter eff.	No. of events
117050	ttbar NoAllHad	PowhegPythia+AFII	253.00	1	0.543	74947917
108343	SingleTopSChanWenu	McAtNloJimmy	0.56	1.074	1.0	169183
108344	SingleTopSChanWmunu	McAtNloJimmy	0.56	1.074	1.0	169100
108345	SingleTopSChanWtaunu	McAtNloJimmy	0.56	1.074	1.0	169061
108346	SingleTopWtChanIncl	McAtNloJimmy	20.57	1.083	1.0	1766958
117360	t-channel $t \to ev$	AcerMCPythia	8.60	1.10	1.0	256853
117361	t-channel $t \to \mu\nu$	AcerMCPythia	8.60	1.10	1.0	256914
117362	t-channel $t \to \tau\nu$	AcerMCPythia	8.60	1.10	1.0	251341

Table B.1: Used $t\bar{t}$ and single t MC samples with their corresponding sample ID, event generator, cross-section[219], k-factor, filter efficiency and number of generated events.

Sample ID	Name	Generator	LO [pb]	k-factor	No. of events
164440	ttbarlnlnNp0_baseline	AlpgenJimmy	4.7930	1.737	799897
164441	ttbarlnlnNp1_baseline	AlpgenJimmy	5.0680	1.737	808897
164442	ttbarlnlnNp2_baseline	AlpgenJimmy	3.2570	1.737	529996
164444	ttbarlnlnNp3_baseline	AlpgenJimmy	1.5211	1.737	410000
164445	ttbarlnlnNp4p_baseline	AlpgenJimmy	0.7710	1.737	187997
164450	ttbarlnqqNp0_baseline	AlpgenJimmy	19.190	1.809	3359080
164451	ttbarlnqqNp1_baseline	AlpgenJimmy	20.290	1.809	3398787
164452	ttbarlnqqNp2_baseline	AlpgenJimmy	13.090	1.809	2209980
164454	ttbarlnqqNp3_baseline	AlpgenJimmy	6.0815	1.809	1499794
164455	ttbarlnqqNp4p_baseline	AlpgenJimmy	3.0844	1.809	556989
116108	ttbbincl	AlpgenJimmy	1.4345	1.689	299998
116109	ttccincl	AlpgenJimmy	2.7150	1.689	499997

Table B.2: Additional $t\bar{t}$ samples with their corresponding sample ID, event generator, NLO cross-section and number of generated events. Applying the k-factor yields the NNLO cross-sections.Those samples have helped validating the analyses and are used to compare to the prediction from the baseline $t\bar{t}$ sample in order to estimate the size of systematic uncertainty of the MC generator.

Sample ID	Name	$p_{\mathrm{T}}^{\mathrm{low}}$ [GeV]	$p_{\mathrm{T}}^{\mathrm{high}}$ [GeV]	Flavor Filter	AFII/FS	NLO [pb]	k-factor	filter eff.	No. of events
167749	Zee	0		BFilter	AFII	1110.7	1.12	0.028034	3999000
167750	Zee	0		CFilterBVeto	AFII	1109.6	1.12	0.28341	2999995
167751	Zee	0		CVetoBVeto	AFII	1107.1	1.12	0.68621	4978999
167752	Zmumu	0		BFilter	AFII	1109.8	1.12	0.027996	3997997
167753	Zmumu	0		CFilterBVeto	AFII	1112	1.12	0.28307	2987995
167754	Zmumu	0		CVetoBVeto	AFII	1108.7	1.12	0.6897	4413999
167755	Ztautau	0		BFilter	AFII	1109.1	1.12	0.02782	3997994
167756	Ztautau	0		CFilterBVeto	AFII	1110.2	1.12	0.28373	2998998
167757	Ztautau	0		CVetoBVeto	AFII	1112.1	1.12	0.68884	4979999
167758	Znunu	0		BFilter	AFII	5990.8	1.12	0.029387	24992972
167759	Znunu	0		CFilterBVeto	AFII	5988.3	1.12	0.28017	19957480
167760	Znunu	0		CVetoBVeto	AFII	5987.5	1.12	0.69045	23359980
180543	Zee	40	70	BFilter	AFII	70.493	1.12	0.070638	600000
180544	Zee	40	70	CFilterBVeto	AFII	70.53	1.12	0.34197	600000
180545	Zee	40	70	CVetoBVeto	AFII	70.431	1.12	0.58761	1049998
180546	Zmumu	40	70	BFilter	AFII	70.511	1.12	0.070707	599000
180547	Zmumu	40	70	CFilterBVeto	AFII	70.469	1.12	0.34141	599000
180548	Zmumu	40	70	CVetoBVeto	AFII	70.534	1.12	0.58768	1398999
180549	Ztautau	40	70	BFilter	AFII	70.441	1.12	0.070859	598999
180550	Ztautau	40	70	CFilterBVeto	AFII	70.538	1.12	0.34163	600000
180551	Ztautau	40	70	CVetoBVeto	AFII	70.528	1.12	0.58755	1399996
167797	Zee	70	140	BFilter	AFII	29.494	1.12	0.082517	1396999
167798	Zee	70	140	CFilterBVeto	AFII	29.487	1.12	0.35497	999999
167799	Zee	70	140	CVetoBVeto	AFII	29.491	1.12	0.56262	1999998
167800	Zmumu	70	140	BFilter	AFII	29.491	1.12	0.082585	1159000
167801	Zmumu	70	140	CFilterBVeto	AFII	29.447	1.12	0.35488	1000000
167802	Zmumu	70	140	CVetoBVeto	AFII	29.521	1.12	0.56196	1996998
167803	Ztautau	70	140	BFilter	FS	29.489	1.12	0.082563	1199396
167804	Ztautau	70	140	CFilterBVeto	FS	29.499	1.12	0.35509	979998
167805	Ztautau	70	140	CVetoBVeto	FS	29.494	1.12	0.56247	1999693
167806	Znunu	70	140	BFilter	AFII	166.63	1.12	0.084058	5078993
167807	Znunu	70	140	CFilterBVeto	AFII	166.64	1.12	0.35211	2998998
167808	Znunu	70	140	CVetoBVeto	AFII	166.62	1.12	0.5636	4999996

Table B.3: Used Sherpa Z+jets MC samples with their corresponding sample ID, event generator, p_{T} slices, flavor filter, detector simulation, NLO cross-section, k-factor, filter efficiency and number of generated events. These simulated with massive c and b quarks and massless light quarks. They are binned in the p_{T} of the Z boson. (continued in table B.4)

Sample ID	Name	p_T^{low} [GeV]	p_T^{high} [GeV]	Flavor Filter	AFII/FS	NLO [pb]	k-factor	filter eff.	No. of events
167809	Zee	140	280	BFilter	AFII	3.9901	1.12	0.095235	200000
167810	Zee	140	280	CFilterBVeto	AFII	3.9811	1.12	0.36919	399999
167811	Zee	140	280	CVetoBVeto	AFII	3.989	1.12	0.53431	600000
167812	Zmumu	140	280	BFilter	AFII	3.9842	1.12	0.095389	200000
167813	Zmumu	140	280	CFilterBVeto	AFII	3.9911	1.12	0.36999	389000
167814	Zmumu	140	280	CVetoBVeto	AFII	3.9841	1.12	0.53441	599500
167815	Ztautau	140	280	BFilter	FS	3.9878	1.12	0.095807	199900
167816	Ztautau	140	280	CFilterBVeto	FS	3.988	1.12	0.36953	399999
167817	Ztautau	140	280	CVetoBVeto	FS	3.9871	1.12	0.53328	598897
167818	Znunu	140	280	BFilter	AFII	22.512	1.12	0.096855	1000000
167819	Znunu	140	280	CFilterBVeto	AFII	22.52	1.12	0.36786	1989998
167820	Znunu	140	280	CVetoBVeto	AFII	22.514	1.12	0.53462	2979999
167821	Zee	280	500	BFilter	FS	0.24182	1.12	0.10851	20000
167822	Zee	280	500	CFilterBVeto	FS	0.24128	1.12	0.38744	49899
167823	Zee	280	500	CVetoBVeto	FS	0.24158	1.12	0.50617	39999
167824	Zmumu	280	500	BFilter	FS	0.24219	1.12	0.10802	19900
167825	Zmumu	280	500	CFilterBVeto	FS	0.24169	1.12	0.38643	50000
167826	Zmumu	280	500	CVetoBVeto	FS	0.24272	1.12	0.50549	50000
167827	Ztautau	280	500	BFilter	FS	0.2412	1.12	0.10653	19999
167828	Ztautau	280	500	CFilterBVeto	FS	0.24102	1.12	0.38481	50000
167829	Ztautau	280	500	CVetoBVeto	FS	0.24147	1.12	0.5072	49899
167830	Znunu	280	500	BFilter	FS	1.3533	1.12	0.10893	199999
167831	Znunu	280	500	CFilterBVeto	FS	1.3555	1.12	0.38402	239999
167832	Znunu	280	500	CVetoBVeto	FS	1.3527	1.12	0.50667	999892
167833	Zee	500		Bfilter	FS	0.013235	1.12	0.11573	9600
167834	Zee	500		CFilterBVeto	FS	0.013454	1.12	0.39846	10000
167835	Zee	500		CVetoBVeto	FS	0.013307	1.12	0.4848	50000
167836	Zmumu	500		BFilter	FS	0.013161	1.12	0.11408	10000
167837	Zmumu	500		CfilterBVeto	FS	0.01348	1.12	0.39857	10000
167838	Zmumu	500		CVetoBVeto	FS	0.013264	1.12	0.48689	10000
167839	Ztautau	500		BFilter	FS	0.013231	1.12	0.11524	10000
167840	Ztautau	500		CFilterBVeto	FS	0.013308	1.12	0.39316	10000
167841	Ztautau	500		CvetoBVeto	FS	0.013284	1.12	0.48562	50000
167842	Znunu	500		BFilter	FS	0.073103	1.12	0.11776	49999
167843	Znunu	500		CFilterBVeto	FS	0.073347	1.12	0.39631	50000
167844	Znunu	500		CVetoBVeto	FS	0.073278	1.12	0.48436	199699

Table B.4: Used Sherpa Z+jets MC samples continued from table B.3.

Sample ID	Name	p_T^{low} [GeV]	p_T^{high} [GeV]	Flavor Filter	AFII/FS	NLO [pb]	k-factor	filter eff.	No. of events
167740	Wenu	0		BFilter	AFII	10973	1.11	0.012778	14977980
167741	Wenu	0		CFilterBVeto	AFII	10971	1.11	0.049039	9998989
167742	Wenu	0		CVetoBVeto	AFII	10987	1.11	0.93804	48415976
167743	Wmunu	0		BFilter	AFII	10973	1.11	0.012823	14989485
167744	Wmunu	0		CFilterBVeto	AFII	10970	1.11	0.04254	9872485
167745	Wmunu	0		CVetoBVeto	AFII	10981	1.11	0.94461	48856968
167746	Wtaunu	0		BFilter	AFII	10974	1.11	0.012791	14850862
167747	Wtaunu	0		CFilterBVeto	AFII	10971	1.11	0.046082	9993984
167748	Wtaunu	0		CVetoBVeto	AFII	10969	1.11	0.94065	49640972
180534	Wenu	40	70	BFilter	AFII	652.82	1.11	0.034473	1100000
180535	Wenu	40	70	CFilterBVeto	AFII	652.83	1.11	0.17142	899999
180536	Wenu	40	70	CVetoBVeto	AFII	653.16	1.11	0.79335	16947492
180537	Wmunu	40	70	BFilter	AFII	652.73	1.11	0.034565	1097999
180538	Wmunu	40	70	CFilterBVeto	AFII	653.14	1.11	0.16599	900000
180539	Wmunu	40	70	CVetoBVeto	AFII	653.06	1.11	0.79983	16978984
180540	Wtaunu	40	70	BFilter	AFII	652.84	1.11	0.034574	1099999
180541	Wtaunu	40	70	CFilterBVeto	AFII	652.58	1.11	0.16931	889999
180542	Wtaunu	40	70	CVetoBVeto	AFII	652.99	1.11	0.79616	15166494
167761	Wenu	70	140	BFilter	AFII	250.55	1.11	0.045931	2000000
167762	Wenu	70	140	CFilterBVeto	AFII	250.71	1.11	0.20099	2996497
167763	Wenu	70	140	CVetoBVeto	AFII	250.43	1.11	0.75298	14908986
167764	Wmunu	70	140	BFilter	AFII	250.55	1.11	0.045919	1988999
167765	Wmunu	70	140	CFilterBVeto	AFII	250.57	1.11	0.19889	2995999
167766	Wmunu	70	140	CVetoBVeto	AFII	250.77	1.11	0.75855	14931984
167767	Wtaunu	70	140	BFilter	FS	250.57	1.11	0.045942	1999893
167768	Wtaunu	70	140	CFilterBVeto	FS	250.61	1.11	0.19889	2999890
167769	Wtaunu	70	140	CVetoBVeto	FS	250.6	1.11	0.75485	14928649

Table B.5: Used Sherpa W+jets MC samples with their corresponding sample ID, event generator, p_T slices, flavor filter, detector simulation, NLO cross-section, k-factor, filter efficiency and number of generated events. These simulated with massive c and b quarks and massless light quarks. They are binned in the p_T of the W boson. (continued in table B.6)

Sample ID	Name	p_T^{low} [GeV]	p_T^{high} [GeV]	Flavor Filter	AFII/FS	NLO [pb]	k-factor	filter eff.	No. of events
167770	Wenu	140	280	BFilter	AFII	31.155	1.11	0.063159	999999
167771	Wenu	140	280	CFilterBVeto	AFII	31.189	1.11	0.22196	1999997
167772	Wenu	140	280	CVetoBVeto	AFII	31.112	1.11	0.71496	2000000
167773	Wmunu	140	280	BFilter	AFII	31.164	1.11	0.063069	997497
167774	Wmunu	140	280	CFilterBVeto	AFII	31.165	1.11	0.21647	1985998
167775	Wmunu	140	280	CVetoBVeto	AFII	31.173	1.11	0.7203	1993999
167776	Wtaunu	140	280	BFilter	FS	31.162	1.11	0.063078	989797
167777	Wtaunu	140	280	CFilterBVeto	FS	31.151	1.11	0.22015	1998688
167778	Wtaunu	140	280	CVetoBVeto	FS	31.176	1.11	0.71609	1999994
167779	Wenu	280	500	BFilter	FS	1.8413	1.11	0.082886	99998
167780	Wenu	280	500	CFilterBVeto	FS	1.837	1.11	0.23454	199898
167781	Wenu	280	500	CVetoBVeto	FS	1.8426	1.11	0.682	499891
167782	Wmunu	280	500	BFilter	FS	1.838	1.11	0.082902	100000
167783	Wmunu	280	500	CFilterBVeto	FS	1.8395	1.11	0.22845	199998
167784	Wmunu	280	500	CVetoBVeto	FS	1.8433	1.11	0.68776	499698
167785	Wtaunu	280	500	BFilter	FS	1.8362	1.11	0.083026	100000
167786	Wtaunu	280	500	CFilterBVeto	FS	1.8395	1.11	0.23271	199998
167787	Wtaunu	280	500	CVetoBVeto	FS	1.8368	1.11	0.68397	499998
167788	Wenu	500		BFilter	FS	0.10188	1.11	0.099655	10000
167789	Wenu	500		CFilterBVeto	FS	0.10101	1.11	0.2444	10000
167790	Wenu	500		CVetoBVeto	FS	0.10093	1.11	0.65741	10000
167791	Wmunu	500		BFilter	FS	0.10163	1.11	0.10004	10000
167792	Wmunu	500		CFilterBVeto	FS	0.1021	1.11	0.23852	10000
167793	Wmunu	500		CVetoBVeto	FS	0.10186	1.11	0.65837	49700
167794	Wtaunu	500		BFilter	FS	0.10208	1.11	0.099663	10000
167795	Wtaunu	500		CFilterBVeto	FS	0.10139	1.11	0.24221	10000
167796	Wtaunu	500		CVetoBVeto	FS	0.10201	1.11	0.66004	49998

Table B.6: Used Sherpa W+jets MC samples continued from table B.5.

Sample ID	Name	Generator	LO [pb]	k-factor	filter eff.	No. of events
107680	WenuNp0	AlpgenJimmy	8037.1	1.186	1	3459718
107681	WenuNp1	AlpgenJimmy	1579.2	1.186	1	2499797
107682	WenuNp2	AlpgenJimmy	477.2	1.186	1	3769889
107683	WenuNp3	AlpgenJimmy	133.9	1.186	1	1009965
107684	WenuNp4	AlpgenJimmy	35.6	1.186	1	249999
107685	WenuNp5	AlpgenJimmy	10.5	1.186	1	70000
107690	WmunuNp0	AlpgenJimmy	8040.0	1.186	1	3469591
107691	WmunuNp1	AlpgenJimmy	1580.3	1.186	1	2499893
107692	WmunuNp2	AlpgenJimmy	477.5	1.186	1	3769890
107693	WmunuNp3	AlpgenJimmy	133.9	1.186	1	1009896
107694	WmunuNp4	AlpgenJimmy	35.6	1.186	1	255000
107695	WmunuNp5	AlpgenJimmy	10.5	1.186	1	20000
107700	WtaunuNp0	AlpgenJimmy	8035.8	1.186	1	3364789
107701	WtaunuNp1	AlpgenJimmy	1579.8	1.186	1	2449991
107702	WtaunuNp2	AlpgenJimmy	477.5	1.186	1	3719888
107703	WtaunuNp3	AlpgenJimmy	133.7	1.186	1	1009993
107704	WtaunuNp4	AlpgenJimmy	35.5	1.186	1	249898
107705	WtaunuNp5	AlpgenJimmy	10.5	1.186	1	65000
117284	WccNp0	AlpgenJimmy	150.19	1.186	1	1274998
117285	WccNp1	AlpgenJimmy	132.68	1.186	1	1049997
117286	WccNp2	AlpgenJimmy	71.80	1.186	1	552899
117287	WccNp3	AlpgenJimmy	30.26	1.186	1	170000
117293	WcNp0	AlpgenJimmy	807.89	1.186	1	6489181
117294	WcNp1	AlpgenJimmy	267.61	1.186	1	2069695
117295	WcNp2	AlpgenJimmy	69.82	1.186	1	519999
117296	WcNp3	AlpgenJimmy	20.54	1.186	1	110000
117297	WcNp4	AlpgenJimmy	4.30	1.186	1	20000
107280	WbbNp0	AlpgenJimmy	55.68	1.186	1	474999
107281	WbbNp1	AlpgenJimmy	45.24	1.186	1	359999
107282	WbbNp2	AlpgenJimmy	23.24	1.186	1	174999
107283	WbbNp3	AlpgenJimmy	11.14	1.186	1	50000

Table B.7: Additionally used W+jets MC samples with their corresponding sample ID, event generator, LO cross-section, k-factor, and number of generated events. The overlap between nominal and heavy flavor samples is removed using the heavy flavor overlap prescription (HFOR).

Sample ID	Name	Generator	LO [pb]	k-factor	filter eff.	No. of events
172001	WenuNp1_susyfilt	AlpgenJimmy	12.70	1.186	1	1999991
172002	WenuNp2_susyfilt	AlpgenJimmy	8.95	1.186	1	1492993
172003	WenuNp3_susyfilt	AlpgenJimmy	4.33	1.186	1	1249989
172004	WenuNp4_susyfilt	AlpgenJimmy	1.70	1.186	1	399498
172005	WenuNp5_susyfilt	AlpgenJimmy	0.55	1.186	1	109899
172006	WenuNp6_susyfilt	AlpgenJimmy	0.19	1.186	1	20000
172011	WmunuNp1_susyfilt	AlpgenJimmy	12.68	1.186	1	1999795
172012	WmunuNp2_susyfilt	AlpgenJimmy	8.96	1.186	1	1499993
172013	WmunuNp3_susyfilt	AlpgenJimmy	4.33	1.186	1	1249296
172014	WmunuNp4_susyfilt	AlpgenJimmy	1.70	1.186	1	399898
172015	WmunuNp5_susyfilt	AlpgenJimmy	0.56	1.186	1	109998
172016	WmunuNp6_susyfilt	AlpgenJimmy	0.19	1.186	1	20000
172021	WtaunuNp1_susyfil	AlpgenJimmy	46.38	1.186	0.3475	3994886
172022	WtaunuNp2_susyfil	AlpgenJimmy	34.30	1.186	0.3349	2794687
172023	WtaunuNp3_susyfil	AlpgenJimmy	17.05	1.186	0.3269	1234793
172024	WtaunuNp4_susyfil	AlpgenJimmy	6.55	1.186	0.3360	549496
172025	WtaunuNp5_susyfil	AlpgenJimmy	2.04	1.186	0.3543	150000
172026	WtaunuNp6_susyfil	AlpgenJimmy	0.66	1.186	0.3812	30000

Table B.8: Additionally used W+jets MC samples with their corresponding sample ID, event generator, LO cross-section, k-factor and number of generated events. These "susyfilt" have been produced with a truth level filter requiring one jet of at least 80 GeV p_{T} and at least 100 GeV of missing transverse energy. Overlap between those and the inclusive samples from table B.8 is removed by applying corresponding veto cuts.

Sample ID	Name	Generator	LO [pb]	k-factor	No. of events
147105	ZeeNp0	AlpgenPythia	718.97	1.18	6298988
147106	ZeeNp1	AlpgenPythia	175.7	1.18	8199476
147107	ZeeNp2	AlpgenPythia	58.875	1.18	3175991
147108	ZeeNp3	AlpgenPythia	15.636	1.18	814995
147109	ZeeNp4	AlpgenPythia	4.0116	1.18	348597
147110	ZeeNp5Incl	AlpgenPythia	1.2592	1.18	219700
147113	ZmumuNp0	AlpgenPythia	719.16	1.18	6288796
147114	ZmumuNp1	AlpgenPythia	175.74	1.18	8088384
147115	ZmumuNp2	AlpgenPythia	58.882	1.18	3175488
147116	ZmumuNp3	AlpgenPythia	15.673	1.18	844799
147117	ZmumuNp4	AlpgenPythia	4.0057	1.18	378200
147118	ZmumuNp5Incl	AlpgenPythia	1.2544	1.18	179200
147121	ZtautauNp0	AlpgenPythia	718.87	1.18	16797868
147122	ZtautauNp1	AlpgenPythia	175.76	1.18	10679582
147123	ZtautauNp2	AlpgenPythia	58.856	1.18	3740893
147124	ZtautauNp3	AlpgenPythia	15.667	1.18	1011994
147125	ZtautauNp4	AlpgenPythia	4.0121	1.18	378798
147126	ZtautauNp5Incl	AlpgenPythia	1.256	1.18	209799

Table B.9: Additionally used Z+jets MC samples for Z decaying to charged leptons listed with their corresponding sample ID, event generator, LO cross section, k-factor and number of generated events.

Sample ID	Name	Generator	LO [pb]	k-factor	No. of events
200332	ZeebbNp0	AlpgenPythia	0.45959	1.18	1629895
200333	ZeebbNp1	AlpgenPythia	0.33059	1.18	619997
200334	ZeebbNp2	AlpgenPythia	0.14807	1.18	170000
200335	ZeebbNp3Incl	AlpgenPythia	0.079647	1.18	109997
200340	ZmuumbbNp0	AlpgenPythia	0.45871	1.18	1529994
200341	ZmumubbNp1	AlpgenPythia	0.33007	1.18	449700
200342	ZmumubbNp2	AlpgenPythia	0.14886	1.18	219999
200343	ZmumubbNp3Incl	AlpgenPythia	0.079763	1.18	109499
200348	ZtautaubbNp0	AlpgenPythia	0.45949	1.18	259999
200349	ZtautaubbNp1	AlpgenPythia	0.32987	1.18	90000
200350	ZtautaubbNp2	AlpgenPythia	0.14796	1.18	50000
200351	ZtautaubbNp3Incl	AlpgenPythia	0.079949	1.18	50000
200432	ZeeccNp0	AlpgenPythia	0.41161	1.18	279998
200433	ZeeccNp1	AlpgenPythia	0.29829	1.18	169499
200434	ZeeccNp2	AlpgenPythia	0.13703	1.18	100000
200435	ZeeccNp3Incl	AlpgenPythia	0.07637	1.18	50000
200440	ZmuumccNp0	AlpgenPythia	0.4114	1.18	289798
200441	ZmumuccNp1	AlpgenPythia	0.29799	1.18	190000
200442	ZmumuccNp2	AlpgenPythia	0.13717	1.18	90000
200443	ZmumuccNp3Incl	AlpgenPythia	0.07637	1.18	40000
200448	ZtautauccNp0	AlpgenPythia	0.41194	1.18	269999
200449	ZtautauccNp1	AlpgenPythia	0.29787	1.18	159900
200450	ZtautauccNp2	AlpgenPythia	0.13705	1.18	100000
200451	ZtautauccNp3Incl	AlpgenPythia	0.07655	1.18	49999

Table B.10: Addtionally used Z+jets MC samples for Z decaying to charged leptons produced with heavy flavor quarks listed with their corresponding sample ID, event generator, LO cross section, k-factor and number of generated events. In the 1τ analysis they entered studies on the Z+jets scale factor. The overlap between nominal and heavy flavor samples is removed using the heavy flavor overlap prescription (HFOR).

Sample ID	Name (event generator: AlpgenJimmy)	NLO [pb]	k-factor	filter eff.	No. of events
156803	ZnunuNp0_filt1jet	4151.5	1.23	0.00646	5000
156804	ZnunuNp1_filt1jet	892.4	1.23	0.455	85000
156808	ZnunuNp1_met70_filt1jet	69.51	1.0	0.999	75000
156805	ZnunuNp1_met140_filt1jet	6.032	1.0	1.0	95000
156806	ZnunuNp1_met280_filt1jet	0.243	1.0	1.0	25000
156807	ZnunuNp1_met500_filt1jet	0.00895	1.0	1.0	5000
156809	ZnunuNp2_filt1jet	282.1	1.23	0.761	40000
156813	ZnunuNp2_met70_filt1jet	60.97	1.0	0.991	100000
156810	ZnunuNp2_met140_filt1jet	8.00	1.0	1.0	150000
156811	ZnunuNp2_met280_filt1jet	0.46	1.0	1.0	50000
156812	ZnunuNp2_met500_filt1jet	0.0229	1.0	1.0	13000
156814	ZnunuNp3_filt1jet	82.0	1.23	0.906	15000
156818	ZnunuNp3_met70_filt1jet	27.54	1.0	0.986	75000
156815	ZnunuNp3_met140_filt1jet	5.244	1.0	1.0	110000
156816	ZnunuNp3_met280_filt1jet	0.392	1.0	1.0	50000
156817	ZnunuNp3_met500_filt1jet	0.0227	1.0	1.0	13000
156819	ZnunuNp4_filt1jet	21.6	1.23	0.965	4000
156823	ZnunuNp4_met70_filt1jet	9.432	1.0	0.993	25000
156820	ZnunuNp4_met140_filt1jet	2.347	1.0	1.0	120000
156821	ZnunuNp4_met280_filt1jet	0.220	1.0	1.0	45000
156822	ZnunuNp4_met500_filt1jet	0.0142	1.0	1.0	10000
156824	ZnunuNp5_filt1jet	6.6	1.23	0.989	8000
156828	ZnunuNp5_met70_filt1jet	3.352	1.0	0.998	19000
156825	ZnunuNp5_met140_filt1jet	1.042	1.0	1.0	30000
156826	ZnunuNp5_met280_filt1jet	0.121	1.0	1.0	17000
156827	ZnunuNp5_met500_filt1jet	0.00876	1.0	1.0	4000

Table B.11: MC samples for Z+jets with the Z decaying to neutrino pairs, generated with AlpgenJimmy and listed with their corresponding sample ID, LO cross section, k-factor, filter efficiency, NNLO cross-section,and number of generated events. The event generator version corresponds to the ATLAS release (tag `e1601`), which has the meson energy deposits correctly simulated. They are filtered for the presence of at least one jet and various levels of $E_{\mathrm{T}}^{\mathrm{miss}}$ from 0 to 500 GeV. Double counting of cross-section is prevented by excluding from a given sample the $E_{\mathrm{T}}^{\mathrm{miss}}$ filtered range of all higher filters.

Sample ID	Generator	Final state	NLO [pb]	k-factor	No. of events
126892	Sherpa	$W^+W^- \to \ell\nu\ell\nu$	5.50	1.06	2699994
126893	Sherpa	$W^\pm Z \to \ell\ell\ell\nu$	9.75	1.05	2699893
126894	Sherpa	$ZZ \to \ell\ell\ell\ell$	8.74	1.00	3799491
126895	Sherpa	$ZZ \to \ell\ell\nu\ell\nu$	0.496	1.05	899899

Table B.12: Used diboson MC samples with their corresponding sample ID, event generator, final state, NLO cross section, k-factor and number of generated events.

Sample ID	Name (event generator: Powheg+Pythia8)	NLO [pb]	k-factor	filter eff.	No. of events
126928	WpWm_ee	0.598	1.078	1.000	599700
126929	WpWm_me	0.597	1.079	1.000	600000
126930	WpWm_te	0.598	1.079	1.000	580000
126931	WpWm_em	0.598	1.078	1.000	589999
126932	WpWm_mm	0.597	1.079	1.000	600000
126933	WpWm_tm	0.597	1.079	1.000	599798
126934	WpWm_et	0.597	1.080	1.000	580000
126935	WpWm_mt	0.598	1.079	1.000	599999
126936	WpWm_tt	0.598	1.079	1.000	580000
126937	ZZ_4e_mll4_2pt5	0.077	1.000	0.908	1099997
126938	ZZ_2e2mu_mll4_2pt5	0.176	1.000	0.827	1599696
126939	ZZ_2e2tau_mll4_2pt5	0.175	1.000	0.583	1079798
126940	ZZ_4mu_mll4_2pt5	0.077	1.000	0.912	1099798
126941	ZZ_2mu2tau_mll4_2pt5	0.175	1.000	0.587	1069799
126942	ZZ_4tau_mll4_2pt5	0.077	1.000	0.106	299999
126949	ZZllnunu_ee_mll4	0.054	3.000	1.000	299400
126950	ZZllnunu_mm_mll4	0.054	3.000	1.000	300000
126951	ZZllnunu_tt_mll4	0.054	3.000	1.000	299999

Table B.13: Used Powheg+Pythia8 diboson MC samples with their corresponding sample ID, final state, NLO cross section, k-factor filter efficiency and number of generated events. These samples are used for computing generator systematics on the DiBosons prediction in the hadronic channels (continued in table B.14).

Sample ID	Name (event generator: Powheg+Pythia8)	NLO [pb]	k-factor	filter eff.	No. of events
129477	WZ_Wm11Z11_mll0p250d0_2LeptonFilter5	1.407	1.122	0.295	190000
129478	WZ_Wm11Z13_mll0p4614d0_2LeptonFilter5	0.938	1.122	0.352	190000
129479	WZ_Wm11Z15_mll3p804d0_2LeptonFilter5	0.175	1.122	0.167	75999
129480	WZ_Wm13Z11_mll0p250d0_2LeptonFilter5	1.399	1.122	0.294	159999
129481	WZ_Wm13Z13_mll0p4614d0_2LeptonFilter5	0.954	1.122	0.351	190000
129482	WZ_Wm13Z15_mll3p804d0_2LeptonFilter5	0.175	1.122	0.169	76000
129483	WZ_Wm15Z11_mll0p250d0_2LeptonFilter5	1.399	1.122	0.143	70000
129484	WZ_Wm15Z13_mll0p4614d0_2LeptonFilter5	0.938	1.122	0.183	76000
129485	WZ_Wm15Z15_mll3p804d0_2LeptonFilter5	0.172	1.122	0.059	9000
129486	WZ_W11Z11_mll0p250d0_2LeptonFilter5	0.980	1.144	0.297	189899
129487	WZ_W11Z13_mll0p4614d0_2LeptonFilter5	0.639	1.144	0.353	190000
129488	WZ_W11Z15_mll3p804d0_2LeptonFilter5	0.113	1.144	0.160	76000
129489	WZ_W13Z11_mll0p250d0_2LeptonFilter5	0.936	1.144	0.298	190000
129490	WZ_W13Z13_mll0p4614d0_2LeptonFilter5	0.649	1.144	0.354	190000
129491	WZ_W13Z15_mll3p804d0_2LeptonFilter5	0.113	1.144	0.160	76000
129492	WZ_W15Z11_mll0p250d0_2LeptonFilter5	0.936	1.144	0.148	76000
129493	WZ_W15Z13_mll0p4614d0_2LeptonFilter5	0.639	1.144	0.187	75999
129494	WZ_W15Z15_mll3p804d0_2LeptonFilter5	0.111	1.144	0.057	19000
178411	ZZ_2e2tau_mll4_taufilter	0.175	1.000	0.084	100000
178412	ZZ_2mu2tau_mll4_taufilter	0.175	1.000	0.082	100000
178413	ZZ_4tau_mll4_taufilter	0.077	1.000	0.324	299998
179385	WZ_Wm11Z15_mll3p80d40_taufilter	0.175	1.122	0.163	76000
179386	WZ_Wm13Z15_mll3p80d40_taufilter	0.175	1.122	0.164	66000
179387	WZ_Wm15Z11_mll0p250d0_taufilter	1.399	1.122	0.053	19000
179388	WZ_Wm15Z13_mll0p4614d0_taufilter	0.938	1.122	0.058	19000
179389	WZ_Wm15Z15_mll3p804d0_taufilter	0.172	1.122	0.198	19000
179390	WZ_W11Z15_mll3p80d40_taufilter	0.113	1.144	0.151	75999
179391	WZ_W13Z15_mll3p80d40_taufilter	0.113	1.144	0.152	76000
179392	WZ_W15Z11_mll0p250d0_taufilter	0.936	1.144	0.057	19000
179393	WZ_W15Z13_mll0p4614d0_taufilter	0.639	1.144	0.066	19000
179394	WZ_W15Z15_mll3p804d0_taufilter	0.111	1.144	0.183	19000

Table B.14: Used Powheg+Pythia8 diboson MC samples with their corresponding sample ID, final state, NLO cross section, k-factor filter efficiency and number of generated events (continued from table B.13).

B.2 Signal Monte Carlo Samples

Sample ID	$m_{\tilde{\tau}}$	$m_{\tilde{g}}$	σ[pb]	Sample ID	$m_{\tilde{\tau}}$	$m_{\tilde{g}}$	σ[pb]
174170	117	700	0.3600	174205	242	640	0.7080
174171	117	860	0.0679	174206	274	700	0.3600
174172	117	940	0.0312	174207	274	860	0.0679
174173	117	1020	0.0147	174208	274	940	0.0312
174174	117	1100	0.0071	174209	274	1020	0.0147
174175	117	1180	0.0035	174210	274	1100	0.0071
174176	117	400	17.2000	174211	274	1180	0.0035
174177	117	520	3.0900	174212	274	400	17.2000
174178	117	640	0.7080	174213	274	520	3.0900
174179	179	700	0.3600	174214	274	640	0.7080
174180	179	860	0.0679	174215	305	700	0.3600
174181	179	940	0.0312	174216	305	860	0.0679
174182	179	1020	0.0147	174217	305	940	0.0312
174183	179	1100	0.0071	174218	305	1020	0.0147
174184	179	1180	0.0035	174219	305	1100	0.0071
174185	179	400	17.2000	174220	305	1180	0.0035
174186	179	520	3.0900	174221	305	400	17.2000
174187	179	640	0.7080	174222	305	520	3.0900
174188	210	700	0.3600	174223	305	640	0.7080
174189	210	860	0.0679	174224	337	700	0.3600
174190	210	940	0.0312	174225	337	860	0.0679
174191	210	1020	0.0147	174226	337	940	0.0312
174192	210	1100	0.0071	174227	337	1020	0.0147
174193	210	1180	0.0035	174228	337	1100	0.0071
174194	210	400	17.2000	174229	337	1180	0.0035
174195	210	520	3.0900	174230	337	400	17.2000
174196	210	640	0.7080	174231	337	520	3.0900
174197	242	700	0.3600	174232	337	640	0.7080
174198	242	860	0.0679	177275	117	1260	0.0020
174199	242	940	0.0312	177276	179	1260	0.0020
174200	242	1020	0.0147	177277	210	1260	0.0020
174201	242	1100	0.0071	177278	242	1260	0.0020
174202	242	1180	0.0035	177279	274	1260	0.0020
174203	242	400	17.2000	177280	305	1260	0.0020
174204	242	520	3.0900	177281	337	1260	0.0020

Table B.15: List of MC samples for the SUSY signal in the nGM model. Masses are quoted in GeV. All samples are generated using Herwig++.

Sample ID	Λ[TeV]	$\tan\beta$	σ[fb]
175821	40	2	0.705
175822	40	5	0.763
175823	40	10	0.769
175824	40	15	0.772
175825	40	20	0.775
175826	40	30	0.797
175827	40	36	0.835
175828	40	37	0.851
175829	50	2	0.178
175830	50	5	0.201
175831	50	10	0.206
175832	50	15	0.207
175833	50	20	0.208
175834	50	30	0.214
175835	50	40	0.232
175836	50	43	0.248
175837	50	44	0.256
175838	60	2	0.0565
175839	60	5	0.0668
175840	60	10	0.0695
175841	60	15	0.0702
175842	60	20	0.0708
175843	60	30	0.0730
175844	60	40	0.0788
175845	60	49	0.0949
175846	60	50	0.0988
175847	70	2	0.0212
175848	70	5	0.0264
175849	70	10	0.0280
175850	70	15	0.0284
175851	70	20	0.0287
175852	70	30	0.0297
175853	70	40	0.0319
175854	70	50	0.0380
175855	70	57	0.0486
175856	70	58	0.0514
175857	80	2	0.00925
175858	80	5	0.0120
175859	80	10	0.0129
175860	80	15	0.0132
175861	80	20	0.0134
175862	80	30	0.0139
175863	80	40	0.0149
175864	80	50	0.0173
175865	80	58	0.0220
175866	80	59	0.0230
175867	90	2	0.00452
175868	90	5	0.00605
175869	90	10	0.00665
175870	90	15	0.00682
175871	90	20	0.00693
175872	90	30	0.00721
175873	90	40	0.00775
175874	90	50	0.00887
175875	90	60	0.0114
175876	90	61	0.0118
175877	90	62	0.0122
175878	100	2	0.00241
175879	100	5	0.00329
175880	100	10	0.00368
175881	100	15	0.00379
175882	100	20	0.00386
175883	100	30	0.00403
175884	100	40	0.00433
175885	100	50	0.00492
175886	100	60	0.00613
175887	100	61	0.00630
175888	100	62	0.00648
175889	110	2	0.00137
175890	110	5	0.00190
175891	110	10	0.00215
175892	110	15	0.00222
175893	110	20	0.00226
175894	110	30	0.00237
175895	110	40	0.00255
175896	110	50	0.00289
175897	110	60	0.00353
175898	110	61	0.00361
175899	110	62	0.00370

Table B.16: List of MC signal samples for various points in the SUSY GMSB parameter grid. All samples are generated using Herwig++. Four out of six parameters defining the GMSB points are the same for all samples: M_{mess}=250 TeV, N_5=3, sign(μ) = +, and $C_{\tilde{G}}$=1. The parameters Λ and $\tan\beta$ are varied as shown in the table.

Sample ID	m_0	$m_{1/2}$	σ[pb]
166957	230	420	0.355
166958	250	460	0.188
166951	280	550	0.0502
166952	300	620	0.0191
166953	320	640	0.0142
166954	320	660	0.011
166955	350	550	0.0457
166956	350	680	0.00817
166732	400	400	0.363
166733	400	450	0.173
166734	400	500	0.0843
166735	400	550	0.0424
166736	400	600	0.0217
166737	400	650	0.0111
166738	400	700	0.00595
166739	400	750	0.00310
166740	400	800	0.00169
166741	600	400	0.244
166742	600	450	0.1179
166743	600	500	0.0580
166744	600	550	0.0296
166745	600	600	0.0153
166746	600	650	0.00801
166747	600	700	0.00429
166748	600	750	0.00233
166749	600	800	0.00126
166750	600	850	0.000654
166751	600	900	0.000371
166752	600	950	0.000200
166801	600	1000	0.000110
166753	800	400	0.167
166754	800	450	0.0787
166755	800	500	0.0388
166756	800	550	0.0198
166757	800	600	0.0103
166758	800	650	0.00549
166759	800	700	0.00295
166760	800	750	0.00160
166761	800	800	0.000872
166762	800	850	0.000477
166763	800	900	0.000247
166764	800	950	0.000144
166802	800	1000	7.96e-05
166765	1000	400	0.123
166766	1000	450	0.0561
166767	1000	500	0.0270
166768	1000	550	0.0134
166769	1000	600	0.00693
166770	1000	650	0.00373
166771	1000	700	0.00198
166772	1000	750	0.00108
166773	1000	800	0.000594
166774	1000	850	0.000327
166775	1000	900	0.000180
166776	1000	950	9.99e-05
166803	1000	1000	5.56e-05
166948	1200	300	0.657
166938	1200	350	0.243
166777	1200	400	0.0989
166778	1200	450	0.0437
166779	1200	500	0.0205
166780	1200	550	0.0101
166781	1200	600	0.00511
166782	1200	650	0.00267
166783	1200	700	0.00142
166784	1200	750	0.000766
166785	1200	800	0.000418
166786	1200	850	0.000230
166787	1200	900	0.000128
166788	1200	950	7.08e-05
166804	1200	1000	3.97e-05
166949	1400	300	0.525
166950	1400	350	0.201
166789	1400	400	0.0832
166790	1400	450	0.0366
166791	1400	500	0.0169
166792	1400	550	0.00818
166793	1400	600	0.00408
166794	1400	650	0.00209
166795	1400	700	0.00110
166796	1400	750	0.000587
166797	1400	800	0.000319
166798	1400	850	0.000175
166799	1400	900	9.65e-05
166800	1400	950	5.38e-05
166805	1400	1000	3.03e-05

Table B.17: List of MC samples for the SUSY signal in the mSUGRA Higgs boson-aware grid (continued in table B.18). Masses are quoted in GeV.

Sample ID	m_0	$m_{1/2}$	σ[pb]
166807	1600	250	1.06
166808	1600	300	0.406
166809	1600	350	0.164
166810	1600	400	0.0702
166811	1600	450	0.0313
166812	1600	500	0.0146
166813	1600	550	0.00706
166814	1600	600	0.00350
166815	1600	650	0.00179
166806	1600	700	0.000931
166825	1600	750	0.000493
166886	1600	800	0.000267
166816	1800	250	0.789
166817	1800	300	0.309
166818	1800	350	0.131
166819	1800	400	0.0583
166820	1800	450	0.0268
166821	1800	500	0.0128
166822	1800	550	0.00625
166823	1800	600	0.00313
166824	1800	650	0.00160
166916	1800	700	0.000836
166906	1800	750	0.000443
166896	1800	800	0.000240
166826	2000	250	0.623
166827	2000	300	0.240
166828	2000	350	0.103
166829	2000	400	0.0473
166830	2000	450	0.0224
166831	2000	500	0.0110
166832	2000	550	0.00551
166833	2000	600	0.00281
166834	2000	650	0.00146
166926	2000	700	0.000770
166936	2000	750	0.000414
166937	2000	800	0.000225
166836	2200	250	0.522
166837	2200	300	0.191
166838	2200	350	0.0816
166839	2200	400	0.0379
166840	2200	450	0.0185
166841	2200	500	0.00932
166842	2200	550	0.0048
166843	2200	600	0.0025
166844	2200	650	0.00132
166846	2400	250	0.457
166847	2400	300	0.161
166848	2400	350	0.0659
166849	2400	400	0.0303
166850	2400	450	0.0151
166851	2400	500	0.00774
166852	2400	550	0.00405
166853	2400	600	0.00217
166854	2400	650	0.00117
166856	2600	250	0.419
166857	2600	300	0.14
166858	2600	450	0.0121
166859	2600	500	0.0063
166860	2600	550	0.00337
166861	2600	600	0.00185
166862	2600	650	0.00102
166864	2800	250	0.391
166865	2800	300	0.125
166866	2800	350	0.0475
166867	2800	400	0.0206
166868	2800	450	0.00994
166869	2800	500	0.00511
166870	2800	550	0.00276
166871	2800	600	0.00154
166872	2800	650	0.000872
166874	3000	250	0.372
166875	3000	300	0.116
166876	3000	350	0.0423
166877	3000	450	0.00821
166878	3000	500	0.00419
166879	3000	550	0.00224
166880	3000	600	0.00126
166881	3000	650	0.000725
166939	3200	250	0.356
166940	3200	300	0.11
166941	3200	350	0.0385
166942	3200	400	0.0156
166943	3200	450	0.00693
166944	3200	500	0.00344
166945	3200	550	0.00183
166946	3200	600	0.00103

Table B.18: List of MC samples for the SUSY signal in the mSUGRA Higgs boson-aware grid (continued from table B.17).

Sample ID	m_0	$m_{1/2}$	σ[pb]
166947	3200	650	0.000598
166835	3500	250	0.338
166845	3500	300	0.102
166855	3500	350	0.035
166863	3500	400	0.0134
166873	3500	450	0.00573
166882	3500	500	0.00267
166883	3500	550	0.00137
166884	3500	600	0.000754
166885	3500	650	0.000438
166887	4000	250	0.314
166888	4000	300	0.0942
166889	4000	350	0.0314
166890	4000	400	0.0115
166891	4000	450	0.00459
166892	4000	500	0.00198
166893	4000	550	0.000934
166894	4000	600	0.000471
166895	4000	650	0.000261
166897	4500	250	0.294
166898	4500	300	0.0879
166899	4500	350	0.0258
166900	4500	400	0.00923
166901	4500	450	0.00353
166902	4500	500	0.00143
166903	4500	550	0.000632
166904	4500	600	0.000298
166905	4500	650	0.000152
166907	5000	250	0.249
166908	5000	300	0.0738
166909	5000	350	0.0242
166910	5000	400	0.00861
166911	5000	450	0.00324
166912	5000	500	0.00129
166913	5000	550	0.00053
166914	5000	600	0.000232
166915	5000	650	0.000109
166917	5500	250	0.235
166918	5500	300	0.0698
166919	5500	350	0.0227
166920	5500	400	0.00812
166921	5500	450	0.00304
166922	5500	500	0.00118
166923	5500	550	0.000482
166924	5500	600	0.000202
166925	5500	650	8.81E-05
166927	6000	250	0.223
166928	6000	300	0.0661
166929	6000	350	0.0217
166930	6000	400	0.00768
166931	6000	450	0.00285
166932	6000	500	0.00111
166933	6000	550	0.000447
166934	6000	600	0.000184
166935	6000	650	7.73E-05

Table B.19: List of MC samples for the SUSY signal in the mSUGRA Higgs boson-aware grid (continued from table B.18).

Sample ID	m_0	$m_{1/2}$	σ[pb]
174053	400	250	6.13
174054	400	300	2.33
174055	400	350	0.998
174056	400	400	0.462
174057	400	450	0.227
174058	400	500	0.117
174059	400	550	0.0629
174060	400	600	0.0350
174061	400	650	0.0202
174062	400	700	0.0121
174063	400	750	0.00749
174064	400	800	0.00481
174065	600	250	4.64
174066	600	300	1.68
174067	600	350	0.719
174068	600	400	0.336
174069	600	450	0.168
174070	600	500	0.0881
174071	600	550	0.0479
174072	600	600	0.0268
174073	600	650	0.0155
174074	600	700	0.00921
174075	600	750	0.00559
174076	600	800	0.00349
174077	800	250	3.93
174078	800	300	1.35
174079	800	350	0.560
174080	800	400	0.260
174081	800	450	0.131
174082	800	500	0.0693
174083	800	550	0.0381
174084	800	600	0.0217
174085	800	650	0.0127
174086	800	700	0.00763
174087	800	750	0.00468
174088	800	800	0.00293
174089	1000	250	3.43
174090	1000	300	1.17
174091	1000	350	0.480
174092	1000	400	0.220
174093	1000	450	0.110
174094	1000	500	0.0586
174095	1000	550	0.0325
174096	1000	600	0.0187
174097	1000	650	0.0111
174098	1000	700	0.00674
174099	1000	750	0.00418
174100	1000	800	0.00264
174101	1200	250	2.90
174102	1200	300	1.05
174103	1200	350	0.435
174104	1200	400	0.200
174105	1200	450	0.100
174106	1200	500	0.0533
174107	1200	550	0.0297
174108	1200	600	0.0172
174109	1200	650	0.0102
174110	1200	700	0.00629
174111	1200	750	0.00393
174112	1200	800	0.00251
174113	1400	250	2.37
174114	1400	300	0.92
174115	1400	350	0.400
174116	1400	400	0.188
174117	1400	450	0.0949
174118	1400	500	0.0507
174119	1400	550	0.0284
174120	1400	600	0.0165
174121	1400	650	0.00993
174122	1400	700	0.00610
174123	1400	750	0.00386
174124	1400	800	0.00246
174125	1600	250	1.93
174126	1600	300	0.810
174127	1600	350	0.365
174128	1600	400	0.176
174129	1600	450	0.0910
174130	1600	500	0.0493
174131	1600	550	0.0279
174132	1600	600	0.0163
174133	1600	650	0.00984
174134	1600	700	0.00607
174135	1600	750	0.00383
174136	1600	800	0.00246

Table B.20: List of MC samples for the SUSY signal in the bRPV model (continued in table B.21). Masses are quoted in GeV. All samples are generated using PYTHIA6.

Sample ID	m_0	$m_{1/2}$	σ[pb]
174137	1800	250	1.61
174138	1800	300	0.703
174139	1800	350	0.331
174140	1800	400	0.166
174141	1800	450	0.0874
174142	1800	500	0.0480
174143	1800	550	0.0275
174144	1800	600	0.0162
174145	1800	650	0.00982
174146	1800	700	0.00609
174147	1800	750	0.00386
174148	1800	800	0.00248
174149	2000	250	1.40
174150	2000	300	0.621
174151	2000	350	0.300
174152	2000	400	0.154
174153	2000	450	0.0832
174154	2000	500	0.0467
174155	2000	550	0.0271
174156	2000	600	0.0160
174157	2000	650	0.00983
174158	2000	700	0.00612
174159	2000	750	0.00389
174160	2000	800	0.00250
174161	2200	250	1.28
174162	2200	300	0.561
174163	2200	350	0.274
174164	2200	400	0.144
174165	2200	450	0.0791
174166	2200	500	0.0450
174167	2200	550	0.0264
174168	2200	600	0.0159
174169	2200	650	0.00978
174980	400	200	20.0
174981	600	200	17.3
174982	800	200	15.6
174983	1000	200	12.6
174984	1200	200	9.16
174985	1400	200	6.61
174986	1600	200	5.10
174987	1800	200	4.30

Table B.21: List of MC samples for the SUSY signal in the bRPV model (continued from table B.21).

B.3 Additional numbers

	$\tau+\mu$ control regions			$\tau+e$ control regions		
	W+jets	Top Truth	Top Fake	W+jets	Top Truth	Top Fake
W+jets	232 182 ± 1005	166 ± 15	1452 ± 39	192 659 ± 901	212 ± 18	1317 ± 38
Top Truth	1955 ± 25	1231 ± 19	2756 ± 28	2144 ± 26	1431 ± 20	2867 ± 28
Top Fake	3265 ± 38	531 ± 13	4439 ± 39	3413 ± 37	581 ± 13	4686 ± 39
Z+jets	12 819 ± 205	22 ± 5	101 ± 6	8328 ± 169	36 ± 3	84 ± 5
Diboson	1151 ± 9	5 ± 1	16 ± 1	1173 ± 9	8 ± 1	14 ± 1
Multijet	482 ± 60	52 ± 20	119 ± 30	11 571 ± 177	87 ± 26	521 ± 53

Table B.22: Number of events of the various backgrounds in the control regions with statistical uncertainties.

B.4 Systematic Uncertainties

Systematic Uncertainty	Package	Version
Jet energy scale	JetUncertainties	00-08-06
Jet energy resolution	JetEnergyResolutionProvider	02-00-02
Tau energy scale	TauCorrUncertProvider	00-00-07
Tau identification	TauCorrUncertProvider	00-00-07
Missing transverse momentum	MissingETUtility	01-02-06
Pileup re-weighting	PileupReweighting	00-02-11
B-tag efficiency	CalibrationDataInterface	00-03-06
Jet-vertex-fraction	JVFUncertaintyTool	00-00-04
Muon identification	MuonEfficiencyCorrections	02-01-16
Muon energy scale	MuonMomentumCorrections	00-08-01
Muon energy resolution	MuonMomentumCorrections	00-08-01
Muon trigger efficiency	TrigMuonEfficiency	00-02-42
Electron identification	ElectronEfficiencyCorrection	00-00-34
Electron energy scale	egammaAnalysisUtils	00-04-52
Electron energy resolution	egammaAnalysisUtils	00-04-52
Electron trigger efficiency	egammaAnalysisUtils	00-04-52

Table B.23: Software packages used for computation of the systematic uncertainties.

	Total	Dibosons	Zjets	Top	Wjets
JES up	-0.01	0.00	-0.02	0.01	-0.03
JES down	-0.08	-0.17	-0.19	0.00	0.03
JER	0.07	-0.17	0.30	-0.03	0.23
TES up	0.09	0.00	0.00	-0.04	0.48
TES down	-0.05	-0.20	-0.03	-0.05	0.10
MET resolution	0.00	0.00	0.00	0.00	-0.01
MET scale up	0.00	0.00	0.01	0.04	-0.05
MET scale down	0.02	0.00	0.00	0.02	0.05
BTAG up	-0.20	-0.60	-0.14	-0.05	-0.03
BTAG down	0.00	0.00	0.00	0.00	0.00
EGZEE up	0.01	0.00	0.00	0.05	-0.02
EGZEE down	0.01	0.00	0.00	0.02	0.02
EGMAT up	0.00	0.00	0.00	-0.01	0.00
EGMAT down	0.00	0.00	0.00	0.01	0.00
EGPS up	0.00	0.00	0.00	0.00	0.00
EGPS down	0.00	0.00	0.00	0.00	0.00
EGLOW up	0.00	0.00	0.00	0.00	0.00
EGLOW down	0.00	0.00	0.00	0.00	0.00
EGRES up	-0.18	-0.60	-0.14	0.01	-0.02
EGRES down	0.01	0.00	0.01	0.01	0.01
EEFF up	-0.17	-0.60	-0.13	0.04	-0.03
EEFF down	-0.01	-0.01	-0.01	0.00	0.00
ETRIG up	0.00	0.00	0.00	0.00	0.00
ETRIG down	0.04	0.00	0.00	0.14	0.00
Pileup up	0.03	0.07	0.02	-0.04	0.11
Pileup down	-0.03	-0.07	-0.02	0.04	-0.08
Tau ID up	0.01	0.02	0.00	0.00	0.01
TAU ID down	-0.01	-0.02	0.00	0.00	-0.01
TAU EVETO up	0.03	0.04	0.07	0.00	0.00
TAU EVETO down	-0.03	-0.04	-0.07	0.00	0.00
JVF up	0.00	0.00	0.00	0.00	0.00
JFV down	0.00	0.00	0.00	0.00	0.00
Top Generator	0.42	0.00	0.00	1.35	-0.02
Top Gen MC stat	0.16	0.00	0.00	0.58	0.00
W Generator	0.01	0.00	0.00	0.05	0.00
W Gen MC stat	0.20	0.00	0.00	0.00	1.00
Z Generator	-0.19	0.00	-0.82	0.02	0.00
Z Gen MC stat	0.09	0.00	0.43	0.00	0.00
DiBos Generator	0.08	0.31	0.00	0.00	0.00
DiBos Gen MC stat	0.10	0.45	0.00	0.00	0.00
Total systematic uncertainty	0.60	0.96	0.97	0.97	1.00
Statistical uncertainty	0.25	0.45	0.43	0.46	0.44
Total uncertainty	0.65	1.06	1.06	1.07	1.09

Table B.24: Breakdown of all systematic and statistical uncertainties for the GMSB signal region in the tau+electron analysis. Systematics are evaluated as relative changes in the background prediction for the signal region including changes in data driven background prediction due to changes in the transfer factor.

	Total	Dibosons	Zjets	Top	Wjets
JES up	0.04	0.19	0.00	0.01	-0.02
JES down	-0.09	0.00	-0.07	-0.19	-0.13
JER	0.05	0.36	-0.07	-0.02	-0.03
TES up	0.15	0.00	0.44	0.01	0.06
TES down	0.01	0.00	0.00	-0.15	0.11
MET resolution	0.00	0.00	0.00	0.00	-0.01
MET scale up	-0.02	0.00	0.00	-0.01	-0.05
MET scale down	0.02	0.00	0.00	0.00	0.05
BTAG up	-0.01	0.00	0.00	-0.05	0.00
BTAG down	0.00	0.00	0.00	0.00	0.00
MMS up	0.00	0.00	0.02	-0.02	0.00
MMS low	0.02	0.00	0.00	0.13	0.00
MID up	0.00	0.00	0.00	0.00	0.00
MID low	0.00	0.00	0.00	0.00	0.00
MEFF up	0.00	0.00	0.00	0.00	0.00
MEFF down	0.00	0.00	0.00	0.00	0.00
MTRIG up	0.09	0.19	0.00	-0.01	0.13
MTRIG down	0.05	0.00	0.00	0.00	0.14
MSCALE up	0.00	0.00	0.00	0.00	0.00
MSCALE down	0.00	0.00	0.00	0.00	0.00
Pileup up	0.01	0.01	-0.02	0.15	-0.03
Pileup down	0.02	0.00	0.03	-0.02	0.03
Tau ID up	0.01	0.03	0.02	-0.01	0.00
TAU ID down	-0.01	-0.03	-0.02	0.01	0.00
TAU EVETO up	0.00	0.00	0.00	0.00	0.00
TAU EVETO down	0.00	0.00	0.00	0.00	0.00
JVF up	0.00	0.00	0.00	0.00	0.00
JFV down	0.00	0.00	0.00	0.00	0.00
Top Generator	-0.03	0.00	0.00	-0.23	0.00
Top Gen MC stat	0.02	0.00	0.00	1.00	0.00
W Generator	0.07	0.00	0.00	0.04	0.21
W Gen MC stat	0.13	0.00	0.00	0.00	0.41
Z Generator	0.01	0.00	0.00	0.01	0.03
Z Gen MC stat	0.25	0.00	1.00	0.00	0.00
DiBos Generator	0.00	-0.01	0.00	0.00	0.00
DiBos Gen MC stat	0.13	0.45	0.00	0.00	0.00
Total systematic uncertainty	0.36	0.54	1.07	0.34	0.26
Statistical uncertainty	0.32	0.45	0.73	1.00	0.63
Total uncertainty	0.48	0.70	1.29	1.06	0.68

Table B.25: Breakdown of all systematic and statistical uncertainties for the GMSB signal region in the $\tau+\mu$ analysis in percent. Systematics are evaluated as relative changes in the background prediction for the signal region including changes in data driven background prediction due to changes in the transfer factor.

	Total	Dibosons	Zjets	Top	Wjets
JES up	0.07	0.02	0.09	0.10	-0.03
JES down	-0.10	-0.14	0.00	-0.12	0.03
JER	-0.05	-0.08	0.00	-0.05	0.01
TES up	0.02	0.00	0.00	0.05	-0.08
TES down	0.01	0.00	0.00	-0.01	0.10
MET resolution	-0.01	0.00	0.00	-0.01	-0.01
MET scale up	-0.02	0.00	-0.05	-0.01	-0.05
MET scale down	0.01	0.00	0.00	0.01	0.05
BTAG up	-0.07	-0.14	-0.01	-0.05	-0.08
BTAG down	0.00	0.00	0.00	0.00	0.00
EGZEE up	-0.01	0.00	0.00	-0.01	-0.02
EGZEE down	0.04	0.00	0.00	0.06	0.02
EGMAT up	0.02	0.00	0.00	0.02	0.00
EGMAT down	0.02	0.00	0.00	0.03	0.00
EGPS up	0.04	0.00	0.00	0.06	0.00
EGPS down	0.02	0.00	0.00	0.04	0.00
EGLOW up	0.01	0.00	0.00	0.01	0.00
EGLOW down	0.00	0.00	0.00	0.00	0.00
EGRES up	-0.03	-0.14	-0.01	0.01	-0.08
EGRES down	0.00	0.00	0.00	0.00	0.01
EEFF up	-0.03	-0.14	0.01	0.01	-0.09
EEFF down	0.01	-0.01	-0.01	0.01	0.00
ETRIG up	0.00	0.00	0.00	0.00	0.00
ETRIG down	0.02	0.00	0.00	0.03	0.00
Pileup up	0.03	0.07	0.07	0.02	-0.02
Pileup down	-0.01	-0.05	-0.06	-0.01	0.03
Tau ID up	0.00	0.02	0.01	0.00	0.00
TAU ID down	0.00	-0.02	-0.01	0.00	0.00
TAU EVETO up	0.00	0.00	0.01	-0.01	0.00
TAU EVETO down	0.00	0.00	-0.01	0.00	0.00
JVF up	0.01	0.00	0.00	0.02	0.00
JFV down	0.01	0.00	0.00	0.02	0.00
Top Generator	0.46	0.00	0.00	0.69	-0.08
Top Gen MC stat	0.18	0.00	0.00	0.29	0.00
W Generator	-0.04	0.00	0.00	0.05	-0.59
W Gen MC stat	0.03	0.00	0.00	0.00	0.31
Z Generator	0.01	0.00	0.00	0.02	-0.06
Z Gen MC stat	0.02	0.00	1.00	0.00	0.00
DiBos Generator	0.02	0.11	0.00	0.00	0.00
DiBos Gen MC stat	0.05	0.29	0.00	0.00	0.00
Total systematic uncertainty	0.48	0.28	1.00	0.70	0.62
Statistical uncertainty	0.20	0.29	0.55	0.27	0.31
Total uncertainty	0.52	0.40	1.14	0.75	0.69

Table B.26: Breakdown of all systematic and statistical uncertainties for the nGM signal region in the $\tau+e$ analysis in percent. Systematics are evaluated as relative changes in the background prediction for the signal region including changes in data driven background prediction due to changes in the transfer factor.

	Total	Dibosons	Zjets	Top	Wjets
JES up	0.08	0.00	0.00	0.11	-0.02
JES down	-0.17	0.00	-0.62	-0.18	-0.13
JER	-0.06	-0.09	-0.04	-0.07	-0.02
TES up	-0.01	0.00	0.09	-0.03	0.08
TES down	0.14	0.00	0.00	0.17	0.11
MET resolution	-0.01	0.00	-0.08	-0.01	-0.01
MET scale up	-0.04	0.00	0.00	-0.05	-0.05
MET scale down	-0.01	0.00	0.00	0.05	-0.35
BTAG up	-0.04	0.00	0.00	-0.05	0.00
BTAG down	0.00	0.00	0.00	0.00	0.00
MMS up	0.00	0.00	0.00	0.00	0.00
MMS low	0.03	0.00	0.00	0.04	0.00
MID up	-0.01	0.00	0.00	-0.01	0.00
MID low	0.02	0.00	0.00	0.03	0.00
MEFF up	0.01	0.00	0.00	0.02	0.00
MEFF down	0.00	0.00	0.00	0.00	0.00
MTRIG up	0.05	0.00	0.00	0.06	0.00
MTRIG down	0.00	0.00	0.00	0.00	0.00
MSCALE up	0.00	0.00	0.00	0.00	0.00
MSCALE down	0.00	0.00	0.00	0.00	0.00
Pileup up	0.04	-0.05	0.10	0.06	-0.01
Pileup down	-0.02	0.06	-0.12	-0.04	0.02
Tau ID up	0.00	0.02	0.04	0.00	0.00
TAU ID down	0.00	-0.02	-0.04	0.00	0.00
TAU EVETO up	0.00	0.00	0.00	0.00	0.00
TAU EVETO down	0.00	0.00	0.00	0.00	0.00
JVF up	0.01	0.00	0.00	0.01	0.00
JFV down	0.01	0.00	0.00	0.01	0.00
Top Generator	0.25	0.00	0.00	0.33	0.00
Top Gen MC stat	0.23	0.00	0.00	0.31	0.00
W Generator	0.04	0.00	0.00	0.01	0.00
W Gen MC stat	0.14	0.00	0.00	0.00	1.00
Z Generator	0.01	0.00	0.00	0.01	0.03
Z Gen MC stat	0.01	0.00	1.00	0.00	0.00
DiBos Generator	0.07	0.86	0.00	0.00	0.00
DiBos Gen MC stat	0.04	0.44	0.00	0.00	0.00
Total systematic uncertainty	0.34	0.87	1.18	0.37	1.09
Statistical uncertainty	0.24	0.44	0.50	0.30	0.38
Total uncertainty	0.42	0.97	1.28	0.48	1.16

Table B.27: Breakdown of all systematic and statistical uncertainties for the nGM signal region in the $\tau+\mu$ analysis in percent. Systematics are evaluated as relative changes in the background prediction for the signal region including changes in data driven background prediction due to changes in the transfer factor.

	Total	Dibosons	Zjets	Top	Wjets
JES up	-0.01	0.40	0.18	-0.04	-0.03
JES down	-0.12	0.00	-0.21	-0.23	0.00
JER	-0.09	0.00	0.14	-0.17	-0.04
TES up	0.11	0.00	0.07	0.05	0.19
TES down	-0.05	0.00	-0.41	-0.12	0.04
MET resolution	0.01	0.00	0.00	0.02	0.00
MET scale up	-0.04	0.00	0.02	-0.02	-0.06
MET scale down	0.03	0.00	0.00	0.04	0.04
BTAG up	-0.14	-0.26	-0.16	-0.15	-0.12
BTAG down	0.00	0.00	0.00	0.00	0.00
EGZEE up	-0.06	0.00	0.01	-0.13	-0.01
EGZEE down	0.02	0.00	0.00	0.05	0.00
EGMAT up	0.01	0.00	0.01	0.02	0.00
EGMAT down	0.01	0.00	0.00	0.03	-0.01
EGPS up	0.00	0.00	0.00	0.02	-0.01
EGPS down	0.00	0.00	0.01	0.01	0.00
EGLOW up	0.00	0.00	0.00	0.00	0.00
EGLOW down	0.00	0.00	0.00	0.00	0.00
EGRES up	-0.12	-0.26	-0.13	-0.10	-0.12
EGRES down	-0.05	0.00	0.02	-0.11	0.01
EEFF up	-0.13	-0.26	-0.15	-0.12	-0.12
EEFF down	0.00	-0.01	-0.01	0.00	0.00
ETRIG up	0.00	0.00	0.00	0.00	0.00
ETRIG down	0.02	0.00	0.00	0.03	0.00
Pileup up	-0.01	-0.03	0.06	0.01	-0.02
Pileup down	0.00	0.02	-0.09	-0.01	0.02
Tau ID up	0.00	0.02	0.00	0.00	0.00
TAU ID down	0.00	-0.02	0.00	0.00	0.00
TAU EVETO up	0.00	0.00	0.09	-0.01	0.00
TAU EVETO down	0.00	0.00	-0.08	0.01	0.00
JVF up	0.00	0.00	0.00	0.00	0.00
JFV down	0.00	0.00	0.00	0.00	0.00
Top Generator	0.07	0.00	0.00	0.25	-0.12
Top Gen MC stat	0.06	0.00	0.00	0.63	0.00
W Generator	-0.08	0.00	0.00	0.05	-0.23
W Gen MC stat	0.13	0.00	0.00	0.00	0.34
Z Generator	0.15	0.00	4.02	0.02	-0.10
Z Gen MC stat	0.02	0.00	0.45	0.00	0.00
DiBos Generator	0.00	-0.07	0.00	0.00	0.00
DiBos Gen MC stat	0.03	0.55	0.00	0.00	0.00
Total systematic uncertainty	0.32	0.55	4.04	0.50	0.36
Statistical uncertainty	0.20	0.55	0.45	0.30	0.34
Total uncertainty	0.38	0.77	4.06	0.58	0.49

Table B.28: Breakdown of all systematic and statistical uncertainties for the bRPV signal region in the $\tau+e$ analysis in percent. Systematics are evaluated as relative changes in the background prediction for the signal region including changes in data driven background prediction due to changes in the transfer factor.

	Total	Dibosons	Zjets	Top	Wjets
JES up	0.09	0.00	0.05	0.21	-0.02
JES down	-0.10	0.00	-0.11	-0.14	-0.07
JER	0.08	0.31	-0.06	0.13	0.00
TES up	0.01	0.00	0.40	-0.03	-0.07
TES down	-0.06	0.00	0.00	0.00	-0.18
MET resolution	-0.01	0.00	0.00	-0.01	-0.01
MET scale up	-0.03	0.00	-0.02	-0.03	-0.05
MET scale down	0.03	0.00	0.00	0.03	0.05
BTAG up	-0.02	0.00	0.00	-0.05	0.00
BTAG down	0.00	0.00	0.00	0.00	0.00
MMS up	-0.01	0.00	-0.11	0.00	0.00
MMS low	0.03	0.00	0.00	0.06	0.00
MID up	0.00	0.00	0.00	0.00	0.00
MID low	0.01	0.00	0.00	0.02	0.00
MEFF up	0.03	0.00	0.00	0.05	0.00
MEFF down	0.00	0.00	0.00	0.00	0.00
MTRIG up	0.03	0.00	0.06	0.05	0.00
MTRIG down	0.01	0.00	0.06	0.00	0.00
MSCALE up	0.00	0.00	0.00	0.00	0.00
MSCALE down	0.00	0.00	0.00	0.00	0.00
Pileup up	0.01	0.04	0.08	0.01	-0.02
Pileup down	0.01	0.00	-0.08	0.01	0.04
Tau ID up	0.00	0.02	0.00	-0.01	0.00
TAU ID down	0.00	-0.02	0.00	0.01	0.00
TAU EVETO up	0.00	0.00	0.00	0.01	0.00
TAU EVETO down	0.00	0.00	0.00	-0.01	0.00
JVF up	0.02	0.00	0.00	0.04	0.00
JFV down	0.02	0.00	0.00	0.04	0.00
Top Generator	0.26	0.00	0.00	0.57	0.00
Top Gen MC stat	0.16	0.00	0.00	0.46	0.00
W Generator	-0.28	0.00	0.00	0.02	-0.85
W Gen MC stat	0.13	0.00	0.00	0.00	0.34
Z Generator	-0.03	0.00	-0.41	0.01	0.03
Z Gen MC stat	0.05	0.00	0.45	0.00	0.00
DiBos Generator	-0.01	-0.08	0.00	0.00	0.00
DiBos Gen MC stat	0.05	0.55	0.00	0.00	0.00
Total systematic uncertainty	0.41	0.45	0.55	0.61	0.86
Statistical uncertainty	0.23	0.55	0.45	0.37	0.39
Total uncertainty	0.47	0.71	0.71	0.72	0.84

Table B.29: Breakdown of all systematic and statistical uncertainties for the bRPV signal region in the $\tau+\mu$ analysis in percent. Systematics are evaluated as relative changes in the background prediction for the signal region including changes in data driven background prediction due to changes in the transfer factor.

	Total	Dibosons	Zjets	Top	Wjets
JES up	0.14	0.09	0.31	0.15	0.01
JES down	-0.10	-0.14	0.00	-0.11	0.00
JER	-0.03	-0.10	0.00	-0.04	0.10
TES up	0.01	0.00	0.00	0.02	-0.06
TES down	0.00	-0.03	0.00	-0.01	0.10
MET resolution	-0.02	0.01	0.00	-0.03	0.04
MET scale up	-0.02	-0.01	-0.03	-0.02	-0.05
MET scale down	-0.01	0.00	0.00	-0.02	0.05
BTAG up	-0.06	-0.10	-0.02	-0.05	-0.12
BTAG down	0.00	0.00	0.00	0.00	0.00
EGZEE up	0.00	0.01	0.00	0.00	-0.02
EGZEE down	0.02	0.00	0.00	0.02	0.02
EGMAT up	0.02	0.01	0.00	0.03	0.00
EGMAT down	0.01	-0.01	0.00	0.01	0.00
EGPS up	0.04	0.00	0.00	0.05	0.00
EGPS down	0.01	0.01	0.00	0.01	0.00
EGLOW up	0.00	0.00	0.00	0.00	0.00
EGLOW down	0.00	0.00	0.00	0.00	0.00
EGRES up	-0.03	-0.10	-0.02	-0.01	-0.12
EGRES down	0.00	0.00	0.00	0.00	0.01
EEFF up	-0.01	-0.10	-0.01	0.02	-0.12
EEFF down	0.01	-0.01	-0.01	0.02	0.00
ETRIG up	0.00	0.00	0.00	0.00	0.00
ETRIG down	0.03	0.00	0.00	0.03	0.00
Pileup up	0.00	0.05	0.06	0.00	-0.03
Pileup down	0.00	-0.03	-0.07	0.01	0.03
Tau ID up	0.00	0.02	0.01	0.00	0.01
TAU ID down	0.00	-0.02	-0.01	0.00	-0.01
TAU EVETO up	0.00	0.00	0.01	-0.01	0.01
TAU EVETO down	0.00	0.00	-0.01	0.01	-0.01
JVF up	0.01	0.00	0.00	0.01	0.00
JFV down	0.01	0.00	0.00	0.01	0.00
Top Generator	0.28	0.00	0.00	0.39	-0.12
Top Gen MC stat	0.12	0.00	0.00	0.19	0.00
W Generator	0.00	0.00	0.00	0.05	-0.41
W Gen MC stat	0.02	0.00	0.00	0.00	0.23
Z Generator	-0.01	0.00	0.00	0.02	-0.10
Z Gen MC stat	0.01	1.00	0.47	0.00	0.00
DiBos Generator	0.01	0.04	0.00	0.00	0.00
DiBos Gen MC stat	0.03	0.20	0.00	0.00	0.00
Total systematic uncertainty	0.30	0.22	1.05	0.41	0.48
Statistical uncertainty	0.14	0.29	0.43	0.17	0.27
Total uncertainty	0.33	0.30	1.15	0.45	0.53

Table B.30: Breakdown of all systematic and statistical uncertainties for the mSugra signal region in the $\tau+e$ analysis in percent. Systematics are evaluated as relative changes in the background prediction for the signal region including changes in data driven background prediction due to changes in the transfer factor.

	Total	Dibosons	Zjets	Top	Wjets
JES up	0.15	0.04	0.31	0.17	0.06
JES down	-0.11	-0.12	-0.62	-0.11	-0.10
JER	0.03	0.13	-0.03	0.03	-0.05
TES up	-0.02	0.00	0.07	-0.03	0.01
TES down	0.06	-0.11	0.00	0.07	0.11
MET resolution	-0.02	-0.11	0.00	-0.01	-0.01
MET scale up	0.00	-0.11	0.00	0.01	-0.05
MET scale down	0.02	0.00	0.00	0.02	0.05
BTAG up	-0.04	0.00	0.00	-0.05	0.00
BTAG down	0.00	0.00	0.00	0.00	0.00
MMS up	0.00	0.00	0.00	0.01	-0.04
MMS low	0.01	0.00	0.00	0.01	0.00
MID up	0.00	0.00	0.00	0.00	0.00
MID low	0.01	0.00	0.00	0.01	0.00
MEFF up	0.01	0.00	0.00	0.01	0.00
MEFF down	0.00	0.00	0.00	0.00	0.00
MTRIG up	0.03	0.00	0.00	0.04	0.00
MTRIG down	0.00	0.00	0.00	0.00	0.00
MSCALE up	0.00	0.00	0.00	0.00	0.00
MSCALE down	0.00	0.00	0.00	0.00	0.00
Pileup up	0.01	0.00	0.11	0.01	-0.02
Pileup down	0.00	0.00	-0.11	0.00	0.02
Tau ID up	0.00	0.02	0.04	0.00	0.00
TAU ID down	0.00	-0.02	-0.04	0.00	0.00
TAU EVETO up	0.00	0.00	0.00	0.00	0.00
TAU EVETO down	0.00	0.00	0.00	0.00	0.00
JVF up	0.00	0.00	0.00	0.00	0.00
JFV down	0.01	0.00	0.00	0.00	0.03
Top Generator	0.32	0.00	0.00	0.38	0.00
Top Gen MC stat	0.13	0.00	0.00	0.18	0.00
W Generator	-0.04	0.00	0.00	0.01	-0.49
W Gen MC stat	0.02	0.00	0.00	0.00	0.27
Z Generator	0.01	0.00	0.00	0.01	0.03
Z Gen MC stat	0.01	0.00	1.00	0.00	0.00
DiBos Generator	0.05	0.72	0.00	0.00	0.00
DiBos Gen MC stat	0.02	0.29	0.00	0.00	0.00
Total systematic uncertainty	0.33	0.77	1.05	0.39	0.50
Statistical uncertainty	0.14	0.20	0.47	0.18	0.23
Total uncertainty	0.36	0.82	1.13	0.42	0.57

Table B.31: Breakdown of all systematic and statistical uncertainties for the mSugra signal region in the $\tau+\mu$ analysis in percent. Systematics are evaluated as relative changes in the background prediction for the signal region including changes in data driven background prediction due to changes in the transfer factor.

List of Figures

List of Tables

Bibliography

[1] ATLAS Collaboration: *Search for Supersymmetry in Events with Large Missing Transverse Momentum, Jets, and at Least One Tau Lepton in 7 TeV Proton-Proton Collision Data with the ATLAS Detector*, Eur. Phys. J. C72 (2012) p. 2215, arXiv: 1210.1314 [hep-ex] (cit. on pp. 2, 122).

[2] ATLAS Collaboration: *Search for supersymmetry in events with large missing transverse momentum, jets, and at least one tau lepton in 20 fb^{-1} of $\sqrt{s}$ = 8 TeV proton-proton collision data with the ATLAS detector*, JHEP 1409 (2014) p. 103, arXiv: 1407.0603 [hep-ex] (cit. on pp. 2, 56, 67, 111, 113–115, 126, 155, 156).

[3] T. Nattermann: *Search for Supersymmetry with Tau Leptons, Muons, Missing Transverse Momentum and Jets with the ATLAS Experiment at the Large Hadron Collider*, PhD Thesis: University of Bonn, 2013, url: http://hss.ulb.uni-bonn.de/2013/3333/3333.htm (cit. on pp. 2, 61).

[4] S. Schaepe: *Search for Supersymmetry in Tau Lepton Final States with the ATLAS Detector*, PhD Thesis: University of Bonn, 2016, url: http://hss.ulb.uni-bonn.de/2016/4238/4238.htm (cit. on p. 2).

[5] T. Sjursen: *Search for Supersymmetry with Tau Leptons in Data from the ATLAS Experiment at the LHC*, PhD Thesis: University of Bergen, 2014, url: http://cds.cern.ch/record/1955577 (cit. on p. 2).

[6] S. L. Glashow: *Partial Symmetries of Weak Interactions*, Nucl. Phys. 22 (1961) pp. 579–588 (cit. on pp. 3–5).

[7] A. Salam: *Weak and Electromagnetic Interactions*, Conf. Proc. C680519 (1968) pp. 367–377 (cit. on pp. 3–5).

[8] S. Weinberg: *A Model of Leptons*, Phys. Rev. Lett. 19 (1967) pp. 1264–1266 (cit. on pp. 3–5).

[9] G 't Hooft and M Veltman: *Regularization and Renormalization of Gauge Fields*, Nucl.Phys. B44 (1972) pp. 189–213 (cit. on pp. 3, 4).

[10] J. Beringer et al.: *Review of Particle Physics*, Phys. Rev. D 86 (2012) p. 010001 (cit. on pp. 4, 6, 12, 14, 25).

[11] F. Halzen and A. Martin: *Quarks & Leptons: An Introductory Course in Modern Particle Physics*, John Wiley & Sons, 1984, isbn: 0471887412 (cit. on p. 4).

[12] W. Cottingham and D. Greenwood: *An Introduction to the Standard Model of Particle Physics*, Cambridge University Press, 1998, isbn: 0521588324 (cit. on p. 4).

[13] F. J. Hasert et al.: *Search for Elastic ν_μ Electron Scattering*, Phys. Lett. B46 (1973) pp. 121–124 (cit. on p. 5).

[14] G. Arnison et al.: *Experimental Observation of Isolated Large Transverse Energy Electrons with Associated Missing Energy at s**(1/2) = 540-GeV*, Phys. Lett. B122 (1983) pp. 103–116, [,611(1983)] (cit. on p. 5).

[15] M. Banner et al.: *Observation of Single Isolated Electrons of High Transverse Momentum in Events with Missing Transverse Energy at the CERN anti-p p Collider*, Phys. Lett. B122 (1983) pp. 476–485 (cit. on p. 5).

[16] G. Arnison et al.: *Experimental Observation of Lepton Pairs of Invariant Mass Around 95-GeV/c**2 at the CERN SPS Collider*, Phys. Lett. B126 (1983) pp. 398–410 (cit. on p. 5).

[17] P. Bagnaia et al.: *Evidence for $Z^0 \to e^+e^-$ at the CERN anti-p p Collider*, Phys. Lett. B129 (1983) pp. 130–140 (cit. on p. 5).

[18] P. W. Anderson: *Plasmons, Gauge Invariance, and Mass*, Phys. Rev. 130 (1963) pp. 439–442 (cit. on p. 6).

[19] P. W. Higgs: *Broken symmetries, massless particles and gauge fields*, Phys. Lett. 12 (1964) pp. 132–133 (cit. on p. 6).

[20] F. Englert and R. Brout: *Broken Symmetry and the Mass of Gauge Vector Mesons*, Phys. Rev. Lett. 13 (1964) pp. 321–323 (cit. on p. 6).

[21] H. Fritzsch, M. Gell-Mann, and H. Leutwyler: *Advantages of the Color Octet Gluon Picture*, Phys. Lett. B47 (1973) pp. 365–368 (cit. on p. 7).

[22] K. G. Wilson: *Confinement of Quarks*, Phys. Rev. D10 (1974) pp. 2445–2459, [,45(1974)] (cit. on p. 7).

[23] D. J. Gross and F. Wilczek: *Ultraviolet Behavior of Nonabelian Gauge Theories*, Phys. Rev. Lett. 30 (1973) pp. 1343–1346 (cit. on p. 7).

[24] H. D. Politzer: *Reliable Perturbative Results for Strong Interactions?*, Phys. Rev. Lett. 30 (1973) pp. 1346–1349 (cit. on p. 7).

[25] A. D. Martin et al.: *Parton distributions for the LHC*, Eur. Phys. J. C63 (2009) pp. 189–285, arXiv: 0901.0002 [hep-ph] (cit. on p. 8).

[26] P. M. Nadolsky et al.: *Implications of CTEQ global analysis for collider observables*, Phys. Rev. D78 (2008) p. 013004, arXiv: 0802.0007 [hep-ph] (cit. on p. 8).

[27] S. P. Martin: *A Supersymmetry primer* (1997), [Adv. Ser. Direct. High Energy Phys.18,1(1998)], arXiv: hep-ph/9709356 [hep-ph] (cit. on pp. 8–11, 13–19).

[28] S. Weinberg: *Implications of Dynamical Symmetry Breaking*, Phys. Rev. D13 (1976) pp. 974–996 (cit. on p. 8).

[29] E. Gildener: *Gauge Symmetry Hierarchies*, Phys. Rev. D14 (1976) p. 1667 (cit. on p. 8).

[30] L. Susskind: *Dynamics of Spontaneous Symmetry Breaking in the Weinberg-Salam Theory*, Phys. Rev. D20 (1979) pp. 2619–2625 (cit. on p. 8).

[31] F. Zwicky: *Die Rotverschiebung von extragalaktischen Nebeln*, Helv. Phys. Acta 6 (1933) pp. 110–127 (cit. on p. 9).

[32] V. C. Rubin, W. K. J. Ford, and N. Thonnard: *Rotational properties of 21 SC galaxies with a large range of luminosities and radii, from NGC 4605 (R = 4kpc) to UGC 2885 (R = 122 kpc)*, Astrophys. J. 238 (1980) pp. 471–487 (cit. on p. 9).

[33] T. van Albada et al.: *The Distribution of Dark Matter in the Spiral Galaxy NGC-3198*, Astrophys. J. 295 (1985) pp. 305–313 (cit. on p. 9).

[34] P. A. R. Ade et al.: *Planck 2015 results. XIII. Cosmological parameters* (2015), arXiv: 1502.01589 [astro-ph.CO] (cit. on p. 9).

[35] P. Fayet: *The Supersymmetric Standard Model* (2015), arXiv: 1506.08277 [hep-ph] (cit. on p. 9).

[36] I. Aitchison, Cambridge University Press, 2007, isbn: 9780521880237 (cit. on pp. 9–12, 14–16).

[37] S. Dawson: *SUSY and such*, NATO Sci. Ser. B 365 (1997) pp. 33–80, arXiv: hep-ph/9612229 [hep-ph] (cit. on p. 9).

[38] S. R. Coleman and J. Mandula: *All Possible Symmetries of the S Matrix*, Phys. Rev. 159 (1967) pp. 1251–1256 (cit. on p. 10).

[39] M. Bertolini: *Lectures on Supersymmetry*, 2016, url: http://people.sissa.it/~bertmat/teaching.htm (visited on 05/24/2016) (cit. on p. 10).

[40] R. Haag, J. T. Lopuszanski, and M. Sohnius: *All Possible Generators of Supersymmetries of the s Matrix*, Nucl. Phys. B88 (1975) p. 257 (cit. on p. 10).

[41] S. Dimopoulos and D. W. Sutter: *The Supersymmetric flavor problem*, Nucl. Phys. B452 (1995) pp. 496–512, arXiv: hep-ph/9504415 [hep-ph] (cit. on p. 12).

[42] R. Barbieri, L. J. Hall, and A. Strumia: *Violations of lepton flavor and CP in supersymmetric unified theories*, Nucl. Phys. B445 (1995) pp. 219–251, arXiv: hep-ph/9501334 [hep-ph] (cit. on p. 12).

[43] G. R. Farrar and P. Fayet: *Phenomenology of the Production, Decay, and Detection of New Hadronic States Associated with Supersymmetry*, Phys. Lett. B76 (1978) pp. 575–579 (cit. on p. 12).

[44] P Langacker: "Precision Tests Of The Standard Model", *Proceedings of the PASCO90 Symposium, (World Scientific)*, 1990 (cit. on p. 13).

[45] J. R. Ellis, S. Kelley, and D. V. Nanopoulos: *Probing the desert using gauge coupling unification*, Phys. Lett. B260 (1991) pp. 131–137 (cit. on p. 13).

[46] U. Amaldi, W. de Boer, and H. Furstenau: *Comparison of grand unified theories with electroweak and strong coupling constants measured at LEP*, Phys. Lett. B260 (1991) pp. 447–455 (cit. on p. 13).

[47] P. Langacker and M.-x. Luo: *Implications of precision electroweak experiments for M_t, ρ_0, $\sin^2\theta_W$ and grand unification*, Phys. Rev. D44 (1991) pp. 817–822 (cit. on p. 13).

[48] S. Mele: "Measurements of the running of the electromagnetic coupling at LEP", *26th International Symposium on Physics in Collision (PIC 2006) Buzios, Brazil, July 6-9, 2006*, 2006, arXiv: hep-ex/0610037 [hep-ex], url: http://www.slac.stanford.edu/econf/C060706/pdf/0610037.pdf (cit. on p. 14).

[49] J. R. Ellis et al.: *Supersymmetric Relics from the Big Bang*, Nucl. Phys. B238 (1984) pp. 453–476 (cit. on p. 15).

[50] H. Goldberg: *Constraint on the Photino Mass from Cosmology*, Phys. Rev. Lett. 50 (1983) p. 1419, [Erratum: Phys. Rev. Lett.103,099905(2009)] (cit. on p. 15).

[51] M. Dine and A. E. Nelson: *Dynamical supersymmetry breaking at low-energies*, Phys. Rev. D48 (1993) pp. 1277–1287, arXiv: hep-ph/9303230 [hep-ph] (cit. on p. 19).

[52] M. Dine, A. E. Nelson, and Y. Shirman: *Low-energy dynamical supersymmetry breaking simplified*, Phys. Rev. D51 (1995) pp. 1362–1370, arXiv: hep-ph/9408384 [hep-ph] (cit. on p. 19).

[53] M. Dine et al.: *New tools for low-energy dynamical supersymmetry breaking*, Phys. Rev. D53 (1996) pp. 2658–2669, arXiv: hep-ph/9507378 [hep-ph] (cit. on p. 19).

[54] C. F. Kolda: *Gauge mediated supersymmetry breaking: Introduction, review and update*, Nucl. Phys. Proc. Suppl. 62 (1998) pp. 266–275, arXiv: hep-ph/9707450 [hep-ph] (cit. on p. 19).

[55] G. F. Giudice and R. Rattazzi: *Theories with gauge mediated supersymmetry breaking*, Phys. Rept. 322 (1999) pp. 419–499, arXiv: hep-ph/9801271 [hep-ph] (cit. on p. 19).

[56] F Salvatore et al.: *Search for Events with Large Missing Transverse Momentum, Jets, and Leptons (e/mu/tau) in 7 TeV Proton-Proton Collision Data with the ATLAS Detector*, tech. rep. ATL-COM-PHYS-2012-567, CERN, 2012, url: https://cds.cern.ch/record/1449784 (cit. on p. 20).

[57] A. Collaboration: *Observation of a new particle in the search for the Standard Model Higgs boson with the ATLAS detector at the LHC*, Phys. Lett. B716 (2012) pp. 1–29, arXiv: 1207.7214 [hep-ex] (cit. on p. 21).

[58] CMS Collaboration: *Observation of a new boson at a mass of 125 GeV with the CMS experiment at the LHC*, Phys. Lett. B716 (2012) pp. 30–61, arXiv: 1207.7235 [hep-ex] (cit. on p. 21).

[59] A. Arbey et al.: *Implications of a 125 GeV Higgs for supersymmetric models*, Phys. Lett. B708 (2012) pp. 162–169, arXiv: 1112.3028 [hep-ph] (cit. on p. 21).

[60] S. P. Martin and J. D. Wells: *Implications of gauge-mediated supersymmetry breaking with vector-like quarks and a 125 GeV Higgs boson*, Phys. Rev. D86 (2012) p. 035017, arXiv: 1206.2956 [hep-ph] (cit. on p. 21).

[61] J. Barnard et al.: *Natural gauge mediation with a bino NLSP at the LHC*, Phys. Rev. Lett. 109 (2012) p. 241801, arXiv: 1208.6062 [hep-ph] (cit. on p. 21).

[62] P. Nath and R. L. Arnowitt: *Generalized Supergauge Symmetry as a New Framework for Unified Gauge Theories*, Phys. Lett. B56 (1975) pp. 177–180 (cit. on p. 21).

[63] R. L. Arnowitt, P. Nath, and B. Zumino: *Superfield Densities and Action Principle in Curved Superspace*, Phys. Lett. B56 (1975) pp. 81–84 (cit. on p. 21).

[64] D. Z. Freedman, P. van Nieuwenhuizen, and S. Ferrara: *Progress Toward a Theory of Supergravity*, Phys. Rev. D13 (1976) pp. 3214–3218 (cit. on p. 21).

[65] S. Deser and B. Zumino: *Consistent Supergravity*, Phys. Lett. B62 (1976) p. 335 (cit. on p. 21).

[66] D. Z. Freedman and P. van Nieuwenhuizen: *Properties of Supergravity Theory*, Phys. Rev. D14 (1976) p. 912 (cit. on p. 21).

[67] E. Cremmer et al.: *Spontaneous Symmetry Breaking and Higgs Effect in Supergravity Without Cosmological Constant*, Nucl. Phys. B147 (1979) p. 105 (cit. on p. 21).

[68] J. A. Bagger: *Coupling the Gauge Invariant Supersymmetric Nonlinear Sigma Model to Supergravity*, Nucl. Phys. B211 (1983) p. 302 (cit. on p. 21).

[69] E. Cremmer et al.: *Yang-Mills Theories with Local Supersymmetry: Lagrangian, Transformation Laws and SuperHiggs Effect*, Nucl. Phys. B212 (1983) p. 413 (cit. on p. 21).

[70] A. H. Chamseddine, R. L. Arnowitt, and P. Nath: *Locally Supersymmetric Grand Unification*, Phys. Rev. Lett. 49 (1982) p. 970 (cit. on p. 21).

[71] R. Barbieri, S. Ferrara, and C. A. Savoy: *Gauge Models with Spontaneously Broken Local Supersymmetry*, Phys. Lett. B119 (1982) p. 343 (cit. on p. 21).

[72] L. E. Ibanez: *Locally Supersymmetric SU(5) Grand Unification*, Phys. Lett. B118 (1982) pp. 73–78 (cit. on p. 21).

[73] L. J. Hall, J. D. Lykken, and S. Weinberg: *Supergravity as the Messenger of Supersymmetry Breaking*, Phys. Rev. D27 (1983) pp. 2359–2378 (cit. on p. 21).

[74] N. Ohta: *GRAND UNIFIED THEORIES BASED ON LOCAL SUPERSYMMETRY*, Prog. Theor. Phys. 70 (1983) p. 542 (cit. on p. 21).

[75] G. L. Kane et al.: *Study of constrained minimal supersymmetry*, Phys. Rev. D49 (1994) pp. 6173–6210, arXiv: hep-ph/9312272 [hep-ph] (cit. on p. 21).

[76] K. Morå: *Dark Matter Searches with ATLAS and Fermi*, Master Thesis: University of Bergen, 2013, url: http://bora.uib.no/handle/1956/7537 (cit. on p. 22).

[77] LHCb Collaboration: *First Evidence for the Decay $B_s^0 \to \mu^+\mu^-$*, Phys. Rev. Lett. 110.2 (2013) p. 021801, arXiv: 1211.2674 [hep-ex] (cit. on p. 21).

[78] D. Asner et al.: *Averages of b-hadron, c-hadron, and τ-lepton properties* (2010), arXiv: 1010.1589 [hep-ex] (cit. on p. 21).

[79] M. A. Diaz, J. C. Romao, and J. W. F. Valle: *Minimal supergravity with R-parity breaking*, Nucl. Phys. B524 (1998) pp. 23–40, arXiv: hep-ph/9706315 [hep-ph] (cit. on p. 22).

[80] W. Porod et al.: *Testing neutrino mixing at future collider experiments*, Phys. Rev. D63 (2001) p. 115004, arXiv: hep-ph/0011248 [hep-ph] (cit. on p. 22).

[81] M. Hirsch and J. W. F. Valle: *Supersymmetric origin of neutrino mass*, New J. Phys. 6 (2004) p. 76, arXiv: hep-ph/0405015 [hep-ph] (cit. on p. 22).

[82] ATLAS Collaboration: *Search for supersymmetry in events containing a same-flavour opposite-sign dilepton pair, jets, and large missing transverse momentum in $\sqrt{s}$ = 8 TeV pp collisions with the ATLAS detector*, Eur. Phys. J. C75.7 (2015) p. 318, [Erratum: Eur. Phys. J.C75,no.10,463(2015)], arXiv: 1503.03290 [hep-ex] (cit. on p. 25).

[83] CMS Collaboration: *Search for Physics Beyond the Standard Model in Events with Two Leptons, Jets, and Missing Transverse Momentum in pp Collisions at sqrt(s) = 8 TeV*, JHEP 04 (2015) p. 124, arXiv: 1502.06031 [hep-ex] (cit. on p. 25).

[84] CMS Collaboration: *Search for new physics in final states with two opposite-sign, same-flavor leptons, jets, and missing transverse momentum in pp collisions at $\sqrt{s}$ = 13 TeV*, Submitted to: JHEP (2016), arXiv: 1607.00915 [hep-ex] (cit. on p. 25).

[85] A. Djouadi, J.-L. Kneur, and G. Moultaka: *SuSpect: A Fortran code for the supersymmetric and Higgs particle spectrum in the MSSM*, Comput. Phys. Commun. 176 (2007) pp. 426–455, arXiv: hep-ph/0211331 [hep-ph] (cit. on p. 25).

[86] C. F. Berger et al.: *Supersymmetry Without Prejudice*, JHEP 02 (2009) p. 023, arXiv: 0812.0980 [hep-ph] (cit. on p. 25).

[87] P. Bechtle et al.: *The Light and Heavy Higgs Interpretation of the MSSM* (2016), arXiv: 1608.00638 [hep-ph] (cit. on p. 25).

[88] A. Collaboration: *SUSY summary plots*, 2016, url: https://atlas.web.cern.ch/Atlas/GROUPS/PHYSICS/CombinedSummaryPlots/SUSY/ATLAS_SUSY_Summary/history.html (visited on 06/29/2016) (cit. on p. 26).

[89] O. S. Bruning et al.: *LHC Design Report Vol.1: The LHC Main Ring* (2004), ed. by O. S. Bruning (cit. on p. 27).

[90] O. Buning et al.: *LHC Design Report. 2. The LHC infrastructure and general services* (2004), ed. by O. Buning (cit. on p. 27).

[91] M. Benedikt et al.: *LHC Design Report. 3. The LHC injector chain* (2004), ed. by M. Benedikt (cit. on p. 27).

[92] L. Evans: *The LHC machine*, PoS EPS-HEP2009 (2009) p. 004 (cit. on pp. 27, 29).

[93] K. Schindl: *The PS booster as preinjector for LHC*, Part.Accel. 58 (1997) pp. 63–78 (cit. on p. 27).

[94] F. Blas et al.: *Conversion of the PS complex as LHC proton preinjector*, Conf.Proc. C970512 (1997) pp. 973–975 (cit. on p. 27).

[95] P. Collier et al.: *The SPS as injector for LHC: Conceptual design* (1997) (cit. on p. 27).

[96] D. Boussard et al.: *The LHC superconducting cavities* (1999) pp. 946–948 (cit. on p. 27).

[97] M. Bajko et al.: *Status Report on the Superconducting Dipole Magnet Production for the LHC*, IEEE Trans. Appl. Supercond. 17.LHC-PROJECT-Report-1002. CERN-LHC-PROJECT-Report-1002. 2 (2007) 1097–1100. 5 p, URL: http://cds.cern.ch/record/1028174 (cit. on p. 28).

[98] C. Wyss: *LHC arc dipole status report* (1999) pp. 149–153 (cit. on p. 28).

[99] ATLAS Collaboration: *The ATLAS Experiment at the CERN Large Hadron Collider*, JINST 3 (2008) S08003 (cit. on pp. 28, 32, 33, 36).

[100] CMS Collaboration: *The CMS experiment at the CERN LHC*, JINST 3 (2008) S08004 (cit. on p. 28).

[101] K. Aamodt et al.: *The ALICE experiment at the CERN LHC*, JINST 3 (2008) S08002 (cit. on p. 28).

[102] J. Alves A. Augusto et al.: *The LHCb Detector at the LHC*, JINST 3 (2008) S08005 (cit. on p. 29).

[103] O. Adriani et al.: *The LHCf detector at the CERN Large Hadron Collider*, JINST 3 (2008) S08006 (cit. on p. 29).

[104] G. Anelli et al.: *The TOTEM experiment at the CERN Large Hadron Collider*, JINST 3 (2008) S08007 (cit. on p. 29).

[105] B. Povh et al.: *Teilchen und Kerne. Eine Einführung in die physikalischen Konzepte*, Sixth, Springer-Verlag GmbH, 2004, ISBN: 3540210652 (cit. on p. 29).

[106] C. Berger: *Elementarteilchenphysik: Von den Grundlagen zu den modernen Experimenten*, Springer-Lehrbuch, Springer Berlin Heidelberg, 2014, ISBN: 9783642417528 (cit. on p. 29).

[107] *Proceedings of the 4th Evian Workshop on LHC beam operation*, Organisers: Chairman: Lamont, M; Scientific Secretary: Meddahi, M; Informatics support: Charrue, P; Woekshop Secretary: Dubourg, S, CERN, Geneva: CERN, 2013, URL: https://cds.cern.ch/record/1562028 (cit. on p. 29).

[108] *Proceedings of the 3th Evian Workshop on LHC beam operation*, Organisers: Chairman: Mike LAMONT; Scientific Secretary: Malika MEDDAHI; Editor of the Proceedings: Brennan GODDARD, Sylvia DUBOURG; Informatics and infrastructure support: Pierre CHARRUE Workshop Secretaries: Sylvia DUBOURG, CERN, Geneva: CERN, 2011, URL: https://cds.cern.ch/record/1451243 (cit. on p. 29).

[109] R. Bruce et al.: *Baseline LHC machine parameters and configuration of the 2015 proton run* (2014), arXiv: 1410.5990 [physics.acc-ph] (cit. on p. 30).

[110] ATLAS Collaboration: *LuminosityPublicResults*, 2013, URL: https://twiki.cern.ch/twiki/bin/view/AtlasPublic/LuminosityPublicResults#2012_pp_Collisions (visited on 04/30/2015) (cit. on p. 30).

[111] ATLAS Collaboration: *Computer generated image of the whole ATLAS detector*, 2008, URL: http://cds.cern.ch/record/1095924/ (visited on 05/01/2015) (cit. on p. 31).

[112] A. Yamamoto et al.: *The ATLAS central solenoid*, Nucl.Instrum.Meth. A584 (2008) pp. 53–74 (cit. on p. 32).

[113] J. P. Badiou et al.: *ATLAS barrel toroid: Technical Design Report*, Technical Design Report ATLAS, Electronic version not available, Geneva: CERN, 1997, URL: https://cds.cern.ch/record/331065 (cit. on p. 32).

[114] ATLAS Collaboration: *ATLAS end-cap toroids: Technical Design Report*, Technical Design Report ATLAS, Electronic version not available, Geneva: CERN, 1997, URL: https://cds.cern.ch/record/331066 (cit. on p. 32).

[115] ATLAS Collaboration: *Computer generated image of the ATLAS inner detector*, 2008, URL: http://cds.cern.ch/record/1095926/ (visited on 05/10/2015) (cit. on p. 33).

[116] ATLAS Collaboration: *ATLAS inner detector: Technical Design Report, 1*, Technical Design Report ATLAS, Geneva: CERN, 1997, URL: https://cds.cern.ch/record/331063 (cit. on p. 32).

[117] S. Haywood et al.: *ATLAS inner detector: Technical Design Report, 2*, Technical Design Report ATLAS, Geneva: CERN, 1997, URL: http://cds.cern.ch/record/331064 (cit. on p. 32).

[118] M. Capeans et al.: *ATLAS Insertable B-Layer Technical Design Report*, tech. rep. CERN-LHCC-2010-013. ATLAS-TDR-19, CERN, 2010, URL: https://cds.cern.ch/record/1291633 (cit. on p. 32).

[119] G. Aad et al.: *ATLAS pixel detector electronics and sensors*, JINST 3 (2008) P07007 (cit. on p. 34).

[120] M. Alam et al.: *ATLAS pixel detector: Technical design report* (1998) (cit. on p. 34).

[121] A. Abdesselam et al.: *The barrel modules of the ATLAS semiconductor tracker*, Nucl.Instrum.Meth. A568 (2006) pp. 642–671 (cit. on p. 34).

[122] A. Abdesselam et al.: *The ATLAS semiconductor tracker end-cap module*, Nucl.Instrum.Meth. A575 (2007) pp. 353–389 (cit. on p. 34).

[123] E. Abat et al.: *The ATLAS Transition Radiation Tracker (TRT) proportional drift tube: Design and performance*, JINST 3 (2008) P02013 (cit. on p. 34).

[124] T. Akesson et al.: *Status of design and construction of the Transition Radiation Tracker (TRT) for the ATLAS experiment at the LHC*, Nucl.Instrum.Meth. A522 (2004) pp. 131–145 (cit. on p. 34).

[125] F. Sefkow and C. Zeitnitz: "Calorimetry: Precise Energy Measurements", *Physics at the Terascale*, ed. by I. Brock and T. Schorner-Sadenius, Wiley-VCH Verlag GmbH & Co. KGaA, 2011 pp. 313–331, ISBN: 9783527634965 (cit. on p. 35).

[126] ATLAS Collaboration: *Computer Generated image of the ATLAS calorimeter*, 2008, URL: https://cds.cern.ch/record/1095927 (visited on 05/10/2015) (cit. on p. 35).

[127] ATLAS Collaboration: *ATLAS liquid-argon calorimeter: Technical Design Report*, Technical Design Report ATLAS, Geneva: CERN, 1996, URL: http://cds.cern.ch/record/331061 (cit. on p. 35).

[128] ATLAS Collaboration: *ATLAS tile calorimeter: Technical Design Report*, Technical Design Report ATLAS, Geneva: CERN, 1996, URL: http://cds.cern.ch/record/331062 (cit. on p. 35).

[129] K. Hoepfner and O. Kortner: "Muon Detectors: Catching Penetrating Particles", *Physics at the Terascale*, ed. by I. Brock and T. Schorner-Sadenius, Wiley-VCH Verlag GmbH & Co. KGaA, 2011 pp. 333–345, isbn: 9783527634965 (cit. on p. 36).

[130] C. Zupancic: *Physical and statistical foundations of TeV muon spectroscopy*, tech. rep. CERN-EP-85-144, CERN, 1985, url: http://cds.cern.ch/record/162367 (cit. on p. 36).

[131] ATLAS Collaboration: *ATLAS muon spectrometer: Technical Design Report*, Technical Design Report ATLAS, Geneva: CERN, 1997, url: https://cds.cern.ch/record/331068 (cit. on p. 37).

[132] S. Palestini: *The muon spectrometer of the ATLAS experiment*, Nuclear Physics B - Proceedings Supplements 125.0 (2003) pp. 337 –345, Innovative Particle and Radiation Detectors, issn: 0920-5632 (cit. on p. 37).

[133] G. Mikenberg: *The ATLAS Muon Spectrometer*, Modern Physics Letters A 25.09 (2010) pp. 649–667 (cit. on p. 37).

[134] M. Curatolo: *The Monitored Drift Tube (MDT) chambers for the muon precision tracking in the ATLAS spectrometer*, Nucl. Phys. Proc. Suppl. 78 (1999) pp. 422–425 (cit. on p. 37).

[135] T. Argyropoulos et al.: *Cathode strip chambers in ATLAS: Installation, commissioning and in situ performance*, IEEE Trans.Nucl.Sci. 56 (2009) pp. 1568–1574 (cit. on p. 37).

[136] ATLAS Collaboration: *Computer generated image of the ATLAS Muons subsystem*, 2008, url: http://cds.cern.ch/record/1095929 (visited on 05/10/2015) (cit. on p. 37).

[137] A. Di Ciaccio: *The ATLAS RPC trigger chamber system*, Nucl.Instrum.Meth. A572 (2007) pp. 48–49 (cit. on p. 37).

[138] K. Nagai: *Thin gap chambers in ATLAS*, Nucl.Instrum.Meth. A384 (1996) pp. 219–221 (cit. on p. 37).

[139] G. Aielli et al.: *The RPC first level muon trigger in the barrel of the ATLAS experiment*, Nucl. Phys. Proc. Suppl. 158 (2006) pp. 11–15, [,11(2006)] (cit. on p. 37).

[140] K. Kordas et al.: *The ATLAS Data Acquisition and Trigger: concept, design and status*, Nuclear Physics B - Proceedings Supplements 172 (2007) pp. 178 –182, Proceedings of the 10th Topical Seminar on Innovative Particle and Radiation DetectorsProceedings of the 10th Topical Seminar on Innovative Particle and Radiation Detectors, issn: 0920-5632, url: http://www.sciencedirect.com/science/article/pii/S0920563207005865 (cit. on p. 37).

[141] F. Pastore: "ATLAS Trigger: design and commissioning", CERN, Geneva: CERN, 2009, url: http://cdsweb.cern.ch/record/1229417/files/ATL-DAQ-PROC-2009-045.pdf (cit. on p. 37).

[142] ATLAS Collaboration: *Performance of the ATLAS Trigger System in 2010*, Eur. Phys. J. C72 (2012) p. 1849, arXiv: 1110.1530 [hep-ex] (cit. on pp. 37–39).

[143] ATLAS Collaboration: *Performance of the ATLAS muon trigger in pp collisions at $\sqrt{s}$ = 8 TeV*, Eur. Phys. J. C75.3 (2015) p. 120, arXiv: 1408.3179 [hep-ex] (cit. on pp. 38, 57).

[144] ATLAS Collaboration: *Performance of the Electron and Photon Trigger in p-p Collisions at sqrt(s) = 7 TeV* (2011) (cit. on p. 39).

[145] S Xella: *Physics objects reconstruction in the ATLAS experiment*, tech. rep. ATL-GEN-PROC-2013-001, CERN, 2013, URL: https://cds.cern.ch/record/1519113 (cit. on pp. 39, 40).

[146] M. Cacciari, G. P. Salam, and G. Soyez: *The anti- k t jet clustering algorithm*, Journal of High Energy Physics 2008.04 (2008) p. 063, URL: http://stacks.iop.org/1126-6708/2008/i=04/a=063 (cit. on p. 40).

[147] M. Cacciari and G. P. Salam: *Dispelling the myth for the jet-finder*, Physics Letters B 641.1 (2006) pp. 57 –61, ISSN: 0370-2693, URL: http://www.sciencedirect.com/science/article/pii/S0370269306010094 (cit. on p. 40).

[148] ATLAS Collaboration: *Measurement of the b-tag Efficiency in a Sample of Jets Containing Muons with 5 fb-1 of Data from the ATLAS Detector*, tech. rep. ATLAS-CONF-2012-043, CERN, 2012, URL: https://cds.cern.ch/record/1435197 (cit. on p. 40).

[149] ATLAS Collaboration: *Commissioning of the ATLAS high-performance b-tagging algorithms in the 7 TeV collision data*, tech. rep. ATLAS-CONF-2011-102, CERN, 2011, URL: http://cds.cern.ch/record/1369219 (cit. on p. 40).

[150] ATLAS Collaboration: *Electron performance measurements with the ATLAS detector using the 2010 LHC proton-proton collision data*, Eur. Phys. J. C72 (2012) p. 1909, arXiv: 1110.3174 [hep-ex] (cit. on p. 41).

[151] ATLAS Collaboration: *Electron efficiency measurements with the ATLAS detector using the 2012 LHC proton-proton collision data* (2014) (cit. on p. 41).

[152] ATLAS Collaboration: *Improved electron reconstruction in ATLAS using the Gaussian Sum Filter-based model for bremsstrahlung* (2012) (cit. on p. 41).

[153] ATLAS Collaboration: *Electron efficiency measurements with the ATLAS detector using the 2012 LHC proton-proton collision data*, tech. rep. ATLAS-CONF-2014-032, CERN, 2014, URL: http://cds.cern.ch/record/1706245 (cit. on pp. 41, 42).

[154] ATLAS Collaboration: *Expected photon performance in the ATLAS experiment*, tech. rep. ATL-PHYS-PUB-2011-007, CERN, 2011, URL: https://cds.cern.ch/record/1345329 (cit. on p. 42).

[155] ATLAS Collaboration: *Measurements of the photon identification efficiency with the ATLAS detector using 4.9 fb-1 of pp collision data collected in 2011*, tech. rep. ATLAS-CONF-2012-123, CERN, 2012, URL: https://cds.cern.ch/record/1473426 (cit. on p. 42).

[156] ATLAS Collaboration: *Expected performance of the ATLAS experiment: detector, trigger and physics*, Geneva: CERN, 2009, URL: https://cds.cern.ch/record/1125884 (cit. on p. 42).

[157] ATLAS Collaboration: *Measurement of the muon reconstruction performance of the ATLAS detector using 2011 and 2012 LHC proton-proton collision data*, Eur. Phys. J. C 74.arXiv:1407.3935. CERN-PH-EP-2014-151 (2014) 3130. 34 p, URL: http://cds.cern.ch/record/1743068 (cit. on pp. 42, 43).

[158] ATLAS Collaboration: *Muon reconstruction efficiency and momentum resolution of the ATLAS experiment in proton-proton collisions at $\sqrt{s}$ = 7 TeV in 2010*, Eur. Phys. J. C74.9 (2014) p. 3034, arXiv: 1404.4562 [hep-ex] (cit. on p. 42).

[159] S. Hassani et al.: *A muon identification and combined reconstruction procedure for the ATLAS detector at the LHC using the (MUONBOY, STACO, MuTag) reconstruction packages*, Nucl. Instrum. Meth. A572 (2007) pp. 77–79 (cit. on p. 43).

[160] T Lagouri et al.: *A Muon Identification and Combined Reconstruction Procedure for the ATLAS Detector at the LHC at CERN* (2003), revised version number 1 submitted on 2003-10-30 18:34:15, url: https://cds.cern.ch/record/681410 (cit. on p. 43).

[161] F. Tarrade: *Reconstruction and identification of hadronic Tau decays in ATLAS*, Nuclear Physics B - Proceedings Supplements 169 (2007) pp. 357 –362, Proceedings of the Ninth International Workshop on Tau Lepton PhysicsTAU06, issn: 0920-5632, url: http://www.sciencedirect.com/science/article/pii/S092056320700268X (cit. on p. 44).

[162] ATLAS Collaboration: *Performance of the Reconstruction and Identification of Hadronic Tau Decays in ATLAS with 2011 Data*, tech. rep. ATLAS-CONF-2012-142, CERN, 2012, url: http://cds.cern.ch/record/1485531 (cit. on p. 44).

[163] ATLAS Collaboration: *Identification and energy calibration of hadronically decaying tau leptons with the ATLAS experiment in pp collisions at $\sqrt{s}$=8 TeV*, Eur. Phys. J. C 75.arXiv:1412.7086. CERN-PH-EP-2014-227 (2014) 303. 21 p, url: https://cds.cern.ch/record/1978197 (cit. on pp. 44–46).

[164] B. P. Roe et al.: *Boosted decision trees, an alternative to artificial neural networks*, Nucl. Instrum. Meth. A543.2-3 (2005) pp. 577–584, arXiv: physics/0408124 [physics] (cit. on p. 44).

[165] ATLAS Collaboration: *Performance of Missing Transverse Momentum Reconstruction in ATLAS studied in Proton-Proton Collisions recorded in 2012 at 8 TeV*, tech. rep. ATLAS-CONF-2013-082, CERN, 2013, url: https://cds.cern.ch/record/1570993 (cit. on pp. 45, 47).

[166] ATLAS Collaboration: *Performance of Missing Transverse Momentum Reconstruction in Proton-Proton Collisions at 7 TeV with ATLAS*, Eur. Phys. J. C72 (2012) p. 1844, arXiv: 1108.5602 [hep-ex] (cit. on p. 45).

[167] P. J. Clark: *The ATLAS detector simulation*, Nucl. Phys. Proc. Suppl. 215 (2011) pp. 85–88 (cit. on p. 47).

[168] ATLAS Collaboration: *The ATLAS Simulation Infrastructure*, Eur. Phys. J. C70 (2010) pp. 823–874, arXiv: 1005.4568 [physics.ins-det] (cit. on p. 47).

[169] G. Duckeck et al.: *ATLAS computing: Technical design report* (2005) (cit. on p. 47).

[170] T. Gleisberg et al.: *Event generation with SHERPA 1.1*, JHEP 02 (2009) p. 007, arXiv: 0811.4622 [hep-ph] (cit. on p. 48).

[171] B. Andersson et al.: *Parton Fragmentation and String Dynamics*, Phys. Rept. 97 (1983) pp. 31–145 (cit. on p. 48).

[172] T. Sjostrand, S. Mrenna, and P. Z. Skands: *PYTHIA 6.4 Physics and Manual*, JHEP 05 (2006) p. 026, arXiv: hep-ph/0603175 [hep-ph] (cit. on p. 48).

[173] R. Kuhn et al.: *APACIC++: A PArton Cascade In C++, version 1.0*, Comput. Phys. Commun. 134 (2001) pp. 223–266, arXiv: hep-ph/0004270 [hep-ph] (cit. on p. 48).

[174] E. Barberio, B. van Eijk, and Z. Was: *PHOTOS: A Universal Monte Carlo for QED radiative corrections in decays*, Comput. Phys. Commun. 66 (1991) pp. 115–128 (cit. on p. 48).

[175] H.-L. Lai et al.: *New parton distributions for collider physics*, Phys. Rev. D82 (2010) p. 074024, arXiv: 1007.2241 [hep-ph] (cit. on p. 48).

[176] W.-K. Tung: *New generation of parton distributions with uncertainties from global QCD analysis*, Acta Phys. Polon. B33 (2002) pp. 2933–2938, arXiv: hep-ph/0206114 [hep-ph] (cit. on p. 48).

[177] G. Corcella et al.: *HERWIG 6: An Event generator for hadron emission reactions with interfering gluons (including supersymmetric processes)*, JHEP 01 (2001) p. 010, arXiv: hep-ph/0011363 [hep-ph] (cit. on p. 48).

[178] G. Corcella et al.: *HERWIG 6.5 release note* (2002), arXiv: hep-ph/0210213 [hep-ph] (cit. on p. 48).

[179] G. Marchesini et al.: *HERWIG: A Monte Carlo event generator for simulating hadron emission reactions with interfering gluons. Version 5.1 - April 1991*, Comput. Phys. Commun. 67 (1992) pp. 465–508 (cit. on p. 48).

[180] S. Jadach et al.: *The tau decay library TAUOLA: Version 2.4*, Comput. Phys. Commun. 76 (1993) pp. 361–380 (cit. on p. 48).

[181] P. Golonka et al.: *The Tauola photos F environment for the TAUOLA and PHOTOS packages: Release. 2.*, Comput. Phys. Commun. 174 (2006) pp. 818–835, arXiv: hep-ph/0312240 [hep-ph] (cit. on p. 48).

[182] M. Bahr et al.: *Herwig++ Physics and Manual*, Eur. Phys. J. C58 (2008) pp. 639–707, arXiv: 0803.0883 [hep-ph] (cit. on p. 48).

[183] M. L. Mangano et al.: *ALPGEN, a generator for hard multiparton processes in hadronic collisions*, JHEP 07 (2003) p. 001, arXiv: hep-ph/0206293 [hep-ph] (cit. on p. 48).

[184] S. Frixione and B. R. Webber: *The MC@NLO 3.3 Event Generator* (2006), arXiv: hep-ph/0612272 [hep-ph] (cit. on p. 49).

[185] S. Frixione, P. Nason, and B. R. Webber: *Matching NLO QCD and parton showers in heavy flavor production*, JHEP 08 (2003) p. 007, arXiv: hep-ph/0305252 [hep-ph] (cit. on p. 49).

[186] S. Frixione and B. R. Webber: *Matching NLO QCD computations and parton shower simulations*, JHEP 06 (2002) p. 029, arXiv: hep-ph/0204244 [hep-ph] (cit. on p. 49).

[187] S. Frixione, P. Nason, and C. Oleari: *Matching NLO QCD computations with Parton Shower simulations: the POWHEG method*, JHEP 11 (2007) p. 070, arXiv: 0709.2092 [hep-ph] (cit. on p. 49).

[188] B. P. Kersevan and E. Richter-Was: *The Monte Carlo event generator AcerMC versions 2.0 to 3.8 with interfaces to PYTHIA 6.4, HERWIG 6.5 and ARIADNE 4.1*, Comput. Phys. Commun. 184 (2013) pp. 919–985, arXiv: hep-ph/0405247 [hep-ph] (cit. on p. 49).

[189] S. Agostinelli et al.: *GEANT4: A Simulation toolkit*, Nucl. Instrum. Meth. A506 (2003) pp. 250–303 (cit. on p. 49).

[190] ATLAS Collaboration: *The simulation principle and performance of the ATLAS fast calorimeter simulation FastCaloSim* (2010) (cit. on p. 49).

[191] *SFM analysis framework*, 2013, URL: https://wiki.physik.uni-bonn.de/atlas/public/index.php/SFM (visited on 06/25/2015) (cit. on p. 49).

[192] D. Berge, J. Haller, and A. Krasznahorkay: *SFrame: A high-performance ROOT-based framework for HEP data analysis*, PoS ACAT2010 (2010) p. 048 (cit. on p. 49).

[193] R. Brun, F. Rademakers, and S. Panacek: *ROOT, an object oriented data analysis framework*, Conf. Proc. C000917 (2000) pp. 11–42 (cit. on p. 49).

[194] *SUSYTools*, 2013, URL: https://svnweb.cern.ch/trac/atlasoff/browser/PhysicsAnalysis/SUSYPhys/SUSYTools (visited on 06/25/2015) (cit. on p. 49).

[195] ATLAS Collaboration: *Measurement of top-quark pair differential cross-sections in the l+jets channel in pp collisions at $\sqrt{s}$ = 7 TeV using the ATLAS detector* (2013) (cit. on p. 50).

[196] W. Beenakker et al.: *Squark and gluino production at hadron colliders*, Nucl. Phys. B492 (1997) pp. 51–103, arXiv: hep-ph/9610490 [hep-ph] (cit. on p. 51).

[197] W. Beenakker et al.: *Squark and Gluino Hadroproduction*, Int. J. Mod. Phys. A26 (2011) pp. 2637–2664, arXiv: 1105.1110 [hep-ph] (cit. on p. 51).

[198] W. Beenakker et al.: *Soft-gluon resummation for squark and gluino hadroproduction*, JHEP 12 (2009) p. 041, arXiv: 0909.4418 [hep-ph] (cit. on p. 51).

[199] A. Kulesza and L. Motyka: *Soft gluon resummation for the production of gluino-gluino and squark-antisquark pairs at the LHC*, Phys. Rev. D80 (2009) p. 095004, arXiv: 0905.4749 [hep-ph] (cit. on p. 51).

[200] A. Kulesza and L. Motyka: *Threshold resummation for squark-antisquark and gluino-pair production at the LHC*, Phys. Rev. Lett. 102 (2009) p. 111802, arXiv: 0807.2405 [hep-ph] (cit. on p. 51).

[201] ATLAS Collaboration: *Jet energy measurement and its systematic uncertainty in proton-proton collisions at $\sqrt{s}$ = 7 TeV with the ATLAS detector*, Eur. Phys. J. C75 (2015) p. 17, arXiv: 1406.0076 [hep-ex] (cit. on pp. 55, 93).

[202] ATLAS Collaboration: *Tagging and suppression of pileup jets* (2014) (cit. on p. 55).

[203] G. Pasztor et al.: *Electron trigger performance in 2012 ATLAS data*, tech. rep. ATL-COM-DAQ-2015-091, CERN, 2015, URL: https://cds.cern.ch/record/2032463 (cit. on p. 58).

[204] ATLAS Collaboration: *Search for Supersymmetry with jets and missing transverse momentum and one lepton at sqrt(s) = 7 TeV*, tech. rep. ATL-PHYS-INT-2011-056, CERN, 2011, URL: https://cds.cern.ch/record/1358865 (cit. on pp. 71, 72).

[205] G. Cowan et al.: *Asymptotic formulae for likelihood-based tests of new physics*, Eur. Phys. J. C71 (2011) p. 1554, [Erratum: Eur. Phys. J.C73,2501(2013)], arXiv: 1007.1727 [physics.data-an] (cit. on pp. 82, 122).

[206] G. Cowan: *Expected discovery significance for counting experiment with background uncertainty*, 2012, URL: http://www.pp.rhul.ac.uk/~cowan/atlas/cowan_statforum_8may12.pdf (visited on 10/24/2015) (cit. on p. 84).

[207] ATLAS Collaboration: *Search for Supersymmetry in Events with Large Missing Transverse Momentum, Jets, and at Least One Tau Lepton in 21 fb^{-1} of $\sqrt{s}$ = 8 TeV Proton-Proton Collision Data with the ATLAS Detector*, tech. rep. ATLAS-CONF-2013-026, CERN, 2013, URL: https://cds.cern.ch/record/1525882 (cit. on p. 86).

[208] ATLAS Collaboration: *Jet energy measurement with the ATLAS detector in proton-proton collisions at $\sqrt{s}$ = 7 TeV*, Eur. Phys. J. C73.3 (2013) p. 2304, arXiv: 1112.6426 [hep-ex] (cit. on p. 93).

[209] ATLAS Collaboration: *Jet energy resolution in proton-proton collisions at $\sqrt{s}$ = 7 TeV recorded in 2010 with the ATLAS detector*, Eur. Phys. J. C73.3 (2013) p. 2306, arXiv: 1210.6210 [hep-ex] (cit. on p. 94).

[210] ATLAS Collaboration: *Identification and energy calibration of hadronically decaying tau leptons with the ATLAS experiment in pp collisions at $\sqrt{s}$=8 TeV*, Eur. Phys. J. C75.7 (2015) p. 303, arXiv: 1412.7086 [hep-ex] (cit. on p. 94).

[211] ATLAS Collaboration: *Preliminary results on the muon reconstruction efficiency, momentum resolution, and momentum scale in ATLAS 2012 pp collision data* (2013) (cit. on p. 95).

[212] ATLAS Collaboration: *Electron and photon energy calibration with the ATLAS detector using LHC Run 1 data*, Eur. Phys. J. C74.10 (2014) p. 3071, arXiv: 1407.5063 [hep-ex] (cit. on p. 95).

[213] ATLAS Collaboration: *Procedure for the LHC Higgs boson search combination in summer 2011* (2011) (cit. on p. 121).

[214] J. Neyman and E. S. Pearson: *On the Problem of the Most Efficient Tests of Statistical Hypotheses*, Philosophical Transactions of the Royal Society of London A: Mathematical, Physical and Engineering Sciences 231.694-706 (1933) pp. 289–337, issn: 0264-3952, eprint: http://rsta.royalsocietypublishing.org/content/231/694-706/289.full.pdf (cit. on p. 121).

[215] M. Baak et al.: *HistFitter software framework for statistical data analysis*, Eur. Phys. J. C75 (2015) p. 153, arXiv: 1410.1280 [hep-ex] (cit. on pp. 122, 129).

[216] K. Cranmer et al.: *HistFactory: A tool for creating statistical models for use with RooFit and RooStats* (2012) (cit. on pp. 129, 131).

[217] H. A. Junkerkalefeld: *Die Suche nach Supersymmetrie mit semileptonischen Zwei-Tau-Ereignissen beim ATLAS-Experiment für Schwerpunktsenergien von 13 TeV*, Bachelor Thesis: University of Bonn, 2016 (cit. on p. 136).

[218] A. Collaboration: *Search for squarks and gluinos in events with hadronically decaying tau leptons, jets and missing transverse momentum in proton-proton collisions at $\sqrt{s}$ = 13 TeV recorded with the ATLAS detector* (2016), arXiv: 1607.05979 [hep-ex] (cit. on p. 136).

[219] ATLAS Top Group: *2012 Top Cross Sections*, tech. rep., 2013, url: https://twiki.cern.ch/twiki/bin/viewauth/AtlasProtected/TopCommonParametersMC12 (cit. on p. 159).